

Chapter 18

OPTICAL AND INFRARED PROPERTIES OF THE ATMOSPHERE

R. W. Fenn
S. A. Clough
W. O. Gallery
R. E. Good
F. X. Kneizys

J. D. Mill Lt. Col. USAF
L. S. Rothman
E. P. Shettle
F. E. Volz

This chapter deals with the absorption, scattering, emission and refractive properties of the natural atmosphere from the ultraviolet through the microwave region. Nonlinear propagation processes (such as thermal blooming) are not covered.

The natural atmosphere includes the range of those average conditions which are not directly affected by limited local processes or sources, such as gases or particulates from a fire or industrial plant, a dust cloud from vehicular traffic etc. The natural atmosphere does include the effects of molecules, aerosol (haze) particles, clouds, fogs, rain, and snow. The vertical extent of the atmosphere is from the surface up to 100 km altitude. A brief discussion is included on the earth's surface reflectance properties since they also affect the atmospheric optical properties.

The chapter includes descriptions of the basic physical relationships of optical propagation as well as the current state of experimental knowledge and modeling of the atmospheric propagation medium. An extensive annotated bibliography covering much of the material of this chapter was compiled by Wiscombe [1983] in *Reviews of Geophysics and Space Physics*.

18.1 ATMOSPHERIC GASES

18.1.1 Atmospheric Molecules, Models of the Atmospheric Composition

The propagation of optical and infrared radiation through the atmosphere depends on the composition and variability of the atmosphere. Systematic variations in the density, pressure, temperature, water vapor, and ozone as a function of latitude and season have been known for many years. The development of model atmospheres goes back to the

1920s. Early Standard Atmosphere Models represented mean conditions of temperature, density, and pressure as a function of altitude. During the 1950s and 1960s extensions and supplemental atmospheres were derived that describe in addition the seasonal and latitudinal variability of atmospheric structure (see Chapters 14 and 15).

For the purpose of modeling the optical properties of the atmosphere, specifically as described in Sections 18.4.1 (FASCODE) and 18.4.2 (LOWTRAN), the 1962 U.S. Standard Atmosphere and supplemental model atmospheres were used as models. Although updated Standard Atmospheres have been published as recently as 1976, differences are limited to altitudes above 50 km where the adopted radiance models were not well characterized.

Pressure, temperature, water vapor density, and ozone density profiles as a function of altitude are provided to describe these molecular atmospheric models. These profiles, taken from McClatchey et al. [1972], correspond to the *U.S. Standard Atmosphere, 1962* and five supplementary models [Cole et al., 1965 or *U.S. Standard Atmosphere Supplements 1966*]: Tropical (15°N), Midlatitude Summer (45°N, July), Midlatitude Winter (45°N, January), Subarctic Summer (60°N, July), and Subarctic Winter (60°N, January). These profiles are identical to the ones used in the LOWTRAN code [Kneizys et al., 1980]. The water vapor and ozone latitude profiles added to the 1962 U.S. Standard Atmosphere by McClatchey et al. [1972] were obtained from Sissenwine et al. [1968] and Hering and Borden [1964] respectively, and correspond to mean annual values. The water vapor densities for the 1962 U.S. Standard Atmosphere correspond to relative humidities of approximately 50% for altitudes up to 10 km, whereas the relative humidity values for the other supplementary models tend to decrease with altitude from approximately 80% at sea level to approximately 30% at 10 km altitude. Above 12 km, the water vapor density profiles depicted here have been replaced by

CHAPTER 18

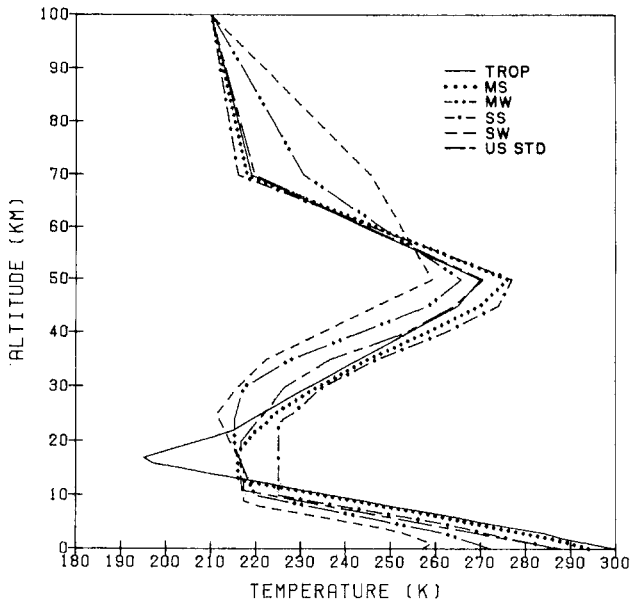


Figure 18-1. Temperature vs altitude for the six model atmospheres: tropical (TROP), midlatitude summer (MS), midlatitude winter (MW), subarctic summer (SS), subarctic winter (SW), and US standard (US STD).

more recent measurements [Remsburg et al., 1984] and are approximately 5 parts per million by volume (ppmv). For all model atmospheres, the gases CO_2 , N_2O , CO , CH_4 , N_2 , and O_2 are considered uniformly mixed, with mixing ratios of 330, 0.28, 0.075, 1.6, 7.905×10^5 , and 2.095×10^5 ppmv, respectively.

The temperature profiles for the six model atmospheres as a function of altitude are shown in Figure 18-1. The pressure profiles are given in Figure 18-2. Figures 18-3 a and b show the water vapor density versus altitude from 0 to 100 km, and an expanded profile from 0 to 30 km. Figures

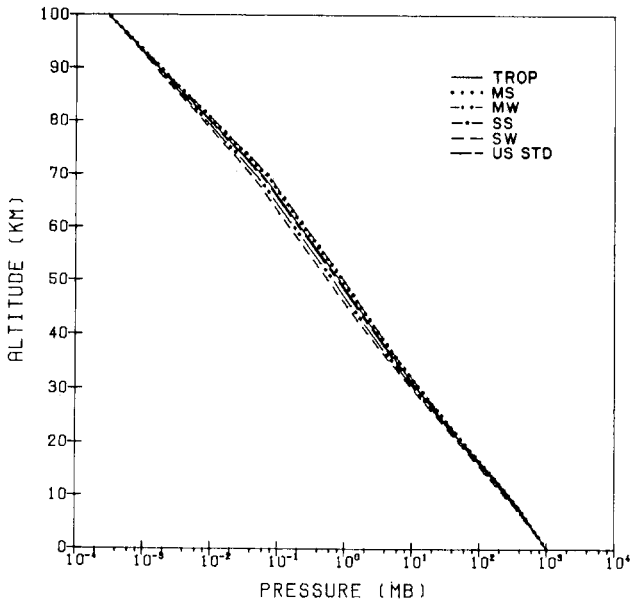


Figure 18-2. Pressure vs altitude for the six model atmospheres.

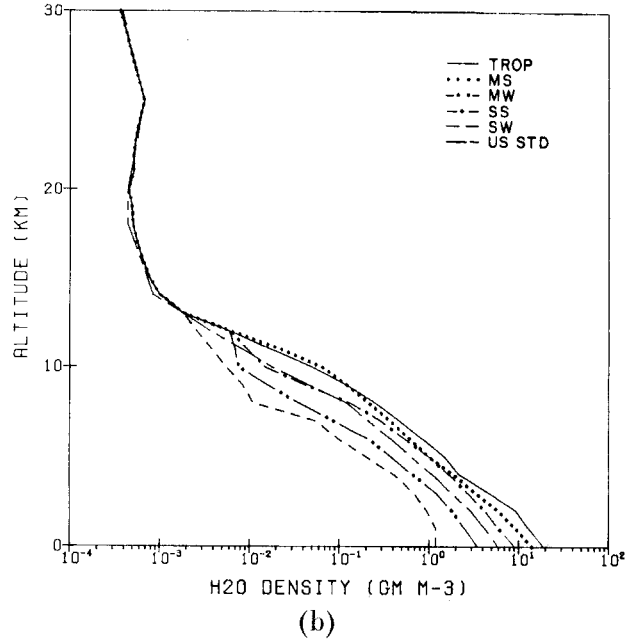
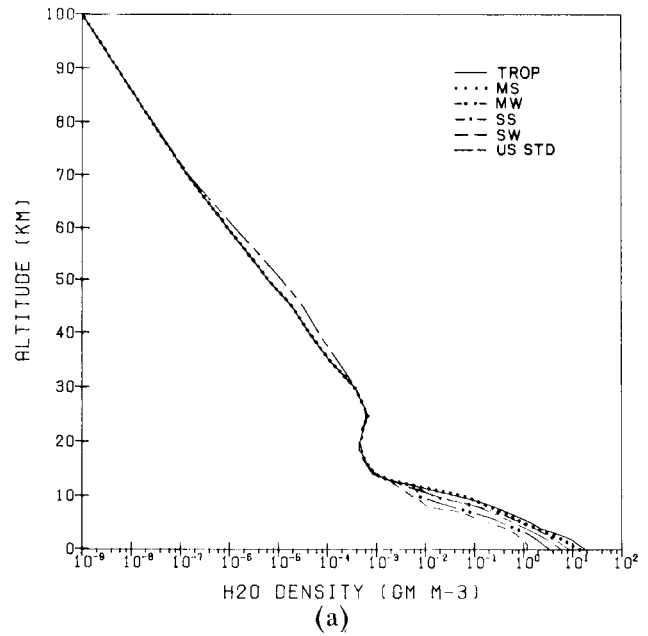


Figure 18-3. (a) Water vapor density profiles vs altitude for the six model atmospheres.

(b) Water vapor density profiles vs altitude for the six model atmospheres with the region from 0 to 30 km expanded.

18-4 a and b and Figures 18-5 a and b show similar profiles for ozone and relative air density.

Measurements made from balloon flights [Murcay et al., 1968] have shown the existence of nitric acid in the earth's atmosphere. Although nitric acid (HNO_3) is of only minor importance in atmospheric transmittance calculations, it has been shown to be a significant source of stratospheric emission, particularly in the atmospheric window region from 10 to 12 μm . The concentration of atmospheric nitric acid varies with altitude and also appears to depend on

OPTICAL AND INFRARED PROPERTIES OF THE ATMOSPHERE

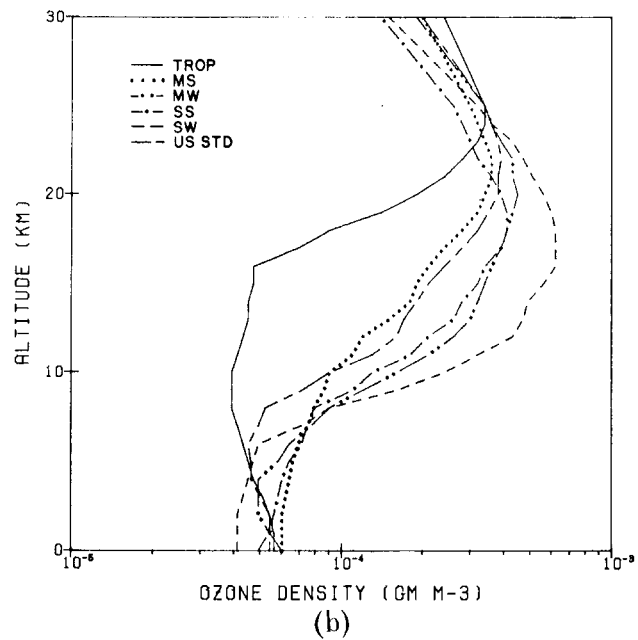
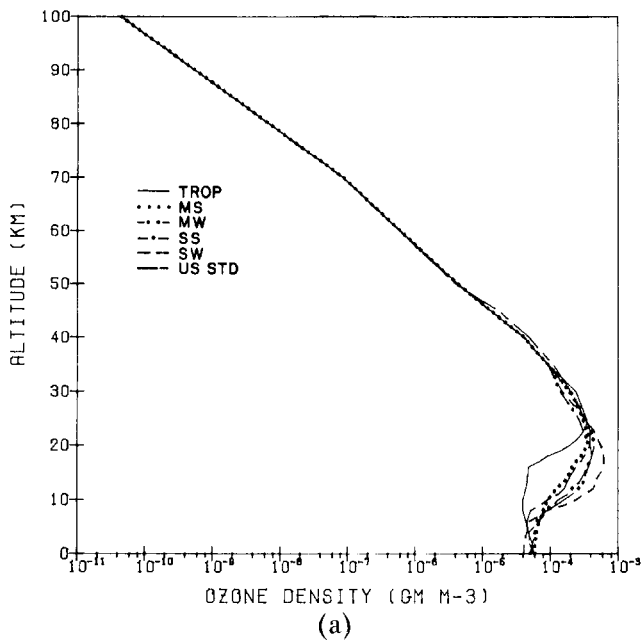


Figure 18-4. (a) Ozone density profiles vs altitude for the six model atmospheres.
 (b) Ozone density profiles vs altitude for the six model atmospheres with the region from 0 to 30 km expanded.

latitude and season. Figure 18-6 shows the volume mixing ratio profile of atmospheric nitric acid as a function of altitude from the measurements of Evans et al. [1975]. This profile has been chosen to represent a mean nitric acid profile for the six model atmospheres.

Since all of the above profiles were constructed, knowledge of the state of the atmosphere has increased. This is particularly true regarding the stratosphere and the concentration of minor constituents. For example, stratospheric water vapor concentrations for the six profiles given in Fig-

ure 18-3a and b are now known to be too high. The model atmospheres can still be considered representative of their respective conditions up to about 50 km for temperature, 30 km for ozone densities, and the tropopause (approximately from 8 km in the article to 15 km in the tropics) for water vapor. These models are still used for cases dominated

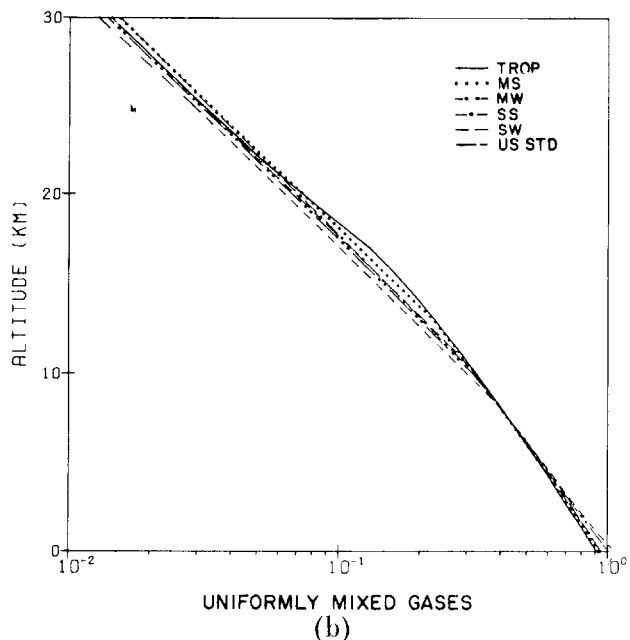
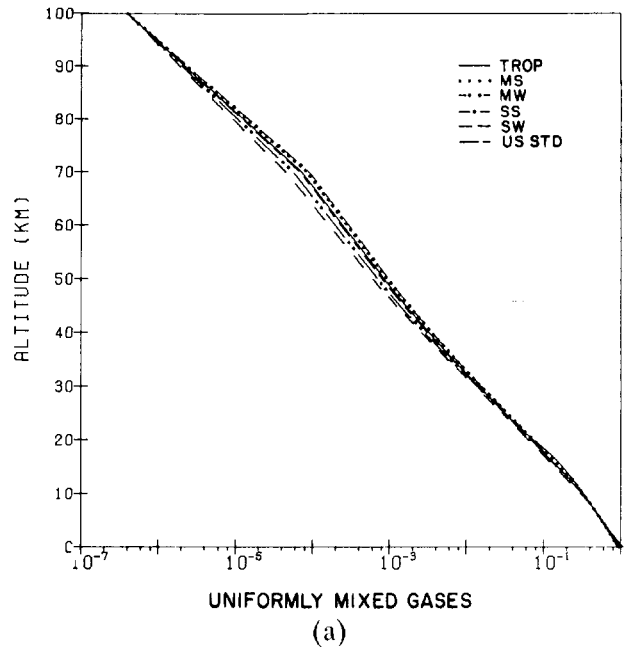


Figure 18-5. (a) Profile of $(P/P_0)(T_0/T)$, the relative air density, vs altitude for the six model atmospheres. The density of the uniformly mixed gases is proportional to this quantity. $P_0 = 1013$ mb and $T_0 = 273$ K.
 (b) Profile of $(P/P_0)(T_0/T)$, the relative air density, vs altitude for the six model atmospheres with the regions 0 to 30 km expanded.

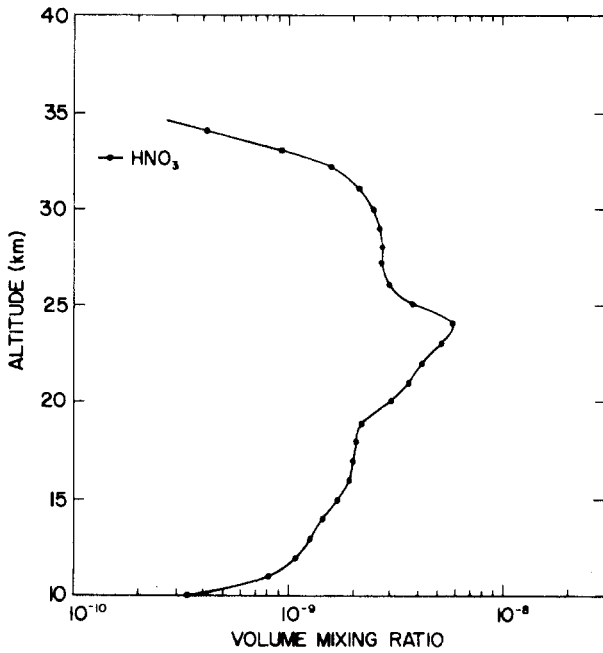


Figure 18-6. Volume mixing ratio profile for nitric acid vs altitude from the measurements of Evans et al. [1975]. This single profile is used with all of the six model atmospheres.

by conditions in the troposphere. For cases dominated by stratospheric conditions or where the distribution of minor constituents is significant, modelers should supply their own profiles.

There are several recent sources for profiles of temperature and minor constituent density. The *U.S. Standard Atmosphere 1976* updates the 1962 Standard for temperature above 50 km and provides revised estimates for the surface concentrations of what was termed previously the “uniformly mixed gases”. The new values for the volume mixing ratios of CO₂, N₂O, CO, and CH₄ are 330, 0.27, 0.19 and 1.50 ppmv. Actually the concentrations of these gases do show significant variations from these values, particularly with altitude in the stratosphere. Cole and Kantor [1978] provide sets of monthly mean temperature profiles up to 90 km at 15° intervals between the equator and the pole. Along with statistics on the variability of these profiles, they also provide models that portray longitudinal variations in monthly mean values of temperature during winter months and the vertical variation that occurs during stratospheric warming and cooling events in the winter arctic and subarctic. Houghton [1977] provides seasonal profile temperatures at 10°N, 40°N and 70°N up to 105 km plus the original references for the data.

For profiles of the minor constituents including ozone and stratospheric water vapor, WMO [1982] provides an up-to-date and exhaustive source. See also Chapter 21. Much of the profile data from this source plus some more recent measurements have been compiled as annual averages in 2 km steps in Smith [1982].

18.1.2 Molecular Absorption and Spectroscopic Parameters

18.1.2.1 The Role of Molecular Absorption.

Molecular absorption, that is, attenuation of electromagnetic radiation by the mechanism of molecules absorbing quanta of energy to alter vibrational and rotational states, is of prime significance in propagation in the atmosphere. Although the terrestrial atmosphere consists primarily of nitrogen, oxygen, and argon, absorption in the infrared region is dominated by species with very low concentrations but very active vibration-rotation bands such as water vapor, carbon dioxide, ozone, and nitrous oxide. Other active species also play an important role depending on the region of the electromagnetic spectrum being investigated or the layer of the atmosphere being probed.

In order to calculate transmittance due to a given spectral line in the atmosphere, it is useful to describe the absorption coefficient as a function of frequency for each line. Assuming superposition of the contribution from individual spectral transitions, the absorption coefficient $k(\nu)$ as a function of wavenumber ν (cm⁻¹) can be considered in general to be a product of the radiation field, the molecular system, and the coupling between them. This can be expressed [Clough et al., 1981] as

$$\tilde{k}(\nu) = \nu \tanh(hc\nu/2kT) \times \sum_i \rho(m_i) \tilde{S}_i(T) [f(\nu, \nu_i) + f(\nu, -\nu_i)], \quad (18.1)$$

where $\rho(m_i)$ (molec/cm³) is the density for the molecular species m_i with transition wavenumber ν_i responsible for the i 'th transition. $\tilde{S}_i(T)$ (molec/cm²)⁻¹ is the intensity of the transition at temperature T (K) appropriate to the line shape $f(\nu, \nu_i)$ (1/cm⁻¹). For most molecular species, the line intensity is a function of the expectation value of an expansion of the electric dipole moment. For some species, for example nitrogen and oxygen [Rothman and Goldman, 1981], the much weaker electric quadrupole and magnetic dipole moments are the means by which the quantum states change. In terms of intensity definition used in the AFGL line compilations, $S_i(T)$, discussed in the next section, we have the relationship

$$S_i(T) = \nu_i \tanh(hc\nu/2kT) \tilde{S}(T) = \nu_i \frac{1 - e^{-hc\nu_i/2kT}}{1 + e^{-hc\nu_i/2kT}} \tilde{S}_i(T). \quad (18.2)$$

The line shape function $f(\nu, \nu_i)$ is dependent on molecular species, broadening density and temperature. For collisional broadening in the impact limit, the form factor is given by the Lorentz line shape

OPTICAL AND INFRARED PROPERTIES OF THE ATMOSPHERE

$$f(\nu_i) = \frac{1}{\pi} \frac{\alpha_i}{(\nu - \nu_i)^2 + (\alpha_i)^2} \quad (18.3)$$

where α_i (cm^{-1}) is the collision broadened halfwidth at half maximum (HWHM). The monochromatic transmittance through a layer of homogeneous medium of thickness ℓ is obtained by the Lambert-Beers law

$$\tau_\nu = e^{-\tilde{k}(\nu)\ell}, \quad (18.4)$$

where the exponent is called the optical thickness.

The line intensity is temperature dependent through the Boltzmann factor and the internal partition function

$$S_i(T) = d_i(1 - e^{-hcE_i^0/kT}) \frac{e^{-hcE_i^0/kT}}{Q(T)} \quad (18.5)$$

where $Q(T)$ is the internal partition sum, E_i^0 (cm^{-1}) the energy of the lowerstate of the transition, and d_i is the transition strength. The collisional halfwidth depends on the specific molecule and can be expressed in terms of density and temperature as

$$\alpha_i(p, T) = \alpha_i^0 \left(\frac{p}{p_0} \right) \left(\frac{T}{T_0} \right)^{X_T} \quad (18.6)$$

(the exponent X_T is 1/2 with the usual classical theory assumption of temperature-independent collision diameters). The ratio of partition sums does not require the knowledge of any further parameters aside from the fundamental frequencies of the vibrational modes. Thus, at least for local thermodynamic equilibrium conditions, calculations of molecular absorption (transmission and emission) at high resolution basically require the knowledge of four essential parameters (1) the resonant frequency of the transition ν , (2) the intensity per absorbing molecule $S_i(T_0)$, (3) the Lorentz line width parameter α_i^0 , and (4) the energy of the lower state E_i^0 . The question of line shape will be discussed in more detail in Section 18.4.1. The effects of molecular (Rayleigh) scattering and of aerosol scattering and absorption will be discussed in Sections 18.1.4 and 18.2.1.5.

18.1.2.2 The Atmospheric Absorption Line Parameter Compilation. From the preceding discussion it can be seen that a compilation of spectroscopic data on individual molecular transitions would facilitate the so-called line-by-line calculations of spectra. These high resolution calculations, that is, calculations capable of reproducing spectra obtained by such instruments as Michelson interferometers, tunable diode lasers, and heterodyne spectrometers have been developed along with the advances in computer technology. In the 1960s a program was initiated at the Air Force Cambridge Research Laboratories (now AFGL) to create such a compilation and the associated codes to produce synthetic spectra [McClatchey et al., 1973]. The scope originally aimed at providing a complete set of data for all

vibration-rotation lines of naturally occurring molecules of significance in the terrestrial atmosphere. Since that time these data have been expanded in terms of the frequency covered, addition of trace species, and inclusion of weaker transitions [Rothman, 1981; Rothman et al., 1981, 1983a,b]. Historically, these data have been divided into two atlases, a Main Compilation comprising transitions of the most active terrestrial absorbers H_2O , CO_2 , O_3 , N_2O , CO , CH_4 , and O_2 , and a Trace Gas Compilation. The species presently covered by these data bases are summarized in Table 18-1. The isotopes are abbreviated by the code 161 $\equiv \text{H}_2^{16}\text{O}$, 162 $\equiv \text{HD}^{16}\text{O}$, etc. The first seven species (incorporated in the Main Atlas) include all transitions contributing to at least 10% absorption over a maximum atmospheric path. This has been determined from standard atmospheric models of the uniformly mixed gases and the two nonuniformly mixed gases, water vapor and ozone. The standard temperature chosen was 296 k. The gases in the Trace Gas Compilation were made available for a variety of problems including stratospheric probing, pollution monitoring, temperature profile retrieval, and laboratory studies. The Main Atlas covers the frequency range 0 to 20 000 cm^{-1} . The low frequency or millimeter and submillimeter limit represents primarily pure rotational transitions while the high frequency domain represents for the most part excited vibration-rotation transitions of water vapor. The Trace Gas Compilation covers the range 0 to 10 000 cm^{-1} . In addition to the four basic parameters, there are included for each transition the unique quantum identification, the molecule and isotope, and a reference code.

The goal of generating these parameters has been to create a theoretically self-consistent set. Ideally, the performance of quantum mechanical calculations from the development of mathematical models of the molecular system would provide the necessary parameters. This has been satisfactorily accomplished in many cases, the hydrogen halides being a prime example. In cases involving complex resonances or anomalous behavior, theory has lagged behind experiment and it has been necessary to utilize available observed parameters. The latter method does not directly allow for interpolating the unobserved or weaker transitions that might play a role in long path or high temperature observations. Nevertheless, a fair amount of success has been achieved deriving the tabulated parameters ν_i , S_i , α_i , E_i^0 and their unique quantum identifications within the framework of general theories of molecular spectroscopy applied to experimental observations. Details of the basic theory, specific data, and treatment of exceptional cases can be found in references contained in the articles on the compilations [Rothman, 1981; Rothman et al, 1981; 1983a; 1983b]. As of this writing, the compilations, representing the culmination of international efforts in molecular spectroscopy, contain about a third of a million transitions. The maintenance, updating, and improvement of these data is ongoing.

CHAPTER 18

Table 18-1. Molecular species on atmospheric absorption line parameter atlases.

Molecule	Isotope	Relative Natural Abundance	Molecule	Isotope	Relative Natural Abundance	
H ₂ O (1)	161	0.9973	HNO ₃ (12)	146	0.9891	
	181	0.0020		OH (13)	61	0.9975
	171	0.0004			81	0.0020
	162	0.0003	62		0.00015	
CO ₂ (2)	626	0.9842	HF (14)	19	0.99985	
	636	0.0111	HCl (15)	15	0.7576	
	628	0.0040		17	0.2423	
	627	0.0008	HBr (16)	19	0.5068	
	638	0.00044		11	0.4930	
	637	0.000009	HI (17)	17	0.99985	
	828	0.000004		ClO (18)	56	0.7559
	728	0.000002	76		0.2417	
O ₃ (3)	666	0.9928	OCS (19)	622	0.937	
	668	0.0040		624	0.0416	
	686	0.0020		632	0.0105	
N ₂ O (4)	446	0.9904		822	0.0019	
	456	0.0036	H ₂ CO (20)	126	0.9862	
	546	0.0036		136	0.0111	
	448	0.0020		128	0.0020	
	447	0.0004		HOCl (21)	165	0.7558
CO (5)	26	0.9865	167		0.2417	
	36	0.011	N ₂ (22)	44	0.9928	
	28	0.0020		HCN (23)	124	0.9852
27	0.0004	CH ₃ Cl (24)	215		0.7490	
CH ₄ (6)	211		0.9883	217	0.2395	
	311	0.0111	H ₂ O ₂ (25)	1661	0.9949	
	212	0.00059		C ₂ H ₂ (26)	1221	0.9776
O ₂ (7)	66	0.9952	C ₂ H ₆ (27)		1221	0.9770
	68	0.0040		PH ₃ (28)	1111	0.99955
	67	0.0008				
NO (8)	46	0.9940				
	SO ₂ (9)	626	0.9454			
646		0.0420				
NO ₂ (10)	646	0.9916				
NH ₃ (11)	4111	0.9960				
	5111	0.0036				

OPTICAL AND INFRARED PROPERTIES OF THE ATMOSPHERE

18.1.3 Index of Refraction

The theory of molecular optics [Born and Wolf, 1975] derives the index of refraction for gases from the scattering properties of molecules (Lorentz-Lorenz formula). In the atmosphere the index of refraction m is very close to 1 so that it is convenient to define the refractive modulus N as

$$N = (m - 1) \times 10^6. \quad (18.7)$$

N is a function of both wavelength and density and is different for dry air and water vapor. For optical wavelengths greater than 0.23 μm and for infrared wavelengths, N for atmospheric conditions is given by the following formula from Edlen [1966]:

$$N = \left[a_0 + \frac{a_1}{1 - (\nu/b_1)^2} + \frac{a_2}{1 - (\nu/b_2)^2} \right] \frac{P}{P_0} \frac{(T_0 + 15.0)}{T} - \left[c_0 - (\nu/c_1)^2 \right] \frac{P_w}{P_0} \quad (18.8)$$

where P is the total air pressure in mb, T is the temperature in K, $P_0 = 1013.25$ mb, $T_0 = 273.15$, P_w is the partial pressure of water vapor in mb, and $\nu = 10^4/\lambda$ is the frequency in cm^{-1} for the wavelength λ in micrometers.

$$\begin{aligned} a_0 &= 83.42 \\ a_1 &= 185.08 \\ a_2 &= 4.11 \\ b_1 &= 1.140 \times 10^5 \\ b_2 &= 6.24 \times 10^4 \\ c_0 &= 43.49 \\ c_1 &= 1.70 \times 10^4 \end{aligned}$$

The formula is valid from 0.23 μm to the infrared. For millimeter and microwaves, the refractive modulus is much more complicated and includes a strong dependence on water vapor density. For reference, Table 18-2 lists the index of refraction for dry air at 1 atmosphere and 288 K for various wavelengths.

18.1.4 Molecular Rayleigh Scattering

When air molecules are subjected to an oscillating electric field such as in a light wave, the molecule temporarily absorbs and immediately re-emits this radiation as a point source. This process is known as scattering. It occurs on

Table 18-2. Refractive modulus of dry air at 1 atmosphere and 288 K.

Wavelength (μm)	Waynumber (cm^{-6})	$N = (m-1) \times 10^6$
0.23	4.35×10^4	308.0
0.25	4.00×10^4	301.5
0.30	3.33×10^4	291.6
0.40	2.50×10^4	282.7
0.50	2.00×10^4	279.0
0.75	1.33×10^4	275.4
1.0	10000	274.2
2.0	5000	272.9
4.0	2500	272.7
10.0	1000	272.6

particles of any size. If the size of a particle is very small compared to the wavelength of the incident light, certain simplifying conditions exist that also simplify the theoretical description of the scattering process. This type of scattering of light, which causes the blue sky light, was first described by Lord Rayleigh in 1871 [McCartney, 1976].

The total volumetric scattering coefficient k_s , λ for molecules is defined by

$$dI_\lambda = -I_\lambda \cdot k_s(\lambda) \cdot dx, \quad (18.9)$$

with

$$k_s(\lambda) = \frac{24 \pi^3}{N' \lambda^4} \left(\frac{m^2 - 1}{m^2 + 2} \right)^2 \quad (18.10)$$

where m is the refractive index of the gas (such as air), N' the concentration of molecules per unit volume, I_λ the intensity at wavelength λ , and dx the path element. This expression is often simplified by taking advantage of the refractive index of air being nearly 1, and writing Equation (18.10) as

$$k_s(\lambda) \approx \frac{8\pi^3}{3N' \lambda^4} (m^2 - 1)^2, \quad (18.11a)$$

or

$$k_s(\lambda) \approx \frac{32\pi^3}{3N' \lambda^4} (m - 1)^2. \quad (18.11b)$$

For standard temperature and pressure, using Equation (18.11a) introduces an error on the order of 0.04% in the visible and using Equation (18.11b) introduces an error of about 0.025%. Since air molecules are not completely isotropic, a small correction factor for anisotropy [see, for example, Chandrasekhar, 1950; Kerker, 1969] must be ap-

CHAPTER 18

Table 18-3. Depolarization factor Δ of atmospheric gases for incident unpolarized light [Young, 1980].

Gas	Rowell et al. [1971]	Alms et al. [1975]	Baas and van den Hout [1979]	Young [1980]
N ₂	0.0214 and 0.0242	0.0210 ± 0.0004	0.0200 ± 0.006	—
O ₂	0.0566 and 0.0587	—	0.0580 ± 0.002	—
CO ₂	0.073 and 0.075	0.0797 ± 0.0010	0.077 ± 0.002	—
Dry Air	—	—	—	0.0279

plied to the molecular scattering in Equations (18.10) or (18.11). With this correction, Equation (18.10) becomes

$$k_s(\lambda) = \frac{24\pi^3}{N'\lambda^4} \left(\frac{m^2 - 1}{m^2 + 2} \right)^2 \frac{6 + 3\Delta}{6 - 7\Delta}, \quad (18.12)$$

where the depolarization Δ is the ratio of the two polarized intensities i_2/i_1 at a 90° scattering angle (see Section 18.2.1.5). Table 18-3 gives depolarization values for atmospheric gases [Young, 1980]. It is often convenient to use the scattering cross section per molecule

$$\sigma_s(\lambda) = \frac{k_s(\lambda)}{N'} = \frac{24\pi^3}{N'2\lambda^4} \left(\frac{m^2 - 1}{m^2 + 2} \right)^2 \frac{6 + 3\Delta}{6 - 7\Delta} \quad (18.13)$$

which has the advantage over the scattering coefficient in that it is independent of air density (or temperature and

pressure). Values of σ_s [Equation (18.13)] and k_s [Equation (18.12)] are presented in Table 18-4 for wavelengths between 0.25 and 4.0 μm . The largest uncertainty in the tabulated values is due to the uncertainty in the values of the depolarization factor Δ used. Young [1980] indicates an error of a "few percent" in his value of Δ for air (Table 18-3). This corresponds to an uncertainty of ± 0.1 to 0.2% in $\sigma_s(\lambda)$ or $k_s(\lambda)$.

The angular distribution of the light scattered by atmospheric molecules is given by the Rayleigh scattering phase function:

$$P(\theta) = \frac{3}{16\pi} \frac{2}{(2 + \Delta)} \left[(1 + \Delta) + (1 - \Delta)\cos^2\theta \right]. \quad (18.14a)$$

Neglecting the correction for depolarization, this simplifies to

Table 18-4. Rayleigh scattering cross section $\sigma_s(\lambda)$ and Rayleigh scattering coefficient $k_s(\lambda)$.

Wavelength (μm)	$\sigma_s(\lambda)$ ($\text{cm}^2/\text{molec.}$)	$k_s(\lambda)$ (for $t = 273.15 \text{ K}$ and $p = 1013.25 \text{ mb}$)
0.25	1.243E-25	3.339E-1
0.30	5.605E-26	1.506E-1
0.35	2.913E-26	7.829E-2
0.40	1.668E-26	4.482E-2
0.45	1.025E-26	2.754E-2
0.50	6.650E-27	1.787E-2
0.55	4.505E-27	1.211E-2
0.60	3.161E-27	8.496E-3
0.65	2.284E-27	6.139E-3
0.70	1.692E-27	4.547E-3
0.80	9.864E-28	2.651E-3
0.90	6.135E-28	1.649E-3
1.0	4.014E-28	1.079E-3
1.2	1.929E-28	5.184E-4
1.4	1.039E-28	2.793E-4
1.6	6.083E-29	1.635E-4
1.8	3.794E-29	1.020E-4
2.0	2.488E-29	6.695E-5
2.5	1.018E-29	2.736E-5
3.0	4.906E-30	1.318E-5
4.0	1.552E-30	4.169E-6

OPTICAL AND INFRARED PROPERTIES OF THE ATMOSPHERE

$$P(\theta) = \frac{3}{16\pi} \left[1 + \cos^2 \theta \right], \quad (18.14b)$$

which is often used for the Rayleigh phase function. The phase function gives the probability distribution for the scattered light, so that $P(\theta) d\Omega$ is the fraction of the scattered radiation that enters a solid angle $d\Omega$ about the scattering angle θ .

18.2 AEROSOLS, CLOUD, AND PRECIPITATION PARTICLES

Propagation of electromagnetic radiation through the atmosphere at optical/infrared frequencies is affected by absorption and scattering from air molecules and particulate matter (haze, dust, fog, and cloud droplets) suspended in the air. Scattering and absorption by haze particles or aerosols becomes the dominant factor in the boundary layer near the earth's surface, especially in the visible, and under low visibility conditions at all wavelengths. Atmospheric aerosol particles in the atmosphere vary greatly in their concentration, size, and composition, and consequently in their effects on optical and infrared radiation.

18.2.1 Aerosols, Geographic, and Temporal Variations

18.2.1.1 Composition, Sources and Sinks, Refractive Index, Particle Shapes. Figure 18-7 summarizes the general characteristics of atmospheric aerosols. Aerosols in the boundary layer of 1–2 km have the greatest variability. These aerosols consist of a variety of natural and manmade chemical compounds, inorganic as well as organic. Particles are transported into the atmosphere from their sources at or near the surface, or they may be formed in the atmosphere by chemical reactions from gaseous components, often with the influence of solar radiation through photochemical processes. Since more than two-thirds of the earth's surface is covered by oceans, the maritime aerosol component, which consists largely of sea salt particles from the sea water, forms the most uniquely identifiable aerosol. Over land areas, soil particles and dust are an important component. Organic particles from vegetation sources are also an important aerosol component. Table 18-5 gives a breakdown of the global atmospheric aerosol composition [SMIC, 1971].

In the troposphere above the boundary layer the distribution and composition of aerosol particles becomes less dependent on the geography and on the variability of sources near the surface. Experimental data [Whitby and Cantrell, 1976 and Whitby, 1973] point toward an aerosol which is composed of several modes, each having a different origin and history. The most clearly identifiable two components are submicron size particles formed from gaseous components and are still going through processes of coagulation

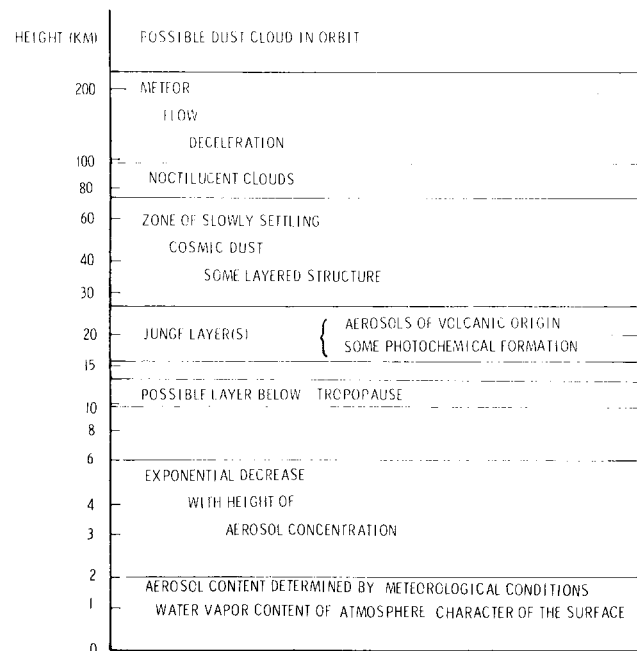


Figure 18-7. Characteristics of atmospheric aerosols.

and agglomeration; this component is called the accumulation mode. The second mode is made up of larger particles approximately 1 μm diameter and larger which are produced by mechanical processes such as resuspension from soil or sea spray; this component is called the coarse particle mode.

Table 18-5. Estimates of particles smaller than 20 μm radius emitted into or formed in the atmosphere (10^6 metric tons/year) [SMIC, 1971].

Natural	
Soil and rock debris*	100–500
Forest fires and slash-burning debris*	3–150
Sea salt	300
Volcanic debris	25–150
Particles formed from gaseous emissions:	
Sulfate from H_2S	130–200
Ammonium salts from NH_3	80–270
Nitrate from NO_x	60–430
Hydrocarbons from plant exudations	75–200
Subtotal	773–2200
Man-made	
Particles (direct emissions)	10–90
Particles formed from gaseous emissions:	
Sulfate from SO_2	130–200
Nitrate from NO_x	30–35
Hydrocarbons	15–90
Subtotal	185–415
Total	958–2615

*Includes unknown amounts of indirect manmade contributions.

CHAPTER 18

In the stratospheric region from 10–30 km, measurements have shown a background aerosol that has a rather uniform global distribution. This aerosol is considered to be mostly composed of sulfate particles formed by photochemical reactions. The stratospheric aerosol background can occasionally be increased by factors of 100 or more due to the injection of dust and SO₂ from massive volcanic eruptions. Once these volcanic particles and gases have been injected into the stratosphere they are spread out over large portions of the globe by the stratospheric circulation. While the dust particles may settle out within a few months, the SO₂ is converted to sulfuric acid through photochemical reactions. This enhanced layer of approximately 75% sulfuric acid droplets may remain for one to two years. For a complete review of the stratospheric aerosols see Turco et al. [1982].

Only a very small portion of the total aerosol content of the atmosphere exists above 30 km. However, when the effects of the lower atmosphere are small, such as in satellite observations of the limb of the earth's atmosphere or determining the ozone distribution by inverting measurements of backscattered ultraviolet from the atmosphere, the effects of the aerosols in the upper atmosphere can be significant.

Newkirk and Eddy [1964] and later Rosen [1969] concluded that the major component of the normal upper atmospheric aerosols is meteoric dust. Meteoric or cometary dust also form layers occasionally observed in the upper atmosphere. The optical effects of small particles are determined largely by their refractive index.

Aerosol samples from all over the world have been collected and analyzed for their optical and infrared refractive index properties. Based on such measurements, the aerosol in rural, non urban areas can be assumed to be composed of a mixture of water soluble substances (ammonium and calcium sulfates and organic compounds) and dust-like aerosols [Volz, 1972 a, b]. In urban areas the rural aerosol gets modified by the addition of aerosols from combustion products and industrial sources. There is no experimental evidence for any systematic change in aerosol refractive index as a function of altitude through the troposphere. The refractive index of the volcanic components in the stratospheric aerosols was measured by Volz [1973] on volcanic dust samples. The refractive index for meteoric dust was determined by Shettle and Volz [1976] based on the composition of meteorites falling on the earth.

Although the aerosol particle size (see Section 18.2.1.2) is the most important parameter determining small particle scattering properties, the effect of particle shape cannot be ignored; it becomes significant especially for particles where size is large compared to the wavelength of the incident radiation. However, because of poor understanding of these shape effects, essentially all applications-oriented aerosol models assume spherical particle shapes. For more information on nonspherical particle scattering properties see Schuerman [1980].

18.2.1.2 Size Distributions. Over the past 20 to 30 years, much emphasis has been put on measurements of the aerosol particle size distribution, realizing that natural aerosols were far from being monodisperse. Junge [1963] suggested that most aerosol size distributions over the radius range from 0.1 to 10 μm, and even larger sizes, could be described by an inverse power law $dN/dr = cr^{-\gamma}$ with c being a constant and γ being between 2 and 4. This means that the number of aerosol particles decreases rapidly with increasing particle size. It has already been mentioned that more detailed measurements point towards a multimodal distribution. This becomes especially noticeable if the distribution is presented as particle volume distribution dv/dr rather than dN/dr . One can assume that these size distributions are the result of a dynamic equilibrium between the various processes which act on the aerosol population. However the interaction of these various processes is complex and no general theory for aerosol formation processes exists at this time.

18.2.1.3 Vertical Profiles. The change in aerosol properties and distribution with altitude is very closely tied to the vertical structure of the atmosphere, and in the troposphere especially to the “weather” processes. In general the number of aerosol particles decreases much more rapidly with altitude than the molecular air density; however, wide variations in the vertical profile do occur. Within the boundary layer of the atmosphere, aerosol vertical mixing is strongly influenced by the temperature profile.

18.2.1.4 Models of the Aerosol Properties. There are many scientific and technical reasons why it is necessary to develop models for atmospheric aerosol and cloud particles. They are needed to make estimates of the transmittance, angular light scattering distribution, contrast reduction, sky radiance, or other atmospheric optical properties or effects (see Section 18.4).

Models for the optical properties of aerosols have been developed at AFGL and elsewhere. [Elterman, 1964, 1968, 1970; Ivlev, 1967; Deirmendjian, 1964, 1969; McClatchey et al., 1970 and 1972; Shettle and Fenn, 1976; Toon and Pollack, 1976; Hanel and Bullrich, 1978; and Nilsson, 1979]. This chapter describes aerosol models and their optical properties for the lower and upper atmosphere [Shettle and Fenn 1976, 1979]. The models presented below are based on a review of the available experimental data on the nature of aerosols, their sizes, distribution, and variability. However, it must be emphasized that these models represent only a simple, generalized version of typical conditions. It is not practical to include all the details of natural particle distributions nor are existing experimental data sufficient to describe the frequency of occurrence of the different conditions. While these particulate models were developed to be as representative as possible of different atmospheric conditions, the following point should be kept in mind when

OPTICAL AND INFRARED PROPERTIES OF THE ATMOSPHERE

Table 18-6. Characteristics of the aerosol models as a function of relative humidity.

Aerosol Model	Size Distribution			Type
	N_i	r_i	σ_i	
Rural	0.999875	0.03	0.35	Mixture of Water Soluble and Dust-Like Aerosols
	0.000125	0.5	0.4	
Urban	0.999875	0.03	0.35	Rural Aerosol Mixtures with Soot-Like Aerosols
	0.000125	0.5	0.4	
Maritime				
Continental Origin	0.99	0.03	0.35	Rural Aerosol Mixture
Oceanic Origin	0.01	0.3	0.4	Sea Salt Solution in Water
Tropospheric	1.0	0.03	0.35	Rural Aerosol Mixture

using any such model: given the natural variability of the atmosphere, almost any particle model is supported by some measurements and no model (or set of models) will be consistent with all measurements.

The size distributions for the different aerosol models are represented by one or the sum of two log-normal distributions:

$$n(r) = \frac{dN(r)}{dr} = \sum_{i=1}^2 \left\{ \left[\frac{N_i}{\ln(10) \cdot r \cdot \sigma_i \sqrt{2\pi}} \right] \times \exp \left[- \frac{(\log r - \log r_i)^2}{2 \sigma_i^2} \right] \right\}, \quad (18.15)$$

where $N(r)$ is the cumulative number density of particles of radius r , σ is the standard deviation, and r_i , N_i are the mode

radius and the number density of r_i . This form of distribution function represents the multimodal nature of the atmospheric aerosols. Following the usual convention, \log is the logarithm to the base 10 and \ln is the logarithm to the base e .

Four different aerosol models for the atmospheric boundary layer have been developed. They differ in particle size distribution and particle refractive index. Table 18-6 lists the parameters defining the size distributions in accordance with Equation (18.15) for these models. These mode radii correspond to moderate humidities (70% to 80%); values of r_i as a function of humidity are given in Table 18-7.

The choices of N in Table 18-6 are normalized to correspond to 1 particle/cm³. The actual size distributions can be renormalized to give the correct extinction coefficients for the altitude and the visibility being used. The continental and oceanic components of the maritime model can be used in various proportions depending on the prevailing winds—particularly in coastal regions.

As the relative humidity increases, water vapor con-

Table 18-7. Mode radii for the aerosol models as a function of relative humidity.

Relative Humidity	Tropospheric r_1	Rural		Maritime	Urban	
		r_1	r_2		r_1	r_2
0%	0.02700	0.02700	0.4300	0.1600	0.02500	0.4000
50%	0.02748	0.02748	0.4377	0.1711	0.02563	0.4113
70%	0.02846	0.02846	0.4571	0.2041	0.02911	0.4777
80%	0.03274	0.03274	0.5477	0.3180	0.03514	0.5808
90%	0.03884	0.03884	0.6462	0.3803	0.04187	0.7061
95%	0.04238	0.04238	0.7078	0.4606	0.04904	0.8634
98%	0.04751	0.04751	0.9728	0.6024	0.05996	1.1691
99%	0.05215	0.05215	1.1755	0.7505	0.06847	1.4858

CHAPTER 18

denses out of the atmosphere on the particulates suspended in the atmosphere. This condensed water increases the size of the aerosols and changes their composition and effective refractive index. The resulting effect of the aerosol on the absorption and scattering of light will correspondingly be modified. There have been a number of studies on the change of aerosol properties as a function of relative humidity. The most comprehensive of these, especially in terms of the resulting effects on the aerosol optical properties, is the work of Hanel [1976].

The "Rural Model" is intended to represent the aerosol under conditions where it is not directly influenced by urban and/or industrial aerosol sources. The rural aerosols are assumed to be composed of a mixture of 70% water soluble substances (ammonium and calcium sulfate and also organic compounds) and 30% dust-like aerosols. The refractive index for these components based on the measurements of Volz [1972a,b; 1973] is shown in Figure 18-8. The refractive index is in general a complex quantity with a real and imaginary part. These refractive index data weighted by the mixing ratio of the two components are consistent with other direct measurements and with values inferred from *in situ* measurements. For the refractive index of water, the survey of Hale and Querry [1973] was used. While there are some minor differences between the optical constants in Hale and Querry's survey and the more recent measurements, these differences are comparable to the experimental errors and are small compared with the other uncertainties in the model parameters. These refractive index data are shown in Figure 18-9. The resulting number density distributions $n(r)$, are shown in Figure 18-10. To allow for the dependence of the humidity effects on the size of the dry aerosol, the growth of the aerosol was computed separately for the accumulation and coarse particle components. In accounting for the aerosol growth, changes in the width of the size distribution were assumed negligible so only the mode radius r_1 was

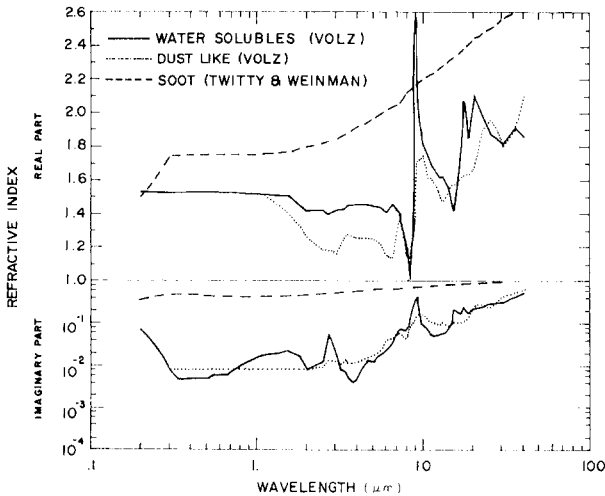


Figure 18-8. Refractive index for the dry rural and urban aerosol components.

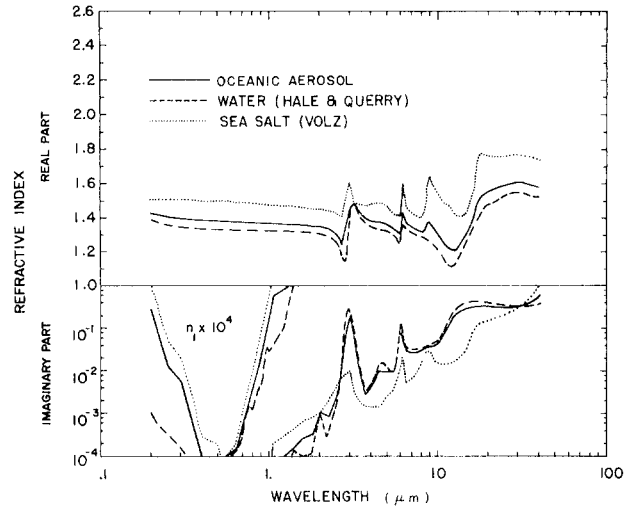


Figure 18-9. Refractive index of oceanic aerosol, water, and sea salt.

modified by humidity changes (Figure 18-10). The effective refractive indices for the two size components were then computed.

In urban areas the air with a rural aerosol background is primarily modified by the addition of aerosols from combustion products and industrial sources. The urban aerosol model therefore was taken to be a mixture of the rural aerosol with carbonaceous aerosols. The proportions of the soot-like carbonaceous aerosols and the rural type of aerosol mixture are assumed to be 20% and 80%, respectively. The soot-like aerosols are assumed to have the same size distribution as both components of the rural model. The refractive index of the soot-like aerosols are based on the soot data in Twitty and Weinman's [1971] survey of the refractive index of carbonaceous materials. As with the rural model, a composite urban aerosol refractive index was determined at each wavelength.

The aerosol compositions and distributions of oceanic origin are significantly different from continental aerosol types. These aerosols are largely sea-salt particles produced by the evaporation of sea-spray droplets that have grown again due to aggregation of water under high relative humidity conditions. However, even over the ocean there is a more or less pronounced continental aerosol background that, mixed with the aerosol of oceanic origin, forms a fairly uniform maritime aerosol. It is representative for the boundary layer in the lower 2-3 km in the atmosphere over the oceans, but also may occur over the continents in a maritime air mass. This maritime model should be distinguished from the fresh sea-spray aerosol that exists in the lower 10-20 m above the ocean surface and is strongly dependent on wind speed.

The maritime aerosol model, therefore, is composed of two components: (1) the sea-salt component and (2) a continental component assumed to be identical to the rural aerosol with the exception that the very large particles are eliminated since they will eventually be lost due to fallout

OPTICAL AND INFRARED PROPERTIES OF THE ATMOSPHERE

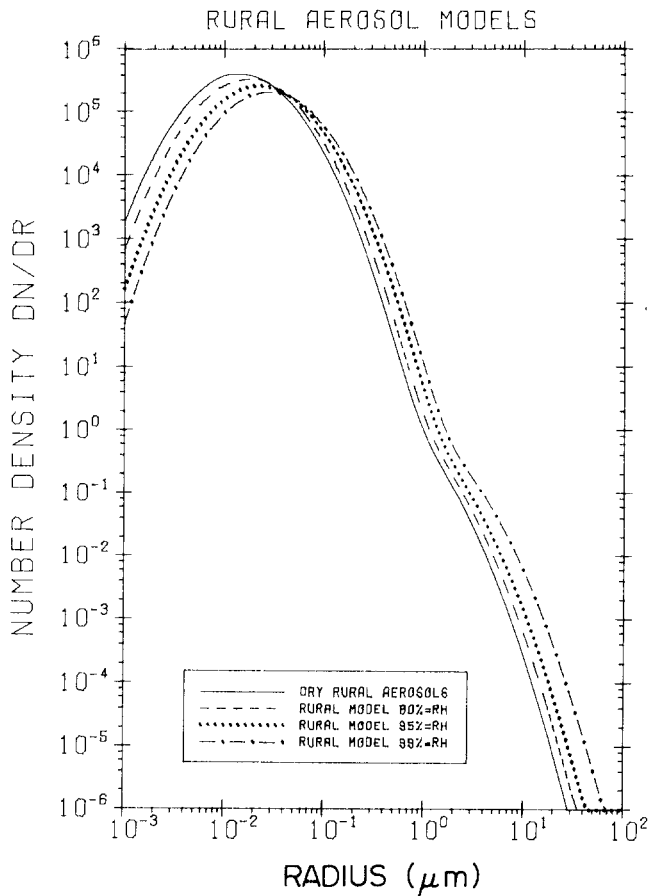


Figure 18-10. Aerosol number distribution ($\text{cm}^{-3} \mu\text{m}^{-1}$) for the rural model at different relative humidities with total particle concentrations fixed at $15\,000 \text{ cm}^{-3}$.

as the air masses move across the oceans. For the size distribution of the oceanic component, a log normal distribution is used with $r_0 = 0.3 \mu\text{m}$ for moderate relative humidity ($=80\%$) and $\sigma = 0.4$. The relative proportions of aerosol of oceanic or continental origins will vary particularly in coastal regions. To account for these variations, the model permits the user to adjust the relative amounts of the oceanic and continental types of aerosol. The number density distribution is shown in Figure 18-11. The refractive index is based on that for a solution of sea salt in water, using a weighted average of the refractive indices of water and sea salt. The refractive index of the sea salt is primarily taken from the measurements of Volz [1972 a, b]. A model for maritime aerosols that accounts for production of oceanic aerosol at the sea surface by white caps and spray as a function of wind speed and the changes in drop size due to varying relative humidity was developed recently by Gathman [1983]. With some modifications this model has been incorporated into LOWTRAN 6 (see Section 18.4.2).

The tropospheric aerosol model represents the aerosols within the troposphere above the boundary layer. These aerosols are assumed to have the same composition as the

rural model (70% water soluble and 30% dust-like). The size distribution is modified from the rural model by eliminating the large (or coarse) particle ($r_i = 0.5 \mu\text{m}$) component of the size distribution because of the longer residence of aerosols above the boundary and the expected differential loss of the larger particles. This leaves the log-normal distribution with the small (or accumulation particle component). This is consistent with the changes in aerosol size distribution with altitude suggested by Whitby and Cantrell [1976]. The dependence of particle size on relative humidity is the same as for the small particle component of the rural model, and is shown in Figure 18-12.

Based on observations of stratospheric aerosol behavior four different vertical distribution models for the stratosphere were developed: a background model and three different volcanic aerosol profiles (moderate, high, and extreme). These models represent either different amounts of volcanic material injected into the stratosphere or the decrease over time from the extreme conditions following a major event such as the Krakatoa explosion. The experimental data also confirm a seasonal trend in the stratospheric aerosol distributions. Figure 18-13 shows these stratospheric models and also for comparison the 1968 Elterman model

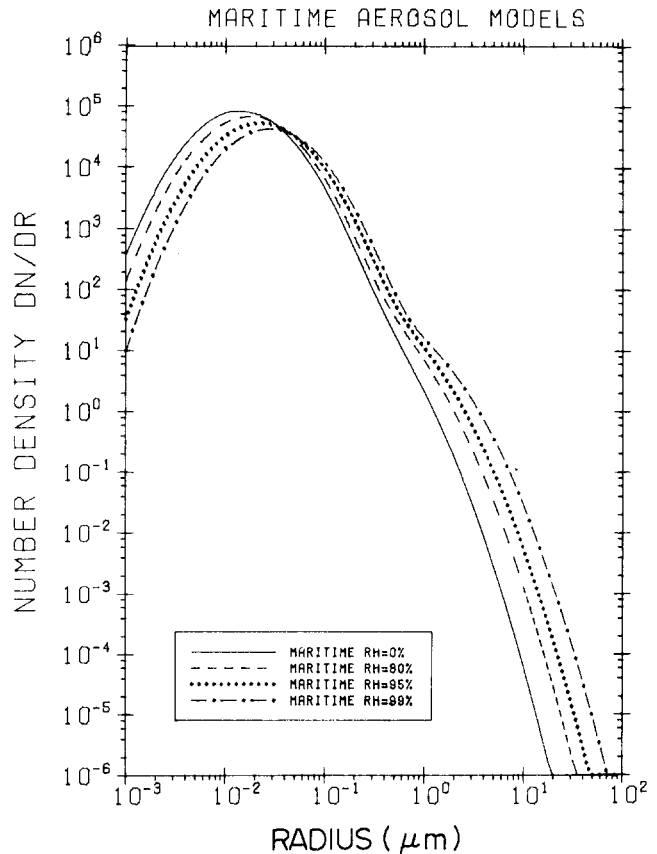


Figure 18-11. Aerosol number distribution ($\text{cm}^{-3} \mu\text{m}^{-1}$) for the maritime model at different relative humidities with total particle concentrations fixed at 4000 cm^{-3} .

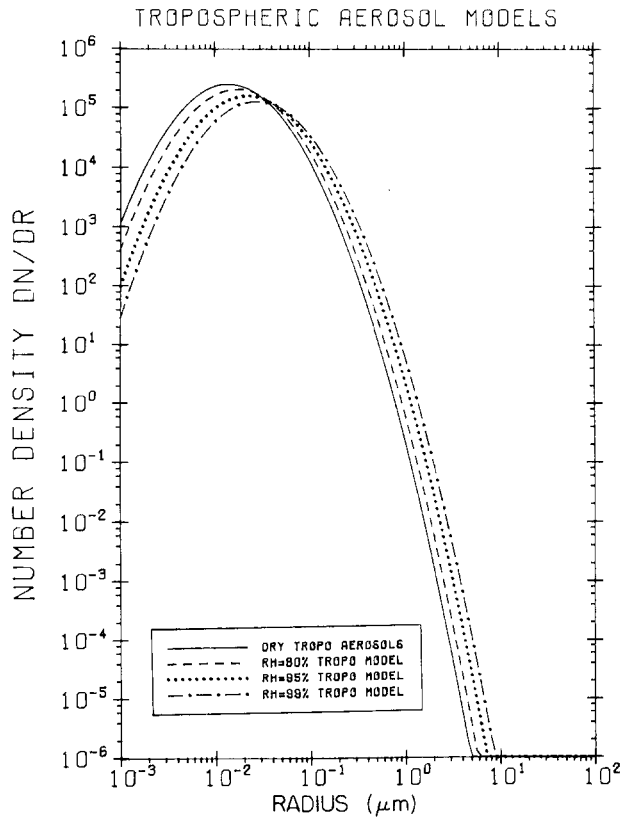


Figure 18-12. Aerosol number distribution ($\text{cm}^{-3} \mu\text{m}^{-1}$) for the tropospheric model at different relative humidities with total particle concentrations fixed at $10\,000 \text{ cm}^{-3}$.

based on data collected during the period several years after the Agung eruption in 1963 and therefore representative for the moderate volcanic conditions.

The stratospheric background aerosols were assumed to be a 75% solution of sulfuric acid in water following the work of Rosen [1971] and Toon and Pollack [1973]. The complex refractive index as a function of wavelength is based on the measurements of Remsburg [1971 and 1973] and Palmer and Williams [1975]. The refractive index for the volcanic models is based on the measurements of Volz [1973] on volcanic dust.

There are two volcanic aerosol size models: a “Fresh Volcanic Model” representing the size distribution of aerosols shortly after a volcanic eruption, and a “Volcanic Model” representing the aerosol about a year after an eruption. Both size distributions were chosen mainly on the basis of Mossop’s [1964] measurements following the eruption of Mt. Agung. The size distribution was also made consistent with the observed wavelength dependence of extinction due to volcanic aerosols, and in the case of the “Fresh Volcanic Model” consistent with the observation of optical phenomena such as Bishop’s rings, and a blue or green sun sometimes observed following major volcanic eruptions. These size distributions are represented by a modified gamma distribution:

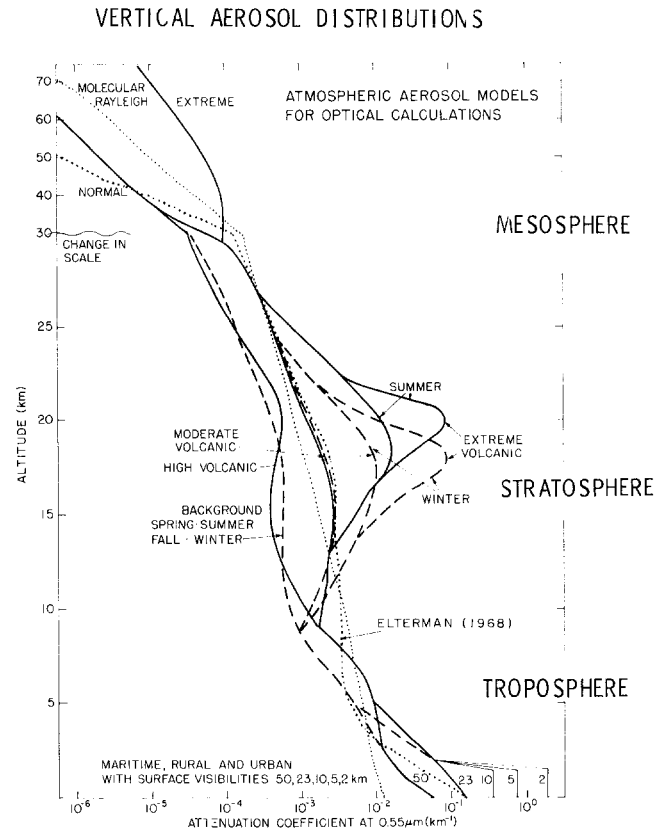


Figure 18-13. The vertical distribution of the aerosol extinction (at 0.55 microns) for the different models. Also shown for comparison are the Rayleigh profile (dotted line) and Elterman’s [1968] model. Between 2 and 30 km, where a distinction on a seasonal basis is made, the spring–summer conditions are indicated with a solid line and fall–winter conditions are indicated by a dashed line.

$$\frac{dN}{dr} = n(r) = Ar^\alpha \exp(-br^\gamma) \quad (18.16)$$

whose parameters are given in Table 18-8. Either of the two volcanic size distribution models are appropriate to use with the “moderate” or “high” volcanic vertical profiles, depending on whether these profiles represent a major eruption after a couple of years or a recent weaker eruption. It should be noted that the profiles may have a much more layered structure than is shown in the model distributions, particularly shortly after a volcanic injection of dust into the atmosphere.

The major component of the normal upper atmospheric

Table 18-8. Modified gamma distribution parameters.

	A	α	γ	b
Background Stratospheric	324.0	1	1	18
Fresh Volcanic	341.33	1	0.5	8
Aged Volcanic	5 461.33	1	0.5	16

OPTICAL AND INFRARED PROPERTIES OF THE ATMOSPHERE

aerosol is considered to be meteoric dust. Meteoric or cometary dust also forms some of the layers occasionally observed in the upper atmosphere. The refractive index of meteoric dust is based on the work of Shettle and Volz [1976] who determined the complex refractive index for a mixture of chondrite dust which represents the major type of meteorite falling on the earth. The size distribution has been represented by a log-normal distribution (equation 18.15 with $i = 1$) whose parameters are given as

$$N_1 = 1 \text{ cm}^{-3}, r = 0.03 \text{ } \mu\text{m}, \sigma_1 = 0.5 .$$

Figure 18-13 shows in addition to the normal upper atmospheric model an extreme model similar to Ivlev's [1969] model for the upper atmosphere. Attenuation coefficients this large occur in layers with thicknesses no greater than a few kilometers. At different times these layers can be either micrometeoritic dust or noctilucent clouds. The wavelength dependent refractive indices for the different aerosol types are listed in Table 18-9.

18.2.1.5 Aerosol Extinction, Scattering, Polarization.

Once the size distribution and refractive index of the aerosol models are specified, the optical properties can be determined. The effects of small particles on the propagation of radiation are defined by the coefficients for extinction, scattering and absorption, the angular scattering function, and the polarization of scattered radiation.

The Mie [1908] theory treats the scattering of light by homogeneous particles of arbitrary size and refractive index (for Rayleigh scattering see Section 18.1.4). For detailed discussions on particle scattering see textbooks by van de Hulst [1957], Kerker [1969], and McCartney [1976]. The spatial distribution of scattered light for incident unpolarized light of intensity $I_{o,\lambda}$ is

$$I_\lambda = I_{o,\lambda} \frac{1}{2 \cdot k^2 \cdot R^2} [i_1(\alpha, m, \theta) + i_2(\alpha, m, \theta)], \quad (18.17)$$

where $k = 2 \pi/\lambda$,

$R =$ Distance from the scattering particle center,

$\alpha = 2 \pi r/\lambda$, the size parameter, r is particle radius,

$m =$ complex refractive index of the particle relative to its surrounding medium,

$\theta =$ angle between the incident and the scattered beams ($\theta = 0^\circ$ is defined as forward scattering).

$i_1 =$ perpendicular polarized component

$i_2 =$ parallel polarized component

The dimensionless intensity functions define degree of linear polarization P :

$$P = \frac{i_1 - i_2}{i_1 + i_2}. \quad (18.18)$$

Integration of the scattered light over all directions (4π steradians) gives

$$\int_0^{4\pi} I_\lambda d\Omega = I_{o,\lambda} \cdot C_s. \quad (18.19)$$

The ratio of C_s (scattering cross section) to the geometrical cross section of the scattering particle, $r^2\pi$, is called scattering efficiency factor Q_s . If light is traveling through a scattering medium containing N particles per unit volume, the loss of light due to scattering per unit path length dx is

$$dI_\lambda = -I_\lambda \cdot C_s \cdot N \cdot dx. \quad (18.20)$$

Integration of Equation (18.20) gives the Bouguer extinction law:

$$I_{\lambda, \text{transmitted}} = I_{o,\lambda} \exp(-k_s x) \quad (18.21)$$

with $k_s = N \cdot C_s$ called the scattering coefficient. Similarly to k_s one can define an absorption coefficient k_a for absorption by absorbing aerosol particles.

$k_e = k_s + k_a$ is called the extinction coefficient.

For Mie scattering calculations, the aerosol particles are assumed to be spherical, which in general is not true. While liquid aerosols are approximately spherical, dry particles usually are irregularly shaped. However, it can be argued that many of the measurements of aerosol size distributions directly measure scattered light from the aerosol particles, and the size "assigned" to the particle is the size of a sphere that has similar scattering properties to the measured particle. Furthermore, the irregularly shaped particles are closest to "equivalent" spheres in their scattering properties in the forward direction generally used for size measurements. Therefore, the resulting size distribution is the size distribution of spheres that have similar optical properties to those of the actual aerosol particles. Also, studies by Chylek et al. [1976] and Holland and Gagne [1970] indicate that for particles of equal overall dimension but different shapes, the spherical particle extinction has the highest values.

The computed attenuation coefficients (extinction, scattering, and absorption) for the model aerosols above are shown in Tables 18-10 a thru c and Figures 18-14 thru 18-22.

The attenuation coefficients for the rural aerosol model at 50% relative humidity as a function of wavelength are shown in Figure 18-14. To show the effect of variations of relative humidity on the aerosol extinction, the rural model extinction has been calculated over a range of humidities for a constant total number density. The resulting extinction versus wavelength is shown in Figure 18-15 for several

CHAPTER 18

Table 18-9a. Refractive indices for different aerosol types.

Wavelength (μm)	Sea Salt		Oceanic		Water		Ice		Meteoric	
	real	imag.	real	imag.	real	imag.	real	imag.	real	imag.
0.200	1.510	-1.00E-04	1.429	-2.87E-05	1.396	-1.10E-07	1.394	-1.50E-08	1.515	-1.23E-05
0.250	1.510	-5.00E-06	1.404	-1.45E-06	1.362	-3.35E-08	1.351	-8.60E-09	1.515	-2.41E-05
0.300	1.510	-2.00E-06	1.395	-5.83E-07	1.349	-1.60E-08	1.334	-5.50E-09	1.515	-4.18E-05
0.337	1.510	-4.00E-07	1.392	-1.20E-07	1.345	-8.45E-09	1.326	-4.50E-09	1.514	-5.94E-05
0.400	1.500	-3.00E-08	1.385	-9.90E-09	1.339	-1.86E-09	1.320	-2.71E-09	1.514	-9.95E-05
0.488	1.500	-2.00E-08	1.382	-6.41E-09	1.335	-9.69E-10	1.313	-1.75E-09	1.513	-1.81E-04
0.515	1.500	-1.00E-08	1.381	-3.70E-09	1.334	-1.18E-09	1.312	-2.19E-09	1.513	-2.13E-04
0.550	1.500	-1.00E-08	1.381	-4.26E-09	1.333	-1.96E-09	1.311	-3.11E-09	1.513	-2.61E-04
0.633	1.490	-2.00E-08	1.377	-1.62E-08	1.332	-1.46E-08	1.308	-1.09E-08	1.512	-3.99E-04
0.694	1.490	-1.00E-07	1.376	-5.04E-08	1.331	-3.05E-08	1.306	-2.62E-08	1.511	-5.30E-04
0.860	1.480	-3.00E-06	1.372	-1.09E-06	1.329	-3.29E-07	1.303	-2.15E-07	1.509	-1.02E-03
1.060	1.470	-2.00E-04	1.367	-6.01E-05	1.326	-4.18E-06	1.300	-1.96E-06	1.506	-1.95E-03
1.300	1.470	-4.00E-04	1.365	-1.41E-04	1.323	-3.69E-05	1.295	-1.32E-05	1.501	-3.72E-03
1.536	1.460	-6.00E-04	1.359	-2.43E-04	1.318	-9.97E-05	1.290	-6.10E-04	1.495	-6.34E-03
1.800	1.450	-8.00E-04	1.351	-3.11E-04	1.312	-1.15E-04	1.282	-1.13E-04	1.488	-1.06E-02
2.000	1.450	-1.00E-03	1.347	-1.07E-03	1.306	-1.10E-03	1.273	-1.61E-03	1.482	-1.51E-02
2.250	1.440	-2.00E-03	1.334	-8.50E-04	1.292	-3.90E-04	1.256	-2.13E-04	1.474	-2.24E-02
2.500	1.430	-4.00E-03	1.309	-2.39E-03	1.261	-1.74E-03	1.225	-7.95E-04	1.467	-3.18E-02
2.700	1.400	-7.00E-03	1.249	-1.56E-02	1.188	-1.90E-02	1.163	-2.93E-03	1.462	-4.10E-02
3.000	1.610	-1.00E-02	1.439	-0.197	1.371	-0.272	1.045	-0.429	1.456	-5.73E-02
3.200	1.490	-3.00E-03	1.481	-6.69E-02	1.478	-9.24E-02	1.652	-0.283	1.454	-6.94E-02
3.392	1.480	-2.00E-03	1.439	-1.51E-02	1.422	-2.04E-02	1.510	-4.01E-02	1.454	-8.15E-02
3.500	1.480	-1.60E-03	1.423	-7.17E-03	1.400	-9.40E-03	1.453	-1.61E-02	1.455	-8.82E-02
3.750	1.470	-1.40E-03	1.398	-2.90E-03	1.369	-3.50E-03	1.391	-7.00E-03	1.459	-0.103
4.000	1.480	-1.40E-03	1.388	-3.69E-03	1.351	-4.60E-03	1.361	-1.00E-02	1.466	-0.116
4.500	1.490	-1.40E-03	1.377	-9.97E-03	1.332	-1.34E-02	1.340	-2.87E-02	1.485	-0.131
5.000	1.470	-2.50E-03	1.366	-9.57E-03	1.325	-1.24E-02	1.327	-1.20E-02	1.500	-0.135
5.500	1.420	-3.60E-03	1.333	-9.31E-03	1.298	-1.16E-02	1.299	-2.17E-02	1.508	-0.132
6.000	1.410	-1.10E-02	1.306	-7.96E-02	1.265	-0.107	1.296	-6.47E-02	1.507	-0.126
6.200	1.600	-2.20E-02	1.431	-6.91E-02	1.363	-8.80E-02	1.313	-6.83E-02	1.504	-0.124
6.500	1.460	-5.00E-03	1.374	-2.94E-02	1.339	-3.92E-02	1.320	-5.59E-02	1.497	-0.121
7.200	1.420	-7.00E-03	1.343	-2.49E-02	1.312	-3.21E-02	1.318	-5.44E-02	1.469	-0.119
7.900	1.400	-1.30E-02	1.324	-2.79E-02	1.294	-3.39E-02	1.313	-4.79E-02	1.422	-0.130
8.200	1.420	-2.00E-02	1.324	-3.08E-02	1.286	-3.51E-02	1.306	-3.90E-02	1.395	-0.142
8.500	1.480	-2.60E-02	1.336	-3.36E-02	1.278	-3.67E-02	1.291	-3.91E-02	1.363	-0.162
8.700	1.600	-3.00E-02	1.366	-3.56E-02	1.272	-3.79E-02	1.282	-4.00E-02	1.339	-0.182
9.000	1.650	-2.80E-02	1.373	-3.65E-02	1.262	-3.99E-02	1.269	-4.29E-02	1.302	-0.228
9.200	1.610	-2.60E-02	1.356	-3.71E-02	1.255	-4.15E-02	1.261	-4.46E-02	1.281	-0.273
9.500	1.580	-1.80E-02	1.339	-3.68E-02	1.243	-4.44E-02	1.245	-4.59E-02	1.272	-0.360
9.800	1.560	-1.60E-02	1.324	-3.88E-02	1.229	-4.79E-02	1.219	-4.70E-02	1.310	-0.450
10.000	1.540	-1.50E-02	1.310	-4.06E-02	1.218	-5.08E-02	1.197	-5.10E-02	1.355	-0.488
10.591	1.500	-1.40E-02	1.271	-5.22E-02	1.179	-6.74E-02	1.098	-0.131	1.419	-0.547
11.000	1.480	-1.40E-02	1.246	-7.31E-02	1.153	-9.68E-02	1.093	-0.239	1.509	-0.691
11.500	1.480	-1.40E-02	1.227	-0.105	1.126	-0.142	1.176	-0.360	1.847	-0.634
12.500	1.420	-1.60E-02	1.208	-0.190	1.123	-0.259	1.387	-0.422	1.796	-0.252
13.000	1.410	-1.80E-02	1.221	-0.223	1.146	-0.305	1.472	-0.389	1.711	-0.219
14.000	1.410	-2.30E-02	1.267	-0.271	1.210	-0.370	1.569	-0.283	1.641	-0.217
14.800	1.430	-3.00E-02	1.307	-0.292	1.258	-0.396	1.579	-0.191	1.541	-0.198
15.000	1.450	-3.50E-02	1.321	-0.297	1.270	-0.402	1.572	-0.177	1.510	-0.206
16.400	1.560	-9.00E-02	1.407	-0.331	1.346	-0.427	1.531	-0.125	1.478	-0.467
17.200	1.740	-0.120	1.487	-0.341	1.386	-0.429	1.534	-0.107	1.441	-0.400
18.000	1.780	-0.130	1.525	-0.341	1.423	-0.426	1.522	-8.39E-02	1.354	-0.557
18.500	1.770	-0.135	1.536	-0.339	1.448	-0.421	1.510	-7.60E-02	1.389	-0.705
20.000	1.760	-0.152	1.560	-0.324	1.480	-0.393	1.504	-6.70E-02	1.803	-0.765
21.300	1.760	-0.165	1.568	-0.318	1.491	-0.379	1.481	-3.85E-02	1.797	-0.556
22.500	1.760	-0.180	1.579	-0.316	1.506	-0.370	1.455	-2.91E-02	1.661	-0.592
25.000	1.760	-0.205	1.596	-0.313	1.531	-0.356	1.414	-2.99E-02	1.983	-0.861
27.900	1.770	-0.275	1.612	-0.320	1.549	-0.339	1.358	-4.90E-02	2.023	-0.666
30.000	1.770	-0.300	1.614	-0.320	1.551	-0.328	1.325	-6.50E-02	2.149	-0.665
35.000	1.760	-0.500	1.597	-0.383	1.532	-0.336	1.226	-0.155	2.146	-0.380
40.000	1.740	-1.000	1.582	-0.561	1.519	-0.385	1.202	-0.344	1.979	-0.359

OPTICAL AND INFRARED PROPERTIES OF THE ATMOSPHERE

Table 18-9b. Refractive indices for different aerosol types.

Wavelength (μm)	Water Soluble		Dust-Like		Soot		75% H ₂ SO ₄		Volcanic	
	real	imag.	real	imag.	real	imag.	real	imag.	real	imag.
0.200	1.530	-7.00E-02	1.530	-7.00E-02	1.500	-0.350	1.498	-1.00E-08	1.500	-7.00E-02
0.250	1.530	-3.00E-02	1.530	-3.00E-02	1.620	-0.450	1.484	-1.00E-08	1.500	-3.00E-02
0.300	1.530	-8.00E-03	1.530	-8.00E-03	1.740	-0.470	1.469	-1.00E-08	1.500	-1.00E-02
0.337	1.530	-5.00E-03	1.530	-8.00E-03	1.750	-0.470	1.459	-1.00E-08	1.500	-8.00E-03
0.400	1.530	-5.00E-03	1.530	-8.00E-03	1.750	-0.460	1.440	-1.00E-08	1.500	-8.00E-03
0.488	1.530	-5.00E-03	1.530	-8.00E-03	1.750	-0.450	1.432	-1.00E-08	1.500	-8.00E-03
0.515	1.530	-5.00E-03	1.530	-8.00E-03	1.750	-0.450	1.431	-1.00E-08	1.500	-8.00E-03
0.550	1.530	-6.00E-03	1.530	-8.00E-03	1.750	-0.440	1.430	-1.00E-08	1.500	-8.00E-03
0.633	1.530	-6.00E-03	1.530	-8.00E-03	1.750	-0.430	1.429	-1.47E-08	1.500	-8.00E-03
0.694	1.530	-7.00E-03	1.530	-8.00E-03	1.750	-0.430	1.428	-1.99E-08	1.500	-8.00E-03
0.860	1.520	-1.20E-02	1.520	-8.00E-03	1.750	-0.430	1.425	-1.79E-07	1.500	-8.00E-03
1.060	1.520	-1.70E-02	1.520	-8.00E-03	1.750	-0.440	1.420	-1.50E-06	1.500	-8.00E-03
1.300	1.510	-2.00E-02	1.460	-8.00E-03	1.760	-0.450	1.410	-1.00E-05	1.500	-8.00E-03
1.536	1.510	-2.30E-02	1.400	-8.00E-03	1.770	-0.460	1.403	-1.37E-04	1.490	-8.00E-03
1.800	1.460	-1.70E-02	1.330	-8.00E-03	1.790	-0.480	1.390	-5.50E-04	1.480	-8.00E-03
2.000	1.420	-8.00E-03	1.260	-8.00E-03	1.800	-0.490	1.384	-1.26E-03	1.460	-8.00E-03
2.250	1.420	-1.00E-02	1.220	-9.00E-03	1.810	-0.500	1.370	-1.80E-03	1.460	-8.00E-03
2.500	1.420	-1.20E-02	1.180	-9.00E-03	1.820	-0.510	1.344	-3.76E-03	1.460	-9.00E-03
2.700	1.400	-5.50E-02	1.180	-1.30E-02	1.830	-0.520	1.303	-5.70E-03	1.460	-1.00E-02
3.000	1.420	-2.20E-02	1.160	-1.20E-02	1.840	-0.540	1.293	-9.55E-02	1.480	-1.30E-02
3.200	1.430	-8.00E-03	1.220	-1.00E-02	1.860	-0.540	1.311	-0.135	1.480	-1.40E-02
3.392	1.430	-7.00E-03	1.260	-1.30E-02	1.870	-0.550	1.352	-0.159	1.490	-1.20E-02
3.500	1.450	-5.00E-03	1.280	-1.10E-02	1.880	-0.560	1.376	-0.158	1.490	-1.10E-02
3.750	1.452	-4.00E-03	1.270	-1.10E-02	1.900	-0.570	1.396	-0.131	1.500	-9.00E-03
4.000	1.455	-5.00E-03	1.260	-1.20E-02	1.920	-0.580	1.398	-0.126	1.500	-7.00E-03
4.500	1.460	-1.30E-02	1.260	-1.40E-02	1.940	-0.590	1.385	-0.120	1.520	-7.50E-03
5.000	1.450	-1.20E-02	1.250	-1.60E-02	1.970	-0.600	1.360	-0.121	1.510	-9.00E-03
5.500	1.440	-1.80E-02	1.220	-2.10E-02	1.990	-0.610	1.337	-0.183	1.510	-1.20E-02
6.000	1.410	-2.30E-02	1.150	-3.70E-02	2.020	-0.620	1.425	-0.195	1.480	-1.50E-02
6.200	1.430	-2.70E-02	1.140	-3.90E-02	2.030	-0.625	1.424	-0.165	1.460	-1.80E-02
6.500	1.460	-3.30E-02	1.130	-4.20E-02	2.040	-0.630	1.370	-0.128	1.450	-2.40E-02
7.200	1.400	-7.00E-02	1.400	-5.50E-02	2.060	-0.650	1.210	-0.176	1.440	-4.50E-02
7.900	1.200	-6.50E-02	1.150	-4.00E-02	2.120	-0.670	1.140	-0.488	1.380	-7.20E-02
8.200	1.010	-0.100	1.130	-7.40E-02	2.130	-0.680	1.200	-0.645	1.340	-9.70E-02
8.500	1.300	-0.215	1.300	-9.00E-02	2.150	-0.690	1.370	-0.755	1.620	-0.121
8.700	2.400	-0.290	1.400	-0.100	2.160	-0.690	1.530	-0.772	1.950	-0.170
9.000	2.560	-0.370	1.700	-0.140	2.170	-0.700	1.650	-0.633	2.200	-0.215
9.200	2.200	-0.420	1.720	-0.150	2.180	-0.700	1.600	-0.586	2.230	-0.240
9.500	1.950	-0.160	1.730	-0.162	2.190	-0.710	1.670	-0.750	2.250	-0.275
9.800	1.870	-9.50E-02	1.740	-0.162	2.200	-0.715	1.910	-0.680	2.280	-0.300
10.000	1.820	-9.00E-02	1.750	-0.162	2.210	-0.720	1.890	-0.455	2.300	-0.320
10.591	1.760	-7.00E-02	1.620	-0.120	2.220	-0.730	1.720	-0.340	2.200	-0.305
11.000	1.720	-5.00E-02	1.620	-0.105	2.230	-0.730	1.670	-0.485	2.150	-0.270
11.500	1.670	-4.70E-02	1.590	-0.100	2.240	-0.740	1.890	-0.374	2.050	-0.240
12.500	1.620	-5.30E-02	1.510	-9.00E-02	2.270	-0.750	1.740	-0.198	1.800	-0.155
13.000	1.620	-5.50E-02	1.470	-0.100	2.280	-0.760	1.690	-0.195	1.760	-0.148
14.000	1.560	-7.30E-02	1.520	-8.50E-02	2.310	-0.775	1.640	-0.195	1.700	-0.145
14.800	1.440	-0.100	1.570	-0.100	2.330	-0.790	1.610	-0.205	1.650	-0.157
15.000	1.420	-0.200	1.570	-0.100	2.330	-0.790	1.590	-0.211	1.650	-0.170
16.400	1.750	-0.160	1.600	-0.100	2.360	-0.810	1.520	-0.414	1.750	-0.200
17.200	2.080	-0.240	1.630	-0.100	2.380	-0.820	1.724	-0.590	1.850	-0.240
18.000	1.980	-0.180	1.640	-0.115	2.400	-0.825	1.950	-0.410	2.000	-0.305
18.500	1.850	-0.170	1.640	-0.120	2.410	-0.830	1.927	-0.302	2.100	-0.325
20.000	2.120	-0.220	1.680	-0.220	2.450	-0.850	1.823	-0.235	2.250	-0.318
21.300	2.060	-0.230	1.770	-0.280	2.460	-0.860	1.780	-0.292	2.400	-0.290
22.500	2.000	-0.240	1.900	-0.280	2.480	-0.870	1.870	-0.315	2.500	-0.350
25.000	1.880	-0.280	1.970	-0.240	2.510	-0.890	1.930	-0.200	2.600	-0.400
27.900	1.840	-0.290	1.890	-0.320	2.540	-0.910	1.920	-0.180	2.500	-0.430
30.000	1.820	-0.300	1.800	-0.420	2.570	-0.930	1.920	-0.180	2.400	-0.450
35.000	1.920	-0.400	1.900	-0.500	2.630	-0.970	1.900	-0.190	2.300	-0.520
40.000	1.860	-0.500	2.100	-0.600	2.690	-1.000	1.890	-0.220	2.250	-0.650

CHAPTER 18

Table 18-10a. Vertical distribution of aerosol extinction (km^{-1}) for a wavelength of 0.550 μm with rural model aerosol boundary layer.

Height (km)	50 km Met. Range	23 km Met. Range	10 km Met. Range	5 km Met. Range	2 km Met. Range			
0.0	6.62E-02	1.58E-01	3.79E-01	7.70E-02	1.94E+00			
1.0	4.15E-02	9.91E-02	3.79E-01	7.70E-01	1.94E+00			
1.5	3.26E-02	7.92E-02	3.79E-01	7.70E-01	1.94E+00			
2.0	2.60E-02	6.21E-02	6.21E-02	6.21E-02	6.21E-02			
	Fall-Winter Profiles				Spring-Summer Profiles			
	50 km Surface Met. Range		2 to 23 km Surface Met. Range		50 km Surface Met. Range		2 to 23 km Surface Met. Range	
2.0	2.60E-02		6.21E-02		2.60E-02		6.21E-02	
3.0	1.14E-02		2.72E-02		1.46E-02		3.46E-02	
4.0	6.43E-03		1.20E-02		1.02E-02		1.85E-02	
5.0	4.85E-03		4.85E-03		9.30E-03		9.30E-03	
6.0	3.54E-03		3.54E-03		7.71E-03		7.71E-03	
7.0	2.30E-03		2.30E-03		6.22E-03		6.22E-03	
8.0	1.41E-03		1.41E-03		3.36E-03		3.36E-03	
9.0	9.80E-04		9.80E-04		1.81E-03		1.81E-03	
	Background Stratosphere	Moderate Volcanic	High Volcanic	Extreme Volcanic	Background Stratospheric	Moderate Volcanic	High Volcanic	Extreme Volcanic
9.0	9.80E-04	9.80E-04	9.80E-04	9.80E-04	1.81E-03	1.81E-03	1.81E-03	1.81E-03
10.0	7.87E-04	1.38E-03	1.70E-03	1.70E-03	1.14E-03	1.85E-03	1.85E-03	1.85E-03
11.0	7.14E-04	1.79E-03	2.31E-03	2.31E-03	8.00E-04	2.11E-03	2.11E-03	2.11E-03
12.0	6.63E-04	2.21E-03	3.25E-03	3.25E-03	6.42E-04	2.45E-03	2.45E-03	2.45E-03
13.0	6.22E-04	2.75E-03	4.52E-03	4.52E-03	5.17E-04	2.80E-03	2.80E-03	2.80E-03
14.0	6.45E-04	2.89E-03	6.40E-03	6.40E-03	4.43E-04	2.89E-03	3.61E-03	3.61E-03
15.0	6.43E-04	2.92E-03	7.80E-03	1.01E-02	3.95E-04	2.92E-03	5.23E-03	5.23E-03
16.0	6.41E-04	2.74E-03	9.42E-03	2.35E-02	3.82E-04	2.74E-03	8.10E-03	8.10E-03
17.0	6.01E-04	2.46E-03	1.07E-02	6.10E-02	4.25E-04	2.46E-03	1.20E-02	1.27E-02
18.0	5.63E-04	2.10E-03	1.10E-02	1.00E-01	5.20E-04	2.10E-03	1.52E-02	2.32E-02
19.0	4.92E-04	1.71E-03	8.60E-03	4.00E-02	5.82E-04	1.71E-03	1.53E-02	4.85E-02
20.0	4.23E-04	1.35E-03	5.10E-03	9.15E-03	5.90E-04	1.35E-03	1.17E-02	1.00E-01
21.0	3.52E-04	1.09E-03	2.70E-03	3.13E-03	5.03E-04	1.09E-03	7.10E-03	5.50E-02
22.0	2.96E-04	8.60E-04	1.46E-03	1.46E-03	4.20E-04	8.60E-04	4.50E-03	6.10E-03
23.0	2.42E-04	6.60E-04	8.90E-04	8.90E-04	3.00E-04	6.60E-04	2.40E-03	2.40E-03
24.0	1.90E-04	5.15E-04	5.80E-04	5.80E-04	1.98E-04	5.15E-04	1.28E-03	1.28E-03
25.0	1.50E-04	4.10E-04	4.10E-04	4.10E-04	1.31E-04	4.10E-04	7.75E-04	7.75E-04
26.0	1.15E-04	3.20E-04	3.20E-04	3.20E-04	9.01E-05	3.20E-04	4.45E-04	4.45E-04
27.0	8.95E-05	2.51E-04	2.51E-04	2.51E-04	6.78E-05	2.51E-04	2.90E-04	2.90E-04
28.0	6.70E-05	2.10E-04	2.10E-04	2.10E-04	5.18E-05	2.10E-04	2.10E-04	2.10E-04
29.0	5.20E-05	1.24E-04	1.24E-04	1.24E-04	4.12E-05	1.24E-04	1.24E-04	1.24E-04
30.0	3.32E-05	7.60E-05	7.60E-05	7.60E-05	3.32E-05	7.60E-05	7.60E-05	7.60E-05
	Normal Upper Atmos.	Transition from Volcanic to			Extreme Upper Atmos.			
30.0	3.32E-05		Normal 7.60E-05	Extreme 7.60E-05				
35.0	1.65E-05		2.45E-05	7.20E-05				
40.0	8.00E-06		8.00E-06	6.95E-05				
45.0	4.02E-06		4.02E-06	6.60E-05				
50.0	2.10E-06							
55.0	1.09E-06							
60.0	5.78E-07							
65.0	3.05E-07							
70.0	1.60E-07							
75.0	6.95E-08							
80.0	2.90E-08							
85.0	1.20E-08							
90.0	5.10E-09							
95.0	2.15E-09							
100.0	9.30E-10							

OPTICAL AND INFRARED PROPERTIES OF THE ATMOSPHERE

Table 18-10b. Vertical distribution of aerosol scattering (km^{-1}) for a wavelength of $0.550 \mu\text{m}$ with rural model aerosol boundary layer.

Height (km)	50 km Met. Range	23 km Met. Range	10 km Met. Range	5 km Met. Range	2 km Met. Range			
0.0	6.35E-02	1.52E-01	3.64E-01	7.39E-01	1.86E+00			
1.0	3.98E-02	9.51E-02	3.64E-01	7.39E-01	1.86E+00			
1.5	3.13E-02	7.60E-02	3.64E-01	7.39E-01	1.86E+00			
2.0	2.49E-02	5.96E-02	5.96E-02	5.96E-02	5.96E-02			
Fall-Winter Profiles			Spring-Summer Profiles					
	50 km Surface Met. Range	2 to 23 km Surface Met. Range		50 km Surface Met. Range	2 to 23 km Surface Met. Range			
2.0	2.49E-02	5.96E-02		2.49E-02	5.96E-02			
3.0	1.09E-02	2.59E-02		1.39E-02	3.30E-02			
4.0	6.13E-03	1.14E-02		9.72E-03	1.76E-02			
5.0	4.62E-03	4.62E-03		8.86E-03	8.86E-03			
6.0	3.37E-03	3.37E-03		7.35E-03	7.35E-03			
7.0	2.19E-03	2.19E-03		5.93E-03	5.93E-03			
8.0	1.34E-03	1.34E-03		3.20E-03	3.20E-03			
9.0	9.34E-04	9.34E-04		1.72E-03	1.72E-03			
	Background Stratosphere	Moderate Volcanic	High Volcanic	Extreme Volcanic	Background Stratospheric	Moderate Volcanic	High Volcanic	Extreme Volcanic
9.0	9.34E-04	9.34E-04	9.34E-04	9.34E-04	1.72E-03	1.72E-03	1.72E-03	1.72E-03
10.0	7.87E-04	1.31E-03	1.45E-03	1.45E-03	1.14E-03	1.75E-03	1.58E-03	1.58E-03
11.0	7.14E-04	1.70E-03	1.98E-03	1.98E-03	8.00E-04	2.00E-03	1.80E-03	1.80E-03
12.0	6.63E-04	2.09E-03	2.78E-03	2.78E-03	6.42E-04	2.32E-03	2.10E-03	2.10E-03
13.0	6.22E-04	2.61E-03	3.87E-03	3.87E-03	5.17E-04	2.65E-03	2.39E-03	2.39E-03
14.0	6.45E-04	2.74E-03	5.47E-03	5.47E-03	4.43E-04	2.74E-03	3.09E-03	3.09E-03
15.0	6.43E-04	2.77E-03	6.67E-03	8.64E-03	3.95E-04	2.77E-03	4.47E-03	4.47E-03
16.0	6.41E-04	2.60E-03	8.06E-03	2.01E-02	3.82E-04	2.60E-03	6.93E-03	6.93E-03
17.0	6.01E-04	2.33E-03	9.15E-03	5.22E-02	4.25E-04	2.33E-03	1.03E-02	1.09E-02
18.0	5.63E-04	1.99E-03	9.41E-03	8.55E-02	5.20E-04	1.99E-03	1.30E-02	1.98E-02
19.0	4.92E-04	1.62E-03	7.36E-03	8.42E-02	5.82E-04	1.62E-03	1.31E-02	4.15E-02
20.0	4.23E-04	1.28E-03	4.36E-03	7.83E-03	5.90E-04	1.28E-03	1.00E-02	8.55E-02
21.0	3.52E-04	1.03E-03	2.31E-03	2.68E-03	5.03E-04	1.03E-03	6.07E-03	4.70E-02
22.0	2.96E-04	8.15E-04	1.25E-03	1.25E-03	4.20E-04	8.15E-04	3.85E-03	5.22E-03
23.0	2.42E-04	6.25E-04	7.61E-04	7.61E-04	3.00E-04	6.25E-04	2.05E-03	2.05E-03
24.0	1.90E-04	4.88E-04	4.96E-04	4.96E-04	1.98E-04	4.88E-04	1.09E-03	1.09E-03
25.0	1.50E-04	3.88E-04	3.51E-04	3.51E-04	1.31E-04	3.88E-04	6.63E-04	6.63E-04
26.0	1.15E-04	3.03E-04	2.74E-04	2.74E-04	9.01E-05	3.03E-04	3.81E-04	3.81E-04
27.0	8.95E-05	2.38E-04	2.15E-04	2.15E-04	6.78E-05	2.38E-04	2.48E-04	2.48E-04
28.0	6.70E-05	1.99E-04	1.80E-04	1.80E-04	5.18E-05	1.99E-04	1.80E-04	1.80E-04
29.0	5.20E-05	1.17E-04	1.06E-04	1.06E-04	4.12E-05	1.17E-04	1.06E-04	1.06E-04
30.0	3.32E-05	7.20E-05	7.20E-05	7.20E-05	3.32E-05	7.20E-05	7.20E-05	7.20E-05
	Normal Upper Atmos.	Transition from Volcanic to		Extreme Upper Atmos.				
30.0	3.32E-05	Normal	Extreme	2.84E-05				
35.0	1.64E-05	7.20E-05	6.50E-05	4.23E-05				
40.0	7.96E-06	2.44E-05	7.16E-05	5.57E-05				
45.0	4.00E-06	7.96E-06	6.91E-05	6.57E-05				
50.0	2.09E-06	4.00E-06	6.57E-05	5.01E-05				
55.0	1.08E-06			3.38E-05				
60.0	5.75E-07			2.29E-05				
65.0	3.03E-07			1.61E-05				
70.0	1.59E-07			1.02E-05				
75.0	6.91E-08			6.67E-06				
80.0	2.89E-08			4.28E-06				
85.0	1.19E-08			2.77E-06				
90.0	5.07E-09			1.54E-06				
95.0	2.14E-09			8.26E-07				
100.0	9.25E-10			4.48E-07				

CHAPTER 18

Table 18-10c. Vertical distribution of aerosol absorption(km^{-1}) for a wavelength of $0.550 \mu\text{m}$ with rural model aerosol boundary layer.

Height (km)	50 km Met. Range	23 km Met. Range	10 km Met. Range	5 km Met. Range	2 km Met. Range				
0.0	2.70E-03	6.45E-03	1.55E-02	3.14E-02	7.92E-02				
1.0	1.69E-03	4.04E-03	1.55E-02	3.14E-02	7.92E-02				
1.5	1.33E-03	3.23E-03	1.55E-02	3.14E-02	7.92E-02				
2.0	1.06E-03	2.53E-03	2.53E-03	2.53E-03	2.53E-03				
Fall-Winter Profiles					Spring-Summer Profiles				
	50 km Surface Met. Range		2 to 23 km Surface Met. Range		50 km Surface Met. Range		2 to 23 km Surface Met. Range		
2.0	1.06E-03		2.53E-03		1.06E-03		2.53E-03		
3.0	5.38E-04		1.28E-03		6.89E-04		1.63E-04		
4.0	3.03E-04		5.66E-04		4.81E-04		8.73E-04		
5.0	2.29E-04		2.29E-04		4.39E-04		4.39E-04		
6.0	1.67E-04		1.67E-04		3.64E-04		3.64E-04		
7.0	1.08E-04		1.08E-04		2.93E-04		2.93E-04		
8.0	6.65E-05		6.65E-05		1.58E-04		1.58E-04		
9.0	4.62E-05		4.62E-05		8.54E-05		8.54E-05		
	Background Stratosphere	Moderate Volcanic	High Volcanic	Extreme Volcanic	Background Stratospheric	Moderate Volcanic	High Volcanic	Extreme Volcanic	
9.0	4.62E-05	4.62E-05	4.62E-05	4.62E-05	8.54E-05	8.54E-05	8.54E-05	8.54E-05	
10.0	4.66E-11	7.27E-05	2.46E-04	2.46E-04	6.75E-11	9.75E-05	2.68E-04	2.68E-04	
11.0	4.22E-11	9.44E-05	3.34E-04	3.34E-04	4.73E-11	1.11E-04	3.05E-04	3.05E-04	
12.0	3.92E-11	1.16E-04	4.70E-04	4.70E-04	3.80E-11	1.29E-04	3.54E-04	3.54E-04	
13.0	3.68E-11	1.45E-04	6.54E-04	6.54E-04	3.06E-11	1.48E-04	4.05E-04	4.05E-04	
14.0	3.82E-11	1.52E-04	9.26E-04	9.26E-04	2.62E-11	1.52E-04	5.22E-04	5.22E-04	
15.0	3.80E-11	1.54E-04	1.13E-03	1.46E-03	2.34E-11	1.54E-04	7.57E-04	7.57E-04	
16.0	3.79E-11	1.44E-04	1.36E-03	3.40E-03	2.26E-11	1.44E-04	1.17E-03	1.17E-03	
17.0	3.56E-11	1.30E-04	1.55E-03	8.83E-03	2.51E-11	1.30E-04	1.74E-03	1.84E-03	
18.0	3.33E-11	1.11E-04	1.59E-03	1.45E-02	3.08E-11	1.11E-04	2.20E-03	3.36E-03	
19.0	2.91E-11	9.01E-05	1.24E-03	5.79E-03	3.44E-11	9.01E-05	2.21E-03	7.02E-03	
20.0	2.50E-11	7.12E-05	7.38E-04	1.32E-03	3.49E-11	7.12E-05	1.69E-03	1.45E-02	
21.0	2.08E-11	5.75E-05	3.91E-04	4.53E-04	2.98E-11	5.75E-05	1.03E-03	7.96E-03	
22.0	1.75E-11	4.53E-05	2.11E-04	2.11E-04	2.49E-11	4.53E-05	6.51E-04	8.83E-04	
23.0	1.43E-11	3.48E-05	1.29E-04	1.29E-04	1.78E-11	3.48E-05	3.47E-04	3.47E-04	
24.0	1.12E-11	2.71E-05	8.39E-05	8.39E-05	1.17E-11	2.71E-05	1.85E-04	1.85E-04	
25.0	8.88E-12	2.16E-05	5.93E-05	5.93E-05	7.75E-12	2.16E-05	1.12E-04	1.12E-04	
26.0	6.80E-12	1.69E-05	4.63E-05	4.63E-05	5.33E-12	1.69E-05	6.44E-05	6.44E-05	
27.0	5.30E-12	1.32E-05	3.63E-05	3.63E-05	4.01E-12	1.32E-05	4.20E-05	4.20E-05	
28.0	3.96E-12	1.11E-05	3.04E-05	3.04E-05	3.07E-12	1.11E-05	3.04E-05	3.04E-05	
29.0	3.08E-12	6.54E-06	1.79E-05	1.79E-05	2.44E-12	6.54E-06	1.79E-05	1.79E-05	
30.0	1.96E-12	4.01E-06	4.01E-06	4.01E-06	1.96E-12	4.01E-06	4.01E-06	4.01E-06	
	Normal Upper Atmos.	Transition from Volcanic to			Extreme Upper Atmos.				
		Normal	Extreme						
35.0	8.35E-08		1.24E-07	3.64E-07		2.15E-07			
40.0	4.05E-08		4.05E-08	3.52E-07		2.83E-07			
45.0	2.03E-08		2.03E-08	3.34E-07		3.34E-07			
50.0	1.06E-08					2.55E-07			
55.0	5.51E-09					1.72E-07			
60.0	2.92E-09					1.16E-07			
65.0	1.54E-09					8.20E-08			
70.0	8.10E-10					5.21E-08			
75.0	3.52E-10					3.39E-08			
80.0	1.47E-10					2.18E-08			
85.0	6.07E-11					1.41E-08			
90.0	2.58E-11					7.84E-09			
95.0	1.09E-11					4.20E-09			
100.0	4.71E-12					2.28E-09			

OPTICAL AND INFRARED PROPERTIES OF THE ATMOSPHERE

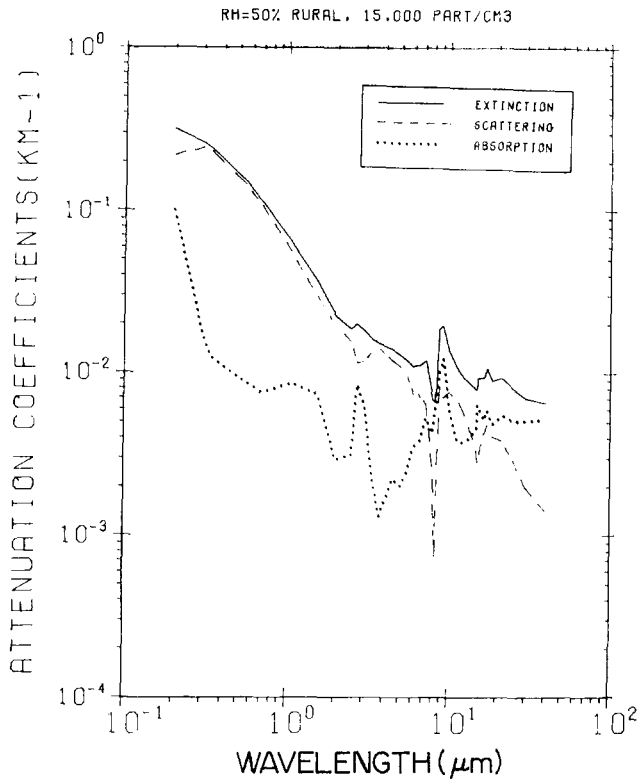


Figure 18-14. Attenuation coefficients vs wavelength for the rural aerosol model at 50% relative humidity.

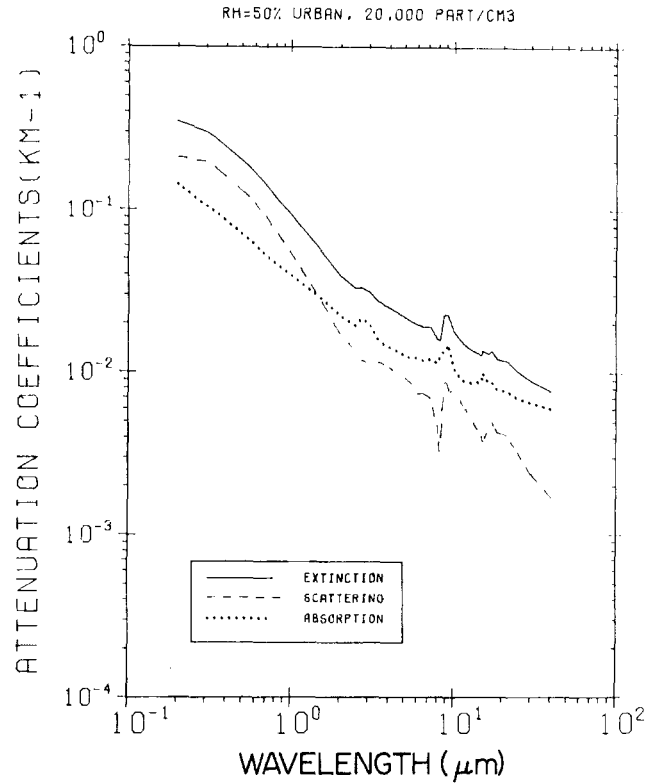


Figure 18-16. Attenuation coefficients vs wavelength for the urban aerosol model at 50% relative humidity.

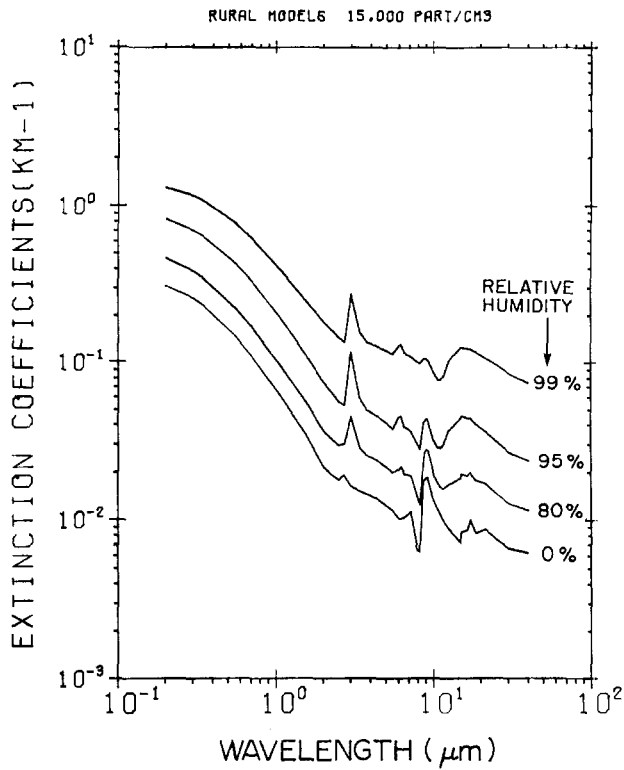


Figure 18-15. Extinction coefficients vs wavelength for the rural aerosol model for different relative humidities and constant number density of particles.

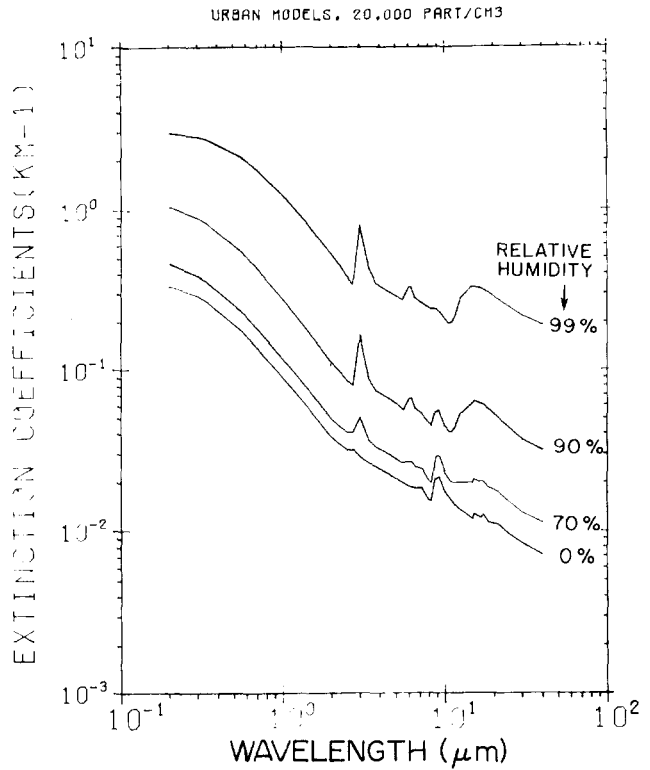


Figure 18-17. Extinction coefficients vs wavelength for the urban aerosol model for different relative humidities and constant number density of particles.

CHAPTER 18

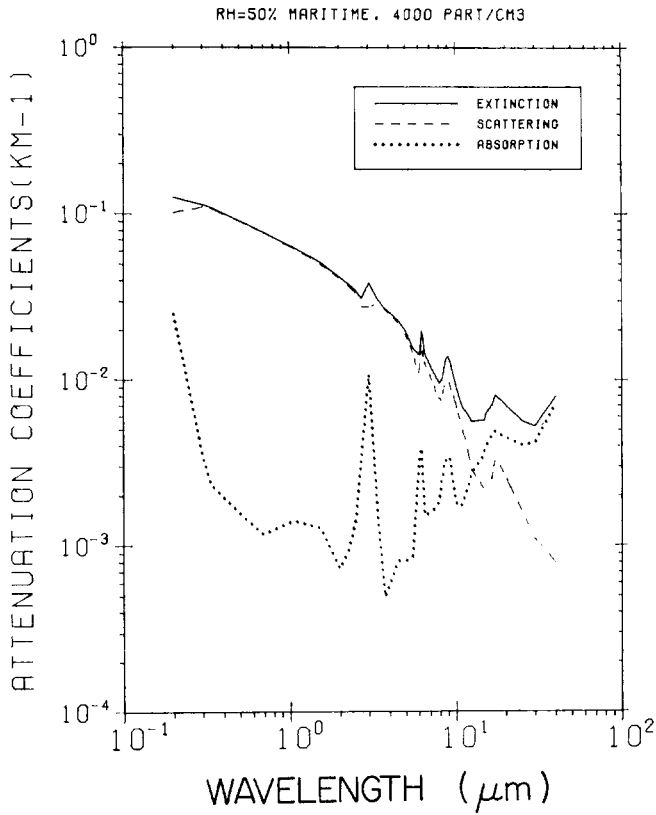


Figure 18-18. Attenuation coefficients vs wavelength for the maritime aerosol model at 50% relative humidity.

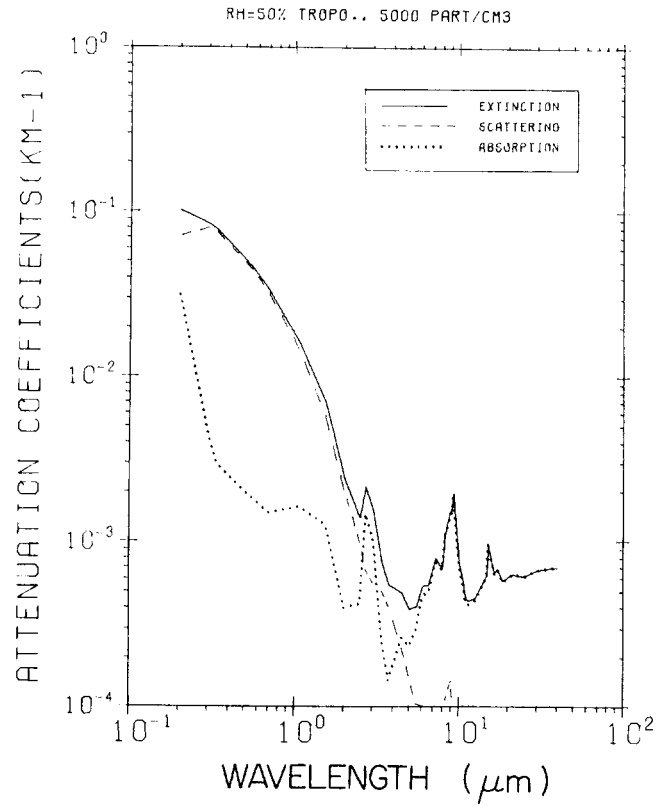


Figure 18-20. Attenuation coefficients vs wavelength for the tropospheric aerosol model at 50% relative humidity.

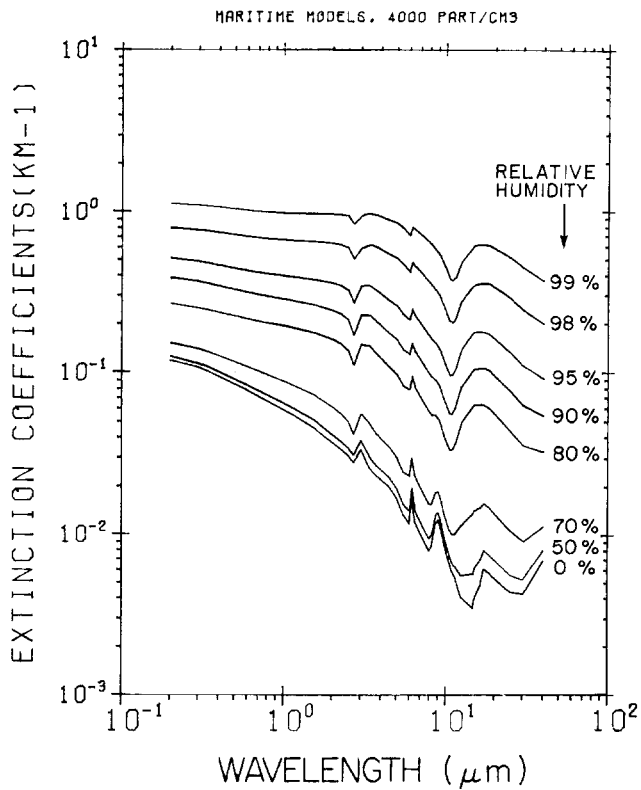


Figure 18-19. Extinction coefficients vs wavelength for the maritime aerosol model for the different relative humidities and constant number density of particles.

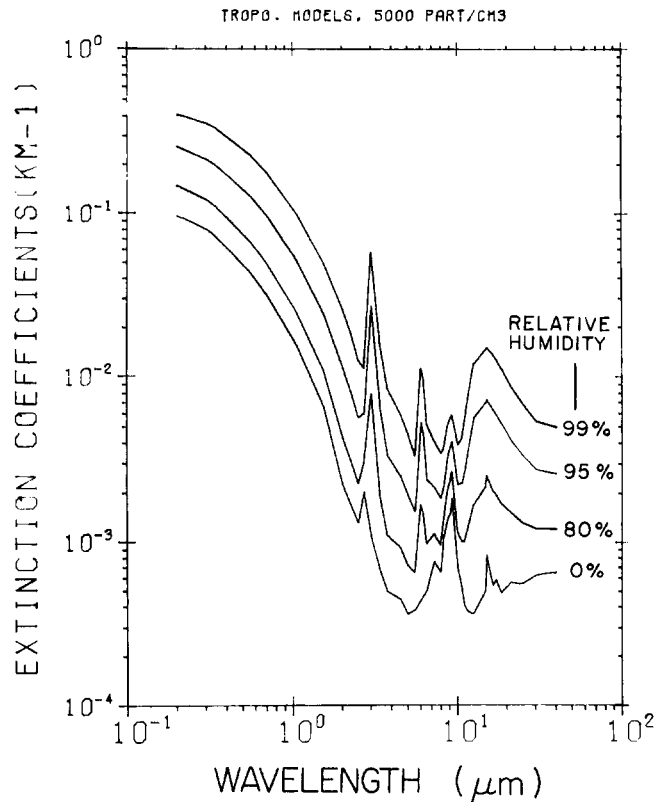


Figure 18-21. Extinction coefficients vs wavelength for the tropospheric aerosol model for different relative humidities and constant number density of particles.

OPTICAL AND INFRARED PROPERTIES OF THE ATMOSPHERE

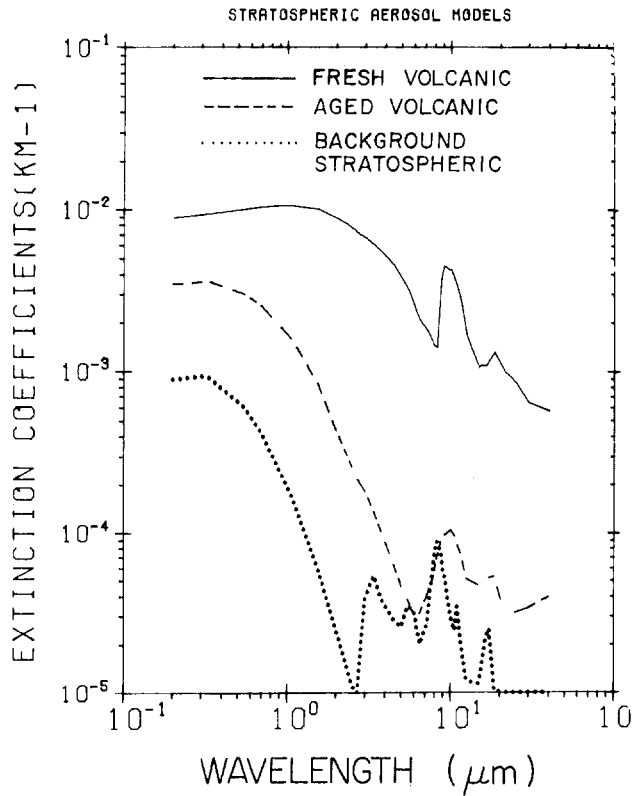


Figure 18-22. Extinction coefficients for the different stratospheric aerosol models (background stratospheric, volcanic, and fresh volcanic). The extinction coefficients have been normalized to values around peak levels for these models (see also Figure 18-13).

relative humidities between 0% and 99% where the number density is fixed at 15 000 particles/cm³, which corresponds to a meteorological range of about 25 km for the dry aerosols and about 5 km at 99% relative humidity.

The attenuation coefficients for the urban aerosol model as a function of wavelength are shown in Figures 18-16 and 18-17 for different humidities. The corresponding results for the maritime and tropospheric aerosol models are shown in Figures 18-18 and 18-19 and Figures 18-20 and 18-21, respectively.

The extinction coefficients for the background stratospheric and volcanic aerosol models are shown in Figure 18-22. Frequently the ratio of the scattering coefficient to total extinction k_s/k_e (single scatter albedo) is used as a measure for the relative contribution of scattering and absorption to the total extinction. Figures 18-23 through 18-27 give the single scatter albedo for the aerosol models discussed above. Notice the rapid change in the relative importance of aerosol scattering and absorption in the middle infrared spectral region. This is due to two factors, an increase in the absorption because of an increase in the imaginary part of the refractive index in the infrared, and a decrease in the contribution from scattering as the wavelength becomes significantly larger than the size of the aerosols.

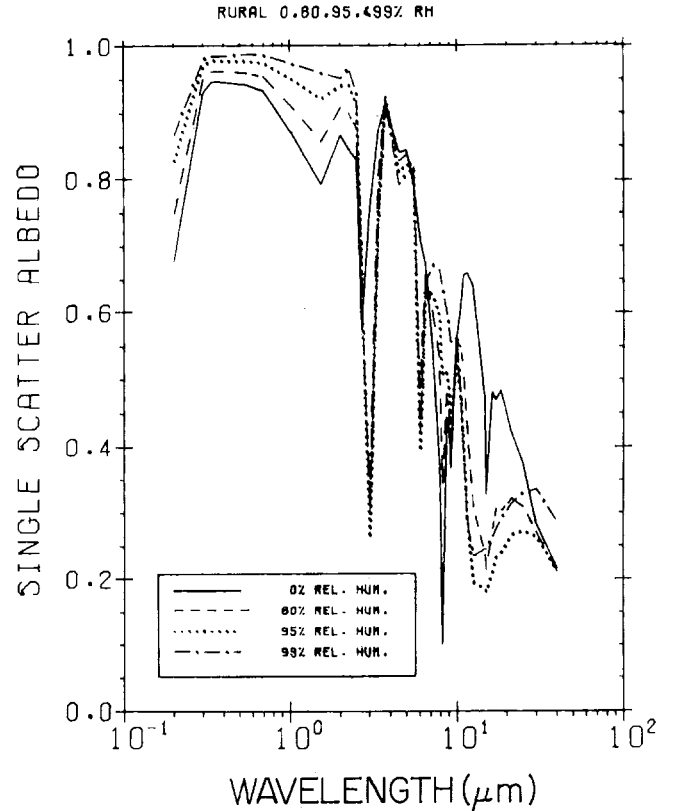


Figure 18-23. Single scattering albedo for the rural aerosol model for different relative humidities.

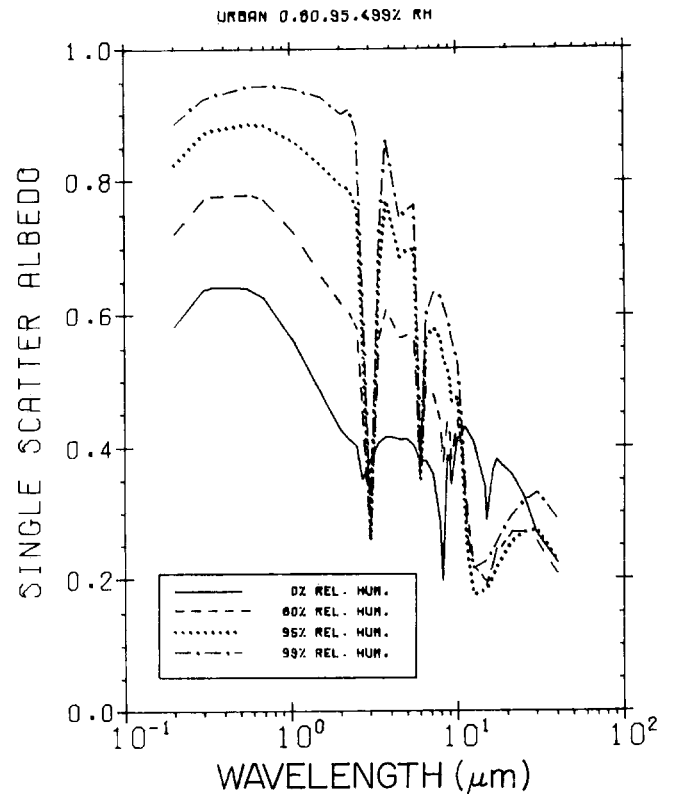


Figure 18-24. Single scattering albedo for the urban aerosol model for different relative humidities.

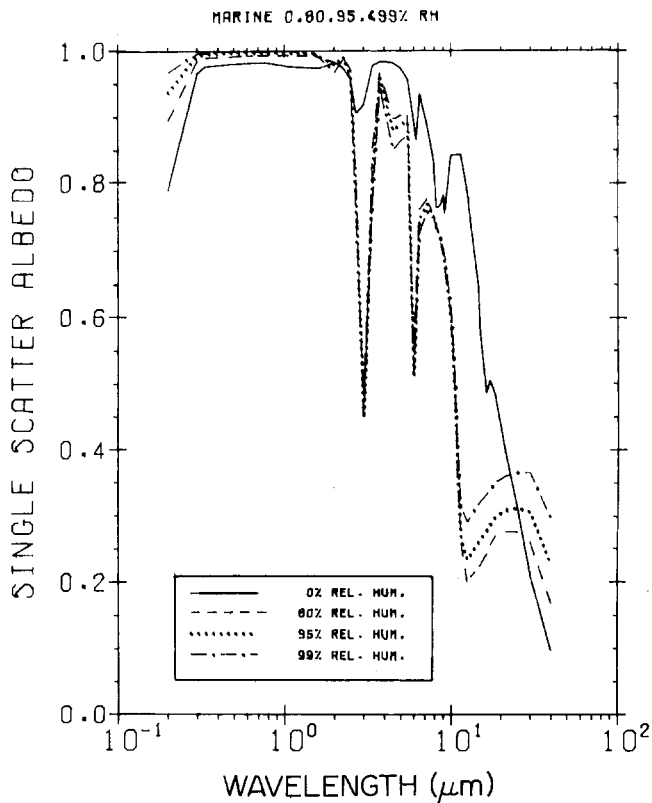


Figure 18-25. Single scattering albedo for the maritime aerosol model for different relative humidities.

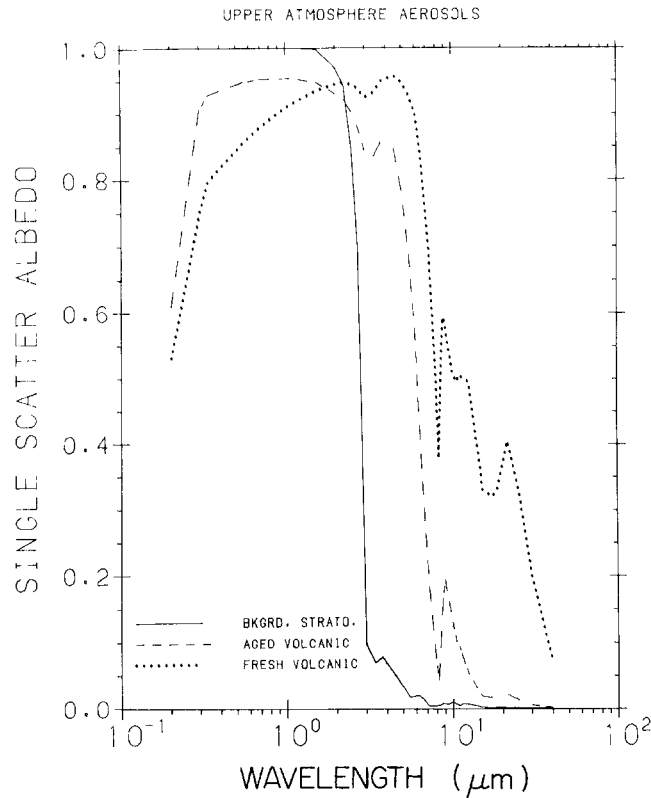


Figure 18-27. Single scattering albedo for the different stratospheric aerosol models versus wavelength.

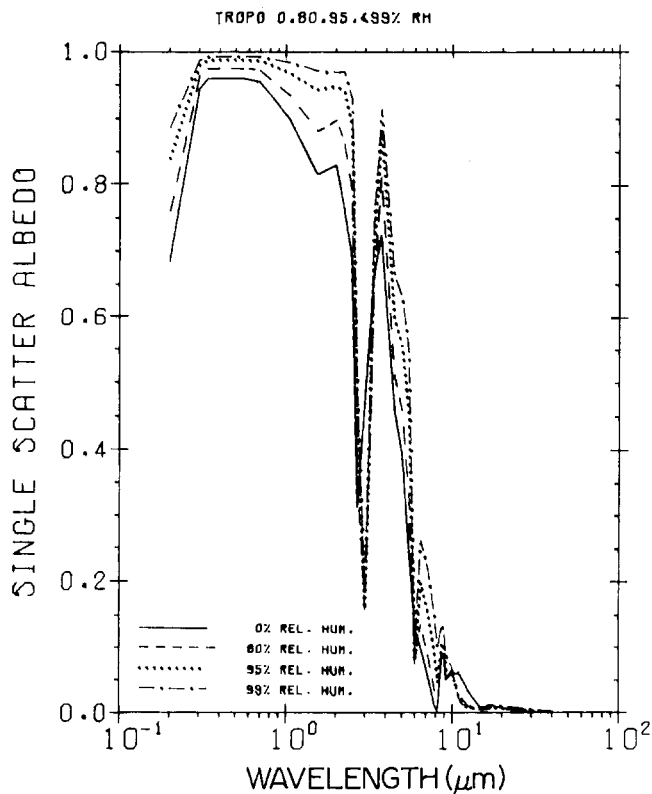


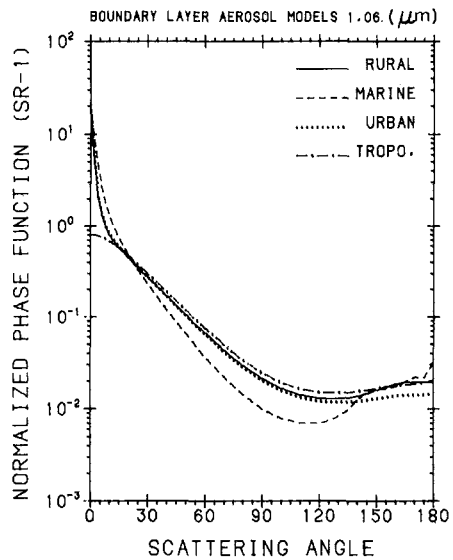
Figure 18-26. Single scattering albedo for the tropospheric aerosol model for different relative humidities.

There are also some noticeable differences between the angular scattering functions of these various aerosol models. Figures 18-28 a, b and 18-29 a, b give examples for two wavelengths 1.06 and 10.6 μm . Both figures give the phase function, defined such that the integral from 0° to 180° becomes 1. For many purposes (see Section 18.5.1) a convenient one-parameter representation for the angular dependence of scattering by aerosols is the asymmetry parameter g . It is defined as the cosine weighted average of the phase function $P(\theta)$:

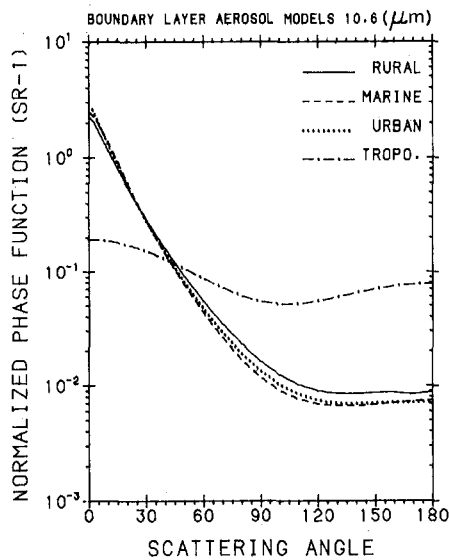
$$g = \frac{\int_{-1}^{+1} \cos \theta P(\theta) d(\cos \theta)}{\int_{-1}^{+1} P(\theta) d(\cos \theta)}, \quad (18.22)$$

where $P(\theta)$ is the differential probability of scattering at an angle θ . The asymmetry factor for the various aerosol models is shown in Figures 18-30 to 18-34.

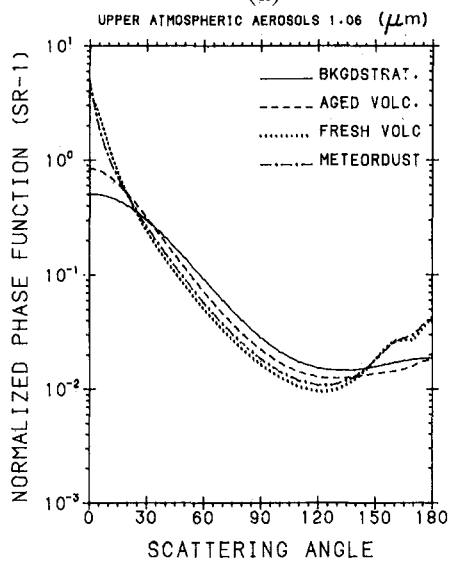
Any quantitative treatment of light scattering must include the polarization of light since in general light becomes polarized in the scattering process, and the angular distribution of scattered light depends on the state of polarization of the light incident on a particle. The degree of polarization P can vary between -1 and $+1$ (see Equation (18.18)).



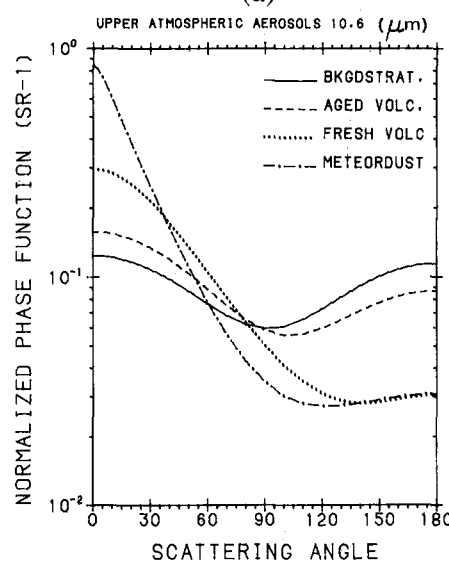
(a)



(a)



(b)



(b)

Figure 18-28. (a) Angular scattering functions of low altitude aerosol models at 1.06 μm .
(b) Angular scattering functions of high altitude aerosol models at 1.06 μm .

Figure 18-29. (a) Angular scattering functions of low altitude aerosol models at 10.6 μm .
(b) Angular scattering functions of high altitude aerosol models at 10.6 μm .

Figure 18-35 gives examples of the angular variation of i_1 and i_2 . The polarization of light scattering is dependent on the particle size and the wavelength of the incident light.

18.2.2 Cloud, Fog, and Precipitation Particles

Cloud, fog, and precipitation particles are discussed separately because of their rather unique and special physical characteristics and life cycle that distinguish them from haze or aerosol particles. First, their composition is uniform, either water or ice, or under some circumstances a combination of both. Second, in liquid phase these particles are drop-shaped, that is, close to spherical. These two char-

acteristics make modeling of these particles much more realistic than for aerosols. Also the formation processes and life cycle for these particles are better understood than those for aerosols. For additional information see Chapter 16. A survey on fog properties was compiled by Stewart and Essenwanger [1982].

18.2.2.1 Particle Types, Water-Ice Refractive Index, Particle Shapes. Liquid, fog, and cloud droplets are the result of condensation of water vapor on condensation nuclei (aerosol particles). This condensation occurs at relative humidities near 100% and is dependent on the physicochemical properties of the condensation nuclei. However, once the condensation has occurred the effect of the condensation nucleus on the total droplet properties becomes negligible.

CHAPTER 18

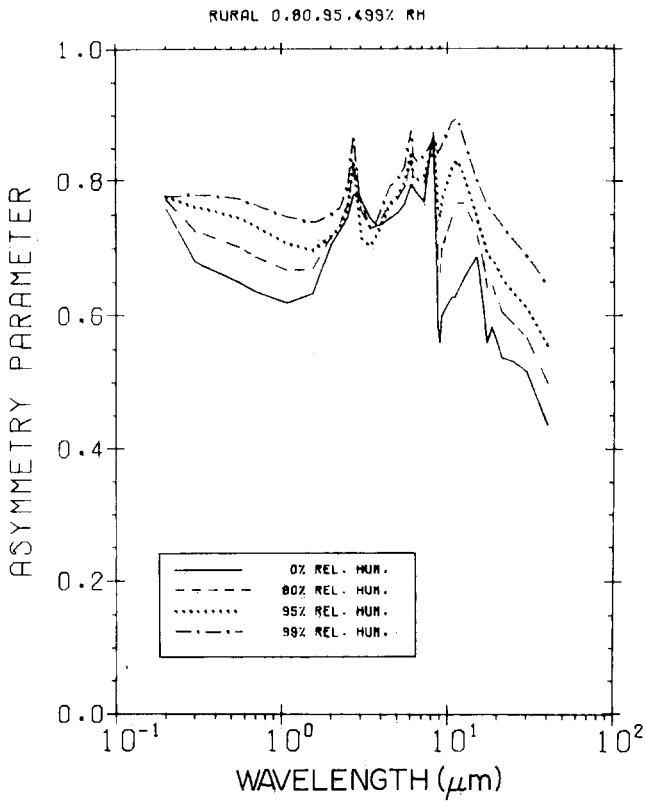


Figure 18-30. Asymmetry parameter of rural aerosol model of different relative humidities.

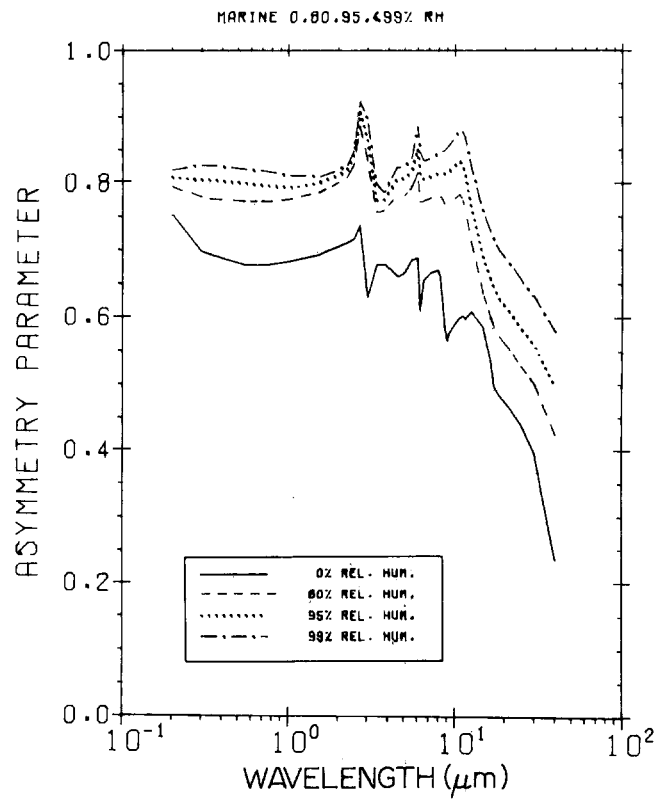


Figure 18-32. Asymmetry parameter of maritime aerosol model of different relative humidities.

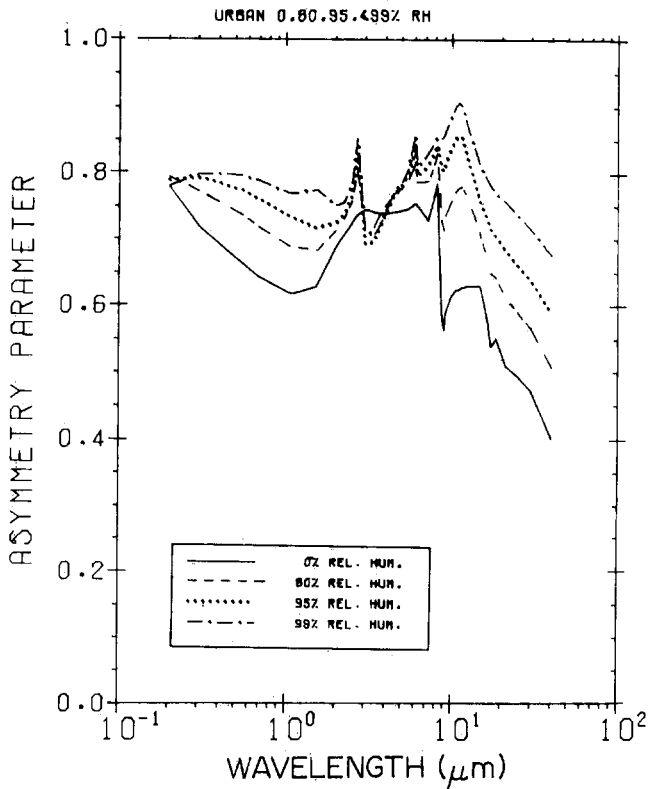


Figure 18-31. Asymmetry parameter of urban aerosol model of different relative humidities.

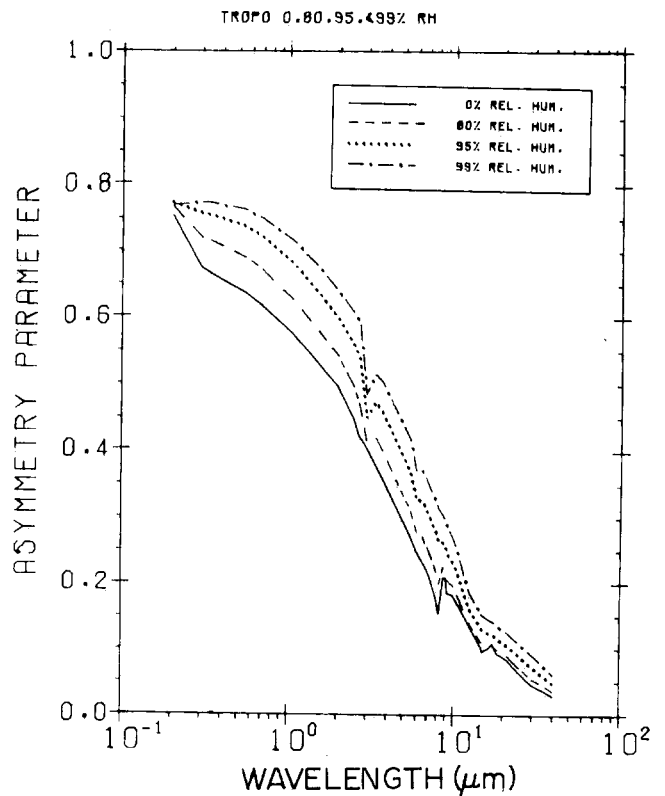


Figure 18-33. Asymmetry parameter of tropospheric aerosol model of different relative humidities.

OPTICAL AND INFRARED PROPERTIES OF THE ATMOSPHERE

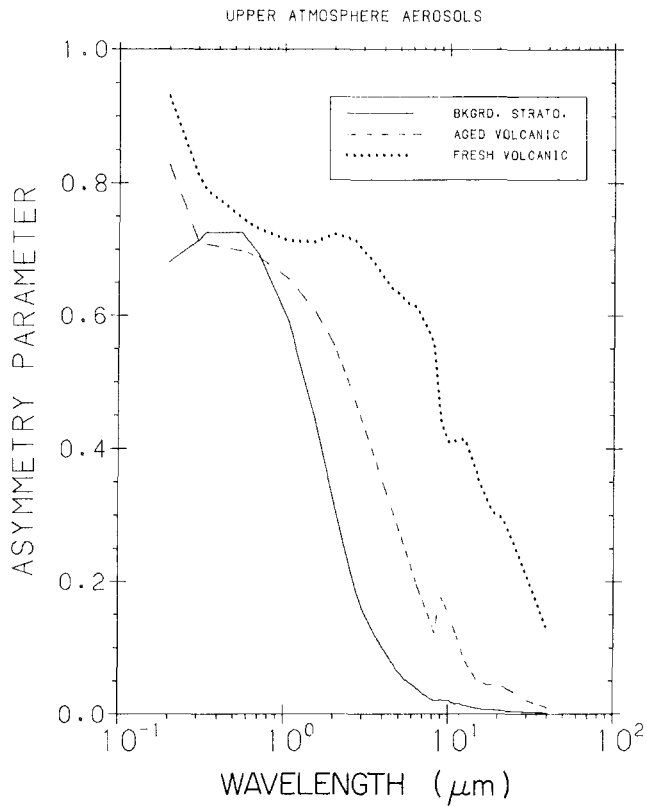


Figure 18-34. Asymmetry parameter of upper atmosphere aerosol models of different relative humidities.

The concentration and size distribution of fog and cloud particles depend in a complex way on the existing meteorological conditions. If fog or cloud droplets become so large that atmospheric buoyancy can no longer balance the gravitational forces, they will fall out as rain.

At temperatures sufficiently below freezing, ice particles will form. Depending on the conditions, they may be single ice crystals such as in ice fog or high altitude cirrus clouds, amorphous ice pellets as in sleet or hail, or complex shaped snowflakes. If ice particles fall from cold air into warmer air, their surface may be coated with a water skin. The refractive index of water at optical and infrared wavelengths is well known [Hale and Querry, 1973; Downing and Williams, 1975]; see Table 18-9.

The complex refractive index of ice in Table 18-9 was derived from several sources [Schaaf and Williams, 1973; Irvine and Pollack, 1967; Grenfell and Perovich, 1981; Hobbs, 1974; and Warren, 1984]. The detailed procedures were as follows:

- A. For the real part of the refractive index:
 1. 0.2–0.4 μm : Warren [1984] using the refractive index of water for guidance.
 2. 0.4–0.7 μm : Table 3.1 in Hobbs [1974].
 3. 0.7–2.5 μm : interpolation between Hobbs [1974] data at 0.7 μm and the value of Schaaf and Williams [1973] at 2.5 μm using a two term dispersion equation follows Irvine and Pollack's [1967] data between 0.95 and 1.3 μm but deviates for longer wavelengths.

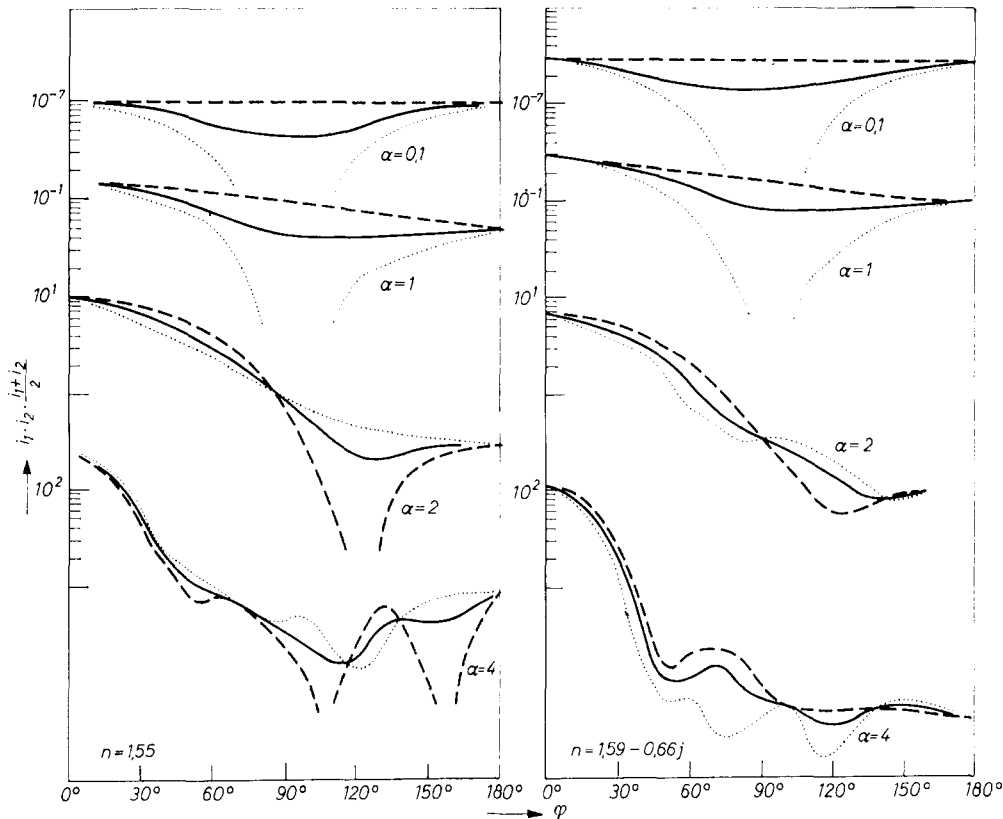


Figure 18-35. Angular dependence of i_1 ---, i_2 ... and $(i_1 + i_2)/2$ — for different aerosol particles. n = complex refractive index; α = size parameters.

CHAPTER 18

4. 2.5 to 25 μm : the measurements of Schaaf and Williams [1973], since more accurate than any available at the time of Irvine and Pollacks' [1967] survey.
 5. 25–40 μm : Warren [1984].
- B. For the imaginary part of the refractive index:
1. 0.2–0.4 μm : Warren [1984]
 2. 0.4–0.95 μm : Grenfell and Perovich's [1981] measurements.
 3. 0.95–1.40 μm : a weighted average between Grenfell and Perovich [1981] and Irvine and Pollack's [1967] survey.
 4. 1.40–2.7 μm : Irvine and Pollack's [1967] values were used since these were based on transmission measurements that are more accurate than the reflectance measurements of Schaaf and Williams for weak absorption.
 5. 2.7–25 μm : Schaaf and Williams [1973].
 6. 25–40 μm : Warren [1984]

Since the original compilation of Table 18-9, a review of the optical constants of ice has been completed by Warren [1984]. His values have replaced the preliminary ones for

wavelengths 0.2–0.4 μm and 25–40 μm . For most of the tabulated data (0.4–25 μm) the differences are the order of experimental uncertainties in the refractive index. For wavelengths outside this range, see Warren [1984].

Cloud and rain drops can be considered more or less perfect spheres. The shape of single ice crystals, although variable depending on conditions, is fairly well known. Under most conditions, simple snow crystals have an approximate hexagonal symmetry; however, size and shape (habit) are influenced by the temperature and humidity conditions extant during their formation and growth. The standard classification scheme is that of Magono and Lee [1966], who describe 80 crystal types and combinations. Further complicating the picture is the essentially infinite variety of agglomerates (what most people refer to as "flakes") that can exist, and the fact that any of the basic crystals can be modified by the attachment of super-cooled drops in a process called riming. For a more detailed discussion of crystal formation and habit, see Chapter 16.

18.2.2.2 Size Distributions. There have been extensive measurements of the the size of fog and cloud droplets.

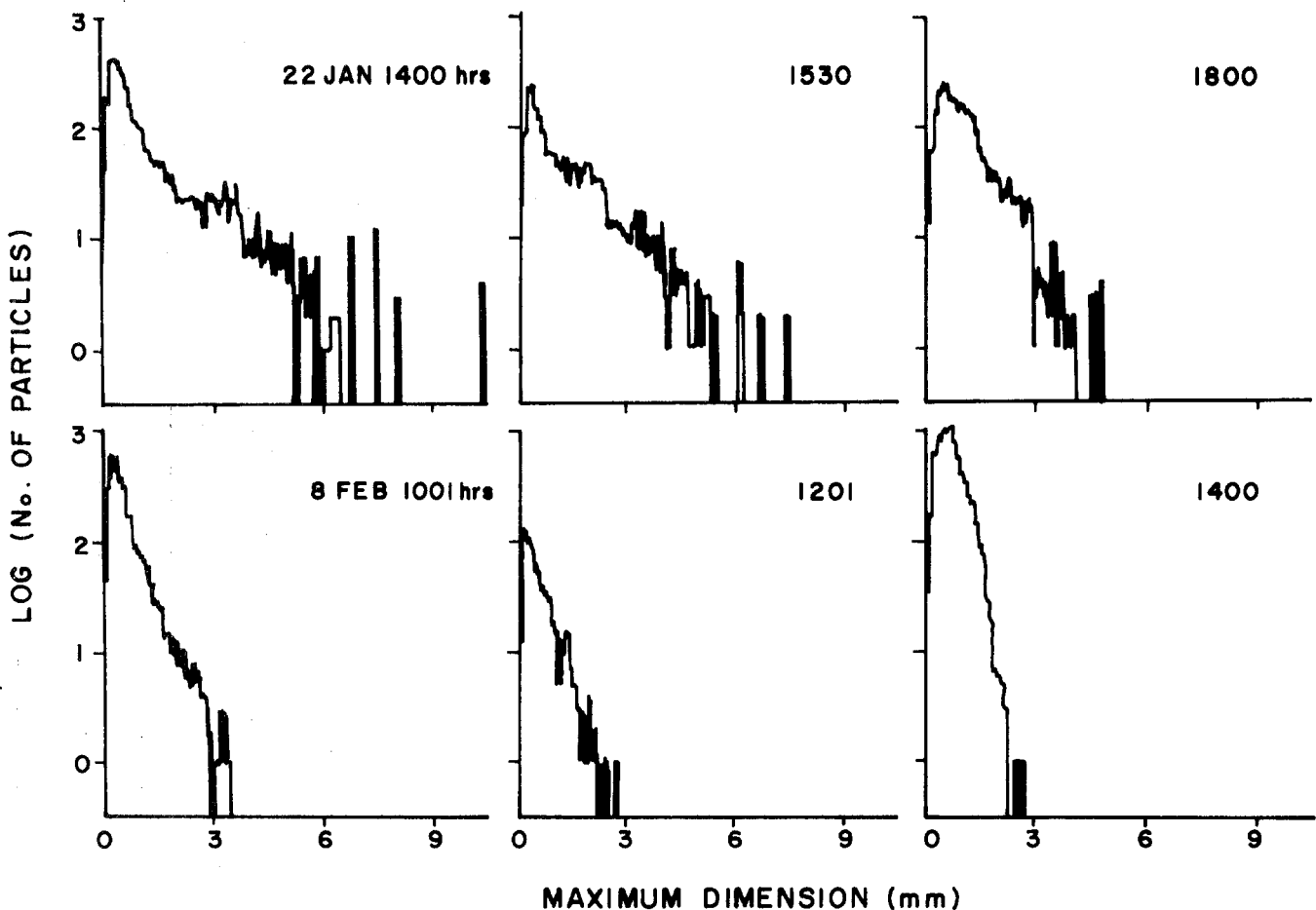


Figure 18-36. Particle size distributions for selected times during snowstorms on 22 January and 8 February 1981 near Burlington, Vermont. Each distribution is for a 5-minute sample period taken with an optical array probe [Berger, 1983].

OPTICAL AND INFRARED PROPERTIES OF THE ATMOSPHERE

Sufficient data exist to differentiate between drop size distributions for different types of fogs and clouds. Drop sizes from 1 to 100 μm can occur; the smaller sizes (1–10 μm range) are found in fogs and stratus type clouds, the larger sizes in convective clouds with strong updraft. Ice crystals in clouds (or ice fog) may be as small as a few micrometers although the size of cirrus cloud particles is more typically of the order of 0.5 to 1 μm . Rain drops are distinguished from cloud drops only by the fact that they have grown large (heavy) enough to fall to the surface of the earth (that is, to precipitate out). Rain drops may be as large as 5 mm, larger drops have an increasing tendency to break up. Snow flakes present an interesting problem with regard to optical effects because of their extremely complex shapes and dimensions. Various data (such as Lo and Passarelli [1982]; Berger [1983]; and Gray and Male [1981]) suggest that a "typical" snowfall consists of particles ranging from single crystals 0.1 mm (100 μm) or smaller to agglomerates several millimeters in diameter.

There is little information on the exact nature of the size distributions. Lo and Passarelli [1982] assumed a simple exponential form and found average diameters of 0.5 to 2 mm for several aircraft measurements using optical array probes. Ground-level measurements with aspirated optical array probes by Berger [1983] and Formvar replicating data of Koh and O'Brien [1982] show a wide range of size distributions; typical examples are shown in Figure 18-36. The reasons for this wide variation are not clearly understood, though ongoing modeling work by Martinez-Sanches et al. [1983] is beginning to unravel some of the causes. The majority of the distributions peak between 0.2 and 0.5 mm. The area-weighted average radius, the size measure with the most influence on extinction, is generally in the range 0.1 to 0.3 mm.

18.2.2.3 Cloud–Precipitation Models. Cloud and fog drop size distributions have been modeled by several researchers. Most commonly used are the models given by Deirmendjian [1969] for cumulus clouds and Silverman and Sprague [1970] for a number of fog types and several types of clouds. Table 18-11 is based on Silverman's compilation. The distribution functions for models 1–12 are shown in Figures 18-37 through 18-39. Advection fog is produced by the transport of moist air over a colder surface resulting in the cooling of the surface layers below their air dew points with condensation taking place in the form of fog. Most sea fogs are advective. Both the size range of particles and the liquid water contents are large (see Models 1 and 2, Table 18-11). Radiative fog is produced when stagnant moist air becomes progressively cooler during the night due to radiative cooling. This type of fog has both a small size range of particles and a small liquid water content.

Cloud droplet size distributions are more difficult to model. However, the optical thickness of most clouds is so large that their transmittance at visible and infrared wavelengths becomes completely diffuse due to multiple scattering (see Section 18.5.1).

The size distribution of rain drops is best expressed in terms of rain rate, since this is the quantity usually measured by the weather services. This formulation goes back to experimental work by Laws and Parsons [1943] and Marshall and Palmer [1948]. According to their work the number of drops of diameter D can be expressed as

$$N_D = N_0 \exp(-a \cdot D)$$

$$\text{where } N_0 = 0.08 \text{ cm}^{-3} \quad (18.23)$$

$$\text{and } a = 41 R^{-0.21} \text{ cm}^{-1}$$

with R being the rain rate in mm/hr.

Table 18-11. Cloud models: drop size distributions and liquid water contents.

$n(r) = a r^\alpha \exp[-br]$						
Cloud Type	Model Number	α	b	N_0 (cm^{-3})	a	M(g/m^3)
Heavy Advection Fog	1	3	0.3	20	0.27	0.37
Moderate Radiation Fog	2	6	3.0	200	607.5	0.02
Cumulus	3	3	0.5	250	2.604	1.00
Altostratus	4	5	1.11	400	6.268	0.41
Stratocumulus	5	5	0.8	200	0.4369	0.55
Nimbostratus	6	1	0.333	100	11.089	0.27
Stratus	7	3	0.667	250	8.247	0.42
Stratus	8	2	0.6	250	27.00	0.29
Stratus-Stratocumulus	9	2	0.75	250	52.734	0.15
Stratocumulus	10	2	0.5	150	9.375	0.30
Nimbostratus	11	2	0.425	200	7.676	0.65
Cumulus-Cumulus Congestus	12	2	0.328	80	1.4115	0.57

M = Liquid water content

N_0 = Total number of particles per unit volume

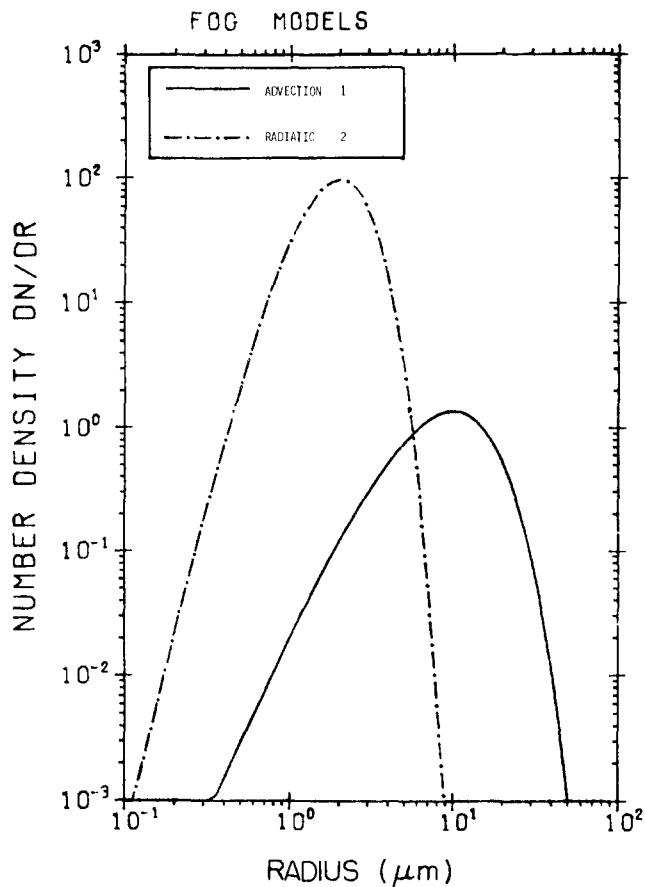


Figure 18-37. The drop size concentration ($\text{cm}^{-3} \mu\text{m}^{-1}$) to particle drop radius (μm) for fog models 1-2 in Table 18-11.

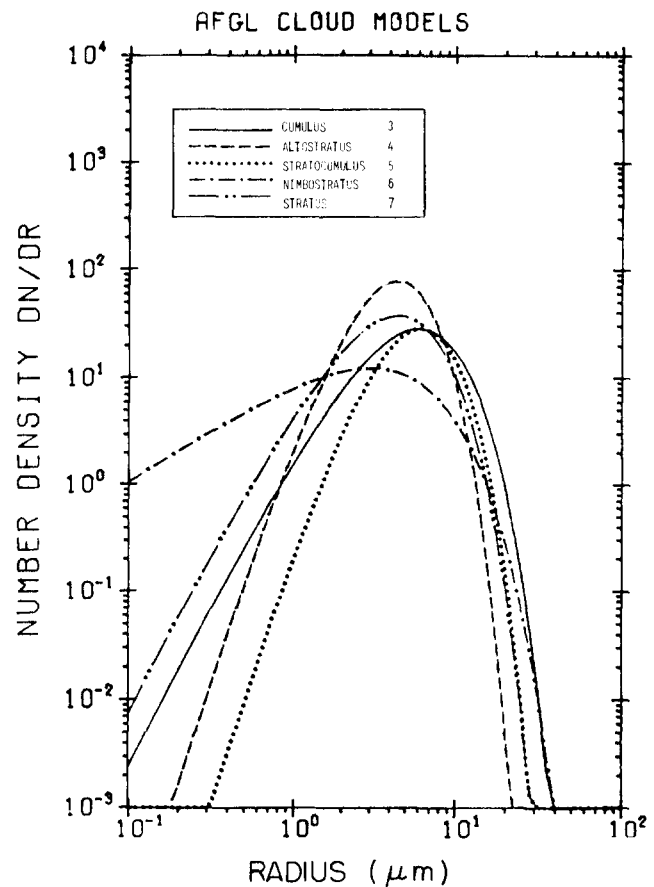


Figure 18-38. The drop size concentration ($\text{cm}^{-3} \mu\text{m}^{-1}$) to particle drop radius (μm) for cloud models 3-7 in Table 18-11.

This relationship is strictly empirical and does not explain the physical significance of the distributions.

18.2.2.4 Extinction, Scattering, Polarization. The attenuation coefficients for the fog models given in Section 18.2.2.3 are presented in Figures 18-40 and 18-41. For the droplet concentrations given in Table 18-11 (20 and 200 for Model 1 and 2, respectively), the resulting meteorological ranges (visibility) are 130m and 450m. However, the models can be scaled to visibilities from less than 50m to over 1 km. The extinction coefficients for different cloud models are shown in Figures 18-42 and 18-43. The single scatter albedo and the asymmetry parameters are given in Figures 18-44 through 18-49 to describe further the scattering properties of fogs and clouds. Because of the much larger size of fog and cloud droplets compared to aerosol (haze) particles, the polarization of light scattered by these particles is very small and has little practical importance.

No theory presently exists to calculate exactly the extinction coefficient for complex shapes such as snow crystals. Mie theory in the geometric limit (the minimum Mie size parameter at 10 μm wavelength is about 30) suggests that extinction in snow (and rain) should be nearly inde-

pendent of wavelength in the visible and infrared. Transmissometer measurements over the past few years by a number of investigators [summarized by Seagraves and Ebersole, 1983], however, have found that the measured infrared extinction coefficient varies from 1.0 to 1.45 times that in the visible, generally increasing with wavelength, and depending somewhat on the type of instrument used.

Mill and Shettle [1983] have shown that most of the apparent wavelength dependence can be explained by instrumental effects. The scattering phase functions of particles that are large compared to the wavelength are characterized by extremely narrow forward lobes due to Fraunhofer diffraction. For snow crystals with average areas equivalent to a sphere of 0.1 to 0.3 mm radius, this peak is comparable to the field-of-view (FOV) of typical transmissometer receivers. Therefore, for a given transmissometer FOV, the longer the wavelength the less forward-scattered radiation is sensed resulting in a lower "apparent" transmission. The relationship between the measured transmittance τ^m and the true radiance transmittance τ is given by [Mill and Shettle, 1983]

$$\tau^m = \tau(1 + D' \ln \tau) \quad (18.24)$$

OPTICAL AND INFRARED PROPERTIES OF THE ATMOSPHERE

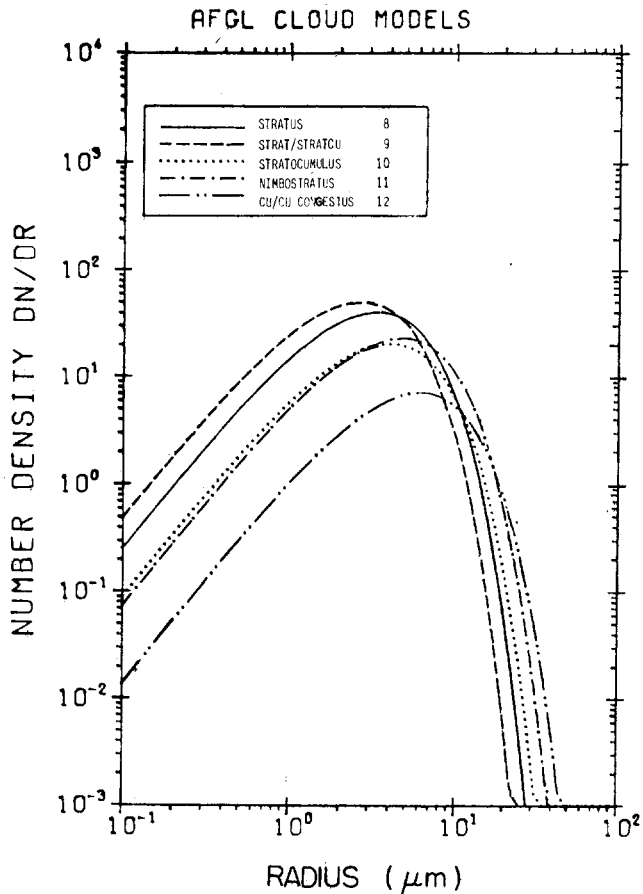


Figure 18-39. The drop size concentration ($\text{cm}^{-3} \mu\text{m}^{-1}$) to particle drop radius (μm) for cloud models 8-12 in Table 18-11.

where

$$D' = x^2 \int_0^\phi \int_0^\theta \left\{ \frac{J_1[x \sin(\theta' + \phi')]}{x \sin(\theta' + \phi')} \right\}^2 f(\theta') d\theta' d\phi' \quad (18.25)$$

- θ = half angle of receiver field of view
- ϕ = half angle of source
- x = $2\pi r/\lambda$, the particle size parameter
- r = particle radius
- λ = wavelength
- J_1 = Bessel function of the first kind, first order, and
- $f(\theta)$ = relative response of the detector over the FOV.
($\equiv 1$ for flat detector response)

This equation assumes that multiple scattering is negligible, θ and ϕ are small (less than 5°), the phase function is adequately represented by the Fraunhofer diffraction, and the size distribution can be represented by a single effective scattering radius. Values of D' have been tabulated [Shettle

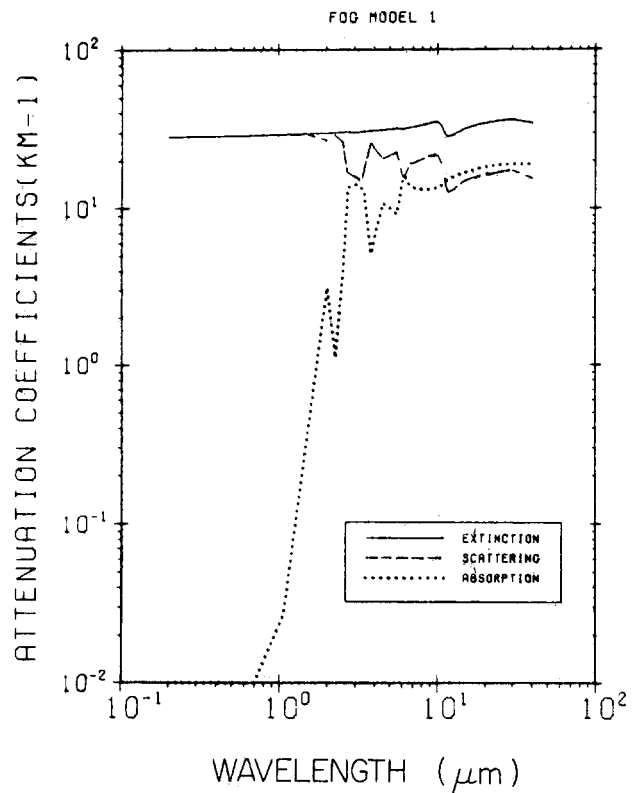


Figure 18-40. Attenuation coefficient versus wavelength; heavy advection fog model 1.

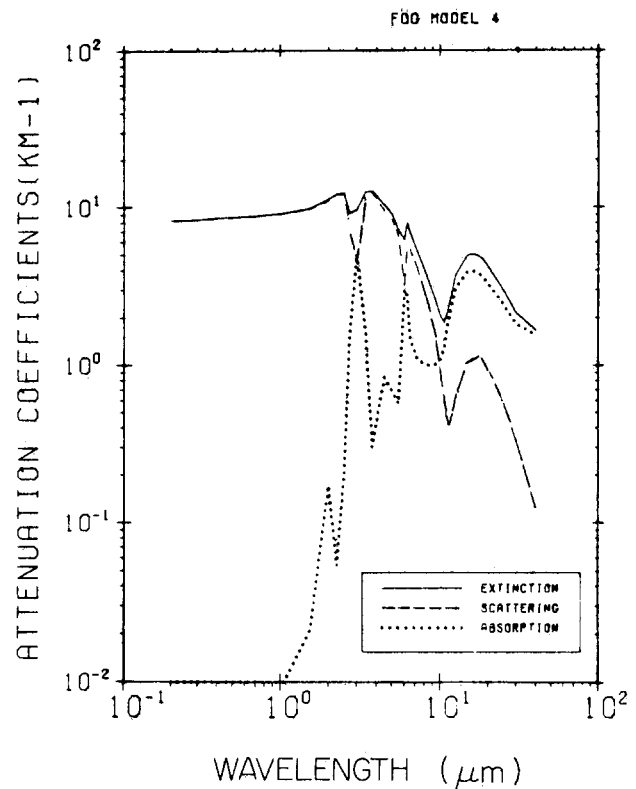


Figure 18-41. Attenuation coefficient vs wavelength; light to moderate radiation fog model 2.

CHAPTER 18

et al., 1985] for various θ , ϕ , and x 's and are summarized in Table 18-12. To use the table, calculate the two table parameters as follows:

$$\rho = \text{Max}(\theta, \phi) / \text{Min}(\theta, \phi) \quad (18.26)$$

$v = x \cdot \text{Min}(\theta, \phi)$, where θ and ϕ are in radians,

where the expression *Max* means use the largest of the arguments in the parentheses. Similarly, *Min* means use the smallest. *Max* and *Min* are, respectively, the larger and smaller of the two arguments. A comparison of uncorrected and diffraction-corrected measured transmittances is shown in Figures 18-50 and 18-51. Seagraves [1983] has compared measured visible and 10.5 μm transmittances to those calculated from geometric optics theory. The calculations assumed a modified gamma size distribution of particle sizes between 84 and 761 μm radius based on replicator data, and used the airborne snow mass concentrations measured by CRREL [see Lacombe, 1983]. These studies strongly suggest that the extinction coefficient in snow is very nearly wavelength independent in the visible and infrared, though particle shape may have a small effect below the resolution of the measurement precision and cannot be ruled out.

Studies by a number of investigators have addressed the question of the relationship between snow fall rate and extinction. Results summarized in Figure 18-52 vary widely

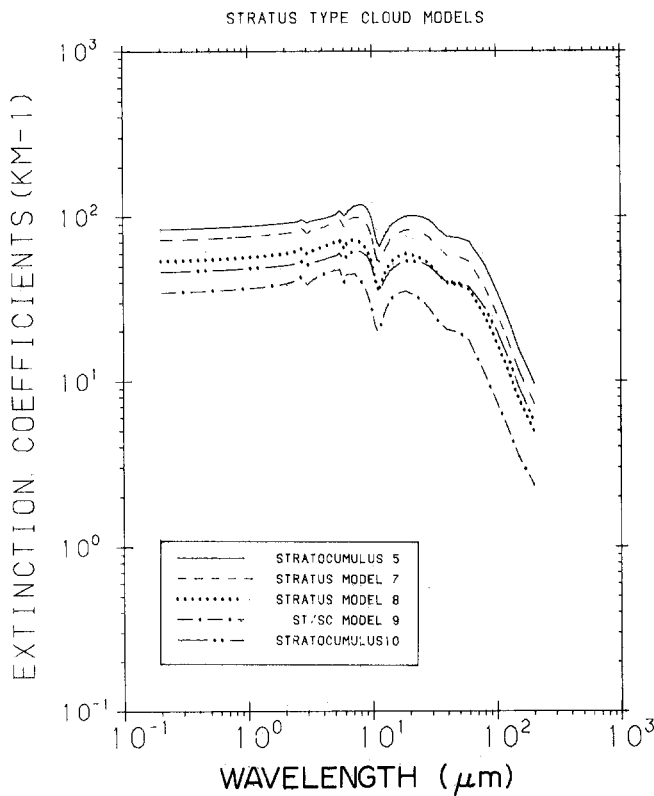


Figure 18-42. Extinction coefficients for stratus cloud models 5, 7, 8, 9, 10 (Table 8-11).

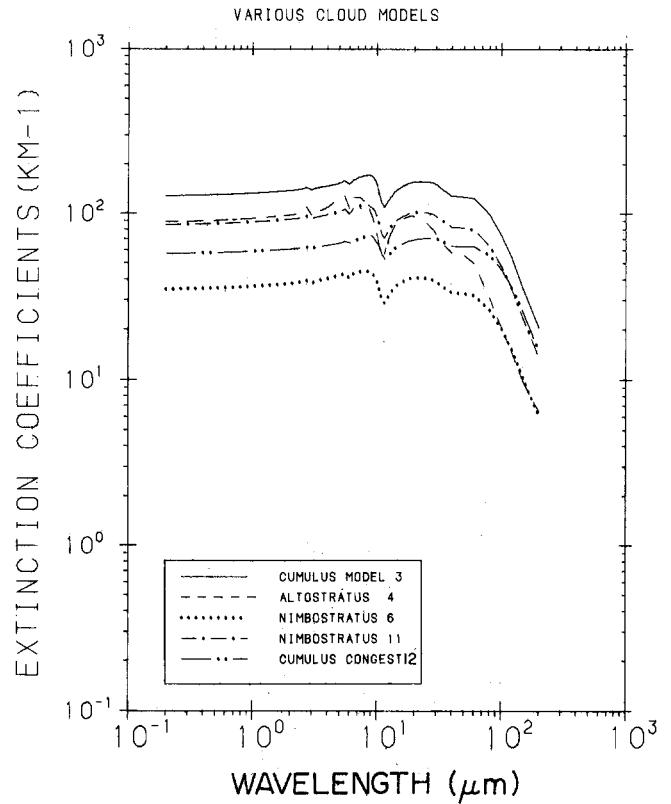


Figure 18-43. Extinction coefficients for cloud models 3, 4, 6, 11, 12 (Table 18-11).

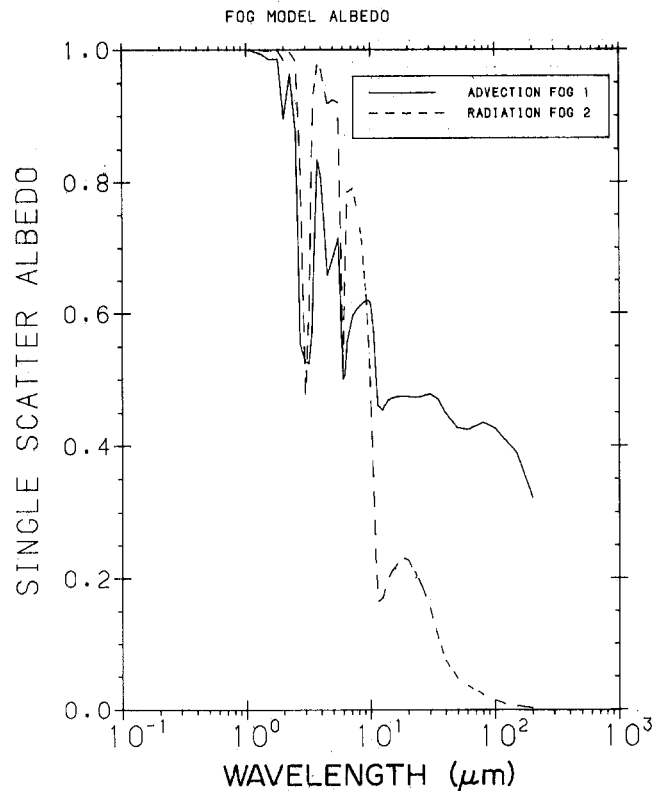


Figure 18-44. Single scatter albedo for fog models 1 and 2 (Table 18-11).

OPTICAL AND INFRARED PROPERTIES OF THE ATMOSPHERE

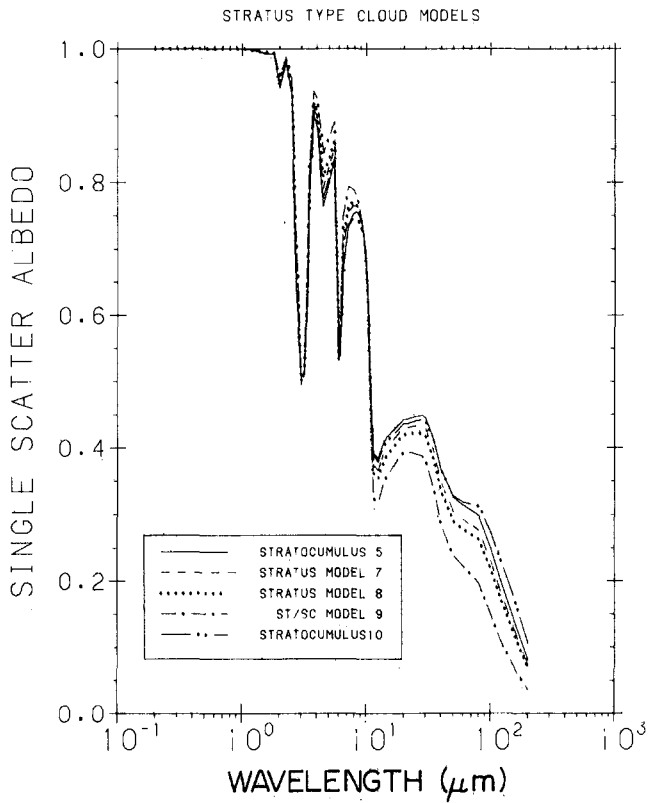


Figure 18-45. Single scatter albedo for stratus cloud models 5, 7, 8, 9, 10 (Table 18-11).

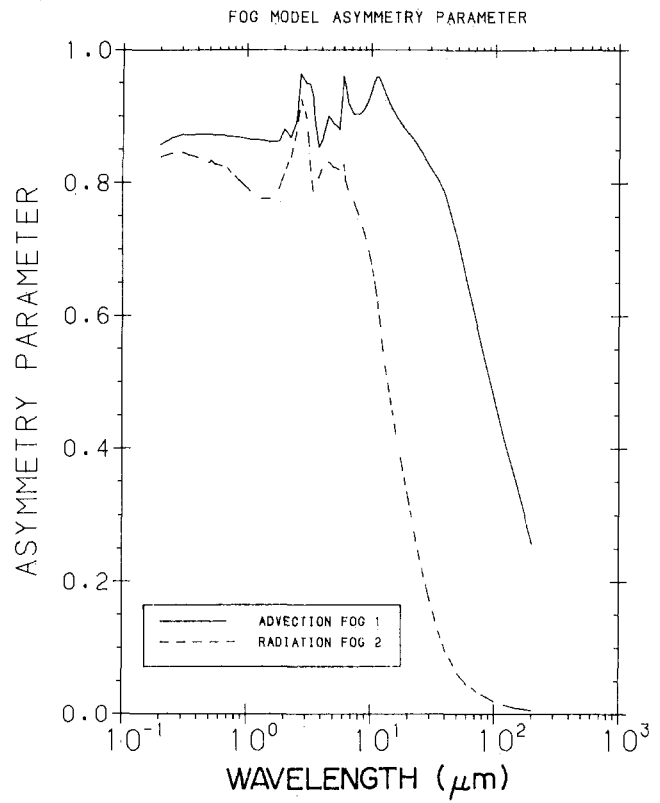


Figure 18-47. Asymmetry parameters for fog models 1 and 2 (Table 18-11).

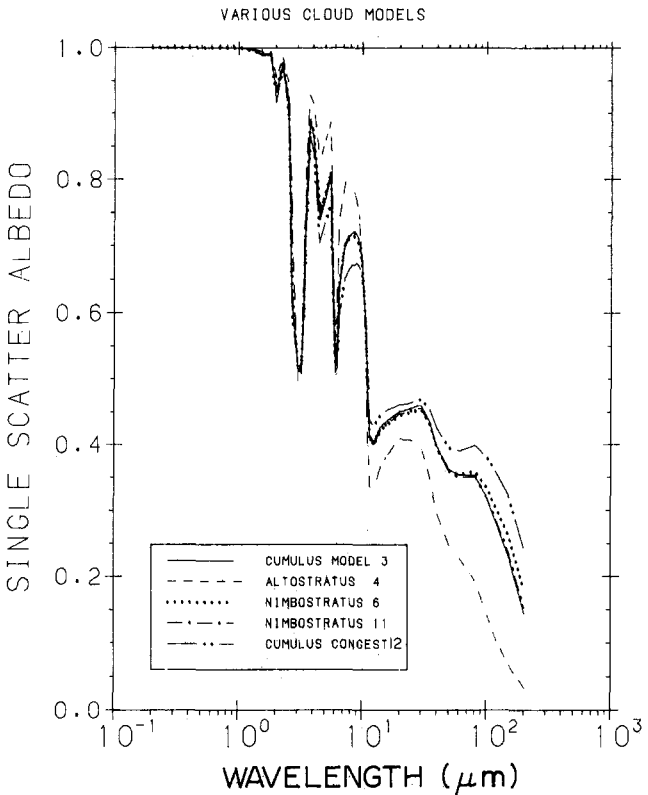


Figure 18-46. Single scatter albedo for cloud models 3, 4, 6, 11, 12 (Table 18-11).

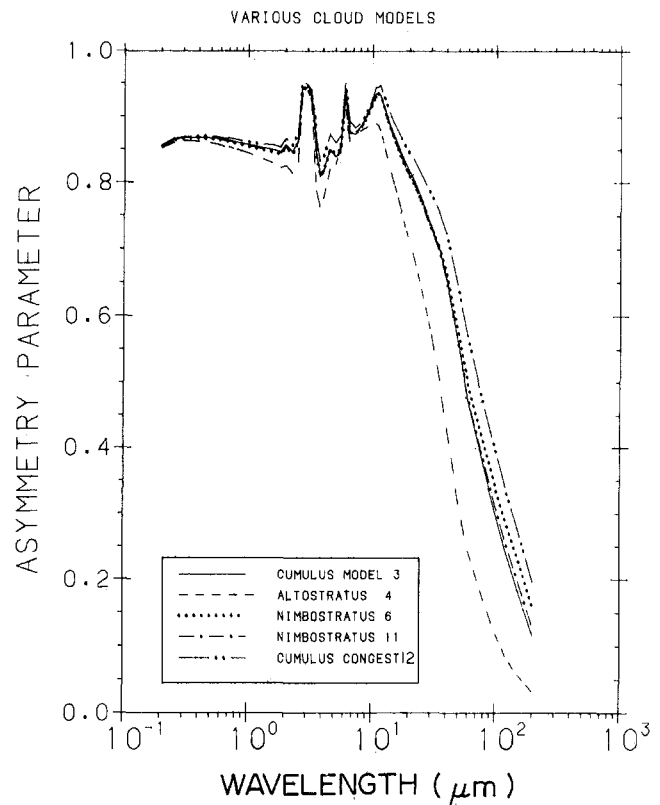


Figure 18-48. Asymmetry parameters for stratus cloud models 5, 7, 8, 9, 10 (Table 18-11).

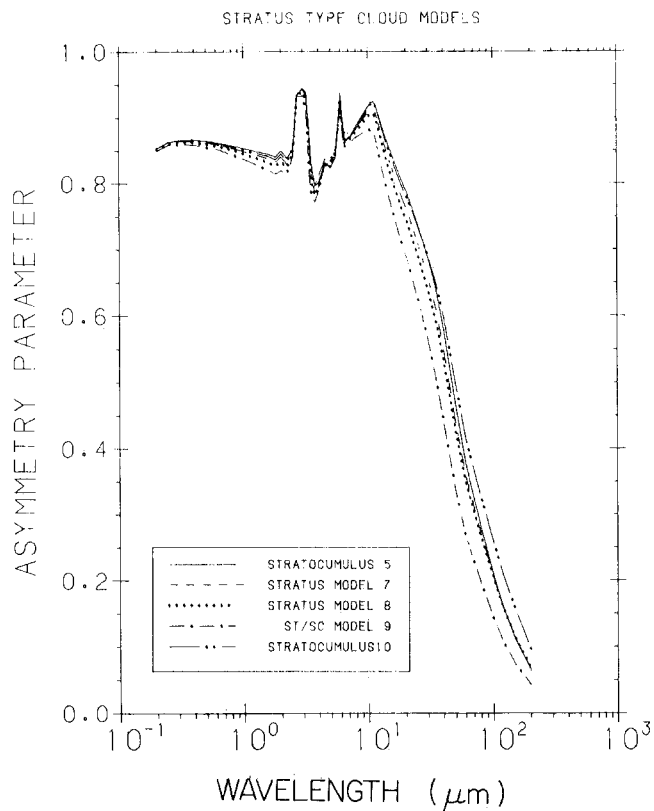


Figure 18-49. Asymmetry parameters for cloud models, 3, 4, 6, 11, 12 (Table 18-11).

Table 18-12. Forward scattering correction factors $D'(x, \theta, \phi)$ for a transmissometer with flat receiver field of view, where $\rho = \max(\theta, \phi) / \min(\theta, \phi)$ and $v = x - \min(\theta/\phi)$, for θ and ϕ in radians.

ρ	100.00	50.00	20.00	10.00	5.00	2.00	1.00
0.04	0.016	0.015	0.008	0.004	0.002	0.001	0.000
0.06	0.025	0.024	0.016	0.009	0.004	0.002	0.001
0.10	0.041	0.040	0.036	0.023	0.012	0.005	0.002
0.15	0.061	0.060	0.059	0.046	0.026	0.011	0.006
0.20	0.080	0.080	0.078	0.070	0.045	0.019	0.010
0.30	0.116	0.116	0.115	0.113	0.089	0.042	0.022
0.40	0.150	0.150	0.149	0.146	0.133	0.072	0.038
0.60	0.210	0.210	0.210	0.208	0.204	0.143	0.081
1.00	0.304	0.304	0.304	0.303	0.299	0.276	0.189
1.50	0.378	0.378	0.378	0.378	0.376	0.364	0.310
2.00	0.418	0.418	0.418	0.418	0.417	0.405	0.381
3.00	0.446	0.446	0.446	0.446	0.446	0.440	0.423
4.00	0.455	0.455	0.455	0.455	0.455	0.452	0.438
6.00	0.468	0.468	0.468	0.468	0.468	0.468	0.461
10.00	0.475	0.475	0.475	0.475	0.475	0.475	0.474
20.00	0.476	0.476	0.476	0.476	0.476	0.476	0.476

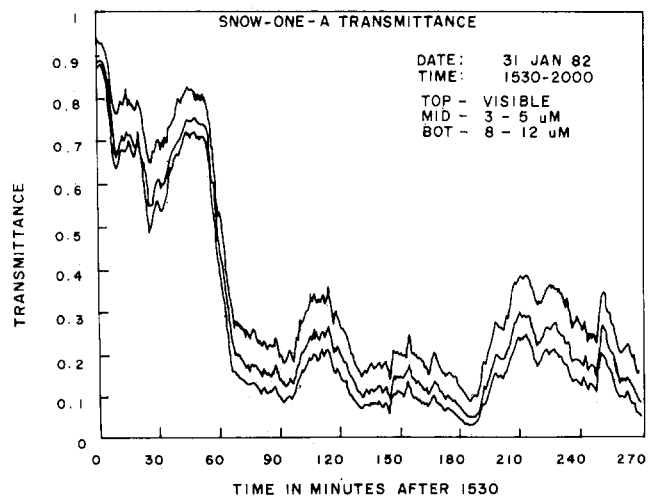


Figure 18-50. Transmittance in the visible, 3-5 μm and 8-12 μm bands during a 31 January 1982 snowstorm near Burlington, Vermont. The apparent increasing extinction with wavelength is typical of measurements in snow [Mill and Shettle, 1983].

due perhaps to both measurement error, particularly in the snow rate data, and to crystal habit or size distribution. Recent results of Lacombe [1983] show that for a given airborne snow mass concentration visible extinction decreases with increasing riming (Figure 18-53) and appears to be greater for plate-like crystals (spacial and plane dendritic, broad branched crystals and plates) than for the more compact types (columns, bullets, side planes, needles and assemblages of plates).

The most extensive set of snow phase function measurements have been made at Michigan Technological University [Winchester et al., 1981]. A typical example is shown in Figure 18-54. These measurements are of high angular resolution but required one to two hours per phase function,

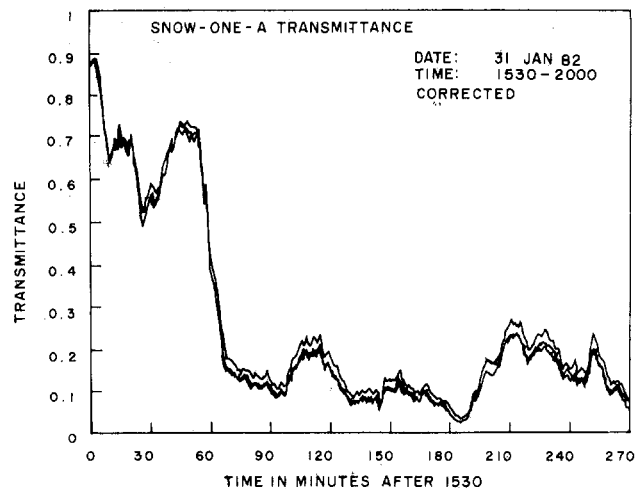


Figure 18-51. Data from Figure 18-44, corrected for forward scatter into the transmissometer field of view, assuming an effective scattering radius of 0.2 mm. Residual wavelength dependence may be due to multiple scattering or shape effects.

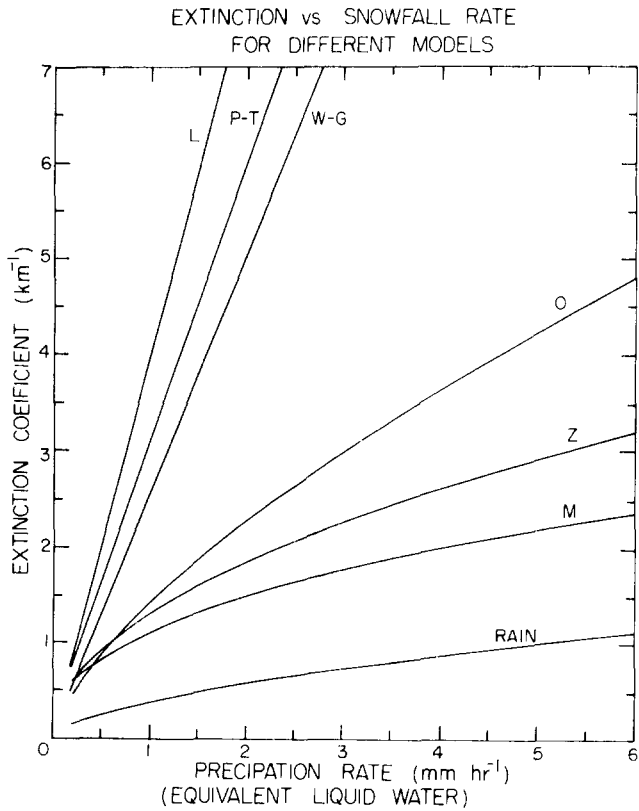


Figure 18-52. Models of visible extinction coefficient versus equivalent snow fall rate. Curve R is for rain while the others are for snow as measured by various investigators [Mason, 1978].

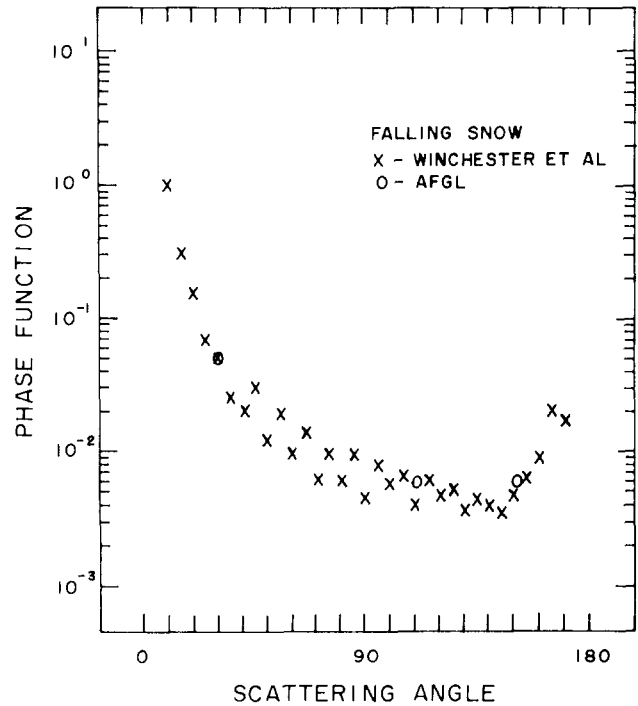


Figure 18-54. Phase function of falling snow measured in Houghton, Mississippi on 26 January 1981 with a polar nephelometer [Winchester et al., 1981]. The dominant crystal was a six-sided dendritic of about 2 mm diameter. Circled points are data from the 31 January 1982 SNOW-ONE-A episode averaged over the 1530–2000 period. Data were taken each minute with a fixed-angle nephelometer at 30°, 110°, and 150° scattering angles.

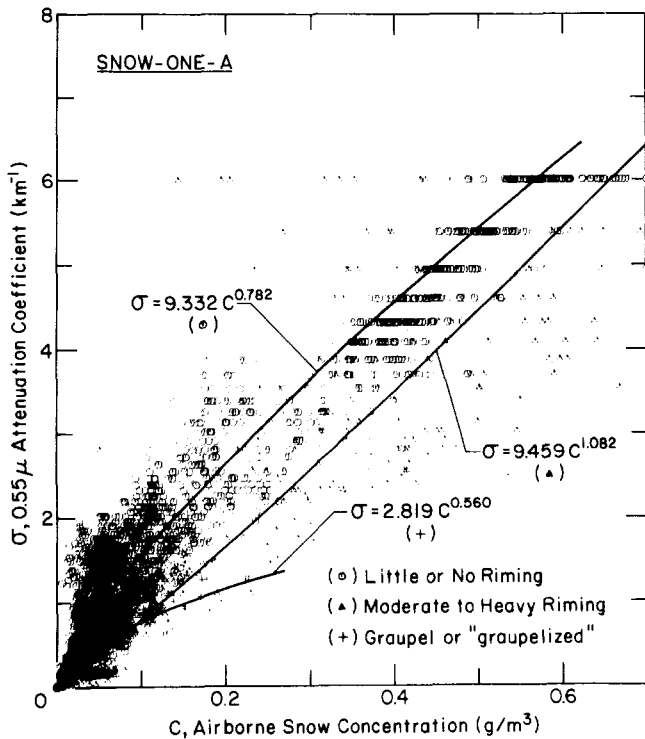


Figure 18-53. Relationship between airborne snow concentration and 0.55 μm extinction for 3 degrees of riming. Data are from SNOW-ONE-A. Curves are power law fits within each category.

raising the question whether they represent any one snowfall “type”. Measurements made by AFGL are also shown in Figure 18-54. They were made simultaneously at three fixed angles and are shown normalized to the Winchester data at 30°; they show good agreement in relative scattered intensity. An absolute comparison is not possible since Winchester’s data are not normalized to total extinction.

18.3 SURFACE REFLECTANCE AND ALBEDO

A fraction of a light beam that is incident on the earth’s surface or on clouds will be reflected back into the atmosphere where it may undergo further scattering and absorption. Surface reflectance consequently affects sky radiance seen from the ground, the radiance of the atmosphere as seen from space, and other atmospheric optical quantities (see Section 18.5). The percentage of light reflected from natural terrain or water surfaces varies with angle of incidence and look angle and is also a function of the wavelength of the radiation. Details of these reflection processes, especially laboratory measurements on surfaces, are often treated by the bidirectional reflectance function (BDRF), while integral reflection effects—for example the brightness of a

CHAPTER 18

planet—are usually characterized by “albedo”. For mirror surfaces (specular reflection), the incident and reflected beam and the normal to the surface at the point of incidence lie in the same plane; the angle between the normal and the direction of incidence and between the normal and the reflected beam are identical.

A brief derivation of the BDRF following Nicodemus [1967] and Leader [1979] will now be given. The radiant power incident on a surface element dA through a beam of solid angle $d\Omega_i$ (from polar angle θ , azimuth angle ϕ) is

$$dP_i = N_i dA d\Omega'_i, \quad (18.27)$$

where N_i is the radiance ($\text{W cm}^{-2} \text{sr}^{-1}$) and $d\Omega'_i = \cos \theta_i d\Omega_i$ is the projected solid angle. The radiant power reflected into $d\Omega_r$ is

$$dP_r = dN_r dA d\Omega'_r. \quad (18.28)$$

Thus the ratio of the radiant power is

$$\frac{dP_r}{dP_i} = \frac{dN_r}{N_i d\Omega'_i} d\Omega'_r = f' d\Omega'_r, \quad (18.29)$$

$f'(\theta_i, \phi_i, \theta_r, \phi_r)$ (sr^{-1}) is called the bidirectional reflectance function (BDRF). This definition is especially useful for narrow (collimated) illuminating beams (sun, laser). If the incident radiance comes from all directions of the hemisphere, then

$$N_r = \int_0^{2\pi} \int_0^{\pi/2} f' N_i \sin \theta \cos \theta d\theta d\phi. \quad (18.30)$$

A perfectly diffuse reflector is characterized by a constant f' in all directions. If such a surface is diffusely irradiated and the reflected radiance in any direction is measured, the directional reflectance is $f_{\text{diff}} = \pi f'$ [dimensionless]. Hence, the BDRF of a reflection standard (barium sulfate) with $f_{\text{diff}} = 1$ is $f' = 1/\pi$.

Comparison of incoming and outgoing shortwave radiance of the earth's surface or the earth's atmosphere in the simplest way is made by a “flat” receiver turned up (for downwelling radiation) and down (for upwelling radiation). The ratio of the fluxes, $P \uparrow / P \downarrow$, is often called albedo or diffuse reflectance.

Eaton and Dirmhirn [1979], for example, have made measurements of BDRFs and albedo of several surfaces for shortwave radiation ($0.3\text{--}3 \mu\text{m}$). Those of a salt flat and a field of corn are shown in Figure 18-55 for two solar elevations. Due to the anisotropy, the nadir values $\pi f'$ of the BDRF are to be multiplied by a factor F to obtain the albedo. At low solar elevation angles, F is generally >1 , but surfaces with vertical structure may make $F < 1$ at high sun (when partial shadowing occurs).

Spectral reflectance from 0.2 to $4 \mu\text{m}$ for several surface types is given in Figures 18-56 through 18-58 [Suits, 1978].

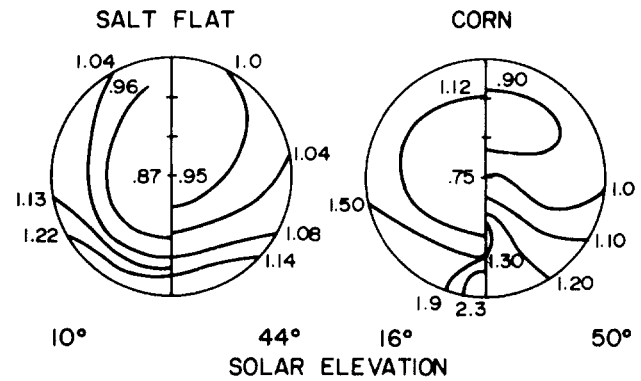


Figure 18-55. Bidirectional reflection function of Bonneville, Utah, Salt Flat (left) and a corn field (right), each for a low and a high solar elevation. $F_s(\pi f')_{\text{Nadir}}$ = albedo for a horizontal receiver. Spectral range 0.3 to $3 \mu\text{m}$ [Eaton and Dirmhirn, 1979].

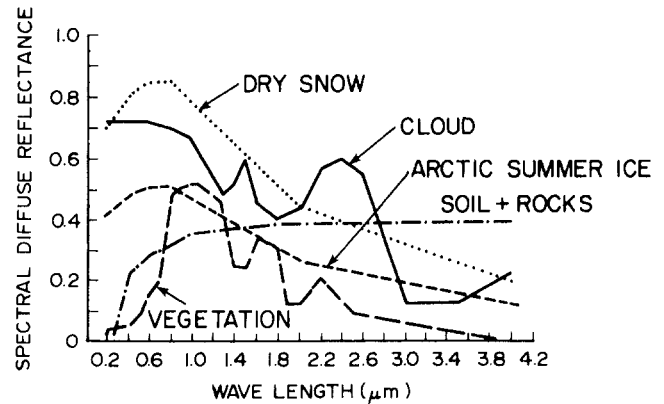


Figure 18-56. Typical spectral diffuse reflectance of snow, ice, soil, and vegetation after Suits [1978, Figure 3-19].

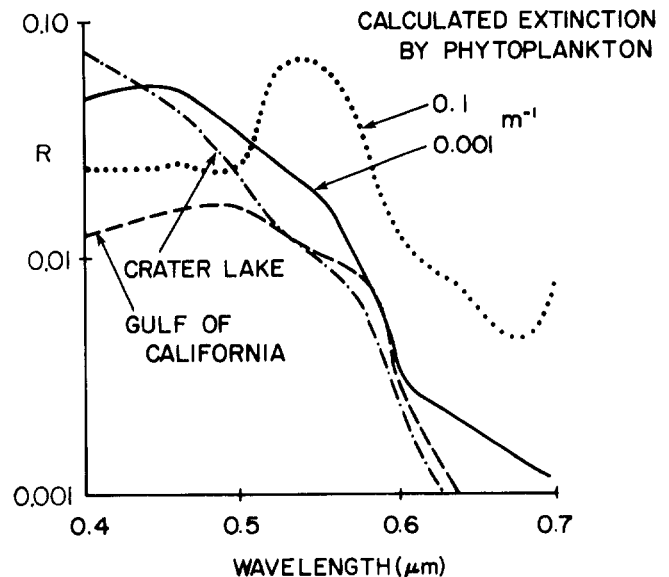


Figure 18-57. Nadir reflectance R $0.4\text{--}0.7 \mu\text{m}$ of some water bodies. Measured value taken from Tyler [1978], calculations from Suits [1978, Figure 3-124].

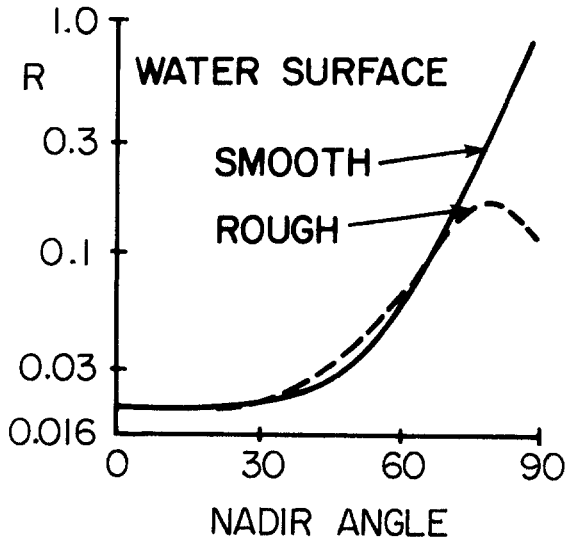


Figure 18-58. Variation with nadir look angle of specular reflectance R of smooth water surface and surface roughened by a beaufort 4 [Suits, 1978, Figure 3-114].

Further examples, citations, and references to data files can be found in Suits [1978]. Fitch [1981] made a theoretical study of the polarized radiance (at 0.4 and 0.6 μm) from the top of the earth's atmosphere for different surfaces and aerosol conditions.

18.4 ATMOSPHERIC TRANSMITTANCE AND RADIANCE

18.4.1 Monochromatic Radiation.

For many purposes, knowledge of the monochromatic optical depth for a specific optical path in the earth's atmosphere is required. The type of calculation necessary to obtain this information is referred to as a line-by-line calculation since it takes into account the contribution of each spectral line to the monochromatic absorption. Consequently, line by line calculations require detailed knowledge of the spectral line parameters associated with each contributing transition. Such computations, performed over an extended wavenumber interval (of the order of 100 cm^{-1}), may require significant computational effort. Several methods for performing such computations have been discussed in the literature. Some are particularly suitable for specialized calculations [Scott and Chedin, 1981; McMillin et al., 1976; Kunde and Maguire, 1973], some make approximations that in certain cases may be acceptable [Karp, 1973; Mankin 1979], and others are accurate and direct but not computationally efficient [Suskind and Searl, 1978]. At

AFGL a computational model, FASCODE (Fast Atmospheric Signature Code), has been developed and made available to the scientific community. Line-by-line calculations are discussed in the following section in the general context of atmospheric calculations and the FASCODE model [Clough et al., 1981; Smith et al., 1978]. Specific details of the model are not discussed, but are available in the literature [for example, Clough and Kneizys, 1979; Clough et al., 1977]. A general reference covering the topic of atmospheric molecular absorption that the reader will find particularly useful is the work by Goody [1964].

18.4.1.1 Line-by-Line Computations (FASCODE). The monochromatic optical depth, $\tilde{k}(\nu)$, at wavenumber value $\nu(\text{cm}^{-1})$, assuming superposition of the contribution from the individual spectral transitions, is given by

$$\tilde{k}(\nu) = \nu \frac{1 - e^{-hc\nu/kT}}{1 + e^{-hc\nu/kT}} \times \sum_i W(m_i) \tilde{S}_i(T) [f(\nu, \nu_i) + f(\nu, -\nu_i)] \quad (18.31)$$

where $W(m_i)$ (mol/cm^2) is the column density for the molecular species, m_i , involved in the i^{th} transition, ν_i is the transition wavenumber and $\tilde{S}_i(T)$ ($1/\text{mol}/\text{cm}^2$) is the intensity at temperature T (K) appropriate to the FASCODE line shape, $f(\nu, \nu_i)$ ($1/\text{cm}^{-1}$). We note that $W(m_i) = \rho(m_i)l$ for path length l and molecular density ($\rho(m_i)$). This line shape formulation is an extension of that used by Van Vleck and Huber [1977] and discussed by Clough et al. [1980; 1983]. Equation (18.31) may be conveniently rewritten in terms of the radiation field dependent term $\nu \tanh(hc\nu/2kT)$ to obtain

$$\tilde{k}(\nu) = \nu \tanh(hc\nu/2kT) \times \sum W(m_i) \tilde{S}_i(T) [f(\nu, \nu_i) + f(\nu, -\nu_i)] \quad (18.32)$$

The intensity, \tilde{S}_i , is expressed in terms of the transition strength $|\mu_i^2|$ debye², as

$$\tilde{S}_i(T) = \frac{8\pi^3 \times 10^{-36}}{3hc} \times |\mu_i^2| \left(1 + e^{-hc\nu_i/kT} \right) \frac{e^{-hcE_i/kT}}{Q_V(m_i, T)Q_R(m_i, T)}, \quad (18.33)$$

where $E_i(\text{cm}^{-1})$ is the lower state energy for the transition and $Q_V(m_i, T)$ and $Q_R(m_i, T)$ are the vibrational and rotational partition functions for the appropriate molecular species, m_i . In terms of the intensity definition, $S_i(T)$, used for the AFGL line compilations [Rothman et al., 1983a,b; McClatchey et al., 1973] we have the relationship

CHAPTER 18

$$\tilde{S}_i(T) = \frac{1 + e^{-hc\nu_i/kT}}{\nu_i \left(1 - e^{-hc\nu_i/kT}\right)} S_i(T). \quad (18.34)$$

The line shape function must satisfy the normalization condition,

$$\int_0^\infty d\nu [f(\nu, \nu_i) + f(\nu, -\nu_i)] = 1, \quad (18.35)$$

As a result, the expression for optical depth, Equation (18.32) satisfies two important conditions: the Nyquist condition,

$$\int_0^\infty d\nu \frac{\tilde{k}(\nu)}{\nu \tanh(hc\nu/2kT)} = \sum_{\nu} |\mu_{\nu}^2| \quad (18.36)$$

that is, the preservation of transition strengths; and the condition that radiation balance be satisfied between emission and absorption for a system in thermal equilibrium.

The line shape function $f(\nu, \nu_i)$ is dependent on molecular species, broadening density, and temperature. For collisional broadening in the impact limit, the form factor is given by

$$f(\nu, \nu_i) = \frac{1}{\pi} \frac{\alpha_i^c}{(\nu - \nu_i)^2 + (\alpha_i^c)^2}, \quad (18.37)$$

where α_i^c (cm^{-1}) is the collision broadened halfwidth at half maximum (HWHM). It proves convenient for computational purposes to define a dimensionless parameter z such that

$$z = \frac{\nu - \nu_i}{\alpha_i^c}. \quad (18.38)$$

Thus, $f(\nu, \nu_i)$ becomes $f(z) = (1/\alpha_i^c) L(z)$ where

$$L(z) = \frac{1}{\pi} \frac{1}{1 + z^2}. \quad (18.39)$$

The functional dependence of $L(z)$ is shown as function L in Figure 18-59a.

The dependence of the collision broadened halfwidth on the number density, n , and temperature, T , of the absorbing media is given by the relation,

$$\alpha_i^c(n, T) = \alpha_i^o (n/n_o) (T/T_o)^{X_T} \quad (18.40)$$

where α_i^o is the collision halfwidth at reference number density n_o defined for 1013 mb and reference temperature T_o (296 K). The quantity X_T , characterizing the temperature dependence of the halfwidth, typically ranges between 0 and 0.5, depending on molecular species and temperature. Classical collision theory gives a value of 0.5 for X_T . Values of X_T appropriate to each molecule type are stored in the program.

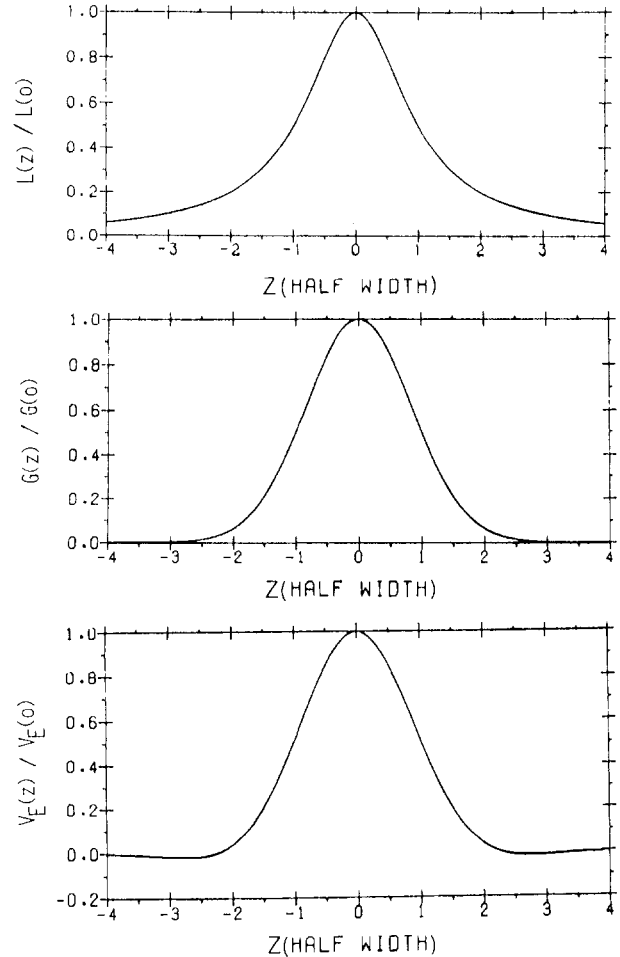


Figure 18-59. (a) The line shape profile appropriate for collisional broadening. (b) The line shape profile appropriate for velocity broadening. (c) The function utilized in FASCODE for the construction of the Voigt line profile.

The extensive computational effort required for atmospheric line by line calculations is a result of three principal factors: the large number of spectral lines contributing to the absorption, the small sampling interval necessary to model the attenuation at higher altitudes and the slow convergence to zero of the Lorentz function given in Equation (18.39). The latter consideration has been treated through the algorithms utilized in FASCODE and the details have been made available in the literature. A computational savings of sixteen is achieved over direct methods for a spectral interval of 512 halfwidths.

For the Doppler regime, in which velocity broadening dominates, the line shape is

$$f(\nu, \nu_i) = \frac{1}{\alpha_i^D} \left(\frac{\ln 2}{\pi}\right)^{1/2} \exp \left[-\ln 2 \left(\frac{\nu - \nu_i}{\alpha_i^D}\right)^2 \right]. \quad (18.41)$$

Letting

$$z = \frac{\nu - \nu_i}{\alpha_i^D} \quad (18.42)$$

then $f(z) = (1/\alpha_i^D) G(z)$ where

$$G(z) = \left(\frac{\ln 2}{\pi}\right)^{1/2} \exp[-(\ln 2)(z^2)]. \quad (18.43)$$

The functional dependence of $G(z)$ is Gaussian and is shown in Figure 18-59b. The Doppler halfwidth (HWHM) is given by

$$\alpha_i^D = \frac{\nu_i}{c} \left[2(\ln 2) \frac{kT}{M/N_o} \right]^{1/2} \quad (18.44)$$

where M is the gram molecular weight of the molecular species of the transition and N_o is Avogadro's number.

In the intermediate regime between collisional broadening and velocity broadening, the line shape is obtained from the convolution of the collisional and Doppler line shape giving the Voigt line profile. The computation of the Voigt line shape using a direct approach is too time consuming for general utilization. These direct methods generally give results to significantly higher precision than the uncertainty in the line parameters and the uncertainty in the line shape itself. An effective approximation to the Voigt line shape may be obtained by using an extension of the method proposed by Whiting [1968]. A Voigt parameter, ζ , is defined in terms of the collisional and Doppler widths

$$\zeta = \frac{\alpha^c}{\alpha^c + \alpha^D} \quad (18.45)$$

for which $\zeta = 0$ in the Doppler limit and $\zeta = 1$ in the collision broadened limit. For $\zeta = 0.5$ the collision and Doppler widths are equal. The Voigt width α^v (HWHM) is obtained through the relation

$$\alpha^v = A_v(\zeta) (\alpha^D + \alpha^c). \quad (18.46)$$

The function $A_v(\zeta)$ shown in Figure 18-60 is obtained from the relations given by Kielkopf [1973] where

$$A_v(\zeta) = (\zeta) \frac{1 + \epsilon}{2} + \left[(\zeta)^2 \left(\frac{1 - \epsilon}{2} \right)^2 + 1 - (1 - \zeta)^2 \right]^{1/2}, \quad (18.47)$$

with $\epsilon = 0.0990 \ln 2$. An appropriate Voigt line shape, $V(\zeta, z)$, is given as

$$V(\zeta, z) = C_c(\zeta) L(z) + C_D(\zeta) G(z) + C_v(\zeta) V_E(z), \quad (18.48)$$

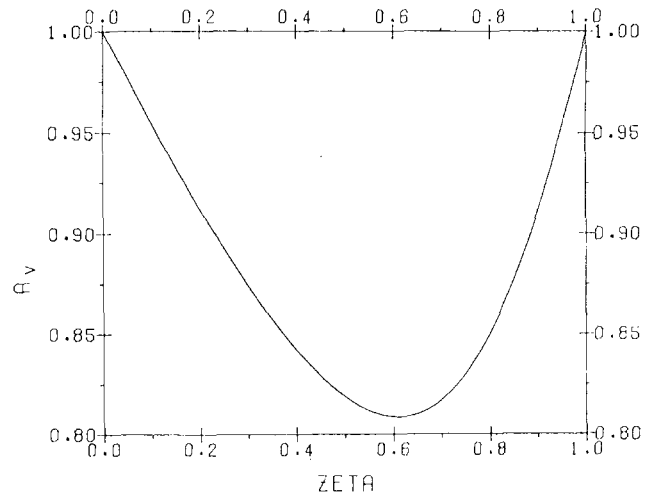


Figure 18-60. The constant relating the Voigt width to the sum of the Doppler and collision widths: collision broadened width over the domain 0.5.

where z is defined as

$$z = \frac{\nu - \nu_i}{\alpha^v} \quad (18.49)$$

The function $V_E(z)$ is an analytic function having the dependence on z shown in Figure 18-59c. The constants $C_c(\zeta)$, $C_D(\zeta)$, and $C_v(\zeta)$ are determined from least square fits of $V(\zeta, z)$ to the exact Voigt function. The Voigt line profiles for four values of ζ and the FASCODE approximation, $V(\zeta, z)$, are shown in Figure 18-61. The computational savings using this approximate approach is on the order of 100 compared with direct methods. The largest error, $\sim 3\%$, occurs for $\zeta \approx 0.05$ at a value of z corresponding to 16 halfwidths from line center at which the function is four orders of magnitude less than the peak value.

18.4.1.2 Continuum Absorption. FASCODE includes continuum contribution from self and foreign density dependent water vapor absorption, foreign density dependent carbon dioxide absorption, and the collision induced band of nitrogen. A more extensive treatment of the approach used in FASCODE in which the continua are developed from the wings of strong lines appears in the literature [Clough et al., 1980 and 1983]. For atmospheric applications it is advantageous to express the density dependence in terms of a self and foreign component. The continuum contribution to the optical depth, \bar{k}_c , is given by the expression

$$\bar{k}_c = W \nu \tanh(hc\nu/2kT) \times \left[(n_s/n_o) \bar{C}_s(\nu, T) + (n_f/n_o) \bar{C}_f(\nu, T) \right], \quad (18.50)$$

where W is the column density of the absorbing molecular species, (n_s/n_o) and (n_f/n_o) the number density ratios for the

CHAPTER 18

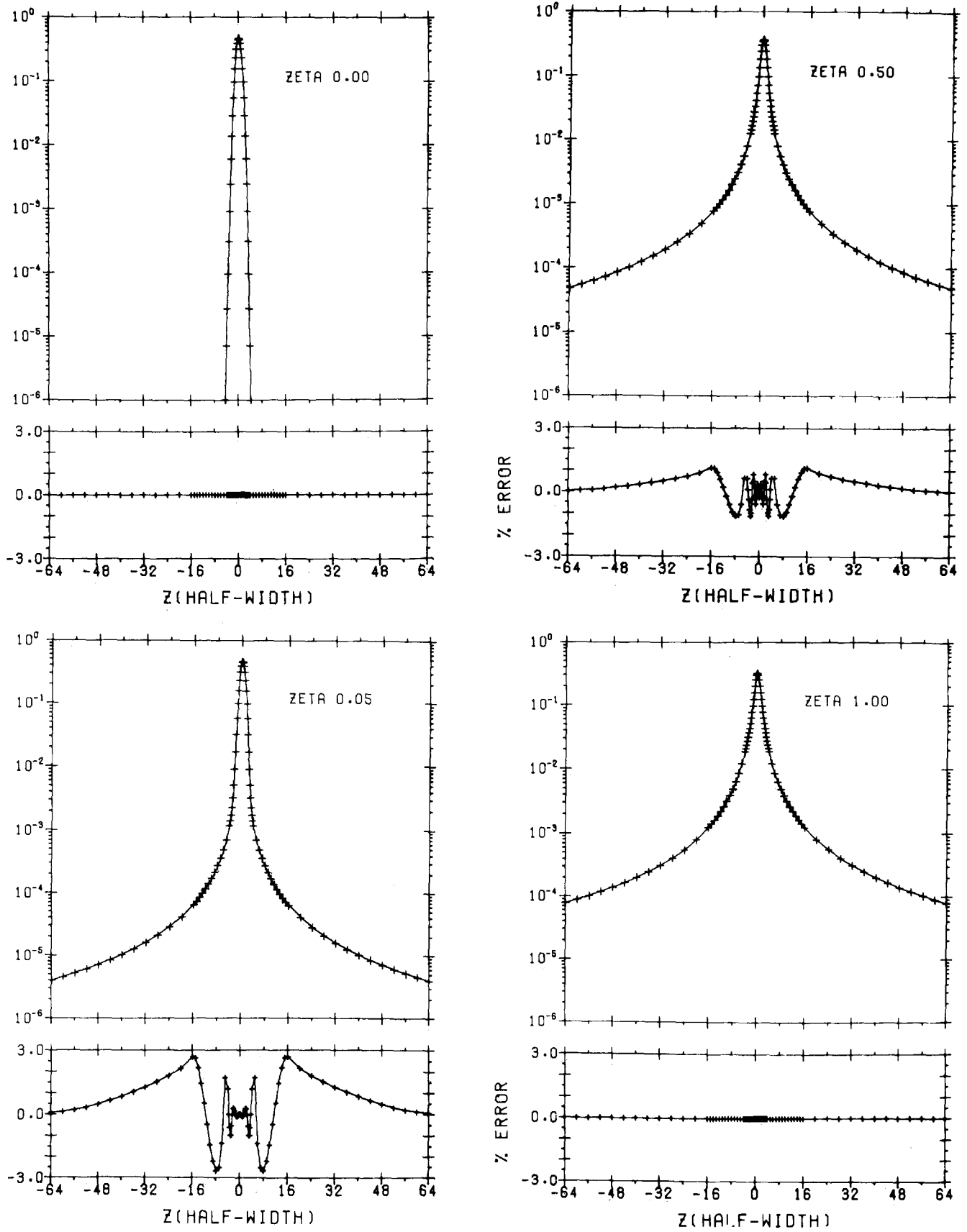


Figure 18-61. Voigt line shape profiles for representative values of zeta. The solid line represents the correct function and the symbol + the FASCOD1 approximation.

OPTICAL AND INFRARED PROPERTIES OF THE ATMOSPHERE

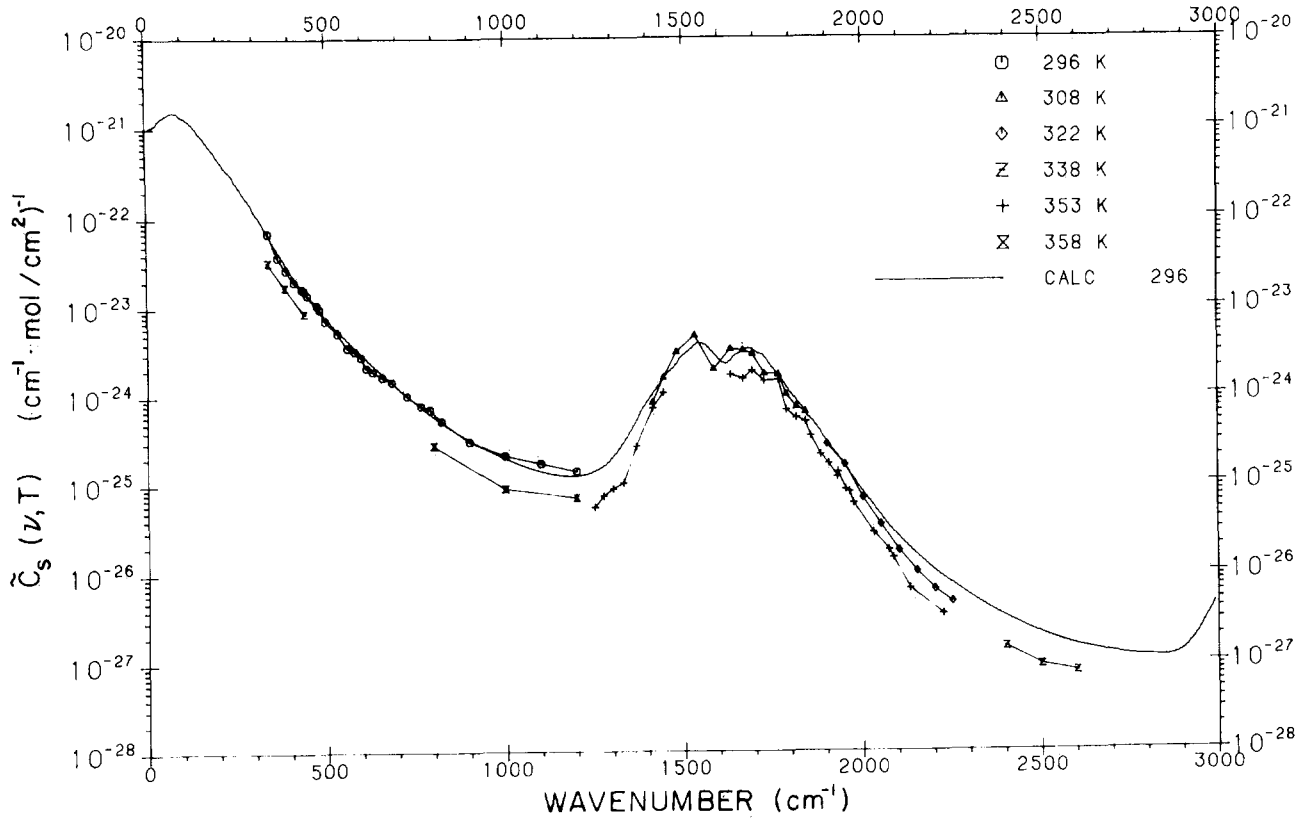


Figure 18-62. The self density dependent continuum values C_s for water vapor as a function of wave number. The experimental values are from Burch [1981].

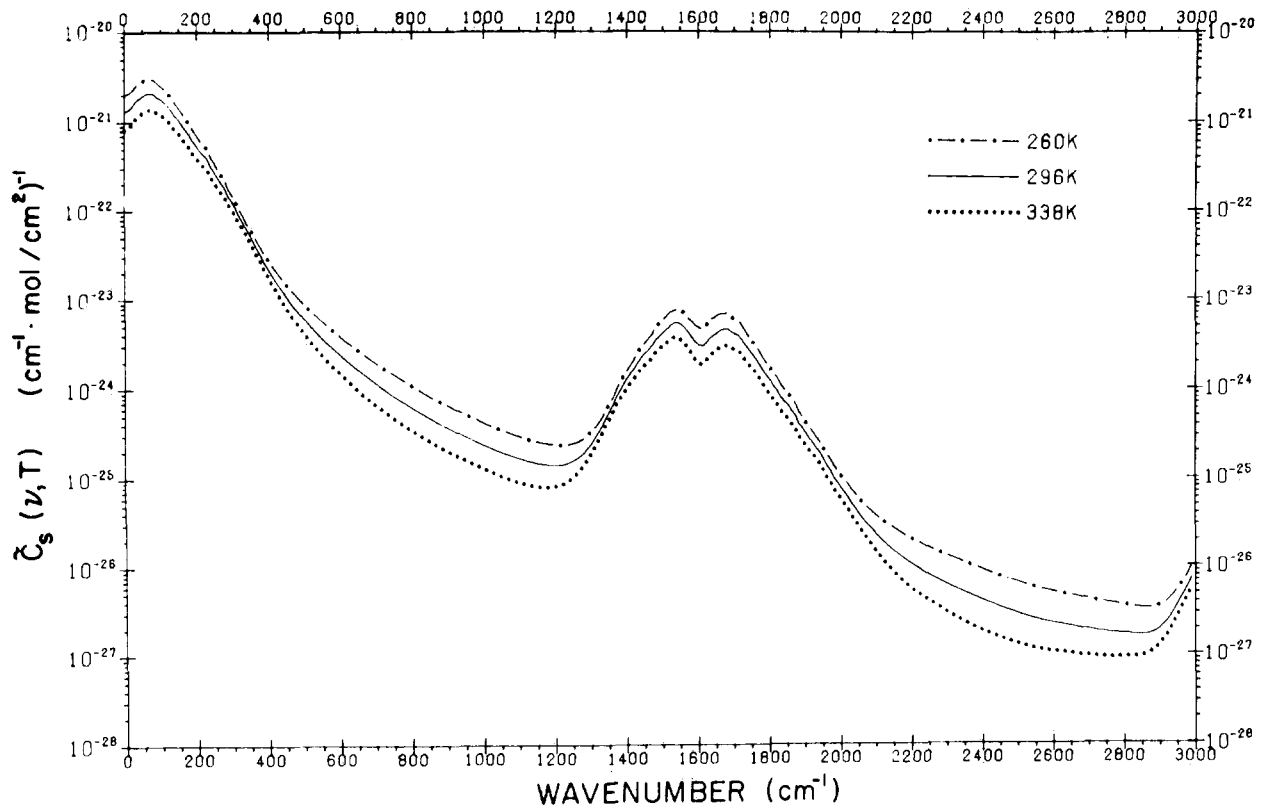


Figure 18-63. The self density dependent continuum values C_s for water vapor as a function of wave number at 260 K, 296 K, and 338 K. The values from 296 K and 338 K are fits to experimental results, the 260 K is extrapolated.

CHAPTER 18

self and foreign continuum, and \bar{C}_s and \bar{C}_f [(cm⁻¹ mol/cm²)⁻¹] the wavenumber dependent continuum absorption parameters for the self and foreign components. The density n_s is the density of the absorbing molecular species and n_f is the density of all other molecular species; consequently, $n_s + n_f$ represents the total density. The quantity, n_0 , is the reference number density defined at 1013 mb and 296 K. In some cases the dependence of \bar{C} on temperature is not known. The present formulation has the advantage that the continuum contribution to the optical depth decreases with increasing temperature through the number density ratio term. The quantities \bar{C}_s and \bar{C}_f for water vapor and \bar{C}_f for carbon dioxide are stored in the program for the spectral range 0 to 20 000 cm⁻¹.

The values for \bar{C}_s for water vapor at 296 K are shown in Figure 18-62 together with the experimental values obtained by Burch [Burch and Gryvnak, 1978 and 1979; Burch et al., 1971; and Burch, 1970]. The 260 K result was obtained by extrapolating the fits to the 353 K and 296 K data of Burch. The results for the three temperatures are shown in Figure 18-63. The strong temperature dependence of the self density dependent water vapor continuum is treated by using exponential interpolation of the 260 K and 296 K values.

Only values near room temperature are available for the foreign dependence of the water vapor continuum. The continuum values \bar{C}_f at 296 K are shown in Figure 18-64 and have been obtained by a fit to the data of Burch. There is considerable uncertainty in the values for the spectral window regions at 1000 and 2500 cm⁻¹.

For nitrogen, continuum values at 296 K are included in FASCODE for the collision induced absorption band at 2350 cm⁻¹. For this case \bar{C}_s is taken to equal \bar{C}_f , so that the effect is dependent on the total density.

18.4.1.3 Radiance and Transmittance for Atmospheric Paths. The layering of the atmosphere is primarily dependent on two considerations: the ratio of the Voigt widths at the layer boundaries and the temperature across the layer. The Voigt width as a function of altitude for the U.S. Standard Atmosphere is shown in Figure 18-65. The sampling interval, DV, for FASCODE is indicated on the figure where nominally DV = $\alpha^2/4$. All calculations are performed commencing at the lowest altitude involved in the problem. Consequently the sampling interval decreases monotonically in the altitude regime for which collisional broadening predominates and becomes essentially constant at altitudes for which the Doppler broadening is dominant. This method of

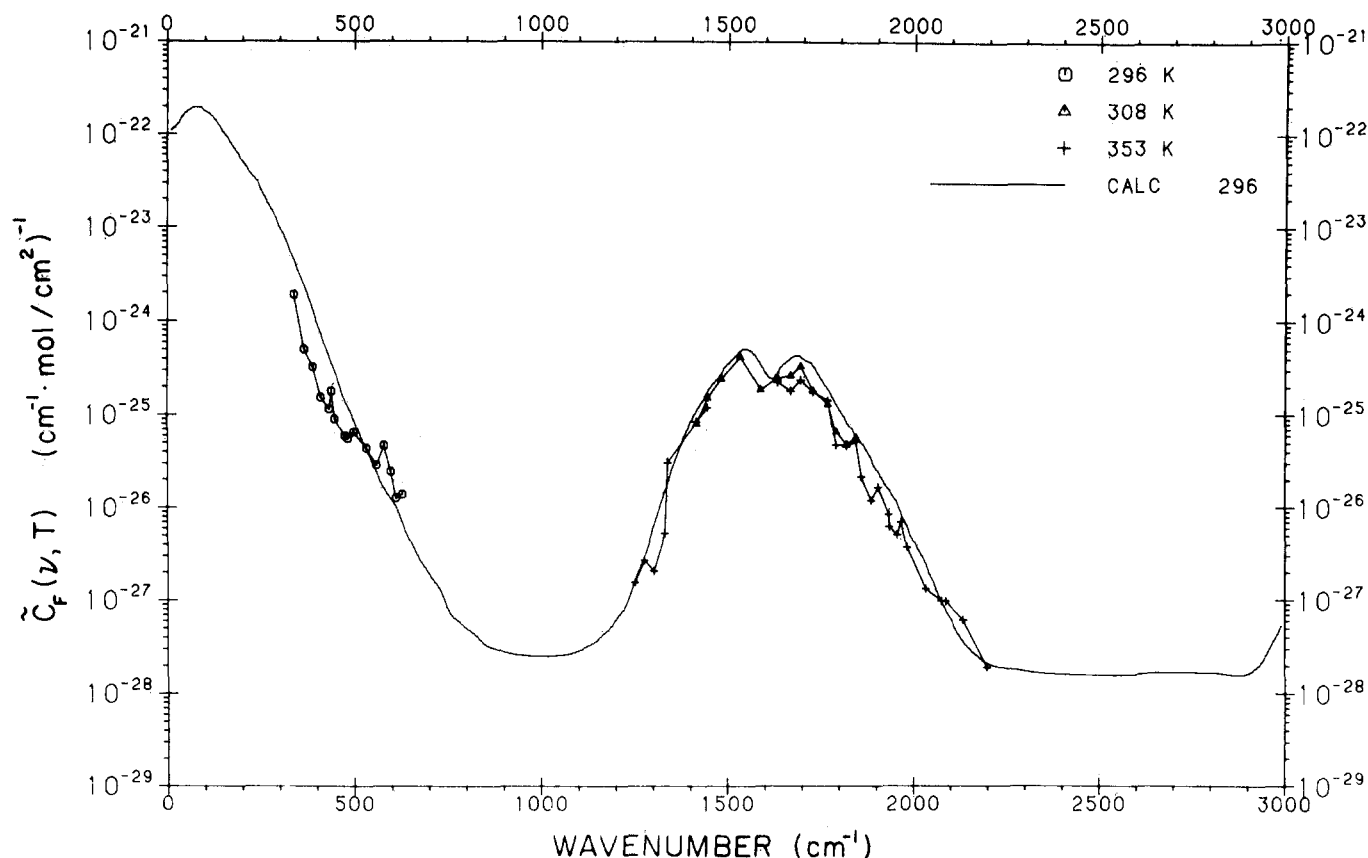


Figure 18-64. The foreign density dependent continuum values \bar{C}_f for water vapor as a function of wave number. The experimental values are from Burch [1981].

OPTICAL AND INFRARED PROPERTIES OF THE ATMOSPHERE

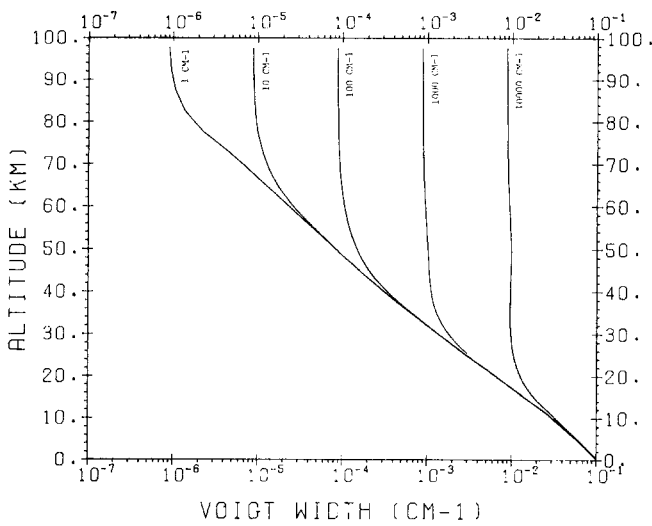


Figure 18-65. The Voigt width (HWHM) as a function of altitude for the U.S. Standard Atmosphere.

performing the calculation ensures that the minimum amount of information is handled at any given stage of the calculation. Figure 18-66 shows the Voigt parameter, ζ , as a function of altitude for the U.S. Standard Atmosphere.

The atmospheric layering is performed by program FSCATM [Gallery et al., 1983]. For specified boundaries and geometric parameters, the program computes the column densities and the density weighted temperature and pressure for each layer. Alternatively, the maximum acceptable ratio of Voigt line widths for the layer boundaries and the maximum temperature differential across the layer may be selected to perform the atmospheric layering. These two parameters are directly related to the accuracy of the radiance and/or the transmittance result.

FASCODE operates in either of two modes: optical depth or radiance/transmittance. In the optical depth mode, the

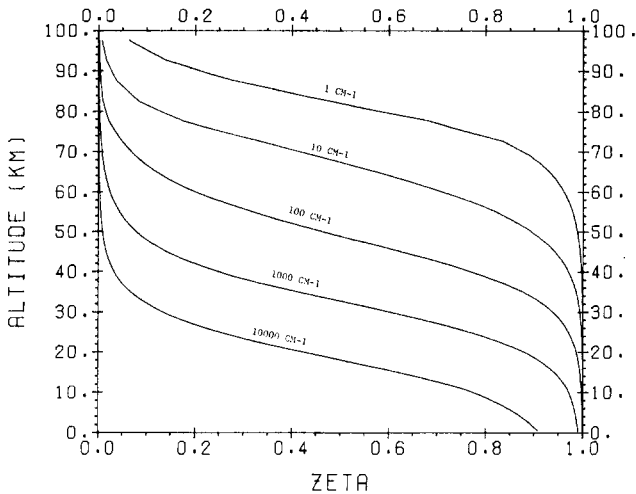


Figure 18-66. The Voigt parameter ζ as a function of altitude for the U.S. Standard Atmosphere.

recursion relation for the accumulated optical depth, \tilde{K}_ℓ , after ℓ layers is expressed as

$$\tilde{K}_\ell = \tilde{K}_{\ell-1} + \tilde{k}_\ell \quad (18.51)$$

where \tilde{k}_ℓ is the optical depth for layer ℓ and $\tilde{K}_0 = 0$. This relationship is implemented layer by layer to obtain the total optical depth for the path.

For the radiance/transmittance mode, the radiant intensity, I_ℓ ($\text{W cm}^{-2} \text{sr}^{-1}/\text{cm}^{-1}$), originating in layer ℓ , is expressed as

$$I_\ell = (1 - \tau_\ell) B(T_\ell), \quad (18.52)$$

where τ_ℓ is the transmittance and B ($\text{W cm}^{-2} \text{sr}^{-1}/\text{cm}^{-1}$) is the Planck black body function at temperature T_ℓ for the layer. Since all calculations are performed from lower to higher altitudes, different recursion algorithms are required for the looking down, the tangent path, and the looking up geometric situation. For the looking down geometry, we obtain the recursion relation for the contribution of the current layer ℓ to the upwelling radiation as

$$I_\ell = \tau_\ell I_{\ell-1} + (1 - \tau_\ell) B(T_\ell) \quad (18.53)$$

with the condition that I_0 , the boundary radiance, is

$$I_0 = \epsilon_0 B(T_0), \quad (18.54)$$

where T_0 is the boundary temperature and ϵ_0 the boundary emissivity. The transmittance relationship for this case becomes

$$T_\ell = \tau_\ell T_{\ell-1} \quad (18.55)$$

where T_ℓ is the total transmittance after layer ℓ .

For tangent path geometry with symmetry about the tangent height, we obtain the recursion relations

$$I_\ell = \tau_\ell I_{\ell-1} + (1 + \tau_\ell T_{\ell-1})(1 - \tau_{\ell-1}) B(T_\ell) \quad (18.56)$$

for the radiance with $I_0 = 0$ and

$$T_\ell = \tau_\ell T_{\ell-1} \quad (18.57)$$

for the transmittance with $T_0 = 1$. This algorithm for the tangent path case involves only a single line-by-line calculation for each layer and enables this case to be handled consistently with the other cases, that is, the calculation commences with the tangent layer and proceeds to higher altitudes.

For looking up geometries, the recursion relation for the downwelling radiance is

$$I_\ell = I_{\ell-1} + T_{\ell-1}(1 - \tau_\ell) B(T_\ell) \quad (18.58)$$

CHAPTER 18

with $I_0 = 0$ and for the transmittance

$$T_\ell = \tau_{\ell-1} T_{\ell-1} \quad (18.59)$$

with $T_0 = 1$. These algorithms are implemented layer by layer starting with the initial layer at the lowest altitude and proceeding to the higher altitude.

In Figure 18-67 we show the comparison of a FASCODE calculation with experimental results obtained by Rice and Ade [Rice and Ade, 1979] in the millimeter spectral region. The data were taken with an interferometer measuring the downwelling radiance at the ground from which atmospheric transmittance was inferred. The calculation was performed with a two layer atmosphere and the water amount given by the measured amount for the Rice and Ade experiment. In Figure 18-68 we show the results for a fifteen layer calculation with a geometry in which the observer is at 100 km looking through a 15 km tangent height. Figure 18-69 shows an expanded view of the Q branch region shown in Figure 18-68. The radiance calculation is plotted in terms of equivalent black body temperature.

18.4.2 Broad-Band Radiation

Band models assume an array of lines having chosen intensities, half-widths, and spacings which can be adjusted to represent the molecular line structure in some part of a real band. For a particular band model, the mean transmittance can be represented by a mathematical expression (transmittance function) expressed in terms of pressure, temperature effective path length (or absorber concentration), and one or more frequency dependent absorption coefficients.

Several band models have been developed [see Goody, 1952 and 1964; Elsasser, 1942; Plass, 1958; King, 1964; and Wyatt et al., 1964]; the Elsasser and Goody models being the most well known. The Elsasser band model con-

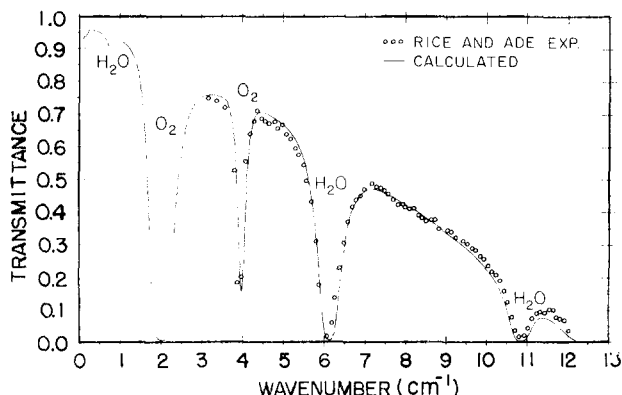


Figure 18-67. Spectral transmittance inferred from a radiance measurement looking up from the ground. The symbols o are the data of Rice and Ade [1979], and the continuous curve is a two-layer FASCOD1B calculation.

sists of an array of equally spaced identical lines of Lorentz shape. This model has been applied to absorption bands that have a regular line structure, for example, to some bands of CO_2 , N_2O , CO , CH_4 , and O_2 . The Goody model, on the other hand, assumes that the band is composed of spectral lines with an exponential intensity distribution and with random spacing between lines. Again the lines are assumed to have a Lorentz shape. This model has generally been applied to bands that have an irregular line structure, for example, some H_2O and O_3 bands.

In practice the wavelength dependent absorption coefficients are determined for each absorbing gas separately using laboratory transmittance values measured under known conditions. The absorption coefficients obtained in this way are then used in the band model transmittance function to determine the average transmittance for each absorber as a function of frequency for other values of path length and pressure. Finally, the total mean transmittance for molecular absorption is given by the product of the mean transmittances of the individual absorbers at each frequency.

Exact analytical expressions have been obtained for most of the band models. However, they are sometimes difficult to use and simpler approximations have been found to apply in two limiting conditions common to all band models. Those simpler expressions are the well known "weak line" and "strong line" approximations [see Goody, 1964, and Plass, 1958] for which the transmittance is a function of the absorber amount, and the product of the pressure and absorber amount, respectively (for a given temperature).

The weak line approximation, which corresponds to the exponential law, is valid when the absorption is small at the line centers (generally for high pressures and low absorber amounts). Unfortunately this case is rarely applicable to conditions existing in the terrestrial atmosphere. The strong line approximation is applicable where the lines are completely absorbing at their centers; the effect of increasing the amount of absorber is then confined to the edges or wings of the lines. The regions of validity of the strong and weak line approximation for the Elsasser and Goody models are discussed by Plass [1958]. For practical purposes most problems fall in either the strong line approximation region or the intermediate region.

In the LOWTRAN band model discussed in the following section, empirical transmittance functions for H_2O , O_3 , and the combined contributions of the uniformly mixed gases have been determined from laboratory and calculated transmittance data. Over a wide range of pressures and absorber amounts, the empirical transmittance functions were found to give better agreement with laboratory and calculated transmittance data than the commonly used band models. An excellent review of the LOWTRAN model and other band models is given in La Rocca [1978].

18.4.2.1 Broad-band Transmission (LOWTRAN). The LOWTRAN model was developed to provide a fairly accurate, simple and rapid means of estimating the transmit-

OPTICAL AND INFRARED PROPERTIES OF THE ATMOSPHERE

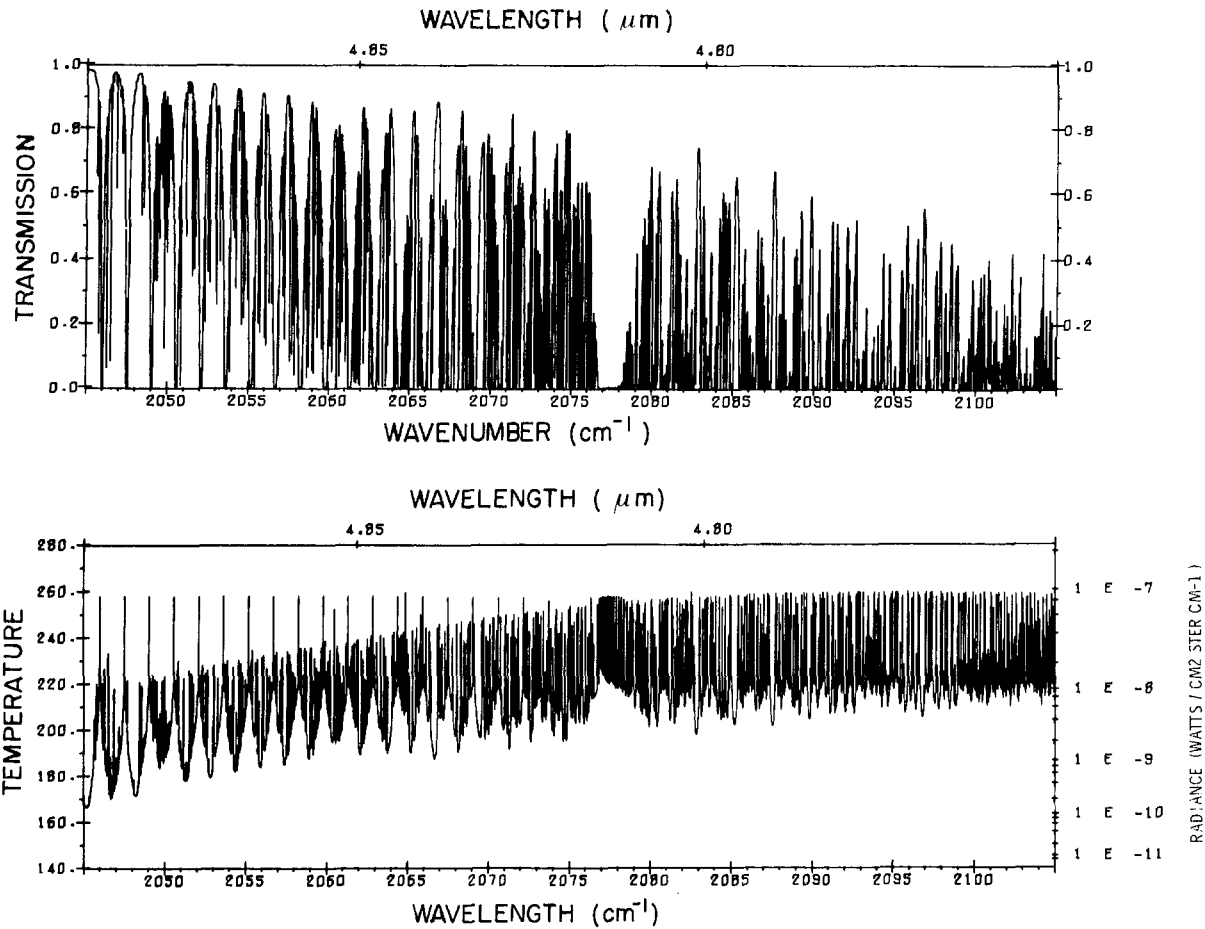


Figure 18-68. The transmittance and equivalent temperature radiance plot at 100 km and a 15 km tangent height. The results are from a 15 layer FASCOD1B calculation.

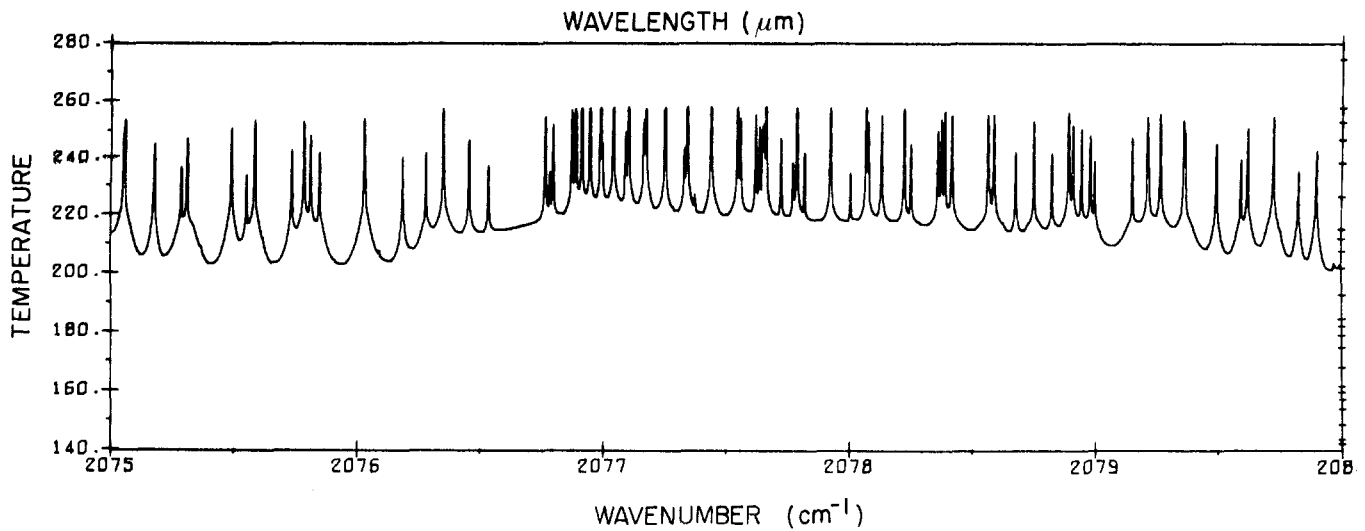


Figure 18-69. An expanded spectral region from the results shown in Figure 18-68.

CHAPTER 18

tance and background radiance of the earth's atmosphere at moderate resolution (20 cm^{-1}) over a broad spectral interval (350 to $40\,000 \text{ cm}^{-1}$). The model was derived using a single parameter band model for molecular absorption and includes the effects of continuum absorption, molecular scattering, and aerosol extinction. It is based on an empirical graphic prediction scheme of transmittance using some techniques originally suggested by Altshuler [1961]. The prediction scheme, derived from laboratory transmittance measurements complemented by line-by-line transmittance calculations was reported by McClatchey et al. [1972] and, subsequently, together with atmospheric models developed into the model and computer code LOWTRAN [Selby et al., 1972; 1975; 1976; 1978; and Kneizys et al., 1980; 1983]. The model contains representative (geographical and seasonal) atmospheric models and representative aerosol models with an option to replace them with user derived or measured values and computes atmospheric transmittance or both atmospheric transmittance and radiance for any given slant path geometry.

18.4.2.2 Assumptions of the LOWTRAN Model. The basic assumptions made in the LOWTRAN Model are as follows:

1. The atmosphere can be represented by a 33 layer model between sea level and 100 km. Each model atmosphere contains the variation of pressure, temperature, water vapor, and ozone with altitude. A mean nitric acid profile is incorporated into the model. It is assumed that the mixing ratios of CO_2 , N_2O , CH_4 , CO , O_2 and N_2 remain constant with altitude. Each layer is assumed to be in thermal equilibrium.

2. Refraction and earth curvature effects are included in the calculation of absorber amounts for slant atmospheric paths.

3. The average transmittance over a 20 cm^{-1} interval (due to molecular absorption) can be represented by a single parameter empirical transmittance function. The argument of the transmittance function is the product of wavenumber (or wavelength) dependent absorption coefficient, and "an equivalent absorber amount" for the atmospheric path.

4. The total transmittance at a given wavenumber averaged over a 20 cm^{-1} interval is given by the product of the average transmittances due to molecular absorption, molecular scattering, aerosol extinction, and continuum absorption. It is further assumed that the molecular absorption is composed of four components, namely the separate transmittances of water vapor, ozone, nitric acid and the uniformly mixed gases.

5. The variation of aerosol optical properties with altitude is modeled by dividing the atmosphere into four height regions each having a different type of aerosol. The aerosol models for the lower atmosphere (RURAL, URBAN, MARITIME and TROPOSPHERIC) are given as a function of relative humidity. Radiation and advection fog models are also included.

6. Atmospheric and earth radiance are calculated by a numerical evaluation of the integral form of the equation of radiative transfer. The emission from aerosols and the treatment of aerosol and molecular scattering are considered only in the zeroth order.

18.4.2.3 LOWTRAN Atmospheric Transmittance. In the LOWTRAN model, the total atmospheric transmittance at a given wavenumber averaged over a 20-cm^{-1} interval is given by the product of the average transmittances due to molecular band absorption, molecular scattering, aerosol extinction, and molecular continuum absorption. The molecular band absorption is composed of four components, namely the separate transmittances of water vapor, ozone, nitric acid and the uniformly mixed gases (CO_2 , N_2O , CH_4 , CO , O_2 and N_2).

The average transmittance $\bar{\tau}$ over a 20-cm^{-1} interval (due to molecular absorption) is represented by a single parameter model of the form

$$\bar{\tau} = f(C_v, \omega^* \cdot DS) \quad (18.60)$$

where C_v is the LOWTRAN wavenumber-dependent absorption coefficient and ω^* is an "equivalent absorber density" for the atmospheric path DS at altitude z , defined in terms of the pressure $P(z)$, temperature $T(z)$, concentration of absorber ω and an empirical constant n as follows

$$\omega^* = \omega \left\{ \frac{P(z)}{P_0} \sqrt{\frac{T_0}{T(z)}} \right\}^n \quad (18.61)$$

where P_0 and T_0 correspond to STP (1 atm, 273 K). If Equation (18.61) is substituted in Equation (18.60) and n is set to zero and unity respectively, Equation (18.61) reverts to the well-known weak-line and strong-line approximations common to most band models.

The form of the function f and parameter n was determined empirically using both laboratory transmittance data and available molecular line constants. In both cases, the transmittance was degraded in resolution to 20 cm^{-1} throughout the entire spectral range covered here. It was found that the functions f for H_2O and the combined contributions of the uniformly mixed gases were essentially identical, although the parameter n differed in the two cases. Mean values of n were determined to be 0.9 for H_2O , 0.75 for the uniformly mixed gases, and 0.4 for ozone.

Figure 18-70 shows the LOWTRAN empirical transmittance functions defined by Equation (18.60) versus the \log_{10} of the effective optical depth ($C_v, \omega^* \cdot DS$). The solid function shown is used for water vapor and the uniformly mixed gases. The dashed function is applicable to ozone.

Absorption coefficients for water vapor, ozone, and the combined effects of the uniformly mixed gases are included as data for LOWTRAN. The absorption coefficients for water vapor, ozone, and the uniformly mixed gases are

OPTICAL AND INFRARED PROPERTIES OF THE ATMOSPHERE

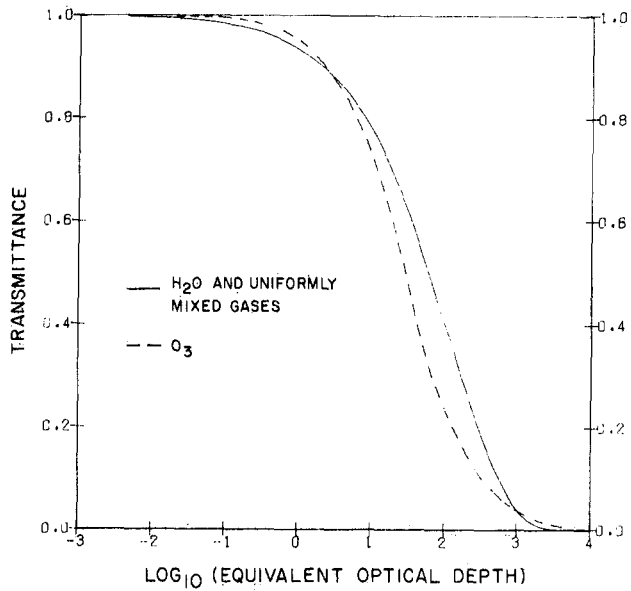


Figure 18-70. LOWTRAN empirical transmittance functions versus Log_{10} of the effective optical depth ($C_v \omega \cdot \text{DS}$).

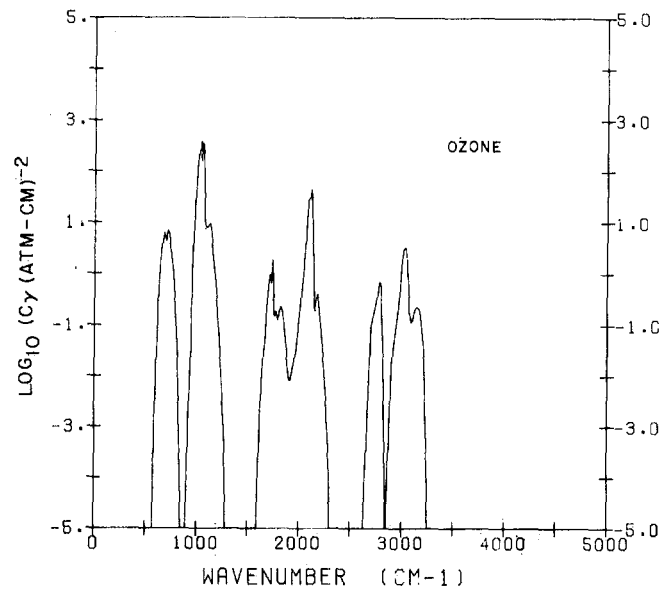


Figure 18-72. Absorption coefficient C_v for ozone from 350 to 5000 cm^{-1} .

shown in Figures 18-71, 18-72 and 18-73 for the spectral region from 350 to 5000 cm^{-1} .

18.4.2.4 LOWTRAN Atmospheric Radiance. The LOWTRAN model and code also calculate atmospheric and earth radiance. A numerical evaluation of the integral form of the equation of radiative transfer is used. The emission from aerosols and the treatment of aerosol and molecular scattering is considered only in the zeroth order. Additional contributions to atmospheric emission from radiation scat-

tered one or more times are neglected. Local thermodynamic equilibrium is assumed in the atmosphere.

The average atmospheric radiance (over a 20- cm^{-1} interval) at the wavenumber, ν , along a given line-of-sight in terms of the LOWTRAN transmittance parameters is given by

$$I(\nu) = \int_{\bar{\tau}_a}^1 d\bar{\tau}_a B(\nu, T) \bar{\tau}_s + B(\nu, T_b) \bar{\tau}_b^b, \quad (18.62)$$

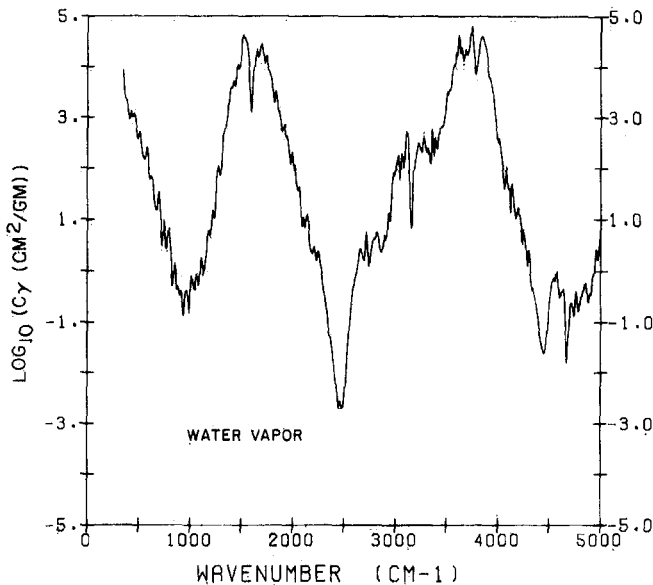


Figure 18-71. Absorption coefficient C_v for water vapor from 350 to 5000 cm^{-1} .

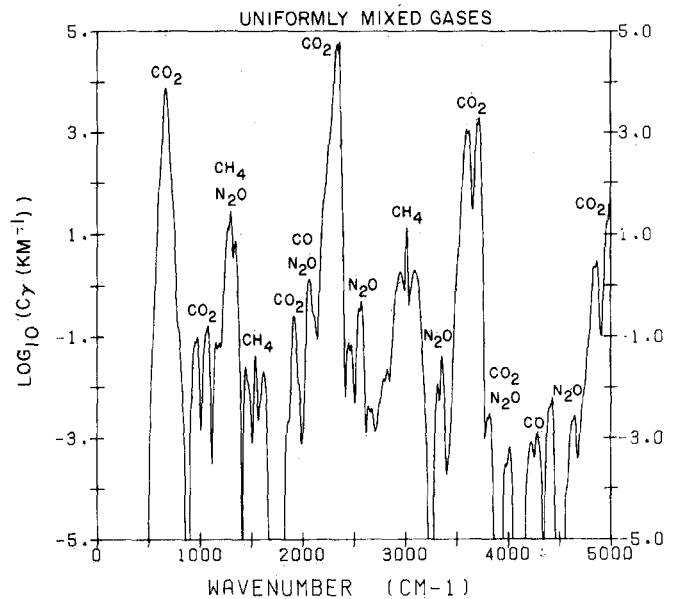


Figure 18-73. Absorption coefficient C_v for the uniformly mixed gases from 350 to 5000 cm^{-1} .

CHAPTER 18

where the integral represents the atmospheric contribution and the second term is the contribution of the boundary, (for example, the surface of the earth), and

$\bar{\tau}_a$ = average transmittance due to absorption,

$\bar{\tau}_s$ = average transmittance due to scattering,

$\bar{\tau}_t = \bar{\tau}_a \bar{\tau}_s$ = average total transmittance,

$\bar{\tau}_a^b, \bar{\tau}_t^b$ = average total transmittances from the observer to boundary,

$B(\nu, T)$ = average Planck (blackbody) function corresponding to the frequency ν and the temperature T of an atmospheric layer,

T_b = temperature of the boundary.

The emissivity of the boundary is assumed to be unity.

The numerical analogue to Equation (18.62) has been incorporated in the LOWTRAN model.

18.4.2.5 Examples of Transmittance and Radiance Spectra. Some examples of transmittance and radiance spectra obtained from the LOWTRAN model are presented in Figures 18-74 through 18-77.

Figure 18-74 shows the transmittance from ground to space from 0.25 to 4 μm . This calculation used the U.S. Standard model atmosphere and the rural aerosol model with a 23-km met. range.

Figure 18-75 shows the variation in transmittance in the spectral region between 400 and 4000 cm^{-1} for the rural, maritime, urban, and tropospheric aerosol models. The calculation is for a 10-km horizontal sea-level path using the U.S. Standard model atmosphere and a 23-km meteorological range.

Figure 18-76 shows the transmittance of the two fog models in LOWTRAN for a 0.2-km horizontal sea-level path and a 1-km meteorological range in the spectral region from 400 to 4000 cm^{-1} .

Figures 18-77 a and b show the transmittance and radiance spectra for a vertical path at 0° zenith angle looking to space as a function of observer altitude (0, 20 and 40

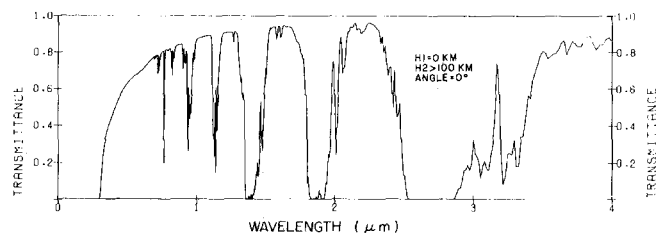


Figure 18-74. Transmittance spectra for a vertical path from ground to space from 0.25 to 4 μ , using the rural aerosol model, 23-km VIS and the U.S. Standard Model Atmosphere.

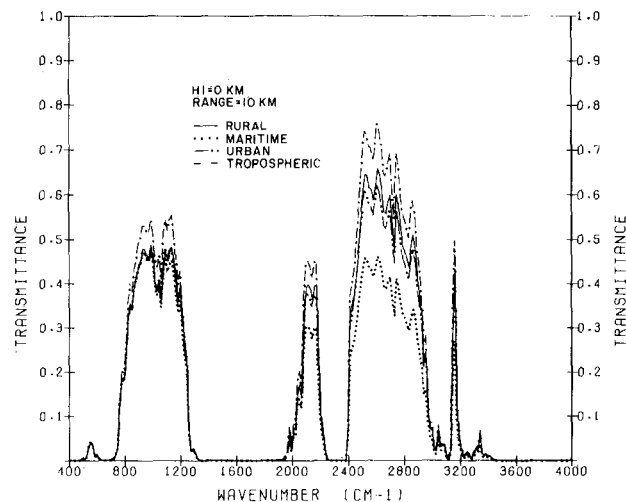


Figure 18-75. Transmittance spectra for a 10-km horizontal path at sea level for the rural, maritime, urban, and tropospheric aerosol models using the U.S. Standard Model Atmosphere and a VIS of 23 km.

km). This calculation for the spectral region from 400 to 4000 cm^{-1} used the rural aerosol model (23 km met. range) and the U.S. Standard model atmosphere.

18.4.2.6 Comparisons of LOWTRAN with Measurements. Comparisons of LOWTRAN with measurements are presented in Figures 18-78 through 18-87. Figures 18-78 and 79 show transmittance comparisons of LOWTRAN with laboratory measurements of Burch et al. [1962] for some important water vapor and carbon dioxide absorption bands.

Figure 18-80 shows a transmittance comparison with a sea-level measurement by Ashley et al. [1973] (General Dynamics). The measurement, made with an interferometer

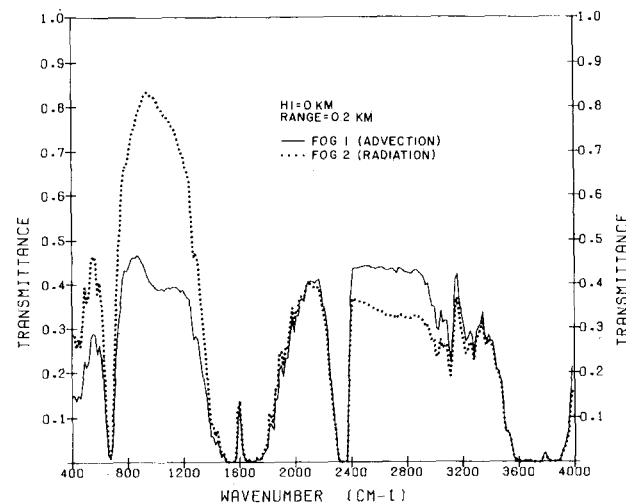


Figure 18-76. Transmittance spectra for the advection fog (Fog 1) and the radiation fog (Fog 2) models, for a 0.2-km horizontal path at sea level, with the U.S. Standard Model Atmosphere and a 1-km VIS, from 400 to 4000 cm^{-1} .

OPTICAL AND INFRARED PROPERTIES OF THE ATMOSPHERE

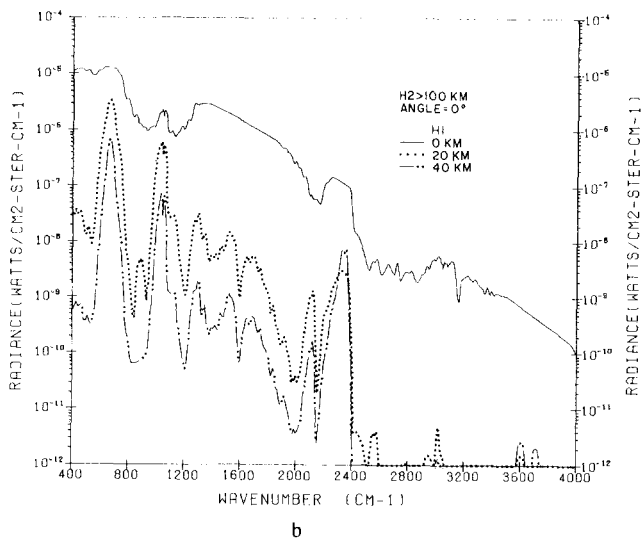
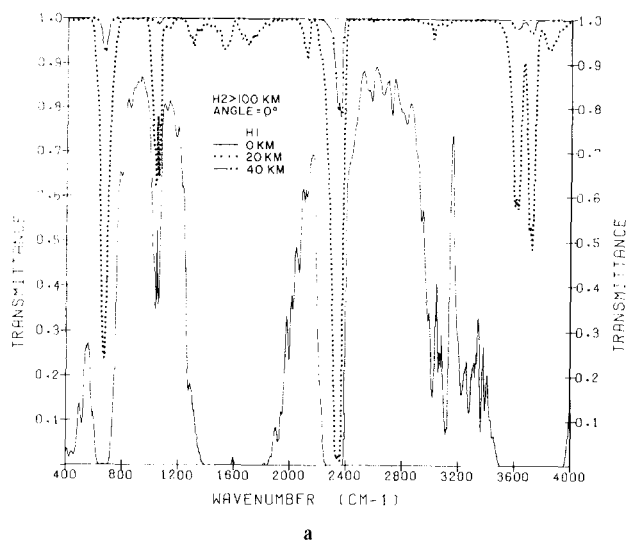


Figure 18-77. Transmittance and radiance spectra for a vertical path looking to space from H1 (H1 = 0, 20 km, 40 km, H2 ≥ 100 km, ANGLE = 0°) the rural aerosol model (IHAZE = 1, VIS = 23 km) and the U.S. Standard Atmosphere (MODEL = 6), from 400 to 4000 cm⁻¹: (a) transmittance, (b) radiance.

of ~4 cm⁻¹ resolution from 1.8 to 5.4 μm, is for a 1.3 km sea-level horizontal path.

Figure 18-81 shows a comparison with Chaney [1969] of the calculated upward atmospheric radiance and an interferometer measurement from a balloon flight over northern Nebraska. The measurement was taken at a float altitude of 34 km. The calculated radiance used the midlatitude winter model with a 23 km met. range and a ground temperature of 280 K.

Figure 18-82 shows a comparison of an interferometer measurement made from the Nimbus 3 satellite [Conrath et al., 1970] looking down over the Gulf of Mexico with the calculated atmospheric radiance. The resolution of the in-

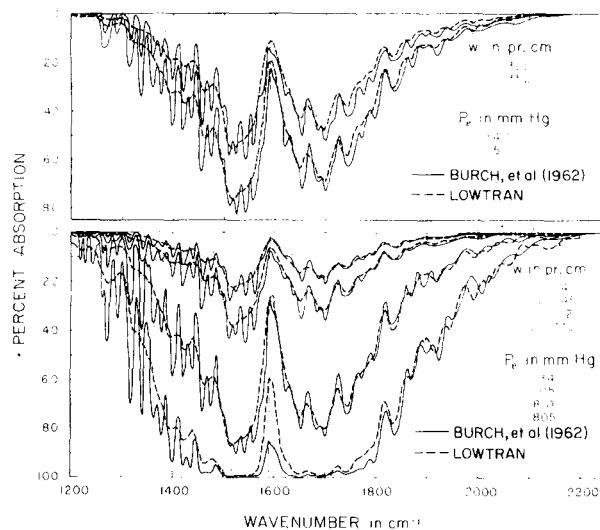


Figure 18-78. Representative absorption curves for the 6.3 μm H₂O Band.

terferometer was 5 cm⁻¹ as compared to the 20 cm⁻¹ resolution of LOWTRAN. As shown in Figure 18-82, two theoretical models (tropical and midlatitude summer) were used for comparison and are displaced two divisions above and below the measured radiance for clarity. Both models assumed a 23 km met. range and used the temperature at 0 km in the model atmosphere as the boundary temperature.

Figure 18-83 shows the comparison of atmospheric ra-

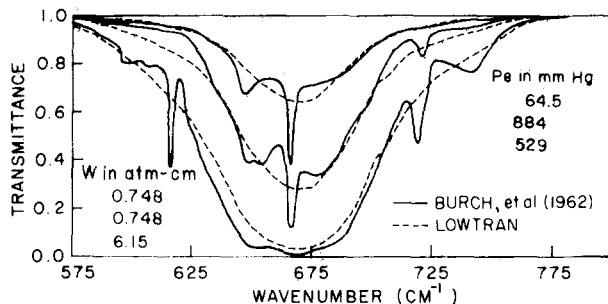
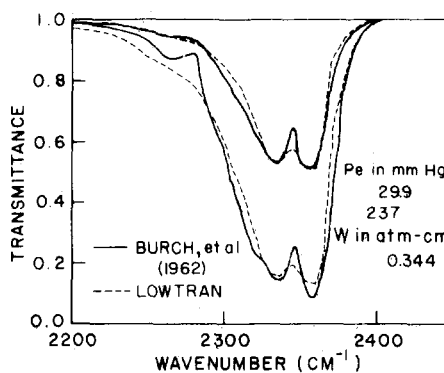


Figure 18-79. Comparison LOWTRAN calculations and Burch et al. [1962] calculations for CO₂ bands at 4.3 μm and 15 μm.

CHAPTER 18

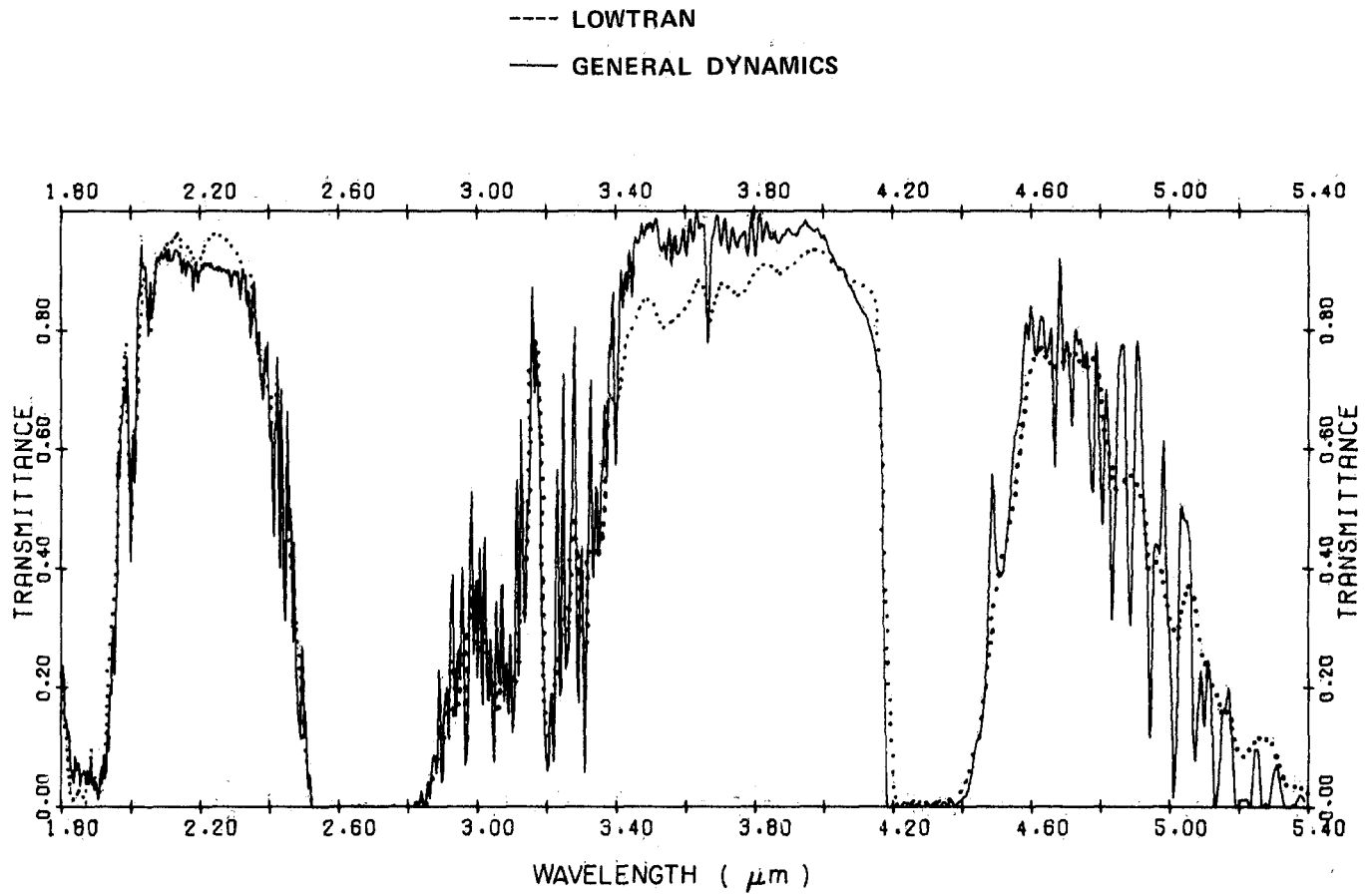


Figure 18-80. Comparison between LOWTRAN and General Dynamics measurements; range = 1.3 km at sea level.

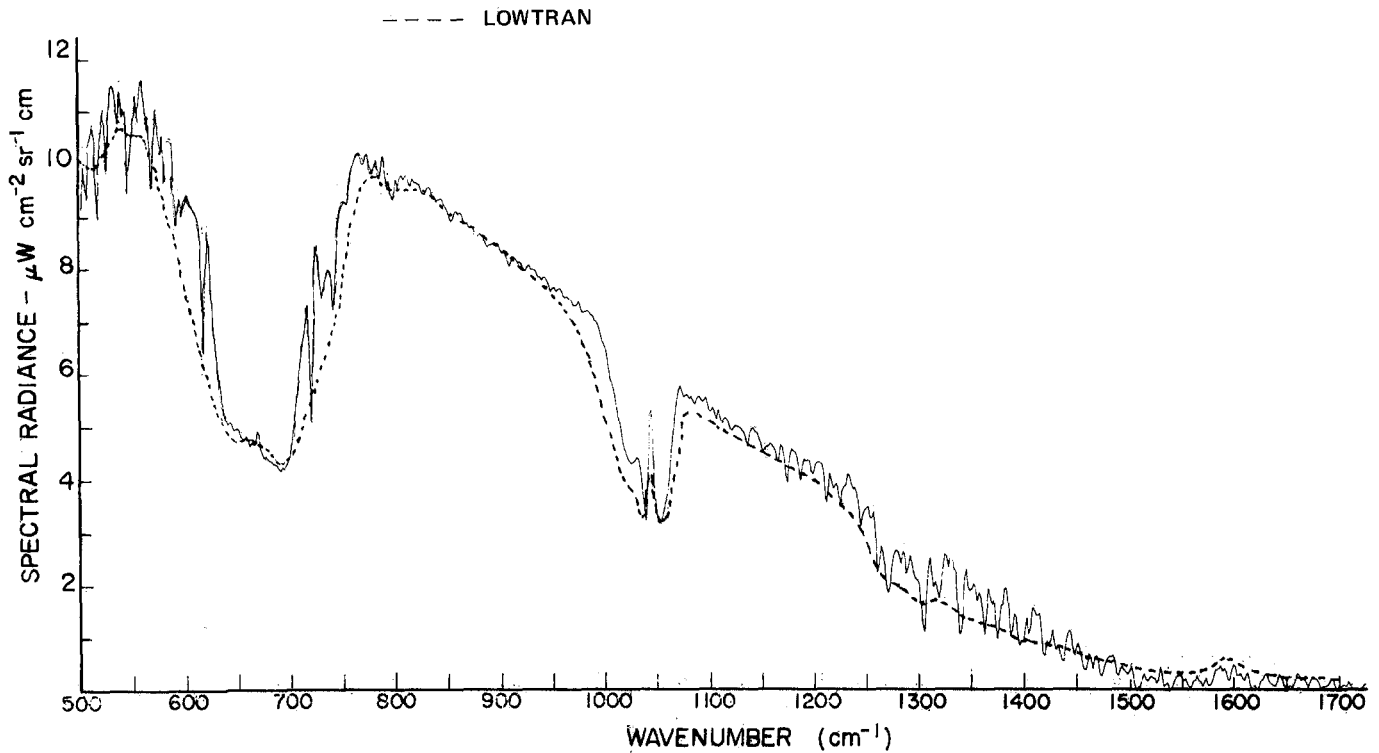


Figure 18-81. Comparison between LOWTRAN prediction and University of Michigan balloon measurement of atmospheric radiance over northern Nebraska.

OPTICAL AND INFRARED PROPERTIES OF THE ATMOSPHERE

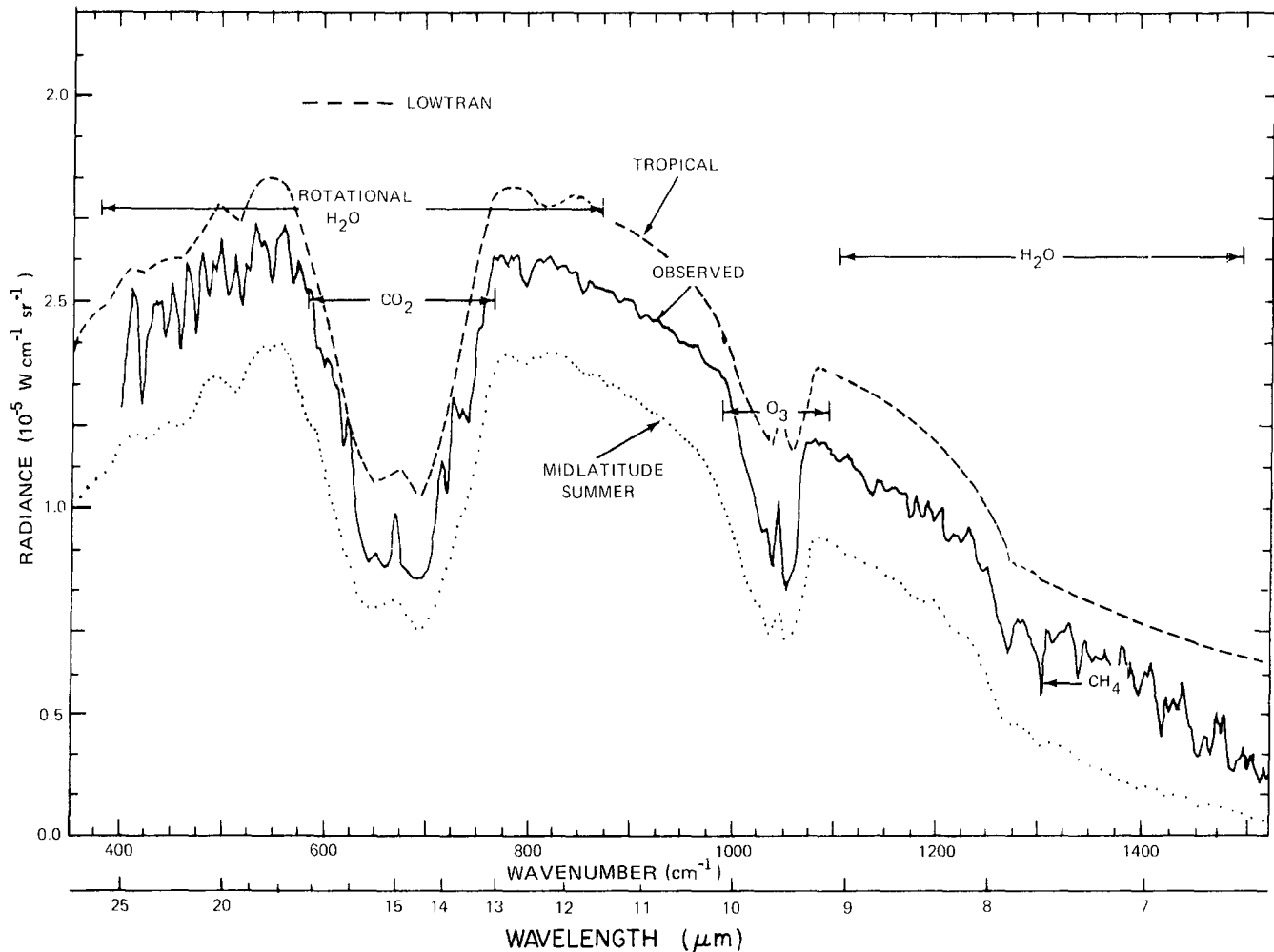


Figure 18-82. Comparison between LOWTRAN prediction and NIMBUS 3 satellite measurement of atmospheric radiance over the Gulf of Mexico.

diance as seen from space between the LOWTRAN calculation and measurements from the Nimbus 4 satellite [Hanel and Conrath, 1970] for three different geographic locations. The spectra, obtained with a Michelson interferometer of resolution 2.8 cm^{-1} , were measured over the Sahara Desert, the Mediterranean, and the Antarctic. The calculated LOWTRAN radiances used the midlatitude winter model and a ground temperature of 320 K for the Sahara, the midlatitude winter model and a ground temperature of 285 K for the Mediterranean; and an arctic winter cold model taken from the *Handbook of Geophysics and Space Environments* [Cole et al., 1965] and a ground temperature of 190 K for the Antarctic comparison. All three calculations assumed a 23 km met. range for aerosols.

Figures 18-84 through 87 show comparisons of calculated and observed atmospheric spectral radiance versus wavelength in the 8 to 14 μm spectral region. The measurements were made on a balloon flight launched from Holloman AFB, New Mexico by Murcray et al. [1977] University of Denver. The instrument used for these observations was a grating spectrometer, operated in the first and second

order of the grating. The resolution was $0.03 \mu\text{m}$ in the 8 to 14 μm region. The data in these figures are presented as a function of altitude and as a function of zenith angle. The LOWTRAN radiance calculation used the pressure, temperature, ozone, and nitric acid profiles from the Murcray report, and the midlatitude winter water vapor profile contained in LOWTRAN.

18.4.2.7 Limitations of LOWTRAN. The overall accuracy in transmittance from LOWTRAN is better than 10%. The largest errors may occur in the distant wings of strongly absorbing bands in regions where such bands overlap appreciably. The reason for this error is twofold. First, the LOWTRAN spectral coefficients are based on a single absorber parameter and cannot be defined for a wide range of atmospheric paths without some loss in accuracy.

Secondly, the transmittance in the window regions between strong bands generally lies in the weak line approximation region where the transmittance is a function of the quantity of absorber present and not of the product of absorber amount and pressure. The one-dimensional prediction

CHAPTER 18

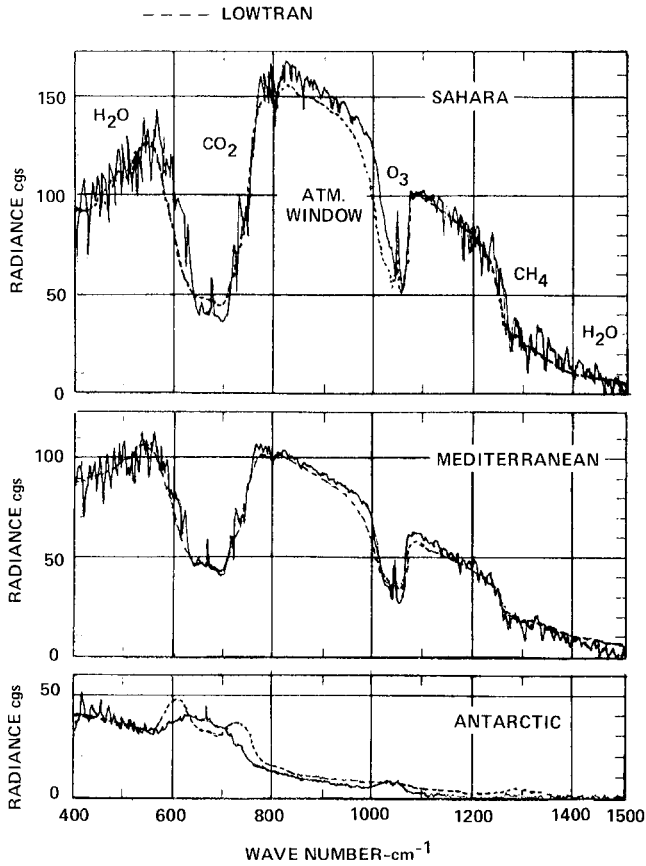


Figure 18-83. Comparison between LOWTRAN predictions and NIMBUS 4 satellite measurements of atmospheric radiance over the Sahara Desert, the Mediterranean, and the Antarctic.

— MURCRAY ET AL, HOLLOMAN AFB, NEW MEXICO, 19 FEBRUARY 1975
 --- LOWTRAN

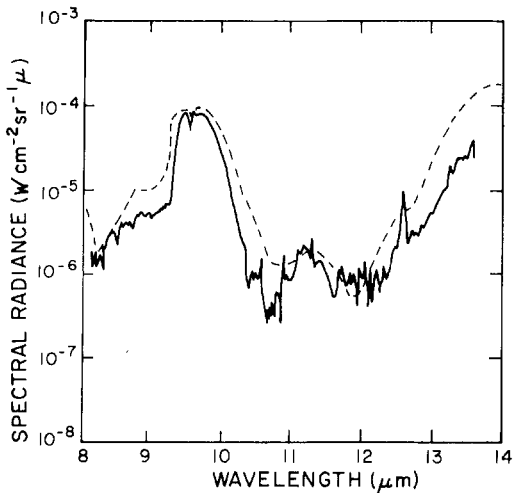


Figure 18-84. Sample spectrum of short wavelength region observed at an altitude of 9.5 km and a zenith angle of 63° on 19 February 1975 and LOWTRAN comparison.

— MURCRAY ET AL, HOLLOMAN AFB, NEW MEXICO, 19 FEBRUARY 1975
 --- LOWTRAN

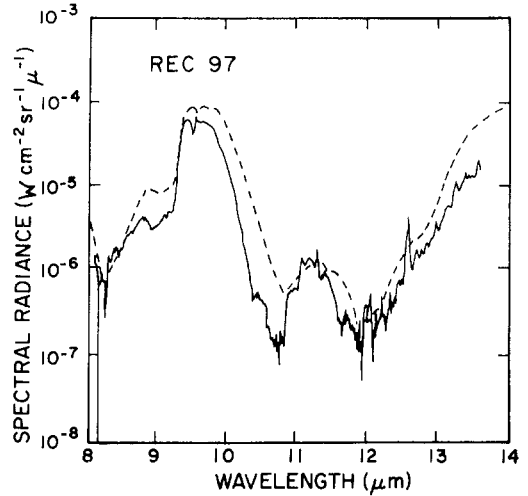


Figure 18-85. Sample spectrum of short wavelength region observed at an altitude of 13.5 km and a zenith angle of 63° on 19 February 1975 and LOWTRAN comparison.

scheme in LOWTRAN is less accurate for such conditions. The digitized spectral data used in LOWTRAN were obtained for conditions representative of moderate atmospheric paths and will tend to overestimate the transmittance for very long paths and underestimate the transmittance for very short paths in the spectral regions described above. As the transmittance approaches 1.0, the percentage error in trans-

— MURCRAY ET AL, HOLLOMAN AFB, NEW MEXICO, 19 FEBRUARY 1975
 --- LOWTRAN

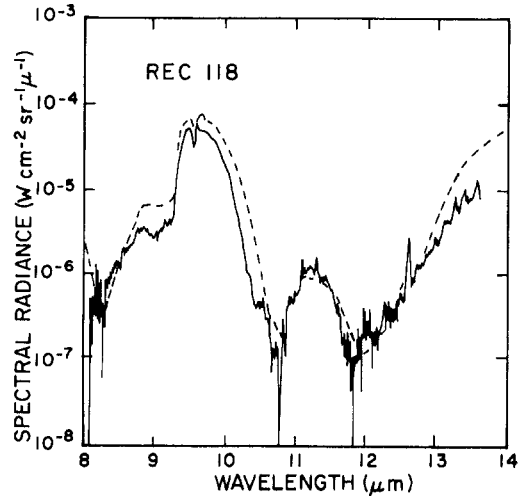


Figure 18-86. Sample spectrum of short wavelength region observed at an altitude of 18.0 km and a zenith angle of 63° on 19 February 1975 and LOWTRAN comparison.

— MURCRAY ET AL, HOLLOWAN AFB, NEW MEXICO,
19 FEBRUARY 1975
---LOWTRAN

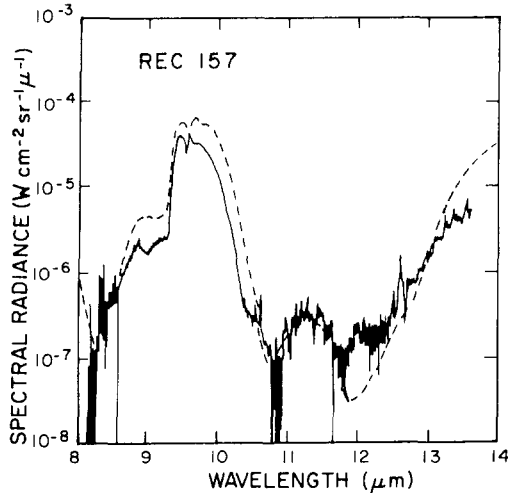


Figure 18-87. Sample spectrum of short wavelength region observed at an altitude of 24.0 km and a zenith angle of 63° on 19 February 1975 and LOWTRAN comparison.

mittance decreases toward zero but the uncertainty in the absorptance (or radiance) increases.

Additional constraints on both the validity of the model as well as the range of applicability are introduced for atmospheric radiance calculations. As mentioned above, the atmospheric radiance becomes less accurate for very short paths. In addition, the radiance calculations assume local thermodynamic equilibrium exists in each layer of the model atmospheres. This assumption will break down for radiance calculations in the upper atmosphere.

For the shorter wavelengths (<5 μm), scattered solar radiation becomes an important source of background radiation. This contribution for radiance calculations at the shorter wavelengths with a sunlit atmosphere would add to the atmospheric radiance calculation using the LOWTRAN model. Single-scattered solar and lunar radiation has been added to the latest LOWTRAN model [Kneizys et al., 1983].

18.5 RADIATION TRANSFER BY ATMOSPHERIC SCATTERING

18.5.1 Multiple Scattering

Scattering of visible and infrared radiation occurs in the atmosphere by air molecules, haze particles, and water droplets in the air (see Sections 18.1.4 and 18.2). Scattering effects from molecules and aerosols are additive. Multiple scattering occurs when scattered light undergoes subsequent scattering on other particles or molecules. The probability

for multiple scattering events increases with increasing optical thickness $t = k_s \cdot x$ [see Equation (18.21)]. Van de Hulst [1957] states that if the optical thickness $t < 0.1$ single scattering prevails, for $0.1 < t < 0.3$ a correction for double scattering may be necessary. For still larger values of the optical depth the full complexities of multiple scattering have to be considered.

Monographs by Chandrasekhar [1950], Sobolev [1975], and van de Hulst [1980] are classical references on theory and approaches to radiation transfer. Recent reviews of multiple scattering have been presented by Hansen and Travis [1974], Herman et al. [1978], and by the Radiation Commission of the International Association of Meteorology and Atmospheric Physics (IAMAP/RC) [Lenoble, 1977 and Fouquart et al., 1980].

The basic radiative transfer equation in a scattering atmosphere defining the diffuse radiance I_ν can be written as

$$\mu \frac{dI_\nu(t_\nu, \mu, \phi)}{dt_\nu} = -I_\nu(t_\nu, \mu, \phi) + J_\nu(t_\nu, \mu, \phi) \quad (18.63)$$

where the source term, J_ν , is given by

$$J_\nu = \frac{\omega_\nu(t_\nu)}{4\pi} \int_0^{2\pi} \int_{-1}^{+1} P_\nu(\mu, \phi; \mu', \phi') I_\nu(t_\nu, \mu', \phi') d\mu' d\phi' + \frac{1}{4} \omega_\nu(t_\nu) P_\nu(\mu, \phi; \mu_0, \phi_0) \exp(-t_\nu/\mu_0) F_{\text{sun}} + [1 - \omega_\nu(t_\nu)] B_\nu(t_\nu, T) \quad (18.64)$$

and where the following notation is used:

$$t_\nu = \int_z^\infty k_\nu(z') dz' \text{ optical depth}$$

$k_\nu(z)$ = extinction coefficient

$\omega_\nu(t_\nu)$ = albedo for single scattering

z = height

$\mu = \cos\theta$

θ = angle between a given direction and the direction of increasing optical depth, t (that is, towards the ground).

ϕ = azimuth angle

$P_\nu(\mu, \phi, \mu', \phi')$ = phase function defining the function of the light incident at μ', ϕ' which is scattered in the direction μ, ϕ .

$B_\nu(t, T)$ = Planck blackbody function at temperature T .

πF_{sun} = solar irradiance perpendicular to the direction of incidence, (μ_0, ϕ_0)

CHAPTER 18

The first term on the right side of Equation (18.63) is the energy lost from the beam of radiation traveling in the direction (μ, ϕ) . This loss is due to either absorption or scattering out of the beam. The second term (known as the source term) represents the diffuse radiation contributed to the direction (μ, ϕ) by scattering processes or self emission by the atmosphere. This source term is expanded in Equation (18.64) into three components (in order): the diffuse radiation scattered into the beam from other directions, the direct sunlight scattered into the beam direction (μ, ϕ) , and the thermal radiation emitted by the atmosphere at frequency ν . For simplicity, the frequency ν will be omitted in subsequent equations. However it should be kept in mind that these equations only apply to spectral intervals sufficiently narrow that the atmospheric absorption and scattering processes do not change significantly with wavelength.

The full radiative transfer Equation (18.63) with the source term as in Equation (18.64) is too cumbersome to solve in general. However for most scattering problems in the earth's atmosphere, there is a natural separation of the parts of the source term. In the temperature region of interest for the earth's atmosphere, $B_\nu(t, T)$ contributes only in the longwave region (infrared and beyond). For wavelengths less than 3 to 4 μm , generally the thermal radiation $B_\nu(t, T)$ can be neglected compared to the solar irradiation F_{so} , and for longer wavelengths F_{so} can be neglected compared to $B_\nu(t, T)$.

Also, for the longer wavelengths (greater than 3 to 4 μm) scattering is negligible except in the presence of clouds or fog. These cases where the source term is limited to the thermal radiation $B_\nu(t, T)$ are discussed in Section 18.4. Sections 18.5.2–18.5.4 will focus on the solution to Equation (18.63) when the thermal radiation can be neglected although many of the methods of solving the multiple scattering problem can easily be generalized to include atmospheric emission. The reduced expression for the source term is given by

$$J(t, \mu, \phi) = \frac{\omega(t)}{4\pi} \int_0^{2\pi} \int_{-1}^{+1} P(\mu, \phi; \mu', \phi') I(t, \mu', \phi') d\mu' d\phi' + \frac{\omega(t)}{4} P(\mu, \phi; \mu_0, \phi_0) \exp(-t/\mu_0) F_0. \quad (18.65)$$

The phase function P used here is a weighted average of the phase functions for molecular scattering and aerosol scattering discussed in Sections 18.1.4 and 18.2.1.5 respectively. The weights are proportional to the scattering coefficients for scattering by air molecules and by aerosol particles.

18.5.1.1 Formal Solution to the Multiple Scattering Problem. The formal solution to the radiative transfer equation is given by

$$I(t, \mu, \phi) = \begin{cases} I^-(t^*, \mu, \phi) \exp\left[-\frac{(t^* - t)}{|\mu|}\right] + \frac{1}{\mu} \int_1^{t^*} J(t', \mu, \phi) \exp\left[-\frac{(t' - t)}{|\mu|}\right] dt', & \mu < 0 \quad (18.66a) \\ J(t, \mu, \phi), & \mu = 0 \quad (18.66b) \\ I^+(0, \mu, \phi) \exp\left(-\frac{t}{\mu}\right) + \frac{1}{\mu} \int_0^t J(t', \mu, \phi) \exp\left[-\frac{(t - t')}{\mu}\right] dt', & \mu > 0 \quad (18.66c) \end{cases}$$

where t^* is the total optical depth of the atmosphere and where $I^-(t^*, \mu, \phi)$ for $\mu < 0$ and $I^+(0, \mu, \phi)$ for $\mu > 0$ (denoting the upward radiance at the ground and the downward radiance at the top of the atmosphere respectively) are specified by the boundary conditions: At the ground, the upwelling radiance is related to the downward radiance by an appropriate surface reflection law (see Section 18.3), and at the "top" of the atmosphere the downward diffuse radiance $I^+(0, \mu, \phi)$ for $\mu > 0$ is usually taken to be zero (that is, the downward radiance at the top of the atmosphere is due only to the incident sunlight). The formal solution [Equation (18.66)] does not completely solve the radiative transfer equation since J is defined in terms of I [Equation (18.65)]. However it is used in the development of several of the methods discussed below.

18.5.1.2 Method of Successive Orders of Scattering.

The method of successive orders of scattering expands the radiance as [see e.g. Dave, 1964, 1965, or Irvine, 1965]

$$I(t, \mu, \phi) = \sum_{n=1}^{\infty} I^{(n)}(t, \mu, \phi) \quad (18.67)$$

where $I^{(n)}$ is the part of the radiance scattered exactly n times. $I^{(n)}(t, \mu, \phi)$ is found by evaluating the formal solution [Equation (18.66)] using $J = J^{(n)}(t, \mu, \phi)$ which is given by Equation (18.65) with $I = I^{(n-1)}$ and starts with $I^{(0)} = 0$. This method has the advantage of easily handling vertically inhomogeneous atmospheres. The main disadvantage is that the computation time becomes very long as ω approaches 1.0 (absorption becomes weak) or as the optical depth becomes large.

18.5.1.3 Gauss-Seidel Iterative Method. The Gauss-Seidel iterative method originally developed by Herman and

Browning [1965] and others [Dave and Gazdag, 1970] also starts with Equations (18.65) and (18.66). Here they initially assume $I = 0$ and numerically integrate Equation (18.66) for small steps Δt for downward radiances ($\mu > 0$) until they reach the ground. They then integrate stepwise from the ground back to the top of the atmosphere using the downward radiances just calculated for the integral in Equation (18.65). The process is then repeated until the solution converges. Recently Herman et al. [1980] improved the computation speed by approximating $I(t, \mu, \phi)$ by polynomials in t which allowed the use of larger step sizes Δt for optically thick atmospheres.

18.5.1.4 The Matrix Operator or Layer Adding Methods. The radiative transfer problem has been solved by using different formations of the matrix operator or layer adding techniques reviewed by Plass, et al. [1973]. One of the first applications to light scattering in the atmosphere was the doubling method discussed by van de Hulst in an unpublished report in 1963 and later used by him and others [e.g. van de Hulst and Grossman, 1968; van de Hulst, 1971]. Hansen [1969a and b] has developed a modified version of this method and used it extensively [Hansen, 1971a and b; Hansen and Pollack, 1970].

An equivalent procedure was independently developed by Twomey et al. [1966] and has been used by them to study multiple scattering of light [Twomey et al., 1967]. A similar approach has been formulated by Grant and Hunt [1968, 1969a, b] based on invariance principles [Chandrasekhar, 1950] and the discrete space theory [Preisendorfer, 1965]. They have applied this matrix operator method to a variety of problems.

If we consider a plane-parallel medium of optical depth t and an incident radiation field $I_{inc}(0, \mu', \phi')$, ($0 \leq \mu' \leq 1$), it is convenient to introduce a scattering function $S(t; \mu, \phi, \mu', \phi')$ and a transmission function $T(t; \mu, \phi, \mu', \phi')$ [see Chandrasekhar, 1950]. Then the angular distribution of the reflected and transmitted light will be given by

$$I_{refl}(0, \mu, \phi) = \frac{1}{4\pi|\mu|} \int_0^1 \int_0^{2\pi} S(t; \mu, \phi, \mu', \phi') I_{inc}(0, \mu', \phi') d\phi' d\mu',$$

$$0 \geq \mu \geq -1 \quad (18.68a)$$

$$I_{trans}(t, \mu, \phi) = \frac{1}{4\pi|\mu|} \int_0^1 \int_0^{2\pi} T(t; \mu, \phi, \mu', \phi') I_{inc}(0, \mu', \phi') d\phi' d\mu'$$

$$1 \geq \mu \geq 0 \quad (18.68b)$$

The basic principle of the layer-adding methods is that given the scattering functions $S(t_1)$ and $S(t_2)$ and transmission function $T(t_1)$ and $T(t_2)$ of two layers, it is possible to find $S(t_1 + t_2)$ and $T(t_1 + t_2)$ for a combination of the layers

in terms of the scattering and transmission functions for the individual layers. For a homogenous atmosphere, it is most efficient to start with $t_1 = t_2 = t_0$, where t_0 is small, and build up to $t = 2^p t_0$ in p steps, by a doubling procedure.

The Neumann series method (iteration in orders of scattering [see Irvine, 1965] has been used to find $S(t_0)$ and $T(t_0)$ for $t_0 \approx 0.125$ by van de Hulst and Grossman [1968] and Irvine [1968b]. Hansen started with an initial optical thickness of $t_0 = 2^{-25}$ where he could approximate $S(t_0)$ and $T(t_0)$ by the appropriate expressions for single scattering.

The formalism developed by van de Hulst and Hansen has only been applied to radiation emerging from an atmosphere and in its present form cannot be used to calculate the radiation within an atmosphere. The approach developed by Grant and Hunt overcomes this drawback by incorporating an algorithm for determining the radiances between the layers used in the calculation. However, this can be quite time consuming for a number of different depths. The advantage in computation time is also weakened if the approach is extended to vertically inhomogeneous atmospheres.

18.5.1.5 Monte Carlo Technique. The Monte Carlo method basically utilizes a random walk approach, following a large number of photons in turn as they scatter through the atmosphere until they are absorbed or emerge from the atmosphere. This procedure was first extensively applied to the study of light in the atmosphere by Collins, Wells, and their associates [Collins and Wells, 1965; Thompson and Wells, 1971; Collins et al., 1972; Blättner et al., 1974]. Subsequently, Plass and Kattawar [1968a, 1968b & 1972] have independently developed a Monte Carlo type of program. The Russian work in this area is covered in the monograph by Marchuk et al. [1980].

The major advantage of the Monte Carlo approach is its great flexibility. It can allow for all of the complications of a realistic atmosphere usually neglected by other methods; these include the spherical nature of the atmosphere, molecular band model type absorption, and horizontal inhomogeneities. The major drawback is that the errors in the calculations are proportional to $N^{-1/2}$, where N is the number of photons counted. This means that to increase the accuracy by an order of magnitude, the number of photons followed (and the computer time) must be increased by two orders of magnitude.

18.5.1.6 Discrete Ordinates. One of the best known solutions of the transfer equation is Chandrasekhar's [1950] method of discrete ordinates. Here, the phase function is expanded as a series of spherical harmonics:

$$P(\mu, \phi, \mu', \phi') = \sum_{m=0}^N (2 - \delta_{0,m}) \times \left[\sum_{\ell=m}^N \omega_{\ell}^m P_{\ell}^m(\mu) P_{\ell}^m(\mu') \right] \cos m(\phi' - \phi), \quad (18.69)$$

CHAPTER 18

where

$$\delta_{0,m} = \begin{cases} 0, & m \neq 0 \\ 1, & m = 0 \end{cases}$$

and the P_l^m are associated Legendre polynomials. Then the radiance is expanded in a cosine series, leading to the following system of equations:

$$\begin{aligned} \mu \frac{dI^m(t, \mu)}{dt} = & -I^m(t, \mu) \\ & + \frac{1}{2} \sum_{\ell=m}^n \omega_\ell^m P_\ell^m(\mu) \int_{-1}^{+1} I^m(t, \mu') P_\ell^m(\mu') d\mu' \\ & + \frac{1}{4} F_0 (2 - \delta_{0,m}) \sum_{\ell=m}^n \omega_\ell^m P_\ell^m(\mu_0) \end{aligned} \quad m = 0, 1, \dots, N, \quad (18.70)$$

where

$$I(t, \mu, \phi) = \sum_{m=0}^n I^m(t, \mu) \cos m(\phi_0 - \phi). \quad (18.71)$$

After suitable manipulations and evaluation of the integral in Equation (18.70) by Gaussian quadrature of order $n(4n > 2N - 1)$, Equation (18.70) is replaced by a system of linear differential equations in terms of $I^{(m)}(t, \mu_i)$, where μ_i ($i = \pm 1, \pm 2, \dots, \pm N$) are the quadrature points. This system of equations can be evaluated quite readily. In principle, as N (and n) $\rightarrow \infty$, the solution becomes exact. Various forms of this approach have been used by Samuelson [1967 and 1969]; Liou [1973]; Shettle and Green [1974]; Stamnes and Swanson [1981]; and Stamnes and Dale [1981].

18.5.1.7 Dodecaton Approach to Radiative Transfer (DART). A different discrete stream approach has been developed by Whitney [1972, 1974], and Whitney and Malchow [1978]. This approach appears to have considerable potential especially for problems requiring consideration of the curved geometry of the earth's atmosphere such as observations of the earth's limb or twilights. This method has several important conceptual differences from the discrete ordinate or two-stream and multichannel methods discussed elsewhere in this section. The DART method achieves discretion by angular integration of the radiance I in a given direction, \hat{r} , with a cosine to the n^{th} power weighting function:

$$S_{\hat{r}} = \int_{\hat{r} \cdot \hat{p} > 0} (\hat{p} \cdot \hat{r})^n I(\hat{r}) d\Omega \quad (18.72)$$

where $\hat{p} \cdot \hat{r}$ is the dot product of the unit vectors \hat{p} and \hat{r} and $S_{\hat{r}}$ is a radiation stream whose nominal propagation

direction is \hat{p} . Application of this integral operator to the radiative transfer equation leads to a system of linear differential equations in terms of the streams, $S_{\hat{p}}$, in the $(n + 1)(n + 2)$ different directions \hat{p} .

For $n = 2$, there are 12 streams that can be arranged to be centered on the faces of a regular dodecahedron. This arrangement minimizes the number of different scattering angles that must be considered. Whitney has used her dodecaton approach in combination with exact single-scattering calculations and has used the shape of the single-scattering results to estimate the multiple-scattered radiances in directions other than for the 12 streams.

Whitney has compared the computation speed of her DART method with the Monte Carlo technique, which is the only other method that has been applied to radiative transfer calculations in realistic spherical atmospheres. She found the DART method to be considerably faster, although it is hard to judge how much faster because of the differences in computers and programming languages and the question of whether more angles and photon histories than necessary were used for the Monte Carlo calculation. In a comparison with other methods such as spherical harmonic or matrix operator for a homogeneous plane-parallel atmosphere [Lenoble, 1977], the DART method appeared to be slower and less accurate.

The primary advantage of the DART method is its applicability to a spherical geometry with reasonable accuracy and computer time. It is not as advantageous for plane parallel geometries or irradiance calculations.

18.5.1.8 Spherical Harmonic Method. The development of the spherical harmonic method goes back half a century [Jeans, 1917 and Eddington, 1926]; however, it has been used more widely for neutron transport problems. In recent years, it has begun to be used more for atmospheric light scattering problems (for example, Devaux and Herman, 1971; Canosa and Penafiel, 1973, Dave, 1975a,b; and Karp et al., 1981). Like the discrete ordinate method, the spherical harmonic method expands the phase function as a sum of associated Legendre polynomial [Equation (18.69)]. However, it differs from the discrete ordinate method in that the radiance is also expanded in a series of spherical harmonics. Equivalently, the Fourier components I^m are expressed as an expansion of Legendre functions:

$$I^m(t, \mu) = \sum_{\ell=0}^n C_\ell^m(t) P_\ell^m(\mu). \quad (18.73)$$

Substituting Equation (18.73) allows the integrals in Equation (18.70) to be evaluated analytically using the orthogonality of the Legendre functions. After additional manipulations of the equations; a linear system of first order differential equations for the $C_\ell^m(t)$ is obtained.

The major advantage of the spherical harmonic method is that it can give the radiances at all depths in the atmosphere and not only those emerging from the atmosphere. Those

timing comparisons made with other methods (the matrix operator method, successive orders of scattering, and Gauss-Seidel iteration) tend to favor the spherical harmonic method [see Lenoble, 1977], especially for cases where the sun is directly overhead and the azimuthal symmetry allows the system of Equation (18.70) to be limited to $m = 0$. The discrete ordinate method should be comparable to the spherical harmonic method in terms of computational efficiencies. The primary disadvantage of these methods is that the computational load increases with the number of terms kept in the expansion of I and P (or the asymmetry of the phase function used); also, the radiance values calculated from the basic solution often have appreciable oscillations about the correct solution unless some smoothing process is used [Dave and Armstrong, 1974 or Karp, 1981].

18.5.1.9 Small-Angle Approximations. When light is scattered by a particle whose dimensions are larger than the wavelength of the incident radiation, it is diffracted in a narrow forward cone. It is this sharp diffraction peak that greatly increases the difficulty of solving the multiple scattering by increasing the number of angles required to evaluate the integral in Equation (18.65). Romanova [1962 and 1963] has developed a procedure in which she separates the radiance for the small-angle scattering \bar{I} from the rest of the radiance:

$$I(t, \mu, \phi) = \bar{I}(t, \mu, \phi) + \bar{I}(t, \mu, \phi) \quad (18.74)$$

and solves for \bar{I} exactly. The rest of the radiation field (\bar{I}) can then be found from a modified form of the transfer equation. Irvine [1968a and b] has made a comparison of Romanova's approach with Neumann series and a doubling procedure and concluded that her method gives radiance accurate to at least 5%.

Weinman [1968] developed an approach in which the diffraction peak of the phase function was represented by a Gaussian distribution and the rest of the phase function by a Legendre expansion. He then solved for the small-angle scattering \bar{I} , using a Neumann solution. It was possible to do the integration analytically because of the use of the Gaussian distributions. The large-angle scattering \bar{I} was then found by applying the discrete coordinate solution.

Potter [1970] approximated the forward peak as a Dirac delta distribution. He then considered this forward-scattered radiation as not being scattered at all but as part of the transmitted radiation and used a truncated phase function. This necessitated a rescaling of the scattering coefficient and correspondingly, the optical depth and the albedo for single scatter, the rescaling depending on the fraction of radiation included in the forward peak that was eliminated. His approach gave quite good results except in the immediate vicinity of the diffraction peak in contrast with Weinman's approach which is most accurate for the diffraction peak.

Wiscombe [1977] discusses the delta M Method which provides a systematic procedure for representing the phase

function as the sum of a Dirac delta-function and a Legendre expansion (with 2M terms). This is a generalization of the approach for the delta-Eddington Approximation [Joseph et al., 1976]. Potter [1970] had basically just truncated the phase function by eye. McKellar and Box [1981] have provided a discussion showing the relationship between these delta-function approximations and the necessary rescaling of the transfer equation, with other scaling laws and similarity relations used in radiative transfer theory.

18.5.1.10 Approximations of Irradiance. Several different methods of calculating radiances within, or emerging from, a scattering atmosphere have been discussed. When interest is mainly in the irradiances F, less accurate solutions of the transfer equation can be used because the errors may cancel out in averaging the radiances over a hemisphere

$$F(t) = \int \int \mu I(t, \mu, \phi) d\phi d\mu \quad (18.75)$$

where $\mu > 0$ corresponds to $F \downarrow$ and $\mu < 0$ to $F \uparrow$. Often it is adequate to have the irradiances computed accurately to a few percent, such as calculating heating rates or the irradiance incident at the ground. Several approximations for irradiances often used are basically simplifications of the closely related discrete ordinate and spherical harmonic methods discussed above. When considering the irradiance, only the first term ($m = 0$) in the cosine expansion of the radiance in Equation (18.71) must be included, since the higher order terms drop out in doing the azimuthal or ϕ integration in Equation (18.75). The most common are the Eddington approximation [Irvine, 1968b; Shettle and Weinman, 1970], various formulations of the "two stream" approximation [Chu and Churchill, 1955; Sagan and Pollack, 1967; Coakley and Chylek, 1975], the delta-Eddington [Joseph et al., 1976], and the delta-two-stream [Schaller, 1979] approximations. These have been discussed and unified in the studies by Meador & Weaver [1980] and by Zdunkowski et al. [1980], [also see Wiscombe & Grams, 1976 and Welch & Zdunkowski, 1982].

They showed that the different Eddington and two-stream approximations all reduce the radiative transfer equation to a pair of coupled differential equations for the upwelling and downwelling irradiances:

$$\frac{dF \downarrow}{dt} = -\gamma_1 F \downarrow + \gamma_2 F \uparrow + \frac{\omega_0}{4} \pi \gamma_3 \exp(-t/\mu_0) F_0 \quad (18.76a)$$

$$\frac{dF \uparrow}{dt} = +\gamma_2 F \downarrow - \gamma_1 F \uparrow + \frac{\omega_0}{4} \pi \gamma_4 \exp(-t/\mu_0) F_0, \quad (18.76b)$$

where the values of the γ_i depend on the choice of approximation used.

CHAPTER 18

18.5.1.11 Approximations for the Radiance. The different approaches to solving the radiative transfer equation described above generally must be solved numerically on a computer and permit tradeoffs between the accuracy of the solution and the computer memory and time. These methods in principle can be made arbitrarily accurate by increasing the number of terms kept in the expansions (such as Equation (18.69) or Equation (18.71)), by decreasing the step size used in numerically evaluating any necessary integrals, or by increasing the number of photon histories following the Monte Carlo Method.

There are also several techniques [Kaufman, 1979; Davies, 1980; and Hering, 1981] developed for solving the transfer equation which are aimed at retaining reasonable accuracy (10% to 20%) for the radiance field while minimizing the computer time requirements. These methods have a commonality in that they all use one of the two-stream/Eddington type solutions for the radiances to allow the integral in Equation (18.65) to be evaluated analytically. They differ in the details of the solution beyond that point; for example, Davies [1980] and Hering [1981] both explicitly include the exact single scattered radiances in their solutions whereas Kaufman [1979] does not.

18.5.2 Background (Sky) Radiance

Atmospheric scattering of solar radiation is responsible for the skylight. For a pure molecular atmosphere, analytic solutions were given by Coulson et al. [1960]. They provide tables of sky radiance and polarization including the Stokes parameters. Since then, much effort has been put into developing capabilities to calculate and model sky radiance for real aerosol containing atmospheres. These attempts were based on the different calculation methods for radiative transfer discussed in the previous section. The intensity, wavelength, and polarization of skylight have been studied over the decades to also derive information on atmospheric aerosols.

For some applications, simplifying assumptions can lead to useful results. As long as only single scattering is important and a homogeneous atmosphere is assumed (aerosol/air mixing ratio constant with height), the angular distribution of skylight at a specific wavelength can be obtained simply from

$$B(M, M', \Psi) = I_0 \left(\frac{M}{M - M'} \right) \left(e^{-tM} - e^{-tM'} \right) \frac{F(\Psi)}{t_s} \quad (18.77)$$

where

I_0 = extraterrestrial solar irradiance ($W \text{ cm}^{-2}$)

B = sky radiance ($W \text{ cm}^{-2} \text{ sr}^{-1}$)

M = secant of the solar zenith angle θ_0

M' = secant of the line of sight angle θ

t = total optical thickness per unit air mass (scattering and absorption by molecules and aerosols)

t_s = scattering optical thickness

$F(\Psi)$ = angular scattering intensity (molecular + aerosol) per unit air mass

The scattering angle Ψ is defined by

$$\cos \Psi = \cos \theta_0 \cos \theta - \sin \theta_0 \sin \theta \cos (\phi - \phi_0)$$

where $\phi - \phi_0$ is the angular azimuth difference between the sun direction and the line of sight. However, if tM or tM' becomes larger than 0.10, higher order scattering can no longer be neglected; this means that illumination of the scattering volume from the sky and the earth's reflecting surface becomes increasingly important. Higher order scattering becomes dominant for tM or $tM' > 0.5$, particularly for high ground albedo. This is particularly true for the radiation leaving the top of the atmosphere (radiation to space). The assumption of a homogeneous (constant mixing-ratio) atmosphere is usually not valid and leads to errors.

The most recent revision of the LOWTRAN transmittance radiance codes, LOWTRAN 6, [Kneizys et al., 1983] contains a subroutine which performs solar (or lunar) single scattering sky radiance calculation for either the atmospheric models built into LOWTRAN or any user provided atmospheric data with nonhomogeneous vertical profiles. Since LOWTRAN also allows a calculation of thermal emitted radiation from atmospheric molecules, the continuity from visible scattered to infrared thermal emitted sky radiance is provided in LOWTRAN for any lookangle, up- or downward. One must always keep in mind that single scattering calculations underestimate sky radiances; for a scattering optical depth of less than 0.7, the ratio of multiple to single radiation is in general less than 1.5. Single scattering is a good approximation for lookangles near the sun.

Procedures for multiple scattering calculations are generally time consuming and complex, especially for cases of strongly anisotropic aerosol scattering. Examples of Monte Carlo calculations for the distribution of the radiance of the hazy atmosphere, seen from both the ground and from space are shown in Figure 18-88 [McClatchey et al., 1972]. Dotted curves of the radiance (per unit solid angle and unit incident solar flux) are for the sun in the zenith and solid lines are for the sun at $\theta = 86.3^\circ$. In Figure 18-88a, the downward or "transmitted" radiance generally increases with decreasing wavelength when the sun is in the zenith. Forward scattering causes the radiance to peak near the sun. Near the horizon, the radiance increases again, except at short wavelengths, and the albedo influence is large. At low solar elevations, downward radiance is generally much smaller especially near the zenith at long wavelengths, and the al-

OPTICAL AND INFRARED PROPERTIES OF THE ATMOSPHERE

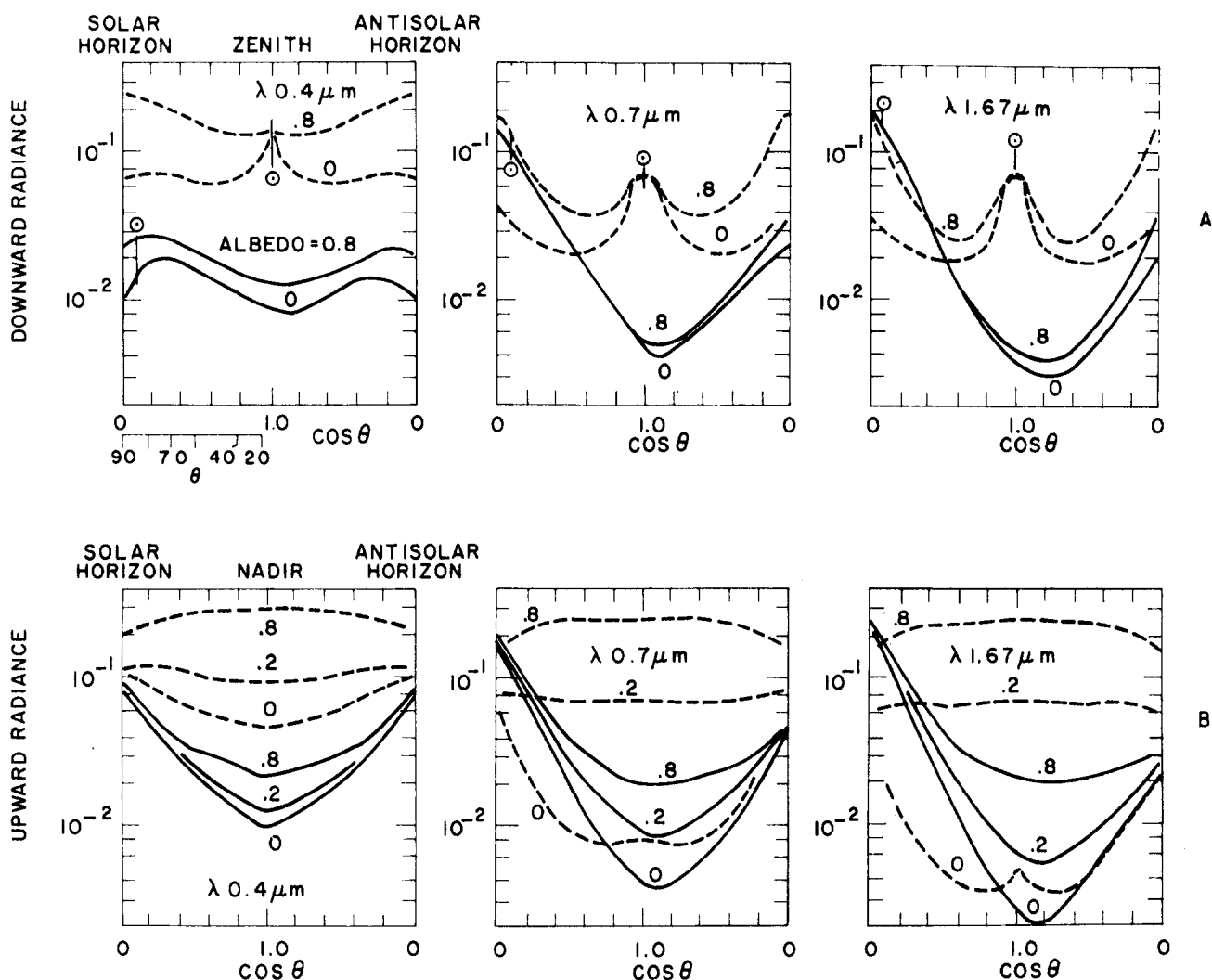


Figure 18-88. Downward (a) and upward (b) radiance computed by Monte Carlo techniques. Solid curves are for the sun at $\theta = 86.3^\circ$. The indicated parameter is the surface albedo and λ is the wavelength. Radiances are per unit solid angle and unit incident solar flux.

bedo influence is significant only at short wavelengths. Since the sky radiance values have been averaged over intervals of 0.1 in $\cos \theta$ (that is, over angular intervals ranging from 5° to 25°), the radiance near the sun actually should be much higher than shown.

In Figure 18-88b upward or reflected radiance, as seen from outside of the atmosphere, is strongly dependent on the albedo of the ground. The contribution of reflected ground radiance becomes dominant, especially in the near infrared and in the nadir direction where the atmospheric backscattered flux becomes small. This effect will be less pronounced in more hazy atmospheres. The distribution of sky radiance in the ultraviolet is dominated by multiple scattering and below $0.35 \mu\text{m}$ by ozone absorption. At high solar elevations, downward as well as upward radiances at $0.30 \mu\text{m}$ are only about 1% of their respective values at $0.40 \mu\text{m}$.

In the case of the radiance from clouds, see Figure 18-89 for a rather dense nimbostratus [Kattawar and Plass,

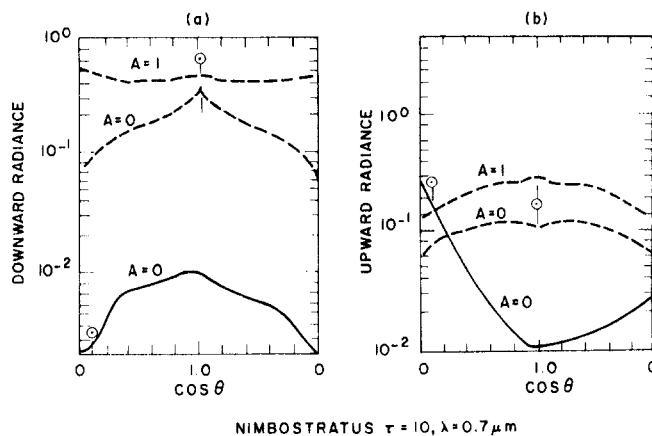


Figure 18-89. Downward (a) and upward (b) radiance computed for a dense Nimbostratus cloud. Dashed curves are for the sun in the zenith. Solid curves are for the sun at $\theta = 86.3^\circ$.

CHAPTER 18

1968]. Aerosol and molecular scattering have been neglected in this model because they would have little effect. The strong downward radiance (Figure 18-89a) for high sun and low albedo is largest near the sun, but with high albedo is nearly independent of the angle of observation. At low sun, the much smaller cloud radiance is largest in the zenith. The radiance of the cloud top (Figure 18-89b) again is very large at high sun. At low sun there is little discrimination between a cloudy and a clear sky (see Figure 18-88b, $\lambda = 0.7 \mu\text{m}$).

Polarization of the cloudless sky is symmetrical to the sun meridian and varies with sun elevation. The degree of polarization [see Equation (18.18)] varies from 0 to as much as 50 to 60% with a maximum around 90° from the sun. Sky light polarization decreases with increasing aerosol content in the atmosphere.

18.5.3 Illuminance-Irradiance

The irradiance at the earth's surface due to direct sunlight, diffuse skylight, moonlight, starlight and airglow varies over approximately nine orders of magnitude (Figure 18-90).

A still frequently referenced publication on natural illumination conditions which provides charts for predicting day and night time illumination levels is a report by Brown [1952]. This report is also included as an appendix in a more easily obtained document by Biberman et al. [1966] on the same subject. Figure 18-91 gives the solar spectral irradiance curves at sea level for various optical air masses. The total solar plus sky irradiance at the surface varies on a clear day between about 0.1 to 1.15 kW/m².

A considerable amount of data on total irradiance over the whole solar spectrum, dependence on time of day, season, and geographic distribution has been accumulated in the literature [for example, Robinson, 1966; Schulze, 1970; SOLMET, 1979].

In addition to astronomical parameters such as sun elevation or moon phase the irradiance at the surface depends largely on the atmospheric scattering properties.

The ratio of diffuse skylight to direct sunlight changes from about 0.6 (at a sun elevation of 10°) to 0.08 (with the sun near the zenith). For a very hazy atmosphere the corresponding ratios would be between 1 and 0.13. Clouds may reduce the total radiance by as much as 90% or more.

During recent years computer programs have been developed at several places to calculate illuminance levels as

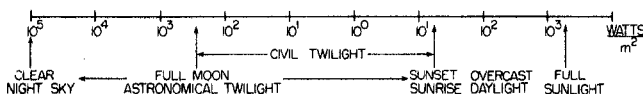


Figure 18-90. Range of natural irradiance levels.

a function of time (day and night) and location. Unfortunately we are not aware of any that have been published. Figures 18-92 and 18-93 are extracted from the report by Brown [1952] and allow an estimate of the natural illuminance levels of the surface during day or night. Figure 18-92 shows the illumination (footcandles) as a function of altitude (or elevation angle) of the sun or moon and Figure 18-93 the relative intensity of moonlight as a function of the phase angle.

It should be pointed out that except for extremely remote regions of the continents night time illumination levels are always more or less affected by illumination from artificial lights, especially with reflection from clouds under overcast conditions.

18.5.4 Contrast Transmittance-Visibility

The "quality" of any image is largely a function of the contrast between different elements in the image scene. Several definitions for contrast exist. One definition frequently used is modulation contrast

$$C_{\text{modulation}} = \frac{\text{Max. Brightness} - \text{Min. Brightness}}{\text{Max. Brightness} + \text{Min. Brightness}} \quad (18.78)$$

The contrast between two elements in the object plane (the inherent contrast) is reduced along the atmospheric path due to scattering and turbulence in the visible and due to absorption and thermal atmospheric emission in the infrared. In a transitional spectral region all processes may be of importance.

The apparent contrast in the image plane is proportional to the inherent object contrast $C_a = C_o \cdot \tau_c$ where τ_c is called contrast transmittance. If the spatial resolution is defined as the minimum separation between two object scene elements that the receiver optical system can resolve, it becomes apparent that spatial resolution is a function of atmospheric contrast reduction.

The contrast transmittance for a target with sinusoidally varying brightness is called the modulation transfer function (MTF). In a turbulent atmosphere (see also Section 18.7), the MTF decreases with increasing spatial frequency of the object scene. For near zero spatial frequencies, turbulence phenomena vanish and contrast loss is due only to atmospheric scattering processes. In this case the apparent radiance of a distant object is the sum of two radiation flux components: residual image forming radiation from the object after propagating through the atmosphere and radiance caused by scattering of ambient light incident on the optical path into the direction of the receiver. This second quantity is called path radiance; it obviously does not contain any information about the object scene. Duntley et al. [1957] has shown that if the contrast is defined as

OPTICAL AND INFRARED PROPERTIES OF THE ATMOSPHERE

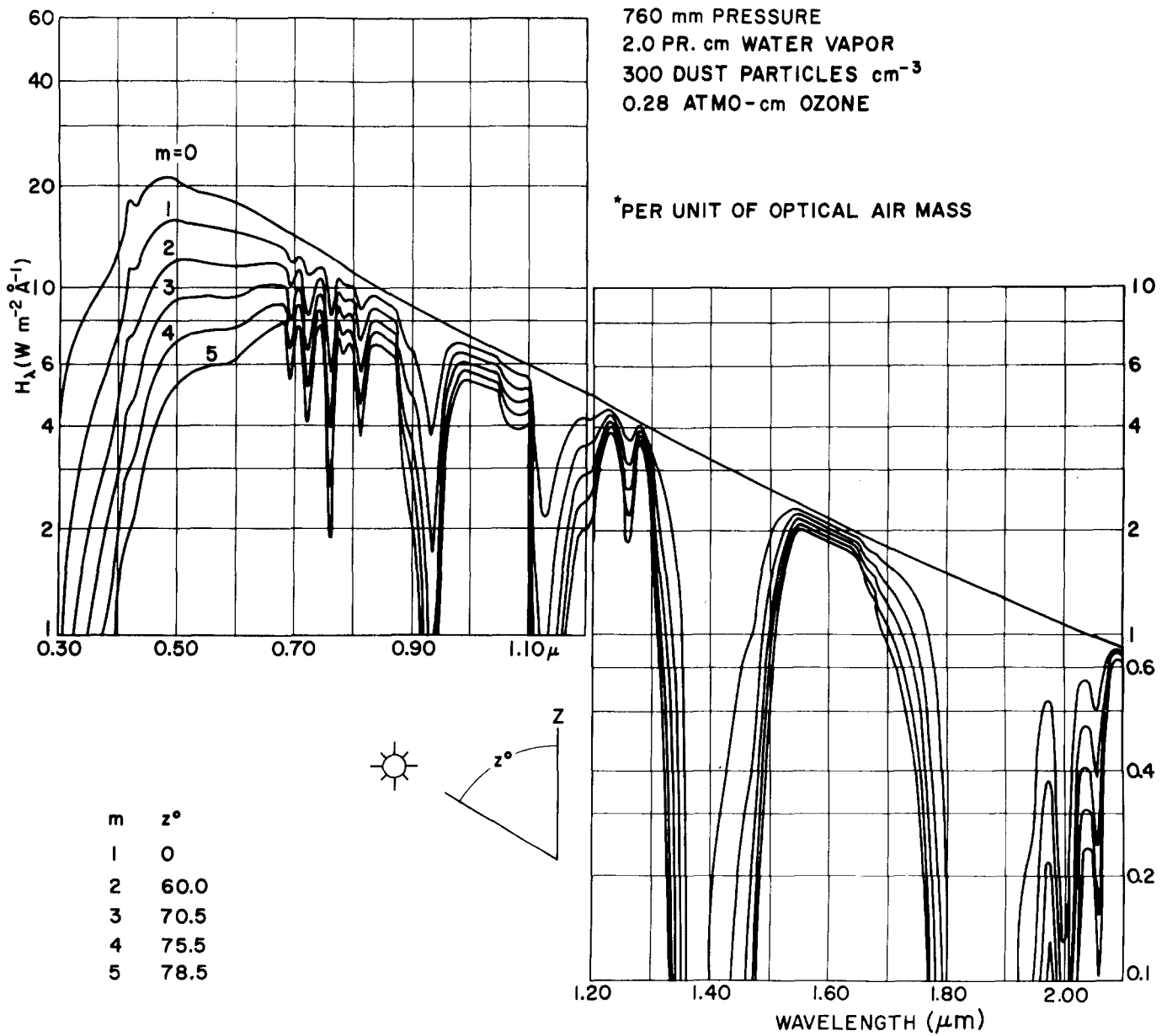


Figure 18-91. Solar spectral irradiance curves at sea level for various optical air masses. The value of the solar constant in this calculation was 1322 W/m² [Moon, 1940].

$$C_{\text{universal}} = \frac{\text{object radiance} - \text{background radiance}}{\text{background radiance}} \quad (18.79)$$

a universal contrast transmittance can be derived as

$$\tau'_{\text{TC, universal}} = \frac{1}{1 + P/(N_{\text{Bo}} \cdot \tau)}$$

where P is the path radiance, N_{Bo} the inherent background radiance, and τ the beam transmittance. The universal con-

trast transmittance is only a function of atmospheric and background properties, not the target.

Whereas the path radiance in the visible spectrum is due to scattered radiation, the physical process for path radiance in the infrared is thermal emitted radiation by each path element. This path emission is a function of the atmospheric composition and its emittance and also of the temperature of the path element. The path emission is related to the absorption by Kirchhoff's law, and it is those gases (and aerosols) that absorb infrared radiation that also emit radiation.

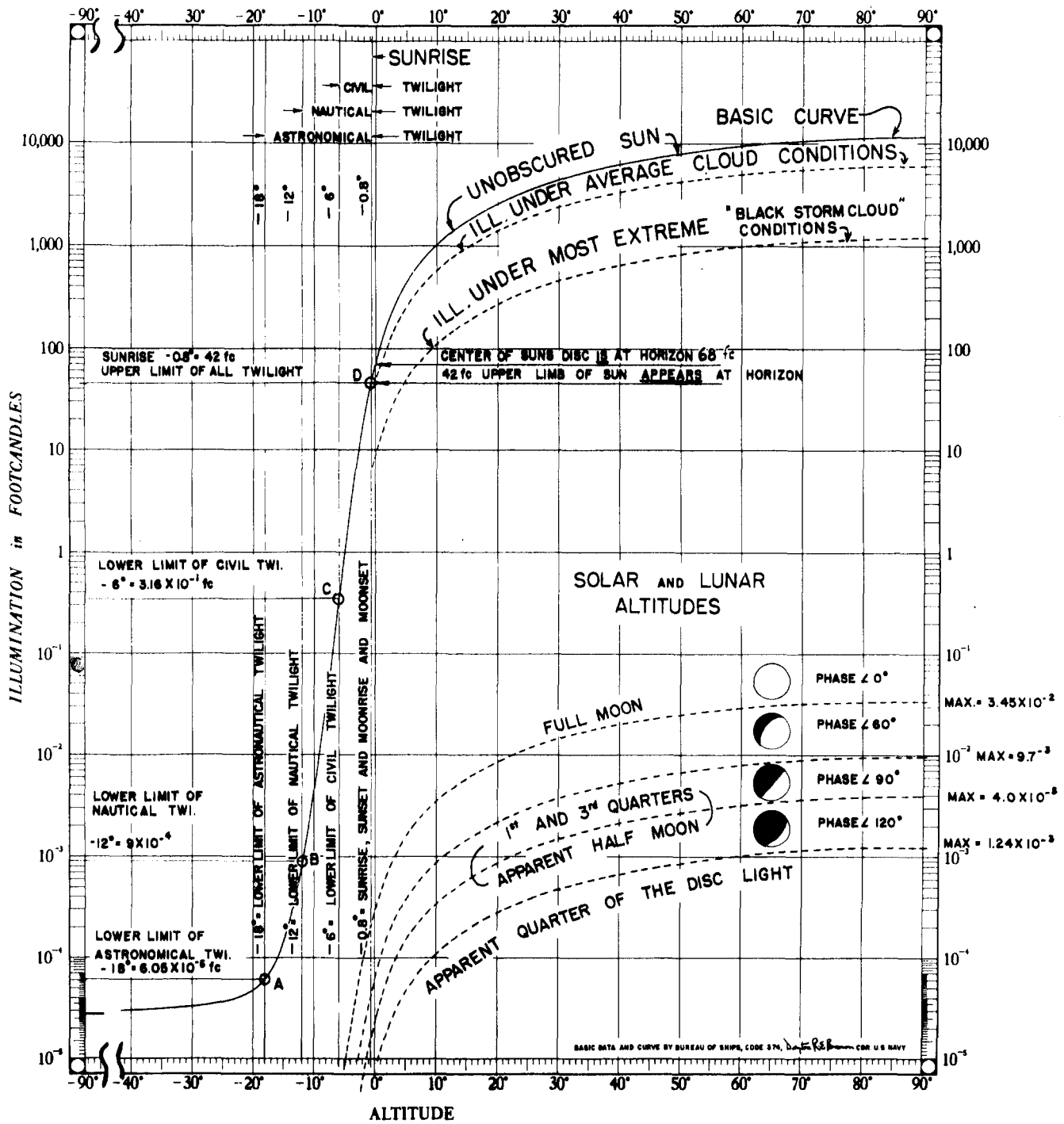


Figure 18-92. Total range of natural illumination levels.

Reduction of scene contrast due to atmospheric scattering varies over several orders of magnitude depending on wavelength, atmospheric turbidity, source-slant path geometry, and ground albedo.

Figure 18-94 gives the universal contrast transmission:

$$\tau_{GC} = \frac{C'_{\text{apparent}}}{C'_{\text{inherent}}} \quad (18.80)$$

for a receiver located on top of the atmosphere looking straight down. The ground albedo, A in Figure 18-94 is 10, 30, and 60% (ground albedo is the ratio of total incident to total reflected radiance from the ground, see Section 18.3). The contrast transmittance is shown for two different atmospheric models, one corresponding to clear conditions with 23 km surface visibility, and one for a hazy atmosphere with 3 km visibility on the ground. The figure shows the

OPTICAL AND INFRARED PROPERTIES OF THE ATMOSPHERE

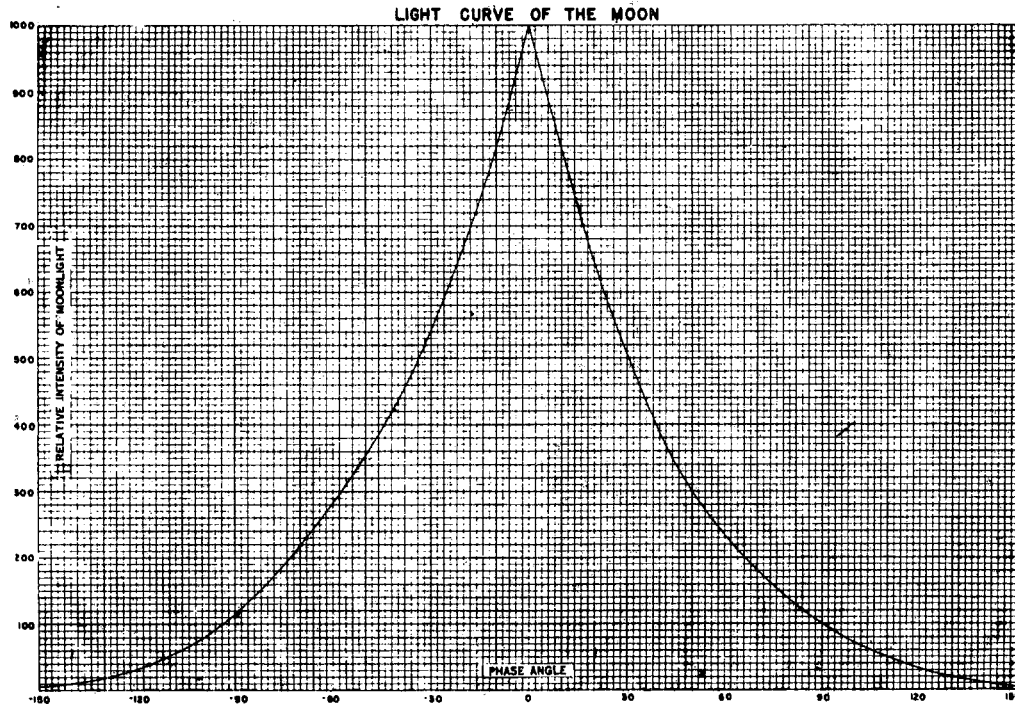


Figure 18-93. Relative intensity of the moon's illumination as a function of phase angle.

dependence of τ'_c on wavelength, sun zenith angle, and albedo. The results of these model calculations illustrate the range of contrast transmittance values that, for instance, will have to be considered in the interpretation of imagery from a satellite platform.

Figure 18-95 shows the effect of different types of aerosols on contrast transmission. In this figure the ratio of contrast transmittance for an urban versus a rural aerosol (see Section 18.2.1.4) is shown under identical visibility of

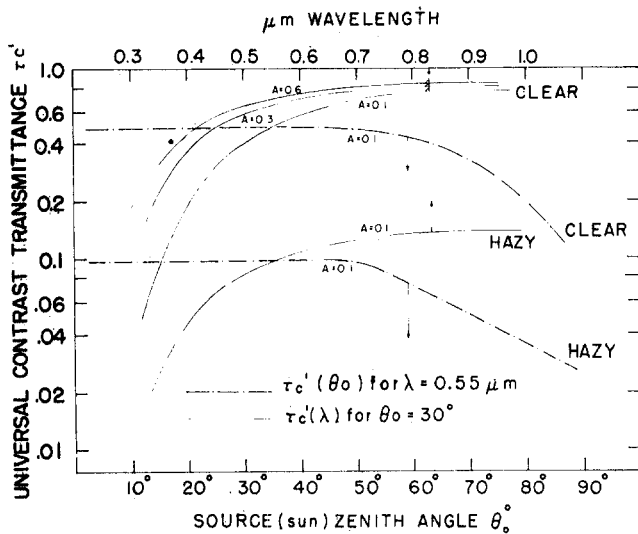


Figure 18-94. Contrast transmittance for a downward looking vertical path through the whole atmosphere.

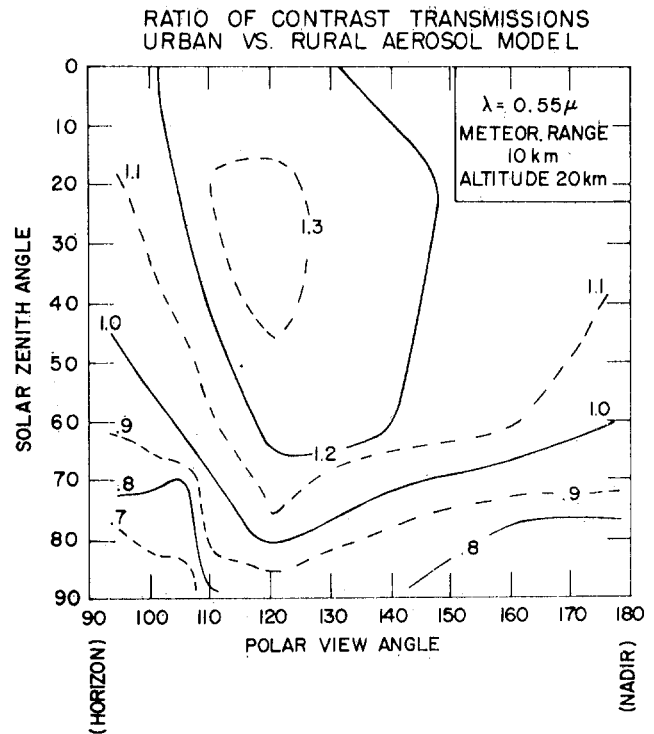


Figure 18-95. Ratio of contrast transmittance τ_c , urban/ τ_c , rural for an urban vs rural aerosol model over downward looking paths. The wavelength is $0.55 \mu\text{m}$, the surface meteorological range is 10 km, sensor altitude is 20 km.

CHAPTER 18

10 km for various sun and look angles. The difference in contrast transmittance is due to the different scattering properties of the two aerosol models:

The theoretical determination of contrast transmittance involves, in the term of the path radiance [Equation (18.79)], the treatment of multiple scattering. Several of the radiation transfer computational methods described in Section 18.5.1 have been used for path radiance and contrast transmittance modeling. The examples given in Figures 18-94 and 18-95 above have been obtained from Monte Carlo calculations.

Figures 18-96 and 18-97 show an example of contrast transmittance and derived target acquisition ranges that were obtained by applying the delta-Eddington method [Hering, 1981] mentioned earlier.

A special case of viewing an object through the atmosphere is the viewing of objects along a horizontal path against the horizon sky. This case is described by the often quoted (but frequently misunderstood) Koschmieder theory

[Middleton, 1952]. It states that the brightness of a black object B_b at distance r is given by

$$B_b = B_h (1 - e^{-\sigma r}) \quad (18.81)$$

where B_h is the horizon sky brightness and σ = extinction coefficient. If one assumes that (based on tests) the contrast threshold necessary to see the object against the background $(B_b - B_h)/B_h$ is 0.02, the limiting visible distance, called meteorological visible range becomes

$$V = \frac{3.912}{\sigma} \quad (18.82)$$

It must be pointed out that this relationship is based on the assumption of a black (dark) object of an angular extent larger than a few minutes of arc. Table 18-13 gives [Hulburt,

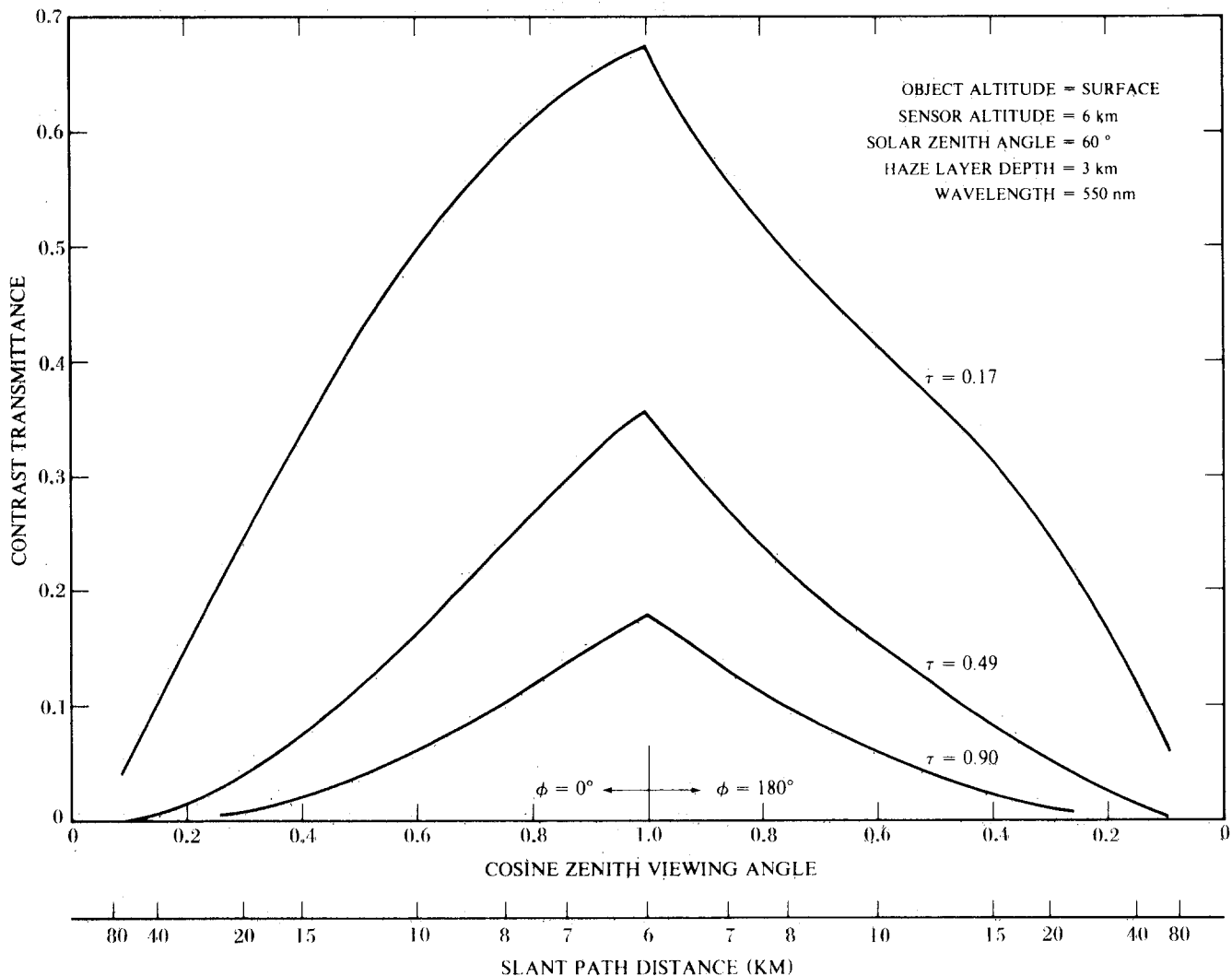


Figure 18-96. Calculations of contrast transmittance as a function of zenith viewing angle for a target viewed against a terrain background. Values of τ are total atmosphere optical depth.

OPTICAL AND INFRARED PROPERTIES OF THE ATMOSPHERE

SENSOR ALTITUDE = 6 km OBJECT ALTITUDE = SURFACE HAZE LAYER DEPTH = 3 km AZIMUTH VIEW ANGLE = SUN + 180° WAVELENGTH = 550 nm

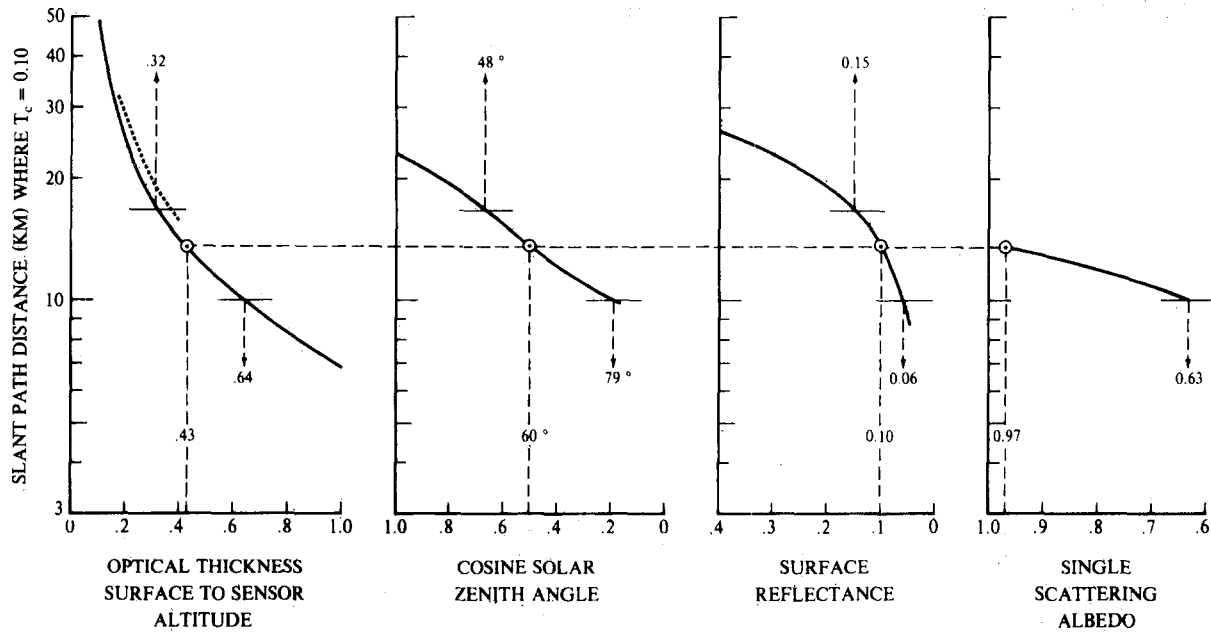


Figure 18-97. Variations in target acquisition range (contrast transmittance $T_c = 0.10$) associated with departures of selected parameters from the assumed reference values. The horizontal dashed line denotes parameter values for this reference atmosphere. The horizontal bars identify a change of $\pm 25\%$ from the slant path distance where $T_c = 0.10$ for the reference atmosphere, for example, 15.5 ± 3.4 km.

1941 or McCartney, 1976] the international visibility code and corresponding weather condition, meteorological range, and scattering coefficients. Since visibility marks are generally not black and often their angular extent is small, a threshold contrast of 0.05 gives usually a better definition for the meteorological range. Table 18-13 contains both the 0.02 and 0.05 contrast threshold scattering coefficients. In going from a measured scattering to an expected observed visibility, the assumption of an 0.02 contrast threshold gives a 30% higher visibility than 0.05. The values for pure air are based on molecular scattering only, for air at standard conditions, and for a spectrally weighted average wavelength for daylight.

18.6 ATMOSPHERIC REFRACTION

Changes in molecular density and the resulting gradient in the index of refraction cause the bending of a light ray traveling through the atmosphere. Over long paths at sunset, refraction causes such phenomena as the flattening of the solar disc and the "green flash." Strong temperature gradients over short paths are responsible for such effects as mirages and looming. Microscale and time dependent variations of the index of refraction cause optical turbulence and scintillation—the twinkling of stars. This section will consider only the large scale effects of refraction.

18.6.1 Refractive Bending

In a spherically symmetric atmosphere, a light ray follows the path defined by the equation

$$m(r) \times r \times \sin \theta = C \quad (18.83)$$

where m is the atmospheric refractive index (Section 18.1.3), r is the radius vector from the center of the earth, θ is the angle formed by the ray and the local zenith, and C is a constant. The radius of curvature R of a light ray is given by

$$\frac{1}{R} = -\frac{1}{m} \frac{dm}{dr} \sin 2\theta. \quad (18.84)$$

The refractive modulus N (see Equation 18.7, Section 18.1.3) is very nearly proportional to the total air density so that it can be approximated, at least over a limited vertical range, by an exponential of the form

$$N(r) = N_0 e^{-(r-r_0)/H} \quad (18.85)$$

where N_0 is the value of N at some reference radius r_0 , and H is the scale height for N . In this case

$$\frac{1}{R} = \sin \theta \left[H \left(\frac{1}{N_0} e^{+(r-r_0)/H} + 1 \right) \right]^{-1} \quad (18.86)$$

CHAPTER 18

Table 18-13. International visibility code, meteorological range, and scattering coefficient.

Code No.	Weather condition	Meteorological Range, R_m		Scattering Coefficient σ (km^{-1})	
		Metric	English	for 0.05 contrast	for 0.02 contrast
0	Dense fog	< 50 m	< 55 yd	> 59.9	> 78.2
1	Thick fog	50–200 m	55–219 yd	59.9–15.0	78.2–19.6
2	Moderate fog	200–500 m	219–547 yd	15.0–5.99	19.6–7.82
3	Light fog	500–1000 m	547–1095 yd	5.99–3.00	7.82–3.91
4	Thin fog	1–2 km	1095 yd–1.1 naut. mile	3.00–1.50	3.91–1.96
5	Haze	2–4 km	1.1–2.2 naut. mile	1.50–0.749	1.96–0.954
6	Light Haze	4–10 km	2.2–5.4 naut. mile	0.749–0.300	0.954–0.391
7	Clear	10–20 km	5.4–11 naut. mile	3.00–0.150	3.91–0.196
8	Very Clear	20–50 km	11–27 naut. mile	0.150–0.060	0.196–0.078
9	Exceptionally clear	> 50 km	727 naut. mile	< 0.060	< 0.078
—	Pure air	277 km	149 naut. mile	—	0.0141

In a typical case from the *U.S. Standard Atmosphere 1976* for a horizontal path at the ground ($\theta = 90^\circ$), the ratio of the radius of the earth r_E to R is 0.16 at $5 \mu\text{m}$.

Since the total air density normally decreases with altitude, light rays are normally bent toward the earth. However, density inversions can occur in the atmosphere, typically as a thin layer above a strongly heated surface such as the desert or a road surface. In such cases, light is bent upwards.

The bending ψ of a ray is shown in Figure 18-98, where θ and ϕ are the zenith angles of the ray at r_1 and r_2 and β is the earth centered angle, and

$$\psi = \pi + \beta - \theta - \phi \quad (18.87)$$

The bending along a path can be calculated by integrating one of the following equations:

$$\begin{aligned} \frac{d\psi}{dr} &= \frac{1}{R} \tan \theta \\ \frac{d\psi}{d\beta} &= \frac{r}{R} \\ \frac{d\psi}{dS} &= \frac{\sin \theta}{R} \end{aligned} \quad (18.88)$$

where S is the distance along the curved path from some point.

The total bending for various paths through the atmosphere is shown in Figures 18-99a,b and 18-100. Figure

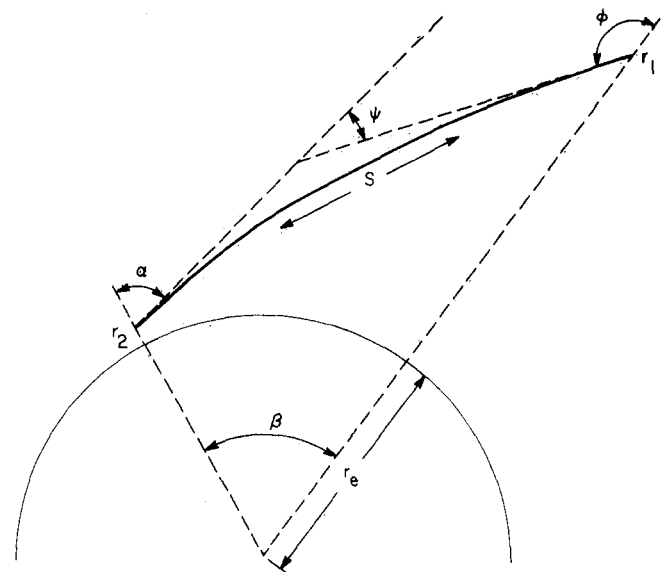


Figure 18-98. Geometry of the refracted path through a single layer.

OPTICAL AND INFRARED PROPERTIES OF THE ATMOSPHERE

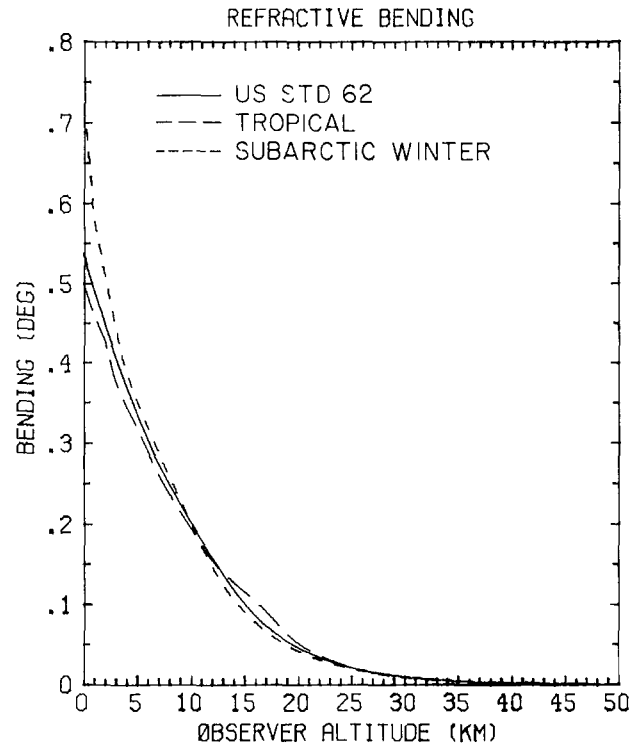
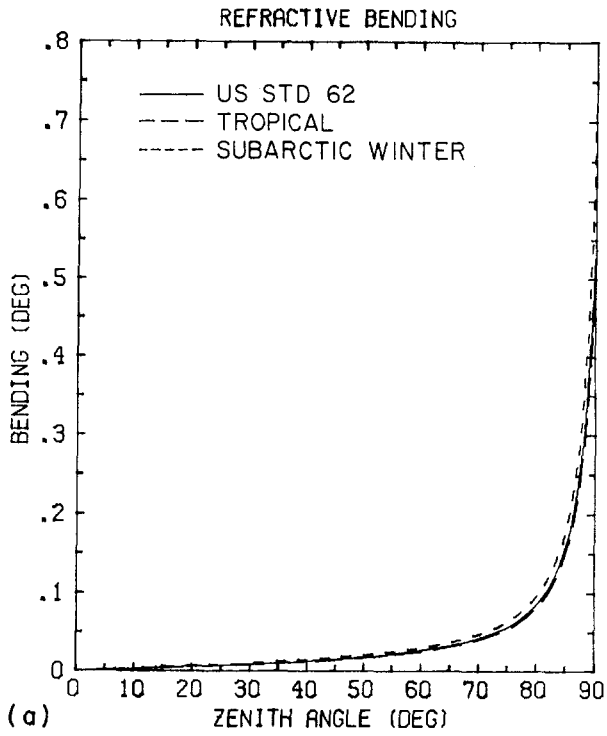


Figure 18-100. Refractive bending vs observed altitude for three atmospheric profiles for path from space to observed altitude tangent height.

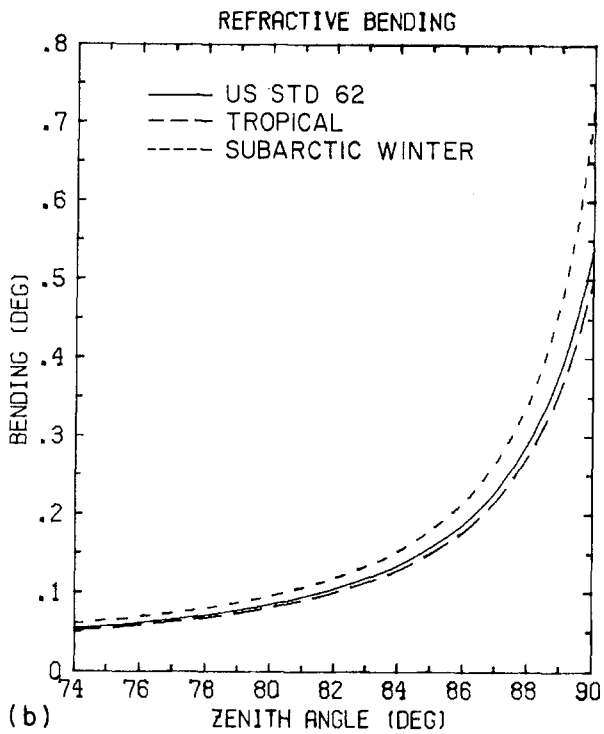


Figure 18-99. Refractive bending vs zenith angle for three atmospheric profiles for a path from 0 to 100 km altitude for zenith angles. (a) 0° - 90° , (b) 74° - 90° .

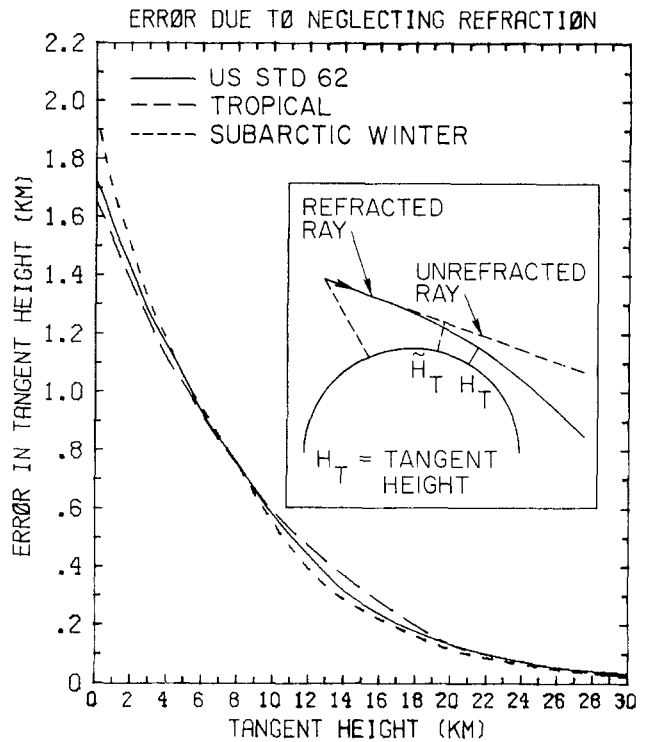


Figure 18-101. Error in predicted tangent height defined as tangent height minus refracted tangent height vs. refracted tangent height for three atmospheric profiles.

CHAPTER 18

18-99a,b shows the bending or zenith angle at the ground for a path from ground to space, for three different atmospheric profiles. The three profiles are the U.S. Standard 1976, the Tropical (15°N), and Subarctic Winter (60°N Jan) profiles [McClatchey et al., 1972]. Figure 18-100 shows the bending for a path looking out horizontally to space from the observer altitude.

Figure 18-101 shows the difference between the refracted tangent height and the unrefracted tangent height versus the refracted tangent height for a ray coming in from infinity. This path corresponds to, for instance, a satellite instrument scanning the earth limb.

18.6.2 Optical Air Mass

Calculations of the absorption and emission of electromagnetic radiation in the atmosphere require knowledge of the amount of the absorbing gases along the path. Examples of such situations are the absorption of solar radiation along a path to the ground and the emission of infrared radiation along a tangent path through the atmosphere.

The quantity of interest is the integrated absorber amount μ along the path, given by

$$\mu = \int \rho ds \quad (18.89)$$

where ρ is the density of the absorbing gas and ds is the element of length along the path. μ is also known as the "column density" and has units of molecules cm^{-2} if ρ is the number density. The value of μ for air for a vertical path from ground (1013.25 mb) to space is μ_0 [molecules cm^{-2}]. The ratio of μ for air for a given path to μ_0 is known as the "air mass;" for example, the air mass value for a path from ground to space where the zenith angle at the ground is 90° is 38.1.

For a spherically symmetric atmosphere and for paths where the zenith angle is less than about 70°, the absorber amount can be calculated to better than 1% using the plane parallel approximation, that is:

$$\mu = \int \rho ds \approx \sec \theta \int \rho dz \quad (18.90)$$

where θ is the zenith angle along the path and z is the vertical coordinate. For a gas whose density follows an exponential profile

$$\rho(z) = \rho(z_1)e^{-(z-z_1)/H}, \quad (18.91)$$

the vertical integral of the density has a particularly simple form

$$\int_1^2 \rho dz = H[\rho(z_1) - \rho(z_2)] \quad (18.92)$$

where the scale height H is

$$H = -\frac{z_2 - z_1}{\ln[\rho(z_2)/\rho(z_1)]} \quad (18.93)$$

The total air density and the density of uniformly mixed gases are well represented by profiles of the form of Equation (18.91) especially over altitude ranges of less than a scale height (the density scale height under normal atmospheric conditions varies between 6 and 9 km).

For zenith angles greater than 70°, the effects of the earth's curvature and of refraction become significant. In this case, plane parallel approximation is no longer valid and a more elaborate integration of Equation (18.92) is necessary. In a case where the density profile is exponential but refraction can be neglected, the absorber amount can be calculated using the "Chapman functions." Non-exponential profiles and cases where refraction is important generally require a numerical integration of Equation (18.92). A computer program for calculating absorber amounts for any profile and an arbitrary path is available.

There are a number of tables of air mass for various geometries and profiles [Chapman, 1931; Smith and Smith, 1972; Gallery et al., 1983; Bemporad, 1968; Kasten, 1966 and 1967; Sneider and Goldman, 1974; Sneider, 1975]. Table 18-14 gives the air mass for selected zenith angles for a path from the ground (1013.25 mb) to space, including the effects of refraction. The profile used is the *U.S. Standard Atmosphere 1976*, and the values are accurate to within 1% for wavelengths from 0.5 micrometers to the far infrared. Table 18-15 gives the air mass for various tangent heights for a path from space to space through the tangent height.

Air mass values for paths with large zenith angles cannot in general be applied to non-uniformly mixed gases, such as water vapor and ozone. This fact is shown in Figures

Table 18-14. Air mass versus zenith angle for a path from ground (1013.25 mb) to space, *U.S. Standard Atmosphere, 1976*, 0.23 μm to the far infrared.

Zenith Angle (Deg)	Air Mass	Zenith Angle (Deg)	Air Mass
70.0	2.90	88.0	19.4
72.0	3.21	88.2	20.5
74.0	3.58	88.4	21.8
76.0	4.07	88.6	23.1
78.0	4.71	88.8	24.6
80.0	5.58	89.0	26.2
82.0	6.87	89.2	28.1
84.0	8.85	89.4	30.2
85.0	10.3	89.6	32.5
86.0	12.3	89.8	35.1
87.0	15.2	90.0	38.1
87.5	17.1		

(For zenith angles less than 70°, the secant approximation is good to better than 1%.)

OPTICAL AND INFRARED PROPERTIES OF THE ATMOSPHERE

Table 18-15. Air mass versus tangent height (H_T) for a path from space to space through the tangent height, *U.S. Standard Atmosphere, 1976*, 0.23 μm to the far infrared.

H_T	Air Mass	H_T	Air Mass	H_T	Air Mass
0.0	76.2	10.0	21.4	30.0	0.920
1.0	67.9	12.0	17.7	35.0	0.43
2.0	60.4	14.0	11.4	40.0	0.208
3.0	53.6	16.0	8.28	45.0	0.107
4.0	47.5	18.0	6.01	50.0	0.0563
5.0	41.9	20.0	4.38		
6.0	36.9	22.0	3.18		
7.0	32.4	24.0	2.32		
8.0	28.6	26.0	1.70		
9.0	25.4	28.0	1.25		

18-102a,b which show the "air mass" value for air, water vapor, and ozone versus zenith angle for a path from ground to space. The "air mass" values for water vapor and ozone are the ratio of the absorber amount for the given zenith angle to the absorber amount for a vertical path for the same profile. The temperature profile used is the *U.S. Standard Atmosphere 1976* while the profiles of water vapor and ozone used are shown in Figure 18-103. At 90° , the "air mass" value for water vapor is 72.2 and for ozone 14.4 compared to 38.1 for air. For the profiles of water vapor and ozone, the absorber amounts can be computed to better than 1% using the secant approximation up to 80° for water vapor and 60° for ozone (compared to 72° for air or a

uniformly mixed gas). These numbers depend upon the profile used and should be taken as guidelines only.

Figure 18-104 shows the air mass value versus tangent height for the three components for a path from the tangent height to space. These curves are similar in shape to the density profiles of the components themselves, since the bulk of the integrated amount is within a few kilometers (vertically) of the tangent height.

Figure 18-105 shows the air mass versus zenith angle for a typical stratospheric balloon-borne spectroscopic measurement: the observer is at 30 km scanning between a zenith angle of 85° to 95.5° at which point the path intersects the earth. (The zenith angle is the apparent or measured zenith angle, not the astronomical zenith angle.) Also shown are the tangent height versus zenith angle and the angular diameter of the sun. If the sun is used as the source for an observation, the absorber amounts to different points on the face of the sun may differ by a factor of 2 for air and an order of magnitude for water vapor. The variation in air mass due to this effect can be the major source of uncertainty in a measurement and must be considered carefully.

18.7 ATMOSPHERIC OPTICAL TURBULENCE

Astronomers have long known that atmospheric turbulence can cause optical propagation effects. The famous "twinkling" of stars is due to such turbulence. When turbulence is at a minimum, astronomers can photograph planets,

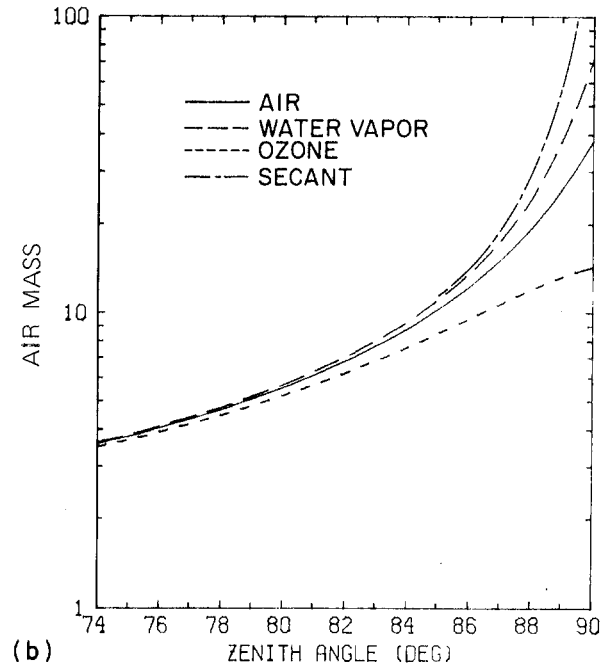
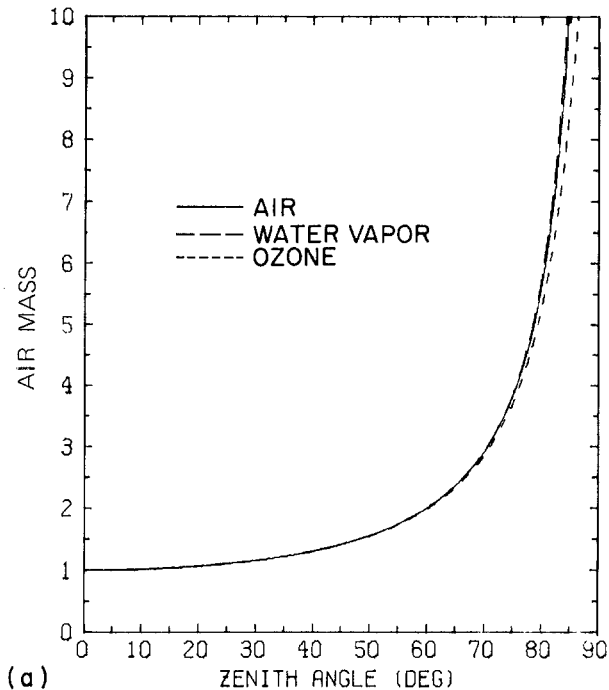


Figure 18-102. Air mass vs zenith angle for a path from 0 to 100 km altitude, *U.S. Standard Atmosphere, 1962*, including refraction (a) 0° - 90° ; (b) 74° - 90° .

CHAPTER 18

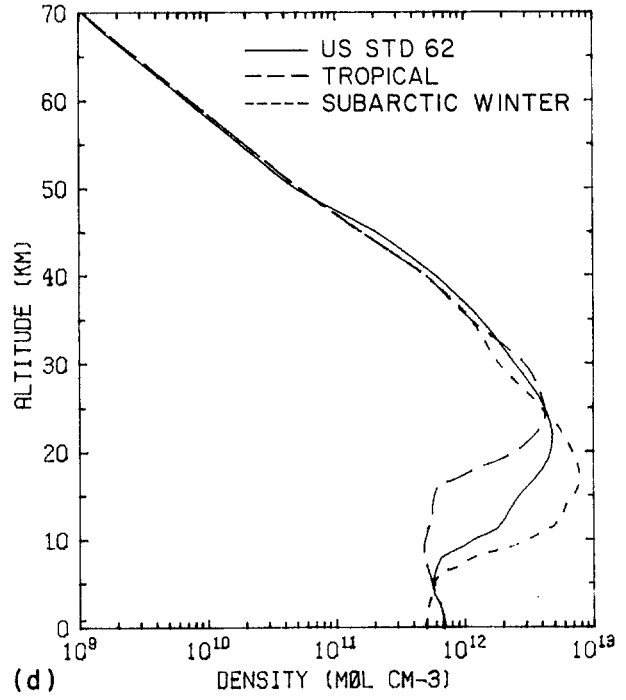
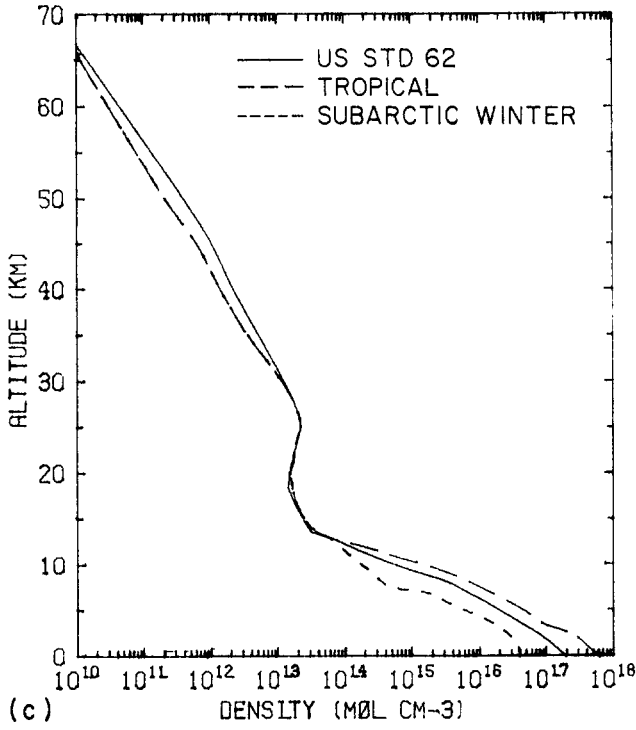


Figure 18-103. a) Water vapor profile of the U.S. Standard model, 1962. b) Ozone profile of the U.S. Standard model, 1962.

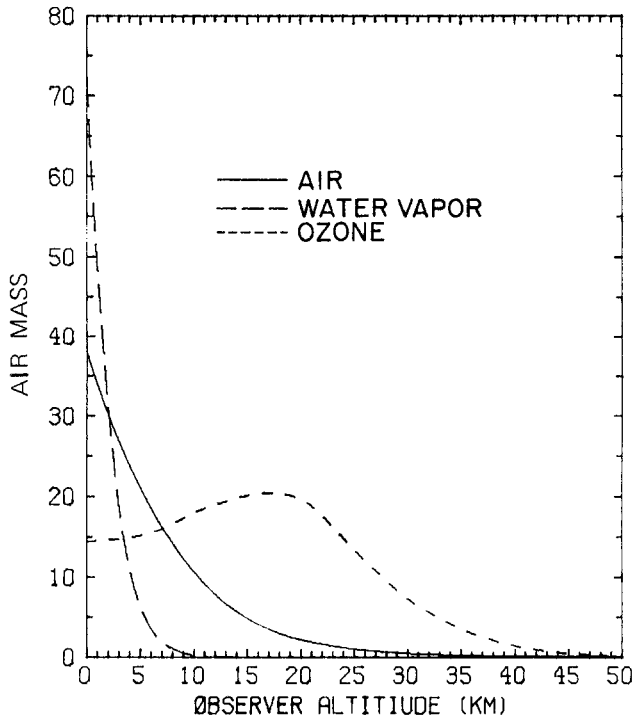


Figure 18-104. Air mass vs observer altitude for a path from 100 km to the observer, zenith angle 90°, U.S. Standard Atmosphere, 1962, including refraction.

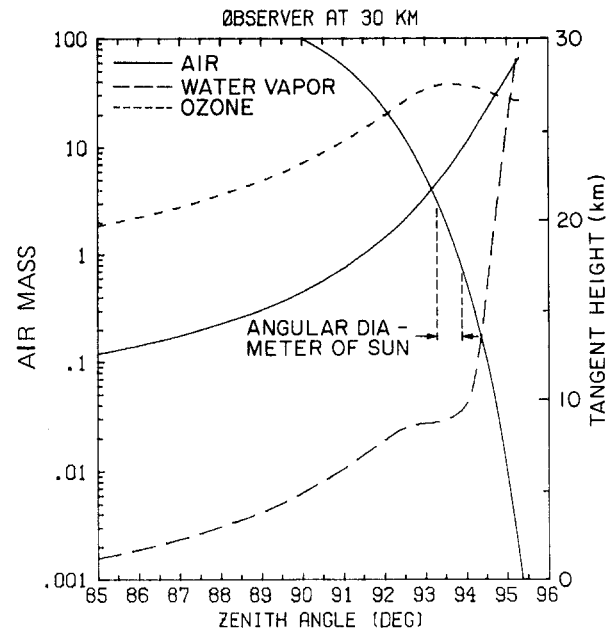


Figure 18-105. Air mass vs zenith angle for a path from 30 to 100 km altitude, U.S. Standard Atmosphere, 1962, including refraction. Also shown are the tangent height versus zenith angle and the angular diameter of the sun.

etc., with a minimum of blur because with less turbulence there is less so-called "image dancing." Brightness fluctuations, or scintillations, also diminish when there is low turbulence. In general, such conditions are called "good seeing conditions." The basic cause of the optical effects is the presence of fluctuations in the index of refraction along the optical path.

A number of excellent reviews exist describing the turbulence effects on optical propagation [Pratt, 1969; Lawrence and Strohbehn, 1970; Hufnagel, 1978; Dewan, 1980]. The following is a brief description of commonly known turbulence effects.

Beam steering: The laser beam can be deviated from the line of sight so that part or all of it will miss the receiving aperture. This is most likely for the case where the turbulence occurs close to the source, as when the receiver is in space and the transmitter is on the ground (partly because a deviated beam will drift farther from the target in proportion to its subsequent distance of travel). Beam steering effects arise when the size of the atmospheric inhomogeneities are larger than the width of the beam.

Image dancing: The atmosphere can cause a modulation of the angle of arrival of the beam's wavefront. This will cause the image of a source in the receiver to be focused at different places in the focal plane. In a photographic image this would cause blurring. Image dancing effects can be reduced by increasing the receiver's aperture.

Beam spreading: Numerous inhomogeneities distributed across the beam cross section cause many small angle scattering events to occur. This has the effect of spreading the beam energy over a wider cross section reducing the signal intensity at the receiver and, in consequence, introducing a decrease in the signal-to-noise ratio. Beam spreading occurs if the beam width is significantly larger than the eddies; beam spreading occurs, therefore, for the downlink of an earth-space laser system (receiver on the ground and transmitter in space or high altitude aircraft).

Spatial coherence degradation: Inhomogeneities in the beam's path also cause losses of phase coherence across the wavefront of the beam. This rapid change of phase with respect to the radial position within the beam cross section reduces the beam's coherence properties.

Scintillation: Within the beam cross-section interference effects can cause destructive and constructive interaction. This causes the power to vary widely from point to point within the cross section, spatially and temporally. Scintillation or amplitude variation effects can be explained by regarding the eddies, or index of refraction variations, as a random distribution of weak lenses distributed within a spatial volume. This volume is to be envisioned as being convected across the beam and thus causing effects that vary with time.

Additional turbulence effects are in transmission, anisoplanatism, thermal blooming, and information band width [Greenwood, 1977], to name a few.

18.7.1 Amplitude Fluctuations (Scintillation)

Derivations of the equations given below will be found in the references cited. Tatarski [1961] has shown that the mean square fluctuations of the logarithm of the plane wave amplitude A are related to a quantity C_n^2 ,

$$\left\langle \left[\ln \left(\frac{A}{A_0} \right) \right]^2 \right\rangle = 0.56 k^{7/6} \int_0^L C_n^2(r) x^{5/6} dx \quad (18.94)$$

C_n^2 is a measure of the strength of the atmospheric turbulence [see for example Hufnagel, 1978]. A_0 in Equation (18.94) is the mean amplitude, k is the wave number of the radiation and x is the distance along the path of the beam. L is the total length of the beam path and r is the position vector. It is assumed that $\ell_1 \ll \sqrt{\lambda L} \ll \ell_0$, that is, that the quantity $\sqrt{\lambda L}$ which is known as the size of the first "Fresnel zone," falls into the size range of inertial range eddies (ℓ_1 and ℓ_0 are the "inner" and "outer" lengths respectively).

It is important to notice that these scintillation effects depend on where they occur along the optical path. This is indicated by the term $x^{5/6}$ in Equation (18.94) under the integral sign where x is the distance from the receiver.

For short path lengths where $\sqrt{\lambda L} \ll \ell_1$ (that is, the Fresnel zone is much smaller than the inner scale), Tatarski [1961] has shown that

$$\left\langle \left[\ln \left(\frac{A}{A_0} \right) \right]^2 \right\rangle = 7.37 \ell_1^{-7/3} \int_0^L C_n^2(r) x^2 dx \quad (18.95)$$

In the simple case where C_n^2 is constant along the path, as it might be for the case of surface to surface propagation, Equation (18.94) becomes

$$\left\langle \left[\ln \left(\frac{A}{A_0} \right) \right]^2 \right\rangle = 0.31 C_n^2 k^{7/6} L^{11/6} \quad (18.96)$$

One of the important parameters in the design of optical receivers is the parameter r_0 [Pratt, 1969 and Fried, 1967] the transverse coherence length. Physically r_0 is the distance such that, if a receiver diameter is increased beyond r_0 , there is significantly less improvement in turbulence degradation. As the turbulence degrades the phase coherence of the radiation, r_0 is reduced. As C_n^2 becomes larger, r_0 becomes smaller. The transverse coherence length is [Fried, 1966]

$$r_0 = 2.1 \left[1.46 k^2 \int_0^L C_n^2(x) dx \right]^{-3/5} \quad (18.97)$$

The isoplanatic angle, that is, the angle over which the optical transfer function is constant, represents a radial coherence scale [Fried, 1979]

CHAPTER 18

$$\theta_o = \left[2.91 k^2 \int_0 C_n^2 x^{5/3} dx \right]^{-3/5} \quad (18.98)$$

The angle θ_o can be considered as the outer limit of an isoplanatic patch of turbulence.

Measurements of C_n^2 can be inferred from path measurements of amplitude fluctuations or transverse coherence length. These approaches require assumption of a uniform distribution of C_n^2 along the path. Point measurements of C_n^2 are possible using an alternative parameter, C_T^2 , which is the mean-square statistical average of the difference in temperature between two points separated by a distance r ,

$$C_T^2 = \langle (T_1 - T_2)^2 \rangle r^{2/3} \quad (18.99)$$

where the angle brackets denote an ensemble average. C_n^2 is related to C_T^2 through the partial derivative of the air density with respect to the temperature,

$$C_n^2 = (79 \times 10^{-6} P/T^2)^2 C_T^2 \quad (18.100)$$

P (mb), T(K)

Expressions defining C_T^2 in terms of atmospheric parameters have been developed by Tatarski [1961] and Hufnagel [1974, Hufnagel and Stanley, 1964].

Experimental data on C_n^2 is limited to few locations (mostly astronomical observatories). Near ground level C_n^2 is found to be dependent upon many local variables. Figure 18-106 represents the variation of C_n^2 at a height of 2 m above the ground on top of a flat mesa in Boulder, Colorado [Lawrence et al., 1970]. Daytime C_n^2 values near ground level can range from $10^{-16} m^{-2/3}$ to $10^{-12} m^{-2/3}$. Order-of-magnitude changes can occur in minutes.

Models of C_T^2 in the atmospheric boundary layer have been developed for stable and unstable conditions. Wyngaard et al. [1971] predicts a power law dependence of C_T^2 with height as

Height dependence	Conditions
$C_T^2 \propto Z^{-4/3}$	local free convection
$C_T^2 \propto Z^{-2/3}$	neutral stability
constant	strongly stable

Actual measurements show some departure from these ideal conditions. Measurements in the New Mexico desert

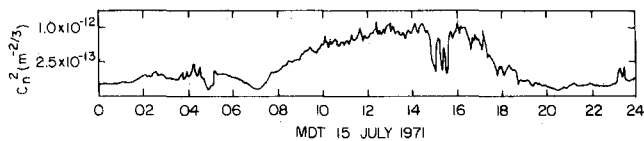


Figure 18-106. Typical diurnal variation of the strength of refractive-index turbulence near the ground. The daytime peak results from heating of the ground; the dips at 15 hours are caused by clouds passing in front of the sun.

and mountains indicate minimum C_n^2 values occur shortly after sunrise and before sunset when there is no temperature difference between the ground and atmosphere. For noon conditions, dominated by a convective boundary layer [Walters and Kunkel, 1981]

$$C_n^2 = (7.7 \div 1.2) \frac{\times}{Z} \times 10^{-13} \left(\frac{Z}{Z_o} \right)^{-(1.16 \pm 0.03)} \text{ for } Z < 1000 \text{ m} \quad (18.101)$$

(where $Z_o = 1\text{m}$). At midnight,

$$C_n^2 = (3.2 \div 1.1) \frac{\times}{\times 10^{-16} e^{-(0.001 \pm 0.00008)Z}} \quad (18.102)$$

The C_n^2 data generally have a log normal probability distribution as illustrated by the scintillometer observations at 9.4 km shown in Figure 18-106.

Altitude profiles of C_n^2 obtained by performing log averages are shown in Figure 18-107. The Loos and Hogge [1979] data are from White Sands Missile Range, New Mexico; Miller and Zieski [1978] data are obtained at Mt. Haleakala, Maui, Hawaii, and the Barletti et al. [1977] data are obtained from three locations in Italy. The Brown and Good [1984a] data are from Mt. Haleakala, Hawaii, the Brown and Good [1984b] data are from Westford, Mass. The upper altitude profiles ($Z > 5$ km) appears to be more constant in time except for possible tropopause effects associated with jet streams diurnal effects. Several models have been presented to describe the C_n^2 altitude profile. Hufnagle [1966] introduced the model

$$C_n^2(z) = 2.7 \times 10^{-16} \left[e^{-z/1500} + 3W^2 \left(\frac{z}{10000} \right)^{10} e^{-z/1000} \right] \quad (18.103)$$

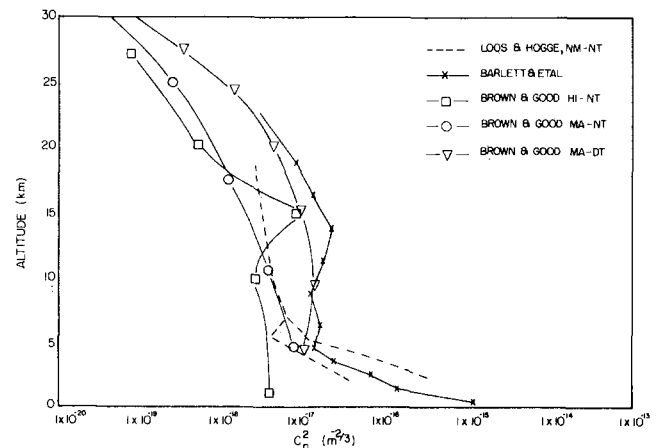


Figure 18-107. Altitude profiles of C_n^2 .

OPTICAL AND INFRARED PROPERTIES OF THE ATMOSPHERE

where $W = \left[\frac{1}{15} \int_{5 \text{ km}}^{20 \text{ km}} V^2(Z) dZ \right]^{1/2}$ is a root mean square of the horizontal wind, $V(Z)$ over the altitude range of the model. Hufnagel [1974] also has a model with a delta function additive term, $2 \times 10^{-16} (h - 12 \text{ km})$, to rep-

resent the tropopause contribution. VanZandt et al. [1981] had developed a model based on statistical behavior of the atmospheric stability and wind shears. This model uses observed rawinsonde measurements of temperature and winds at 300 m altitude resolution to infer optical turbulence at higher altitude resolution.

CHAPTER 18

REFERENCES

- Alms, G.R., A.K. Burnham, and W.H. Flygare, "Measurement of the Dispersion in Polarity Anisotropies," *J. Chem. Phys.*, **63**:3321-3326, 1975.
- Altshuler, T.L., *Infrared Transmission and Background Radiation by Clear Atmospheres*, GE Report 61 SD 199, AD401923, 1961.
- Ashley, G.W., L. Gastineau, and B. Blay, (private communication) 1973.
- Baas, F. and K.D. van den Hout, "Measurements of Depolarization Ratios and Polarizability Anisotropies of Gaseous Molecules," *Physica*, **95A**:597-601, 1979.
- Barletti, R., G. Ceppatelli, L. Paterno, A. Righini, and N. Speroni, "Astronomical Site Testing with Balloon-Borne Radiosondes," *Astron. Astrophys.*, **54**:649-659, 1977.
- Bemporad, reprinted in List, K.J., *Smithsonian Meteorological Tables 6th Rev. Ed.*, Smithsonian Institution Press, Washington, D.C., 1968.
- Berger, R.H., "Characterization of Snow for Evaluation of its Effects on Electromagnetic Wave Propagation," *Optical Engineering for Cold Environments, Proc. Soc. Photo-Optical Inst. Eng.*, **414**:35, 1983.
- Biberman, M., L. Dunkelmann, M.L. Fickett, R.G. Fink, "Levels of Nocturnal Illumination," Institution for Defense Analyses Research Paper, **SD-50**, January 1966.
- Blättner, W.G., H.G. Horak, D.G. Collins, and M.B. Wells, "Monte Carlo Studies of the Sky Radiation at Twilight," *Appl. Opt.*, **13**:534-547, 1974.
- Born, M. and E. Wolf, *Principles of Optics*, Pergamon Press, New York, 1975.
- Brown, D., "Natural Illumination Charts," Dept. of the Navy R&D Project NS 714-100, September 1952.
- Brown, J.H. and R.E. Good, "Thermosonde C_n^2 Measurements in Hawaii—August 1982, AFGL TR-84-0110, ADA148016, 1984a.
- Brown, J.H. and R.E. Good, "Thermosonde and UHF C_n^2 Measurements at Westford, Massachusetts—July 1981," AFGL TR-84-0109, ADA145398, 1984b.
- Burch, D.E., *Semi-Annual Technical Report*, Aeronutronic Report No. U-4784, January 1970.
- Burch, D.E., "Continuum Absorption by H_2O ," AFGL TR-81-0300, ADA112264, 1981.
- Burch, D.E. and D.A. Gryvnaк, *Infrared Absorption by CO_2 and H_2O* , AFGL TR-78-0154, ADA060079; Aeronutronic Report No. U-6417, May 1978.
- Burch, D.E. and D.A. Gryvnaк, *Method of Calculating H_2O Transmission Between 333 and 633 cm^{-1}* , AFGL TR-79-0054, ADA072850; Aeronutronic Report No. U-6503, April 1979.
- Burch, D.E., D. Gryvnaк, E.B. Singleton, W.L. France, and D. Williams, *Infrared Absorption by Carbon Dioxide, Water Vapor, and Minor Atmospheric Constituents*, AFCRL62-698, AD287406, 1962.
- Burch, D.E., D.A. Gryvnaк, and J.D. Pembroke, *Investigation Absorption by Atmospheric Gases*, AFCRL-71-0124, AD 882876; Aeronutronic Report No. U-4897, January 1971.
- Canosa, J. and H.R. Penafiel, "A Direct Solution of the Radiative Transfer: Application to Rayleigh and Mie Atmospheres," *J. Quant. Spectrosc. Radiat. Transfer*, **13**:21-39, 1973.
- Chandrasekhar, S., *Radiative Transfer*, Oxford University Press, London, 393, 1950.
- Chaney, L.W., *An Experimental Fourier Transform Asymmetrical Interferometer for Atmospheric Radiance Measurements*, University of Michigan Technical Report 05863-18-T, 1969.
- Chapman, S., "The Absorption and Dissociative or Ionizing Effect of Monochromatic Radiation in an Atmosphere on a Rotating Earth II Grazing Incidence," *Proc. Phys. Sci. (London)* **43**:483-501, 1931.
- Chu, C.M. and S.W. Churchill, "Numerical Solution of Problems in Multiple Scattering of Electromagnetic Mediation," *J. Phys. Chem.*, **59**:855-863, 1955.
- Chýlek, P., G.W. Grams, and R.G. Pinnick, "Light Scattering by Irregularly Randomly Oriented Particles," *Science*, **193**:480-482, 1976.
- Clough, S.A., and F.X. Kneizys, "Convolution Algorithm for the Lorentz Function," *Appl. Opt.*, **18**:2329, 1979.
- Clough, S.A., F.X. Kneizys, and J.H. Chetwynd, Jr., "Algorithm for the Calculation of Absorption Coefficient-Pressure Broadened Molecular Transitions," AFGL TR-77-0164, ADA047515, 1977.
- Clough, S.A., F.X. Kneizys, R. Davies, R. Gamache, and R.H. Tipping, "Theoretical Line Shape for H_2O Vapor; Application to the Continuum," in *Atmospheric Water Vapor*, edited by A. Deepak, T.D. Wilkerson and L.H. Ruhnke, Academic Press, New York, 1980.
- Clough, S.A., F.X. Kneizys, L.S. Rothman, and W.O. Gallery, "Atmospheric Spectral Transmittance and Radiance: FASCODE," *Proc. Soc. Photo-Optical Inst. Eng.*, **277**:152, 1981.
- Clough, S.A., R.W. Davies, and R.H. Tipping, "The Line Shape for Collisionally Broadened Molecular Transitions: A Quantum Theory Satisfying the Fluctuation Dissipation Theorem," in *Spectral Line Shapes*, edited by K. Burnett, Walter de Gruyter, New York, 1983.
- Coakley, J. and P. Chýlek, "The Two-Stream Approximation in Radiative Transfer: Including the Angle of the Incident Radiation," *J. Atmos. Sci.*, **32**:409-418, 1975.
- Cole, A.E. and A.J. Kantor, "Air Force Reference Atmospheres," AFGL TR-78-0051, ADA058505, 1978.
- Cole, A.E., A. Court, and A.J. Kantor, "Model Atmospheres," in *Handbook of Geophysics and Space Environments*, edited by S. Valley, McGraw-Hill, New York, NY 1965, (also available from NTIS as ADA056800) 1965.
- Collins, D.G. and M.B. Wells, "Monte Carlo Codes for the Study of Light Transport in the Atmosphere," ECOM-00240-F, Radiation Research Associates, Inc. (Rep. RRA-174) Fort Worth, Texas (Avail. from NTIS, AD625225), 1965.
- Collins, D.G., W.G. Blattner, M.B. Wells, and H.G. Horak, "Backward Monte Carlo Calculations of the Polarization Characteristics of the Radiation Emerging from Spherical-Shell Atmospheres," *Appl. Opt.*, **11**:2684-2696, 1972.

OPTICAL AND INFRARED PROPERTIES OF THE ATMOSPHERE

- Conrath, B.J., R.A. Hanel, V.G. Kunde, and C. Prabhakara, *The Infrared Interferometer Experiment on Nimbus 3*, Goddard Space Flight Center, Maryland, Report X-620-70-213, 1970.
- Coulson, K.L., J.V. Dave, and Z. Sekera, *Tables Related to Radiation Emerging from a Planetary Atmosphere with Rayleigh Scattering*, University of California Press, Berkeley Calif., 1960.
- Dave, J.V., "Meaning of Successive Iteration of the Auxiliary Equation in the Theory of Radiative Transfer," *Astrophys. J.*, **140**:1292-1303, 1964.
- Dave, J.V., "Multiple Scattering in a Non-Homogenous Rayleigh Atmosphere," *J. Atmos. Sci.*, **22**:273-279, 1965.
- Dave, J., "A Direct Solution of the Spherical Harmonics Approximation to the Radiative Transfer Equation for an Arbitrary Solar Elevation," *J. Atmos. Sci.*, **32**:790-800, 1975a.
- Dave, J., "A Direct Solution of the Spherical Harmonics Approximation to the Radiative Transfer Equation for an Arbitrary Solar Evaluation. II: Results," *J. Atmos. Sci.*, **32**:1463-1474, 1975b.
- Dave, J.V. and B.H. Armstrong, "Smoothing of the Intensity Curve Obtained from a Solution of the Spherical Harmonics Approximation to the Transfer Equation," *J. Atmos. Sci.*, **31**:1934-1937, 1974.
- Dave, J.V. and J. Gazdag, "A Modifier Fourier Transform Method for Multiple Scattering Calculations in a Plane-Parallel Mie Atmosphere," *Appl. Opt.*, **9**:1457-1466, 1970.
- Davies, R. "Fast Azimuthally Dependent Model of the Reflection of Solar Radiation by Plane-Parallel Clouds," *Appl. Opt.*, **19**:250-255, 1980.
- Deirmendjian, D., *Electromagnetic Scattering on Spherical Polydispersions*, American Elsevier, New York, 129-139 and 290, 1969.
- Diermendjian, D., "Scattering and Polarization Properties of Water, Clouds and Hazes in the Visible and Infrared," *Appl. Opt.*, **3**:187-196, 1964.
- Devaux, C. and M. Herman, "Remarques sur l'Utilization de la Methode des Harmoniques Spheriques dans les Calculs de Transfert Radiatif," *Comptes Rendus, Acad. Sci. Paris*, **B273**:849-852, 1971.
- Dewan, E.M., "Optical Turbulence Forecasting: A Tutorial," AFGL TR-80-0030, ADA086863, 1980.
- Downing, H. and D. Williams, "Optical Constants of Water in the Infrared," *J. Geophys. Res.* **80**:1656-1661, 1975.
- Duntley, S.Q., A.R. Boileau, and R.W. Preisendorfer, "Image Transmission by the Troposphere," *J. Opt. Soc. Am.*, **47**:499-506, 1957.
- Earing, D.G. and J.A. Smith, *Target Signatures Analysis Center: Data Compilation*, AFAL, AD489968, 1966.
- Eaton, F.D. and I. Dirmhirn, "Reflected Irradiance Indicatrices of Natural Surfaces and Their Effect on Albedo," *Appl. Opt.*, **18**(7), Apr 1979.
- Eddington, A.S., *The Internal Constitution of the Stars*, 407, Cambridge University Press, Cambridge, Eng., 1926.
- Edlen, B., "The Refractive Index of Air," *Meteorol.*, **2**:71-80, 1966.
- Elsasser, W.M., "Mean Absorption and Equivalent Absorption Coefficient of a Band Spectrum," *Phys. Rev.*, **54**:126, 1942. Also as Harvard Meteorological Studies, No. 6, Blue Hill Met. Obs., Harvard Univ., Milton, Mass., 1942.
- Elterman, L., "Atmospheric Attenuation Model, 1964, in the Ultraviolet, Visible, and Infrared Regions for Altitudes to 50 km," AFCRL-64-740, AD607859, 1964.
- Elterman, L., "UV, Visible, and IR Attenuation for Altitudes to 50 km," AFCRL-68-0153, ADA671933, 1968.
- Elterman, L., "Vertical Attenuation Model with Eight Surface Meteorological Ranges 2 to 13 kilometers," AFCRL-70-0200, AD 707488, 1970.
- Evans, W.F., J.B. Kerr, and D.I. Wardle, *The AES Stratospheric Balloon Measurements Project: Preliminary Results*, Report No. APRB 30X4, Atmospheric Environment Service, Downsview, Ontario, Canada, 1975.
- Falcone, V.J., L.W. Abreu, and E.P. Shettle, *Atmospheric Attenuation of Millimeter Waves, Models and Computer Code*, AFGL TR-79-0253, ADA084485, 1979.
- Fitch, B.W., "Effects of Reflection by Natural Surfaces on the Radiation Emerging from the top of the Earth's Atmosphere," *J. Atmos. Sci.*, **38**:2717-2719, 1981.
- Fouquart, Y., W.M. Irvine, and J. Lenoble, eds., *Standard Procedures to Compute Atmospheric Radiative Transfer in a Scattering Atmosphere, Vol. II, Part A. Review of Methods for Horizontally Inhomogeneous Atmospheres, and Spherical Atmospheres, Part B. Problems of Scattering with Gaseous Absorption*, National Center for Atmospheric Research, Boulder, Colorado, for the International Association of Meteorology and Atmospheric Physics, 1980.
- Fried, D.L., "Optical Resolution Looking Down Through a Randomly Homogeneous Medium for Very Long and Very Short Exposures," *J. Opt. Soc. Am.*, **56**:1372-1379, 1966.
- Fried, D.L., "Optical Heterodyne Detection of an Atmospheric Distorted Signal Wave Front," *Proc. IEEE*, **55**:57, 1967.
- Fried, D.L., "Angular Dependence of the Atmospheric Turbulence Effect in Speckle Interferometry," *Opt. Acta*, **26**:597-613, 1979.
- Gallery, W., F.X. Kneizys, and S.A. Clough, *Air Mass Computer Program for Atmospheric Transmittance/Radiance Calculation: FASCATM*, AFGL TR-83-0065, ADA132108, 1983.
- Gathman, S.G., "Optical Properties of the Marine Aerosol as Predicted by the Navy Aerosol Model," *Opt. Eng.*, **22**:57-62, 1983.
- Goody, R.M. "A Statistical Model for Water Vapour Absorption," *Quart. J. Roy. Meteorol. Soc.*, **78**:165, 1952.
- Goody, R.M., *Atmospheric Radiation, Vol. I Theoretical Basis*, Oxford University Press, London, 1964.
- Grant, I.G. and G.E. Hunt, "Solution of Radiative Transfer Problems Using the Invariant S_N Method," *Mon. Notices Roy. Astron. Soc.*, **141**:27-41, 1968.
- Grant, I.G. and G.E. Hunt, "Discrete Space Theory of Radiative Transfer, 1, Fundamentals," *Proc. Roy. Soc. London*, **A313**:183-197, 1969a.
- Grant, I.G. and G.E. Hunt, "Discrete Space Theory of Radiative Transfer, 2, Stability and Non-Negativity," *Proc. Roy. Soc. London*, **A313**:199-216, 1969b.

CHAPTER 18

- Gray, D.M. and D.H. Male, (eds.) *Handbook of Snow*, Pergamon Press, New York, 1981.
- Greenwood, D.P., "Bandwidth Specification for Adaptive Optics System," *J. Opt. Soc. Am.*, **67**:390–392, 1977.
- Grenfell, T.C. and D.K. Perovich, "Radiation Absorption Coefficients of Polycrystalline Ice from 400–1400 nm," *J. Geophys. Res.*, **86**:7447–7450, 1981.
- Hale, G.M. and M.R. Querry, "Optical Constants of Water in 200 nm to 200 μ m Wavelength Region," *Appl. Opt.*, **12**:555–563, 1973.
- Hanel, G., "The Properties of Atmospheric Aerosols Particles as Functions of the Relative Humidity at Thermodynamic Equilibrium with the Surrounding Moist Air," in *Advances in Geophysics*, **19**:73–188, edited by H.E. Landsberg and J. van Miefhem, 1976.
- Hanel, R.A. and B.J. Conrath, *Thermal Emission Spectra of the Earth and Atmosphere Obtained from the Nimbus 4 Michelson Interferometer Experiment*, Goddard Space Flight Center, Greenbelt, Maryland, Report X-620-70-244, 1970.
- Hänel G. and K. Bullrich, "Physico-Chemical Property Model of Tropospheric Aerosol Particles," *Beitr. Phys. Atm.*, **51**:129–130, 1978.
- Hansen, J.E., "Radiative Transfer by Doubling Very Thin Layers," *Astrophys. J.*, **155**:565–573, 1969a.
- Hansen, J.E., "Exact and Approximate Solutions for Multiple Scattering by Cloudy and Hazy Planetary Atmospheres," *J. Atmos. Sci.*, **26**:478–487, 1969b.
- Hansen, J.E., "Multiple Scattering of Polarized Light in Planetary Atmospheres, Part 1. The Doubling Method," *J. Atmos. Sci.*, **28**:120–125, 1971a.
- Hansen, J.E., "Multiple Scattering of Polarized Light in Planetary Atmospheres, Part 2. Sunlight Reflected by Terrestrial Clouds," *J. Atmos. Sci.*, **28**:1400–1426, 1971b.
- Hansen, J.E. and J.B. Pollack, "Near-Infrared Light Scattering by Terrestrial Clouds," *J. Atmos. Sci.*, **27**:265–281, 1970.
- Hansen, J.E. and L.D. Travis, "Light Scattering in Planetary Atmospheres," *Space Sci. Rev.*, **16**:527–610, 1974.
- Hering, W.S., "An Operational Technique for Estimating Visible Spectrum Contrast Transmittance," AFGL TR-81-0198, ADA111823, 1981.
- Hering, W.S. and T.R. Borden, "Ozonesonde Observation Over North America," AFCRL-64-30, vol. 2, AD604880, 1964.
- Herman, B.M., "Multiple Scatter Effects on the Radar Return from Large Hail," *J. Geophys. Res.*, **70**:1215–1225, 1965.
- Herman, B.M. and S.R. Browning, "A Numerical Solution to the Equation of Radiative Transfer," *J. Atmos. Sci.*, **22**:559–566, 1965.
- Herman, B.M., S.R. Browning, and R.J. Curran, "The Effect of Atmospheric Aerosols on Scattered Sunlight," *J. Atmos. Sci.*, **28**:419–428, 1971.
- Herman, B.M., A.J. LaRocca and R.E. Turner, "Atmospheric Scattering" Chapter 4 in *The Infrared Handbook*, edited by W.L. Wolfe and G.J. Zissis, Office of Naval Research, Washington, D.C., 1978.
- Herman, B.M., W. Asous, and S. Browning, "A Semi-Analytic Technique to Integrate the Radiative Transfer Equation Over Optical Depth," *J. Atmos. Sci.*, **37**:1828–1838, 1980.
- Hobbs, P.V., *Ice Physics*, p. 202, Clarendon Press, Oxford, U.K., 1974.
- Holland, A.C. and G. Gagne, "The Scattering of Polarized Light of Polydisperse Systems of Irregular Particles," *Appl. Opt.*, **9**:1113–1121, 1970.
- Houghton, J.T., *The Physics of Atmospheres*, Cambridge University Press, Cambridge, Eng., 1977.
- Hufnagel, R.E., *Restoration of Atmospherically Degraded Images*, Vol. 2, Woods Hole Summer Study, July 1966, National Academy of Sciences—National Research Council, Washington, D.C., 1966.
- Hufnagel, R.E., "Variations of Atmospheric Turbulence," *Proc. Topical Meeting on Optical Propagation through Turbulence*, Optical Society of America, Washington, D.C. 9–11 July, 1974.
- Hufnagel, R.E., "Propagation Through Atmospheric Turbulence," in *The Infrared Handbook*, edited by W.L. Wolfe and G.J. Zissis, Office of Naval Research, Washington, D.C., 1978.
- Hufnagel, R.E., and N.R. Stanley, "Modulation Transfer Function Associated with Image Transmission through Turbulent Media," *J. Opt. Soc. Am.*, **54**:52–61, 1964.
- Hulburt, E.O., "Optics of Atmospheric Haze," *J. Opt. Soc. Am.*, **31**:467–476, 1941.
- Irvine, W.M., "Multiple Scattering by Large Particles," *Astrophys. J.*, **142**:1563–1575, 1965.
- Irvine, W.M., "Diffuse Reflection and Transmission by Cloud and Dust Layers," *J. Quant. Spectrosc. Radiat. Transfer*, **8**:471–485, 1968a.
- Irvine, W.M., "Multiple Scattering by Large Particles, 2, Optical Thick Layers," *Astrophys. J.*, **152**:823–834, 1968b.
- Irvine, W.M. and J.B. Pollack, "Infrared Optical Properties of Water and Ice Spheres," *Icarus*, **8**:324–360, 1967.
- Ivlev, L.S., "Aerosol Model of the Atmosphere," *Prob. Fiz. Atmos.* No. 7: 125–160, Leningrad, translated by Foreign Science and Technology Ctr, Dept. of the Army, NTIS No. AD760393, 1967.
- Ivlev, L.S., "Atmospheric Aerosol," in *Radiation Characteristics of the Atmosphere and the Earth's Surface*, edited by K. YaKondratev, Amerind, New York, NTIS No. TT-71-58003, 1969.
- Jeans, J.M., "The Equations of Radiative Transfer," *Mon. Notices Roy. Astron. Soc.*, **78**:28–36, 1917.
- Johnson, J.C. *Physical Meteorology*, New York Technical Press, MIT, and Wiley, 393, 1954.
- Joseph, J.H., W.J. Wiscombe, and J.A. Weinman, "The Delta Eddington Approximation for Radiation Flux Transfer," *J. Atmos. Sci.*, **33**:2452–2459, 1976.
- Junge, Ch.E., *Air Chemistry and Radioactivity*, p. 382, Academic Press, New York, 1963.
- Karp, A., "Efficient Computation of Spectral Line Shapes," *J. Quant. Spectrosc. Radiat. Transfer*, **14**:803–817, 1973.
- Karp, A., "Computing the Angular Dependence of the Radiation of a Planetary Atmosphere," *J. Quant. Spectrosc. Radiat. Transfer*, **25**:403–412, 1981.
- Karp, A., J. Greenstadt, and J. Fillmore, "Radiative Transfer Through an Arbitrarily Thick Scattering Atmo-

OPTICAL AND INFRARED PROPERTIES OF THE ATMOSPHERE

- sphere," *J. Quant. Spectrosc. Radiat. Trans.*, **24**:391–406, 1981.
- Kasten, F., "A New Table and Approximation Formula for the Relative Optical Air Mass," *Arch. Meteor. Geophys. Bioklim*, **B14**:206–223, 1966.
- Kasten, F., "Effect of Variation of the Vertical Air Density Profile in the Relative Optical Air Mass," *Arch. Meteor. Geophys. Bioklim*, **B15**:62–66, 1967.
- Kattawar, G.W. and G.N. Plass, "Influence of Particle Size Distribution on Reflected and Transmitted Light from Clouds," *Appl. Opt.*, **7**:869–878, 1968.
- Kaufman, Y.J., "Effect of the Earth's Atmosphere on Contrast for Zenith Observation," *J. Geophys. Res.*, **84**:3165–3172, 1979.
- Kerker, M., *The Scattering of Light and Other Electromagnetic Radiation*, Academic Press, New York, 1969.
- Kielkopf, J.F., "New Approximation to the Voigt Function with Applications to Spectral Line Profile Analysis," *J. Opt. Soc. Am.*, **63**, 987, 1973.
- King, J.I.F., "Band Absorption Model for Arbitrary Line Variance," *J. Quant. Spectrosc. Radiat. Transfer*, **4**:705–711, 1964.
- Kneizys, F.X., E.P. Shettle, W.O. Gallery, J.H. Chetwynd, Jr., L.W. Abreu, J.E.A. Selby, R.W. Fenn, and R.A. McClatchey, *Atmospheric Transmittance/Radiance: Computer Code LOWTRAN 5*, AFGL TR-80-0067, AD088215, 1980.
- Kneizys, F.X., E.P. Shettle, W.O. Gallery, J.H. Chetwynd, Jr., L.W. Abreu, J.E.A. Selby, S.A. Clough, and R.W. Fenn, *Atmospheric Transmittance/Radiance: Computer Code LOWTRAN 6*, AFGL TR-83-184, ADA140012, August 1983.
- Koh, G. and H. O'Brien, "Snow Crystal Habit," SNOW-ONE-A Data Report, edited by Aitken, CRREL Special Report 82-8, U.S. Army Corps. of Engineers Cold Regions Research and Engineering Lab., Hanover, N.H., 1982.
- Krinov, E.L., "Spectral Reflectance Properties of Natural Formations" (in Russian 1942), Nat. Res. Council of Canada (Ottawa) Tech. Transl. TT-439, 1953.
- Kunde, V.G. and W.C. Maguire, "Direct Integration Transmittance Model," *J. Quant. Spectrosc. Radiat. Transfer*, **14**:803–817, 1973.
- Lacomb, J., "Techniques for Measuring the Mass Concentration of Falling Snow," *Optical Engineering for Cold Environments, Proc. Soc. Photo-Optical Inst. Eng.*, **414**:17, 1983.
- LaRocca, A.J., "Atmospheric Absorption," Chapter 5 in *Infrared Handbook*, edited by W.L. Wolfe, G.J. Zisis, Office of Naval Research, Washington, D.C., 1978.
- Lawrence, R.S., G.R. Ochs, and S.F. Clifford, "Measurements of Atmospheric Turbulence Relevant to Optical Propagation," *J. Opt. Soc. Am.*, **60**:826, 1970.
- Lawrence, R.S. and J.W. Strohbehn, "A Survey of Clear Air Propagation Effects Relevant to Optical Communications," *Proc. IEEE*, **58**:1523–1545, 1970.
- Laws, J.O. and Parsons, "The Relation of Rain Drop Size to Intensity," *Trans. Am. Geophys. Union*, **24**:452–460, 1943.
- Leader, J.L., "Analysis and Prediction of Loss Scattering from Rough Surface Material," *J. Opt. Soc. Am.*, **69** (4), April 1979.
- Lenoble, J. (ed.) *Standard Procedures to Compute Atmospheric Radiative Transfer in a Scattering Atmosphere, Vol. I*. International Association of Meteorology and Atmospheric Physics, Radiation Commission, printed at National Center for Atmospheric Research, Boulder, Colorado, 1977.
- Liou, K.N., "A Numerical Experiment on Chandrasekhar's Discrete-Ordinate Method for Radiative Transfer: Applications to Cloudy and Hazy Atmospheres," *J. Atmos. Sci.*, **30**:1303–1326, 1973.
- Lo, K.K. and R.E. Passarelli, Jr., "The Growth of Snow in Winter Storms: An Airborne Observational Study," *J. Atmos. Sci.*, **39**:697–706, 1982.
- Loos, G.C. and C.B. Hogge, "Turbulence of the Upper Atmosphere and Isoplanatism," *Appl. Opt.*, **18**:2654–2661, 1979.
- Magono, C. and C. Lee, "Meteorological Classification of Natural Snow Crystals," *J. Fac. Sci.*, Hokkaido University, Series VII, **2**:321–335, 1966.
- Mankin, W.G., "Fourier Transform Method for Calculating the Transmittance of Inhomogeneous Atmospheres," *Appl. Opt.*, **18**:3426–3433, 1979.
- Marchuk, G.I., G.A. Mikhailov, M.A. Nazaraliev, R.A. Darbinjan, B.A. Kargin, and B.S. Elepov, *The Monte Carlo Methods in Atmospheric Optics*, Springer-Verlag, New York, 1980.
- Marshall, J.S. and W.M.K. Palmer, "The Distribution of Raindrops with Size," *J. Meteor.*, **5**:165–166, 1948.
- Martinez-Sanchez, M., V. Yousefian, D. Dvore, and R. Vaglio-Laurin, "Numerical Modeling of Optically Significant Characteristics of Falling Snow," *Opt. Eng.*, **22**:78–85, 1983.
- Mason, J.B., "Light Attenuation in Falling Snow," ASL-TR-0018, U.S. Army Atmospheric Sciences Laboratory, White Sands Missile Range, New Mexico, 1978.
- McCartney, E.J., *Optics of the Atmosphere*, Wiley, New York, 1976.
- McClatchey, R.A., R.W. Fenn, J.E.A. Selby, F.E. Volz, and J.S. Garing, "Optical Properties of the Atmosphere," AFCRL TR70-0527, AD715270, 1970.
- McClatchey, R.A., W.S. Benedict, S.A. Clough, D.E. Burch, R.F. Calfee, K. Fox, L.S. Rothman, and J.S. Garing, "AFCRL Atmospheric Absorption Line Parameters Compilation," AFCRL TR-0096, AD 762904, 1973.
- McClatchey, R.A., R.W. Fenn, J.E.A. Selby, F.E. Volz, and J.S. Garing, "Optical Properties of the Atmosphere," (Third Edition), AFCRL 72-0497, AD 753075, 1972.
- McKellar, B. and M. Box, "The Scaling Group of the Radiative Transfer Equation," *J. Atmos. Sci.*, **38**:1063–1068, 1981.
- McMillin, L.M., H.E. Fleming, and M.L. Hill, "Atmospheric Transmittance of an Absorbing Gas: A Computationally Fast and Accurate Transmittance Model for Absorbing Gases with Variable Mixing Ratios," *Appl. Opt.*, **18**:1600–1606k 1976.

CHAPTER 18

- Meador, W. and W. Weaver, "Two-Stream Approximation to Radiative Transfer in Planetary Atmospheres: A Unified Description of Existing Methods and a New Improvement," *J. Atmos. Sci.*, **37**:630–643, 1980.
- Middleton, W.E.K., *Vision Through the Atmosphere*, U. of Toronto Press, 1952.
- Mie, G., "Bertrage z. Phys. Truber Medien, spezeziell kolloidaler Metallosungen," *Am. Physik*, **25**:377–445, 1908.
- Mill, J.D. and E.P. Shettle, "A Preliminary LOWTRAN Snow Model," AFGL TR-83-0148, AD A129826, 1983.
- Miller, M.G. and P.L. Zeiske, "Experimental Turbulence Profile and Parameters," *SPIE Symp. on Optical Properties of the Atmosphere, Proc. Soc. Photo-Optical Inst. Eng.*, **142**:98–103, 1978.
- Moon, P. "Proposed Standard Solar Radiation Curves for Engineering Use," *J. Franklin Inst.*, **230**(5): 583, 1940.
- Mossop, "Volcanic Dust Collected at an Altitude of 20 km," *Nature*, **103**:824–827, 1964.
- Murcray, D.G., T.G. Kyle, F.H. Murcray, and W.G. Williams, "Nitric Acid and Nitric Oxide in the Lower Stratosphere," *Nature*, **218**:78, 1968.
- Murcray, D.G., J.N. Brooks, A. Goldman, J.J. Kusters, and W.J. Williams, *Water Vapor Nitric Acid and Ozone Mixing Ratio Height Derived from Spectral Radiometric Measurements*, University of Denver, Contract Report No. 322, 1977.
- National Climatic Center, NOAA: Environmental Data Service, Federal Building, Asheville, North Carolina 28801.
- Newkirk, G., Jr., and J.A. Eddy, "Light Scattering by Particles in the Upper Atmosphere," *J. Atmos. Sci.*, **21**:35–60, 1964.
- Nicodemus, F.E., "Radiometry" in *Applied Optics and Optical Engineering*, edited by R. Kingslake, Academic Press, New York, 1967.
- Nilsson, B., "Meteorological Influence on Aerosol Extinction in the 0.2–40 μm Wavelength Range," *Appl. Opt.*, **18**:3457–3473, 1979.
- Palmer, K.F. and D. Williams, "Optical Constants of Sulfuric Acid: Application to the Clouds of Venus," *Appl. Opt.*, **14**:208–219, 1975.
- Penndorf, R., "Luminous and Spectral Reflectance as well as Colors of Natural Objects," AFCRLTR-56-203, AD98766, 1956.
- Plass, G.N., "Models for Spectral Band Absorption," *J. Opt. Soc. Am.*, **48**:690–703, 1958.
- Plass, G.N. and G.W. Kattawar, "Influence of Single Scattering Albedo on Reflected and Transmitted Light from Clouds," *Appl. Opt.*, **7**:361–367, 1968a.
- Plass, G.N. and G.W. Kattawar, "Monte Carlo Calculations of Light Scattering from Clouds," *Appl. Opt.*, **7**:415–419, 1968b.
- Plass, G.N. and G.W. Kattawar, "Radiative Transfer in the Earth's Atmosphere-Ocean System," *J. Phys. Ocean*, **2**:139–156, 1972.
- Plass, G.N., G.W. Kattawar and F.E. Catchings, "Matrix Operator Theory of Radiative Transfer, 1, Rayleigh Scattering," *Appl. Opt.*, **12**:314–329, 1973.
- Potter, J.F., "The Delta Function Approximation in Radiative Transfer Theory," *J. Atmos. Sci.*, **27**:945–951, 1970.
- Pratt, W.K., *Laser Communication Systems*, Wiley, New York, 1969.
- Preisendorfer, R., *Radiative Transfer on Discrete Spaces*, Pergamon Press, New York, 1965.
- Remsberg, E.E., "Radiative Properties of Several Probable Constituents of Atmospheric Aerosols," Ph.D. Thesis Dept. Meteorology, University of Wisconsin, Madison, 1971.
- Remsberg, E.E., "Stratospheric Aerosols Properties and Their Effect on Infrared Radiation," *J. Geophys. Res.*, **78**:1401–1408, 1973.
- Remsberg, E.E., J.M. Russel III, L.L. Gordley, J.C. Gille, and P.L. Bailey, "Implications of the Stratospheric Water Vapor Distribution as Determined from the Nimbus 7 LIMS Experiment," *J. Atmos. Sci.* **41**:2934–2945, 1984.
- Rice, D.P. and P.A.R. Ade, "Absolute Measurements of the Atmospheric Transparency at Short Millimeter Wavelengths," *Infrared Phys.*, **19**:575, 1979.
- Robinson, N., ed., *Solar Radiation*, Elsevier, Amsterdam, 1966.
- Romanova, L.M., "The Solution of the Radiative Transfer Equation for the Case When the Indicatrix of Scattering Greatly Differs from the Spherical One," *Opt. Spektrosk.*, **13**:429–435, 1962.
- Romanova, L.M., "Radiative Field in Plane Layers of a Turbid Medium with Highly Anisotropic Scattering," *Opt., Spektrosk.*, **14**:262–269, 1963.
- Rosen, J.M., "The Boiling Point of Stratospheric Aerosols," *J. Appl. Meteorol.*, **10**:1044–1046, 1971.
- Rosen, J.M., "Stratospheric Dust and Its Relationship to the Meteoric Influx," *Space Sci. Rev.*, **9**:58–89, 1969.
- Rothman, L.S., "AFGL Atmospheric Absorption Line Parameters Compilation: 1980 Version," *Appl. Opt.*, **20**:291, 1981.
- Rothman, L.S. and A. Goldman, "Infrared Electric Quadrupole Transitions of Atmospheric Oxygen," *Appl. Opt.*, **20**:2182, 1981.
- Rothman, L.S., A. Goldman, J.R. Gillis, R.H. Tipping, L.R. Brown, J.S. Margolis, A.G. Maki, and L.D.G. Young, "AFGL Trace Gas Compilation: 1980 Version," *Appl. Opt.*, **20**:1323, 1981.
- Rothman, L.S., A. Goldman, J.R. Gillis, R.R. Gamache, H.M. Pickett, R.L. Poynter, N. Husson, and A. Chedin, "AFGL Trace Gas Compilation: 1982 Version," *Appl. Opt.*, **22**:1616–1627, 1983a.
- Rothman, L.S., R.R. Gamache, A. Barbe, A. Goldman, J.R. Gillis, L.R. Brown, R.A. Toth, J.-M. Flaud, and C. Camy-Peyret, "AFGL Atmospheric Absorption Line Parameters Compilation: 1982 Edition," *Appl. Opt.*, **22**:2247–2256, 1983b.
- Rowell, R.L., G.M. Aval, and J.J. Barrett, "Rayleigh-Raman Depolarization of Laser Light Scattered by Gases," *J. Chem. Phys.*, **54**:1960–1964, 1971.
- Sagan, C. and J.B. Pollack, "Anisotropic Nonconservative Scattering and the Clouds of Venus," *J. Geophys. Res.*, **72**:469–477, 1967.
- Samuelson, R.E., "The Transfer of Thermal Infrared Radiation in Cloudy Planetary Atmospheres," Ph.D. Thesis, Georgetown University, p. 309, 1967.
- Samuelson, R.E., "The Thermal Radiation Field Emitted

OPTICAL AND INFRARED PROPERTIES OF THE ATMOSPHERE

- by Anisotropically Scattering Cloudy Planetary Atmospheres," *Icarus*, **10**:258-273, 1969.
- Schaaf, J.B. and D. Williams, "Optical Constants of Ice in the Infrared," *J. Opt. Soc. Am.*, **63**:726-732, 1973.
- Schaller, E., "A Delta-Two-Stream Approximation in Radiative Flux Calculations," *Beitr. Phys. Atmos.*, **52**:17-26, 1979.
- Schuerman, D.W. (ed.) *Light Scattering by Irregularly Shaped Particles*, Plenum Press, New York, 1980.
- Schulze, R., *Strahlenklima der Erde*, D. Steinkopff Verlag, Darmstadt, Germany, 1970.
- Scott, N.A. and A. Chedin, "A Fast Line-by-Line Method for Atmospheric Absorption Computations: The Automated Absorption Atlas," *J. Appl. Meteor.*, **20**:802-812, 1981.
- Seagraves, M.A., "Visible and Infrared Extinction and Precipitation Rate in Falling Snow," *Optical Engineering for Cold Environments, Proc. Soc. Photo-Optical Inst. Eng.*, **414**:78, 1983.
- Seagraves, M.A. and S.F. Ebersole, "Visible and Infrared Transmission through Snow," *Opt. Eng.*, **22**:90-93, 1983.
- Selby, J.E.A. and R.A. McClatchey, "Atmospheric Transmittance from 0.25 to 28.5 μm : Computer Code LOWTRAN 2," AFCRL 72-0745, AD 763721, 1972.
- Selby, J.E.A. and R.A. McClatchey, "Atmospheric Transmittance from 0.25 to 28.5 μm : Computer code LOWTRAN 3," AFCRL TR75-0255, AD 017734, 1975.
- Selby, J.E.A., E.P. Shettle, and R.A. McClatchey, "Atmospheric Transmittance from 0.25 to 28.5 μm : Supplement LOWTRAN 3B," AFCRL TR-76-0258, AD 040701, 1976.
- Selby, J.E.A., F.X. Kneizys, J.H. Chetwynd Jr., and R.A. McClatchey, *Atmospheric Transmittance/Radiance: Computer Code LOWTRAN 4*, AFGL TR-078-0053, ADA 058643, 1978.
- Shettle, E.P. and R.W. Fenn, "Models of the Atmospheric Aerosols and Their Optical Properties," in AGARD Conference Proceedings No. 183, *Optical Propagation in the Atmosphere*. Presented at the Electromagnetic Wave Propagation Panel Symposium, Lyngby, Denmark, 27-31 October 1975, AGARD-CP-183, ADA028-615, 1976.
- Shettle, E.P. and R.W. Fenn, "Models of the Aerosols of the Lower Atmosphere and the Effects of Humidity Variations on Their Optical Properties," AFGL TR-79-0214, ADA 085951, 1979.
- Shettle, E.P. and A.E.S. Green, "Multiple Scattering Calculations of the Middle Ultraviolet Reaching the Ground," *Appl. Opt.*, **13**:1567-1581, 1974.
- Shettle, E.P. and F.E. Volz, "Optical Constants for Meteoric Dust Aerosol Models" in *Atmospheric Aerosols: Their Optical Properties and Effects*, a Topical Meeting on Atmospheric Aerosols sponsored by Opt. Soc. Am. and NASA Langley Res. Cen., Williamsburg, Virginia, NASA Conference Publication CP 2004, 13-15 Dec 1976.
- Shettle, E.P. and J.A. Weinman, "The Transfer of Solar Irradiance Through Inhomogeneous Turbid Atmospheres Evaluated by Eddington's Approximation," *J. Atmos. Sci.*, **27**:1048-1055, 1970.
- Shettle, E.P., R.W. Fenn, and J.D. Mill, "The Optical and Infrared Properties of Atmospheric Particulates," AFGL to be published, 1985.
- Sidran, M., "Broadband Reflectance and Emissivity of Specular and Rough Water Surfaces," *Appl. Opt.*, **20**:3126, 1981.
- Silverman, B.A. and E.D. Sprague, "Airborne Measurements of In Cloud Visibility," Preprints, National Conference on Weather Modification of the Am. Meteorol. Soc., Santa Barbara, California, 6-9 April 1970.
- Sissenwine, N., D.D. Grantham, and H.A. Salmela, "Humidity Up to the Mesopause," AFCRLTR-68-0550, AD 679996, 1968.
- SMIC, *Inadvertent Climate Modification: Report of the Study of Man's Impact on the Climate*, MIT Press, Cambridge, Mass., 1971.
- Smith, F.L. and C. Smith, "Numerical Evaluation of Chapman's Gracing Incidence Integral $ch(x/\psi)$," *J. Soc. Res.*, **77**:3502-3597, 1972.
- Smith, H.J.P., D.B. Dube, M.E. Gardner, S.A. Clough, F.X. Kneizys, and L.S. Rothman, "FASCODE—Fast Atmospheric Signature Code (Spectral Transmittance and Radiance)," AFGLTR-78-0081, ADA057359, 1978.
- Smith, M.A.H., *Compilation of Atmospheric Gas Concentration Profiles from 0 to 50 km*, NASA TM-83289, 1982.
- Sneider, D.E., "Refractive Effects in Remote Sensing of the Atmosphere with Infrared Transmission Spectroscopy," *J. Atmos. Sci.*, **32**:2178-2184, 1975.
- Sneider, D.E., and A. Goldman, *Refractive Effects in Remote Sensing of the Atmosphere with Infrared Transmission Spectroscopy*, Ballistic Res. Labs Report 1790, Aberdeen, Maryland ADA011253, 1974.
- Sobolev, V.V., *Light Scattering in Planetary Atmospheres*, Translated by W.M. Irvine, Pergamon Press, New York, p. 256, 1975.
- SOLMET, *Hourly Solar Radiation—Surface Meteorological Observations*, Vol 2, TD 9724 NOAA Environmental Data Service, Asheville, N.C., Feb. 1979.
- Stamnes, K. and H. Dale, "A New Look at the Discrete Ordinate Method for Radiative Transfer Calculations in Anisotropically Scattering Atmospheres II. Intensity Computation," *J. Atmos. Sci.*, **38**:2696-2706, 1981.
- Stamnes, K. and R. Swanson, "A New Look at the Discrete Ordinate Method for Radiative Transfer Calculations in Anisotropically Scattering Atmospheres," *J. Atmos. Sci.*, **38**:387-399, 1981.
- Stewart, D.A. and O.M. Essenwanger, "A Survey of Fog and Related Optical Propagation Characteristics," *Rev. Geophys. Space Phys.*, **20**: 481-195, 1982.
- Suits, G.M., *The Infrared Handbook*, Chapter 3, "Natural Sources," edited by W.L. Wolfe and G.L. Zissis, Office of Naval Research, Washington D.C., 1978.
- Susskind, J. and J.E. Searl, "Synthetic Atmospheric Transmittance Spectra Near 15 and 4.3 μm ," *J. Quant. Spectrosc. Radiat. Transfer*, **19**:195-215, 1978.
- Tatarski, V.I., *Wave Propagation in a Turbulent Medium*, McGraw-Hill, New York, 1961.
- Thompson, L. (ed.), "Advanced Scanners and Imaging Systems for Earth Observations," NASA SP-335, 1972.

CHAPTER 18

- Thompson, B.C. and M.B. Wells, "Scattered and Reflected Light Intensities Above the Atmosphere," *Appl. Opt.*, **10**:1539–1549, 1971.
- Toon, O.B. and J.B. Pollack, "A Global Average Model of Atmospheric Aerosols for Radiative Transfer Calculations," *J. Appl. Meteorol.*, **15**:225–246, 1976.
- Toon, O.B. and J.B. Pollack, "Physical Properties of the Stratospheric Aerosol," *J. Geophys. Res.*, **78**:7057–7056, 1973.
- Turco, R.P., R.C. Whitten, and O.B. Toon, "Stratospheric Aerosols: Observation and Theory," *Rev. Geophys. Space Res.*, **20**:233–279, 1982.
- Twitty, J.T. and J.A. Weinman, "Radiative Properties of Carbonaceous Aerosols," *J. Appl. Meteorol.*, **10**:725–731, 1971.
- Twomey, S., H. Jacobowitz, and H.B. Howell, "Matrix Method for Multiple Scattering Problems," *J. Atmos. Sci.*, **23**:289–296, 1966.
- Twomey, S., H. Jacobowitz, and H.B. Howell, "Light Scattering by Cloud Layers," *J. Atmos. Sci.*, **24**:70–79, 1967.
- Tyler, J.E., "Optical Properties of Water," Section 15 in *Handbook of Optics*, edited by W.G. Dirscol and W. Vaughan, McGraw-Hill, New York, 1978.
- U.S. Standard Atmosphere 1962*, U.S. Government Printing Office, Wash., D.C., 1962.
- U.S. Standard Atmosphere Supplements 1966*, U.S. Government Printing Office, Wash., D.C., 1966.
- U.S. Standard Atmosphere 1976*, NOAA S/T 76-1562, U.S. Government Printing Office, Wash. D.C., 1976.
- van de Hulst, H.C., *Light Scattering by Small Particles*, Wiley, New York, 1957.
- van de Hulst, H.C., "Multiple Scattering in Planetary Atmospheres," *J. Quant. Spectrosc. Radiat. Transfer*, **11**:785–795, 1971.
- van de Hulst, H., *Multiple Light Scattering Tables, Formulas and Applications*, Vols. 1 and 2, Academic Press, New York, 1980.
- van de Hulst, H.C. and K. Grossman, "Multiple Scattering in Planetary Atmospheres" in *The Atmosphere of Venus and Mars*, edited by J.C. Brandt and M.B. McElroy, 35–55, Gordon and Breach, New York, 1968.
- Van Vleck, J.H. and D.L. Huber, "Absorption, Emission and Linebreadths: A Semi-historical Perspective," *Rev. Mod. Phys.*, **49**:939, 1977.
- VanZandt, T.E., K.S. Gage, and J.M. Warnock, "An Improved Model for the Calculations of Profiles of C_n^2 and in the Free Atmosphere from Background Profiles of Wind, Temperature, and Humidity," in *Preprints*, Radar Meteorology, Conf. 20th, 1981, Boston, Mass., Amer. Meteorol. Soc., Boston, Mass., 1981.
- Volz, F.E., "Infrared Absorption by Atmospheric Aerosol Substance," *J. Geophys. Res.*, **77**:1017–1031, 1972a.
- Volz, F.E., "Infrared Refractive Index of Atmospheric Aerosol Substances," *Appl. Opt.*, **11**:755–759, 1972b.
- Volz, F.E., "Infrared Optical Constants of Ammonium Sulfate, Sahara Dust, Volcanic Pumice and Flyash," *Appl. Opt.*, **12**:564–568, 1973.
- Walters, D.L. and K.E. Kunkel, "Atmospheric Modulation Transfer Function for Desert and Mountain Locations: The Atmospheric Effects on r_o ," *J. Opt. Soc. Am.*, **71**:397–405, 1981.
- Warren, S.G. "Optical Constants of ice from the Ultraviolet to the Microwave," *Appl. Opt.*, **23**:1206–1225, 1984.
- Weinman, J.A., "Axially Symmetric Transfer of Light Through a Cloud of Anisotropically Scattering Particles," *Icarus*, **9**:67–73, 1968.
- Welch, R. and W. Zdunkowski, "Backscattering Approximations and Their Influence on Eddington-Type Solar Flux Calculations," *Contrib. Atmos. Phys.*, **55**:28–42, 1982.
- Whitby, K.T., "On the Multimodal Nature of Atmospheric Aerosol Size Distributions," Presented at VII Intern. Conf. on Nucleation, Leningrad, USSR, September 1973.
- Whitby, K.T. and B. Cantrell, "Atmospheric Aerosols—Characteristics and Measurements," Proc. Intern. Conf. on Environ. Sensing and Assessment, 3rd, Las Vegas, Nev., 14–19 September, IEEE, New York, 1976.
- Whitby, K.T., R.B. Hugar, and B.Y. Liu, "The Aerosol Size Distribution of Los Angeles Smog," *J. Colloid and Interface Sci.*, **30**:177–204, 1972.
- Whiting, E.E., "An Empirical Approximation to the Voigt Profile," *J. Quant. Spectrosc. Radiat. Trans.*, **8**:1379, 1968.
- Whitney, C.K., "Implications of a Quadratic Stream Definition in Radiative Transfer Theory," *J. Atmos. Sci.*, **29**:1520–1530, 1972.
- Whitney, C.K., "Efficient Stream Distributions in Radiative Transfer Theory," *J. Quant. Spectrosc. Radiat. Transfer*, **14**:591–611, 1974.
- Whitney, C.K. and H.L. Malchow, "Study of Radiative Transfer in Scattering Atmospheres," AFGL-TR-78-0101, ADA057359, June 1978.
- Winchester, L.W., Jr., G.G. Gimstead, and R.B. Wetzel, "Measurements of the Phase Function of Natural Particles," in *Atmospheric Effects on Systems Performance*, Proc. Soc. Photo-Optical. Int. Eng., **304**:106–118, 1981.
- Wiscombe, W., "The Delta-M Method: Rapid Yet Accurate Radiative Flux Calculations for Strongly Asymmetric Phase Functions," *J. Atmos. Sci.*, **34**:1408–1422, 1977.
- Wiscombe, W., "Atmospheric Radiation 1975–1983," *Rev. Geophys. Space Phys.*, **21**:997–1021, 1983.
- Wiscombe, W. and G. Grams, "The Backscattered Fraction in Two-Stream Approximations," *J. Atmos. Sci.*, **33**:2440–2451, 1976.
- WMO, "The Stratosphere 1981 Theory and Measurements," WMO Global Ozone Research and Monitoring Project Report No. 11, World Meteorological Organization, Geneva, 1982.
- Wyatt, P.J., V.R. Stull, and G.N. Plass, "Infrared Transmittance of Water Vapor," *Appl. Opt.*, **3**:229, 1964.
- Wyngaard, J.C., Y. Izumi, and S.A. Collins, "Behavior of the Refractive-Index Structure Parameter Near the Ground," *J. Opt. Soc. Am.*, **61**:1646–1650, 1971.
- Young, A.T., "Revised Depolarization Corrections for Atmospheric Extinction," *Appl. Opt.*, **19**:3427–3428, 1980.
- Zdunkowski, W., R. Welch, and G. Korb, "An Investigation of the Structure of Typical Two-Stream Methods for the Calculations of Solar Fluxes and Heating Rate in Clouds," *Contrib. Atmos. Phys.*, **53**:147–165, 1980.